

Laser power increase for GEO 600

Commissioning aspects towards an operation of GEO 600 at high laser power

Von der QUEST-Leibniz-Forschungsschule
der Gottfried Wilhelm Leibniz Universität Hannover
zur Erlangung des Grades

Doktor der Naturwissenschaften
– Dr. rer. nat. –

genehmigte Dissertation von

Dipl.-Phys. Christoph Affeldt

geboren am 26. Mai 1981 in Bad Pyrmont

2014

Referent: Prof. Dr. Karsten Danzmann (Leibniz Universität Hannover)
Korreferent: Dr. Stefan Hild (University of Glasgow)
Korreferent: Prof. Dr. Kenneth A. Strain (University of Glasgow)
Tag der Promotion: 25.03.2014

Abstract

The second generation upgrade of large-scale laser-interferometric *gravitational wave* (GW) detectors is almost completed. Their main goal is to surpass the sensitivity of the first generation instruments by one order of magnitude to significantly increase the probability of a first direct detection of GWs.

One of these GW detectors is GEO 600 that is located near Hanover. GEO 600 has a smaller baseline compared to its larger cousins LIGO and VIRGO. This difference in size is partly compensated by the application of several second generation techniques which have been in use for about one decade. To achieve similar sensitivities than expected for the Advanced Detectors at high frequencies, the GEO-HF upgrade program was proposed [Dan05]. It comprises several modifications of GEO 600 and is now almost completed. One part of the GEO-HF upgrade is a large increase of laser power which comes with various challenges. Coping with several of these challenges is the topic of this thesis.

Already before the GEO-HF upgrade started, it was impossible to make use of the full initially available laser power. The first topic of this thesis addresses this crucial problem. It is shown that the coupling of laser stray light to the displacement sensors of the local control system of the main suspensions prevented a stable operation of GEO 600 with increasing laser power. This investigation led to the implementation of a modulation-demodulation scheme for the local controls which rejects the stray light coupling signal from the error signals. This allowed for a routinely operation of GEO 600 at the maximum laser power that was available prior to GEO-HF.

Subsequently, a new laser system was installed to increase the available laser power. The initial in-vacuum *input optics* (IO) were not capable of being operated with significantly higher power due to thermal and stability reasons. Thus, the IOs were upgraded by replacing the electro-optical modulators, reducing the finesse of the two input mode cleaners and by modifying the mode-matching telescope onto the power-recycling cavity. In sum, the new laser system and the modified input optics provide 4.5 times more laser power for the main interferometer.

The interferometer cannot operate at such large laser power levels unless further limitations are removed. Important examples that are described and for which solutions are presented are optimizations in the frequency stabilization loop and at the automatic alignment of the Michelson interferometer. Sequentially, laser power levels up to almost a factor of three larger as compared to prior to GEO-HF are now achievable inside of the interferometer in DC lock. The heterodyne lock appears to be more stable and can be operated at even slightly higher laser power. At such high powers, the beam splitter thermal lens increasingly prevents further improvement.

Ultimately, the increase of laser power is meant to enhance the sensitivity at high frequencies. It is presented that the sensitivity of GEO 600 at high frequencies improves with the square root of laser power as expected. However, it is also shown that a not yet understood noise source, which increases with the laser power, limits the sensitivity at medium frequencies. Initial experiments to investigate this noise were performed and are summarized here. To understand and remove this laser power dependent noise at medium frequencies is one of the most important tasks to improve GEO 600.

Keywords: Gravitational wave detector, laser power increase, stray light

Zusammenfassung

Die zweite Generation der großen laserinterferometrischen Gravitationswellendetektoren steht kurz vor ihrer Fertigstellung. Ihr Hauptziel ist es, die Empfindlichkeit der ersten Generation um eine Größenordnung zu übertreffen und somit die Wahrscheinlichkeit einer ersten direkten Detektion von Gravitationswellen signifikant zu erhöhen.

Einer dieser Detektoren ist GEO 600 in der Nähe von Hannover. GEO 600 ist vergleichsweise kleiner als seine Verwandten LIGO und VIRGO. Dieser Größenunterschied wird teilweise kompensiert, indem schon seit etwa einem Jahrzehnt Techniken der zweiten Generation verwendet werden. Um auch in Zukunft vergleichbare Empfindlichkeiten bei hohen Frequenzen zu erreichen, wie sie für die anderen Detektoren erwartet werden, wurde das GEO-HF-Upgrade-Programm vorgeschlagen [Dan05]. Es beinhaltet eine Vielzahl von Modifikationen an GEO 600 und ist inzwischen weitestgehend abgeschlossen. Eine dieser Modifikationen ist eine enorme Erhöhung der verwendeten Laserleistung, welche mannigfaltige Herausforderungen mit sich bringt. Die Bewältigung vieler dieser Herausforderungen ist das Thema dieser Arbeit.

Bereits vor dem GEO-HF Upgrade bestand das Problem, dass die gesamte verfügbare Laserleistung nicht genutzt werden konnte. Das erste Thema dieser Arbeit behandelt dieses entscheidende Problem. Es wird gezeigt, dass die Kopplung von Laserstreulicht in die optischen Sensoren der Abstandsregelungen an den Testmassenaufhängungen einen stabilen Betrieb von GEO 600 mit zunehmender Laserleistung verhindert hat. Diese Untersuchung führte zu der Implementierung eines Modulation-Demodulations Schemas für die Abstandsregelsysteme der Testmassenaufhängungen, welches diese Kopplung aus den Fehlersignalen entfernt. Dadurch wurde der routinemäßige Betrieb bei der zu dieser Zeit maximal verfügbaren Leistung möglich gemacht.

Zur Steigerung der verfügbaren Laserleistung wurde ein neues Lasersystem installiert. Die ursprünglichen Eingangsoptiken sind aus thermischen- und Stabilitätsgründen nicht in der Lage bei deutlich höheren Laserleistungen betrieben zu werden. Somit wurden Modifikationen an den Eingangsoptiken notwendig, die aus einem Austausch von elektrooptischen Modulatoren, einer Reduzierung der Finesse der beiden Eingangsmodenfiltern und einer Änderung an dem Teleskop, das zur Modenanpassung der Eingangsmode auf die Mode des Power Recycling Resonators bestehen. Zusammengefasst stellen der neue Laser und die modifizierten Eingangsoptiken 4,5-mal mehr Leistung für das Interferometer zur Verfügung.

Das Interferometer kann mit so hohen Leistungen nicht betrieben werden, ohne dass vorher weitere Limitierungen beseitigt werden. Wichtige Beispiele, die beschrieben werden, sind Optimierungen an der Frequenzstabilisierungskette und an der automatischen

Strahlausrichtung des Michelson Interferometers. Dadurch wurden Laserleistungen erreicht, die im DC Betrieb beinahe um ein dreifaches über den üblichen Werten von vor dem GEO-HF Upgrade liegen. Der heterodyne Betrieb zeigt sich als noch stabiler und kann bei etwas größeren Leistungen ausgeführt werden. Allerdings erreicht die thermische Linse im zentralen Strahlteiler bei diesen hohen Laserleistungswerten eine Stärke, die eine weitere Leistungserhöhung zunehmend erschwert.

Letztendlich dient die Erhöhung der verwendeten Laserleistung der Verbesserung der Empfindlichkeit bei hohen Frequenzen. Deshalb wird am Schluss gezeigt, dass sich die Empfindlichkeit von GEO 600 bei hohen Frequenzen mit der Quadratwurzel der Laserleistung im Power Recycling Resonator verbessert. Allerdings wird auch beschrieben, wie eine bisher unverstandene Rauschquelle im mittleren Frequenzband von GEO 600, die mit der verwendeten Laserleistung ansteigt, die Empfindlichkeit einschränkt. Es werden erste Experimente zusammengefasst, die zur Untersuchung dieser Rauschquelle durchgeführt wurden. Die Beseitigung dieser Rauschquelle ist eine der wichtigsten Aufgaben zur Verbesserung von GEO 600.

Stichworte: Gravitationswellendetektor, Laserleistungserhöhung, Streulicht

Contents

Glossary	vi
List of Figures	vii
List of Tables	xi
1 Introduction	1
2 The GEO 600 gravitational wave detector	5
2.1 The Laser system	7
2.2 The in-vacuum input optics	9
2.2.1 The input mode cleaners	9
2.2.2 The mounting units	10
2.2.3 The mode matching telescope onto the power-recycling cavity	11
2.3 The dual-recycled Michelson interferometer	13
2.3.1 The Michelson interferometer	13
2.3.2 Power-recycling	15
2.3.3 Signal-recycling	16
2.4 From output to detection	18
2.4.1 Suspended output optics	18
2.4.2 The output mode cleaner	19
2.4.3 Squeezing in GEO 600	20
2.4.4 The GEO 600 sensitivity	20
2.5 The GEO 600 suspension systems and its local controls	23
2.5.1 The suspensions system	23
2.5.2 The suspension local control	25
2.6 The GEO-HF upgrade	27
3 High power instabilities and the influence of laser stray light on suspension local controls	29
3.1 Lock instabilities at high laser powers	30
3.1.1 A typical lock loss while using high laser power	31
3.2 Stray light coupling to the main suspension local controls	33
3.2.1 Influence of laser stray light to the operation of a local control	33
3.2.2 Determining the amount of stray light contamination	35
3.2.3 Amount of laser stray light at all main suspensions of GEO 600	40
3.3 A modulation-demodulation scheme for the local controls	44
3.3.1 Basic idea and requirements	44
3.3.2 The Modulation Drive	45
3.3.3 Primary tests at the test suspension	48

3.3.4	MD testing at the local control of the power-recycling suspensions	56
3.3.5	Local control noise projected to the GEO 600 sensitivity	58
3.3.6	Modulation Drive implementation at the GEO 600 main suspensions	62
3.3.7	Sensitivity at full laser power	64
3.4	Laser power limited operation during the VIRGO GEO 600 science run	67
3.4.1	A reminder: the upgrade of the output mirror suspensions	67
3.4.2	Sensitivity and stability during the science run	67
3.4.3	Scientific focus of the science run from a GEO 600 perspective	69
3.5	Stray light coupling to local controls of the remaining suspensions	70
3.5.1	Stray light at the BDIPR LC and resulting MD installation	70
3.5.2	Stray light at the BDO suspension local controls	72
3.5.3	Stray light coupling at the old input optics local controls	73
3.5.4	The effect of stray light coupling to the LCs of the reaction masses	76
4	The upgrade of the GEO 600 input optics	77
4.1	A 35 W laser for GEO 600	79
4.1.1	The Frontend	79
4.1.2	The optical layout on the laser bench	81
4.1.3	The need to limit the laser power until November 2012	83
4.2	The new RTP EOMs	85
4.2.1	EOM basics	86
4.2.2	The old LiNbO ₃ EOMs of GEO 600	88
4.2.3	Thermal properties of LiNbO ₃ and RTP	90
4.2.4	The new RTP EOMs	92
4.2.5	RF matching of GEO 600 EOMs	95
4.2.6	Initial experimental tests of the new RTP EOMs	95
4.2.7	Implementation in GEO 600	99
4.3	The new input mode cleaners	102
4.3.1	The need for a finesse reduction of the mode cleaners	102
4.3.2	The new input and output mirrors	103
4.3.3	The new mode cleaners in operation	106
4.4	Improvement of the PR mode matching	110
5	Towards higher laser power levels	115
5.1	Modifying the frequency stabilization loop	117
5.1.1	The frequency stabilization loop	117
5.1.2	Gain peaking and a double gain normalization	119
5.1.3	Further investigations at the frequency stabilization loop	120
5.1.4	New frequency stabilization loop electronics	122
5.2	High power instabilities in the Michelson automatic alignment	123
5.2.1	Gain peaking in the MIAA in DC lock	123
5.2.2	A possible reason for gain peaking in the MIAA	125
5.2.3	Changing the feed forward loop shape	126

5.3	Signal-recycling automatic alignment and power up in GEO 600	129
5.3.1	The effect of the alignment of the signal-recycling mirror on the circulating power	129
5.3.2	SRAA offset adjustment at high laser power	131
5.4	A trivial consequence of the laser power increase: PD saturation	133
5.5	Power fluctuations at high laser power	134
5.6	The thermal lens in the beam splitter	135
5.6.1	Observation of the beam splitter thermal lens	136
5.7	Partial thermal compensation and first indications for a cold locking issue	139
5.7.1	Laser power increase with a partially compensated thermal lens	139
5.7.2	First indications for cold locking issues	141
5.8	The current limit and how to beat it	143
6	The sensitivity of GEO 600 at high laser power	145
6.1	Laser power dependent noise at medium frequencies	146
6.1.1	A closer look into the mid-frequency noise	147
6.1.2	The reason for not routinely using higher laser power	148
6.1.3	The sensitivity at high frequencies	149
6.2	A summary of mid-frequency noise investigations	151
6.2.1	A first step	151
6.2.2	Saturation effects	151
6.2.3	Influence of the LG ₁₀ mode in the output beam	153
6.2.4	General influence of HOMs in the output beam	154
6.2.5	The effect of the SRAA on the medium frequencies	155
6.2.6	Scattering	155
7	Summary and outlook	159
A	Straylight measurements at all main suspensions	163
A.1	Projection factors and stray light projections for all main suspensions	163
B	The effect of stray light coupling to the LCs of the reaction masses	171
C	Further information about the modulation drive	173
C.1	Modulation drive circuit diagram	173
C.2	Further issues at the LCs of MFE and MFN if operated with MD	179
D	Further information about the EOMs of GEO 600	181
D.1	Thermal lens measurements of GEO EOMs	181
D.1.1	A direct comparison of various thermal lenses	181
D.1.2	LiNbO ₃ crystals	182
D.1.3	RTP crystals	183
D.2	RF matching of the EOMs	186
	Bibliography	189
	Acknowledgments	195
	Curriculum vitae	197

Glossary

AA	automatic alignment
AC	alternating current
AOM	acousto-optic modulator
AR	anti reflective
BDIPR	beam directing (mirror) into power-recycling cavity
BDO	beam directing (mirror at the) output
DC	originally: direct current. In this work also used for frequencies very close to 0 Hz such as for DC readout
DRMI	dual-recycled Michelson interferometer
EOM	electro-optical modulator
ESD	electro static drives
GW	gravitational wave
h	main gravitational wave channel
HPD	photodiode which detects the GW signal
HR	high reflective
IFO	interferometer
IO	input optics
LC	local control
LIGO	laser interferometric gravitational wave observatory
LiNbO ₃	Lithium Niobate
LO	local oscillator
MC	mode cleaner
MCE	end mirror of east arm
MCN	end mirror of north arm
MD	modulation drive
MFE	folding mirror in the east building
MFN	folding mirror in the north building
MI	Michelson interferometer
MMC	mirror mode cleaner (followed by 1 or 2 and a,b or c)
MPR	power recycling mirror
MSR	signal recycling mirror
OMC	output mode cleaner
PDBS	a photo diode monitoring a pick off beam from the BS AR coating
PRC	power recycling cavity
QPD	quadrant photo diode
RF	radio frequency
RIN	relative intensity noise
rms	root mean square
rot	misalignment in horizontal direction (rotation, yaw)
RTP	Rubidium Titanyle Phosphate
SB	side band
snr	signal to noise ratio
SR	signal recycling
SRC	signal recycling cavity
tilt	misalignment in vertical direction (tilt, pitch)

List of Figures

2.1	Simplified GEO 600 layout	6
2.2	The optical setup on the laser bench	8
2.3	Optical layout of the input optics	10
2.4	A schematic drawing of MU3	11
2.5	Schemata of heterodyne and DC readout	15
2.6	Calculated shot noise level of GEO 600 for different SR configurations	18
2.7	Exemplary sensitivity of GEO 600	21
2.8	A schematic drawing of a GEO 600 triple suspension system	24
2.9	A calibrated spectral density of the BS flag 1 error signal	26
2.10	Calculated shot noise of GEO 600 over the course of the GEO-HF upgrade	28
3.1	A typical lock loss at high laser power	31
3.2	Dependance of power fluctuations on the laser power	32
3.3	Flag assembly at a GEO like suspension model	34
3.4	A flag error signal before and during a lock loss	35
3.5	Spectral density of the circulating power in the main IFO during a stray light projection	36
3.6	Spectral density of a flag error signal during a stray light projection	37
3.7	A stray light projection for MFE flag 4	39
3.8	Stray light projections for all BS flags	42
3.9	A further glance on an exemplary lock loss	43
3.10	Modulation drive scheme in its final version	46
3.11	The GEO 600 test suspension	50
3.12	Modulation drive tests (1)	51
3.13	Modulation drive tests (2)	52
3.14	Modulation drive tests (3). Error signals versus feedback signals	55
3.15	Error signal spectral densities of the MPR suspension LC flag 1 with and without MD	56
3.16	Coherence between the error signal of the MPR suspension LC flag 1 with MD and the GEO 600 sensitivity	57
3.17	A noise injection at 129 Hz to the LC feedback in tilt of the MCN suspension and its effect on h	59
3.18	The displacement noise of the MCN flag 3 error signal projected to h	60
3.19	Error point spectral densities of BS flag 1 with and without MD	63

3.20	Relative power fluctuations of the circulating power with and without MDs	64
3.21	GEO 600 sensitivity in April 2011 for 2 kW and 3 kW impinging on the BS	65
3.22	Sensitivity before and after the BDO suspension upgrade	68
3.23	Typical sensitivities of VIRGO and GEO 600 during the joint run in summer 2011	69
3.24	Laser stray light projection for all four BDIPR flags	71
3.25	Laser stray light projection for all four BDO flags	74
3.26	Stray light projection for MMC1b flag 4	75
4.1	The principal setup of the four stage amplifier with a NPRO as seed source	80
4.2	Optical layout of the Frontend	81
4.3	The new optical setup on the laser bench	84
4.4	A module carrying two LiNbO ₃ EOMs	88
4.5	RTP EOMs (1)	94
4.6	RTP EOMs (2)	94
4.7	RF matching test setup	95
4.8	Optical setup for the measurement of the achievable modulation depth with the new EOMs	97
4.9	An EOM unit on MU3 during the replacement.	101
4.10	Spectral densities of one of the MC1 automatic alignment error signal for three different input laser powers	107
4.11	Spectral densities of one of the MC2 automatic alignment error signal for three different input laser powers	108
4.12	Circulating laser power in the IFO versus laser power reflected by MPR for the initial mode matching telescope	111
4.13	Laser power reflected by MPR divided by the power injected into the IFO for the initial mode matching telescope	112
4.14	Circulating laser power in the IFO versus laser power reflected by MPR for the modified mode matching telescope	113
4.15	Laser power reflected by MPR divided by the injected power into the IFO for the modified mode matching telescope	114
5.1	A schematic overview of the power-recycling lock and the associated frequency stabilization of GEO600	118
5.2	Gain peaking in the longitudinal error signal of the PRC	120
5.3	An in loop measurement of the MC2 lock that is part of the frequency stabilization loop.	121
5.4	A measurement of the MIAA tilt loop in heterodyne lock at two different values for the circulating laser power in the IFO	124
5.5	A measurement of MIAA tilt loop in DC lock at three different values for the circulating laser powers	125
5.6	The old shape of the MIAA longitudinal to tilt feed forward at MCN	127

5.7	The new shape of the MIAA longitudinal to tilt feed forward at MCN . . .	127
5.8	A measurement of MIAA tilt loop in DC lock at 2.2 kW and at 3.5 kW impinging on the BS	128
5.9	The effect of MSR alignment on the amount of fluctuations in the circulat- ing laser power	130
5.10	Relative intensity noise of the circulating laser power at different laser powers	134
5.11	The change of the dark port power, caused by the BS thermal lens at different laser power levels	138
5.12	Reduction of the dark port power by partially compensating for the BS thermal lens	140
5.13	Circulating laser power in the PRMI in heterodyne lock during a fast power up experiment	143
6.1	Typical sensitivities of GEO 600 in 2012 at different laser powers	147
6.2	Typical sensitivities of GEO 600 in 2013 at different laser power	148
6.3	Spectral ratios of the sensitivity at three different power levels compared to low power	149
6.4	The influence of the SRAA on noise at medium frequencies	156
7.1	Typical sensitivities of GEO 600 compared to exemplary sensitivities of VIRGO+ and Enhanced LIGO	162
A.1	Laser stray light projections for all six BS flags	165
A.2	Laser stray light projections for all six MCE flags	166
A.3	Laser stray light projections for all six MCN flags	167
A.4	Laser stray light projections for all six MFE flags	168
A.5	Laser stray light projections for all six MFN flags	169
A.6	Laser stray light projections for all six MPR flags	170
C.1	Modulation drive circuit diagram (1)	174
C.2	Modulation drive circuit diagram (2)	175
C.3	Modulation drive circuit diagram (3)	176
C.4	Modulation drive circuit diagram (4)	177
C.5	Circuit diagram of the modulation drive's local oscillator source	178
C.6	A spectrogram of one of the MFN LC error signals	180
D.1	A thermal lensing measurements of LiNbO ₃ EOMs	183
D.2	A thermal lensing measurements of the new RTP EOM unit that was in- stalled on MU2	184
D.3	A thermal lensing measurements of the new RTP EOM unit that was in- stalled on MU3	185
D.4	A simplified RF matching circuit	187

List of Tables

3.1	Coupling factors for all main suspension local controls	40
4.1	RF frequencies, powers and voltages before the corresponding matching circuits of the LiNbO ₃ EOMs	90
4.2	A comparison of selected properties of LiNbO ₃ and RTP	91
4.3	RF frequencies, powers and voltages before the corresponding matching circuits of the new RTP EOMs.	100
4.4	Specified transmittance of the old MC mirrors	104
4.5	Specified properties of the new MC mirrors	105
4.6	Specified and measured transmittance T of the HR coatings and residual reflexion R of the AR coatings	106
6.1	Relative power in the LG ₁₀ mode at the dark port for different circulating powers in the DRMI	153
A.1	Projection factors that were used for the stray light projections	164
D.1	Measured thermal lenses for the GEO 600 RTP EOMs compared to selected other components	181

1 Introduction

The General Theory of Relativity was invented by Einstein in 1916 [Ein16]. One consequence of the General Theory of Relativity is the existence of *Gravitational Waves* (GWs). GWs are perturbations in space-time that propagate with the speed of light. Sources of GWs are accelerated masses such as coalescing compact binary systems or supernovae [Bis02]. The observation of GWs and the detailed studies of the corresponding waveforms will provide new possibilities of astronomy. New insights can be expected into the physics in the in-spiral, merger and ring down phases of the aforementioned coalescing compact binary systems or into processes which occur during a supernova explosion. Furthermore, GWs could increase the knowledge about the early phases of the universe at a time before it became transparent for electro-magnetic radiation.

The important effect of GWs with respect to the ongoing attempt to detect them directly, is that they change the distance between freely falling test masses. However, this effect on space time is – from the point of view of an observer on earth – rather small. It is predicted that astrophysical sources cause amplitudes or strains in space which are in the order of 10^{-21} or lower in the case of ground-based observations [Gra12]. To date, no GWs were observed by direct means but an indirect confirmation of the existence of GWs was accomplished. R. A. Hulse and J. H. Taylor observed the orbital decay of a binary system by using radio-signals. Their observations agreed well with the predictions made by the General Theory of Relativity [Hul75].

To make use of the expected scientific insights which GWs provide about their sources, massive efforts have been taken to detect and observe GWs. This effort started with the construction of so-called resonant bar detectors [Web60]. One major disadvantage of resonant bar detectors is that they only reach a significant sensitivity to GWs at a small frequency band around their resonance frequencies, but it is desirable to have a detection band over several orders of magnitude in frequency. A different type of instrument is capable of providing a much wider detection band. These instruments are interferometric GW detectors.

Interferometric GW detectors are based on kilometer scale *Michelson interferometers* (MI). They make use of the MI's property to detect tiny length changes in their two arms. Such length changes can be caused by a GW. If a GW passes the MI, it modulates the effective arm length of the MI differentially and thus changes the resonance condition of the two interfering light fields in their arms. A detailed description of these instruments can be found in [Sau94], for instance. Prominent examples of GW detectors are the two LIGO observatories, VIRGO and GEO 600. These instruments were constructed in the late 90ies and started the search for GWs shortly after.

The initial sensitivities of the interferometric GW detectors were already impressive but not sufficient to deliver first detections. After first upgrades, LIGO and VIRGO even surpassed a sensitivity of $10^{-22}/\sqrt{\text{Hz}}$ between approximately 100 Hz and 1 kHz. These upgrades, called Enhanced LIGO [Smi09] and VIRGO+ [Ace08] were only an intermediate step on the road to second generation GW observatories. The so-called Advanced LIGO and Advanced VIRGO detectors are expected to surpass the initial sensitivity of the first generation by one order of magnitude. In Japan, a further second generation detector which is called KAGRA is in the process of being built.

A main difference of GEO 600 to the other interferometric GW detectors is its smaller baseline. While LIGO and VIRGO have an arm length of 4 km and 3 km, respectively, GEO 600's arms are only 600 m long. To partially compensate for this obvious disadvantage, several second generation techniques have already been used since about one decade. In order to further be able to partly compete with the expected sensitivities of Advanced LIGO and Advanced VIRGO at high frequencies, the GEO-HF upgrade was proposed [Dan05]. The GEO-HF upgrade aims at an improvement of the GEO 600 sensitivity at high frequencies, i.e. above roughly 600 Hz. Above 600 Hz, GEO 600's sensitivity is limited by shot noise. The shot noise h_{SN} is white in spectral density. Its effect on the amplitude spectral density strain sensitivity of a GW detector which consists of a MI can be described by the following formula [Sau94]:

$$h_{\text{SN}} = \frac{1}{L} \sqrt{\frac{\hbar c \lambda}{2\pi P}}. \quad (1.1)$$

Here, L is the arm length of the interferometer, \hbar is the Planck constant, c is the speed of light, λ is the wavelength of the light used in the GW detector and P is the light power which circulates inside the interferometer. One can see that there are not many parameters to tune with respect to a reduction of shot noise. The most obvious parameter to be tuned is the light power P which circulates inside the MI. The shot noise level decreases with the square root of the power. Therefore, the sensitivity of an interferometric GW detector to GWs can be improved at frequencies at which shot noise is the dominant noise source if the light power is increased. Such an increase of circulating power is a main part of the GEO-HF upgrade.

However, an increase of the circulating light power is not a simple task. The thesis at hand addresses various challenges that had to be overcome in order to successfully increase the circulating light power in GEO 600's MI.

This thesis starts with an overview about the GEO 600 GW detector in chapter 2 to support the topics which are discussed throughout this thesis.

Chapter 3 discusses the first obstacle and its solution towards an operation at higher laser power. This is the coupling of laser stray light to the so-called shadow sensors of the local control systems of the main test mass suspensions. This coupling mechanism

prevented a stable operation of GEO 600 at high power. To reject the stray light caused component from the local control error signals, a modulation-demodulation scheme was developed, tested and implemented at the respective local controls. Its installation enabled a stable operation of GEO 600 at the maximum laser power which was available at that time.

To provide more laser power, a new laser system was installed. To allow for operation at higher laser power, modifications at the input optics were needed. These Modifications, called the input optics upgrade is described in chapter 4 as well as the new laser system. A main benefit of the input optics upgrade is an additional enhancement of the available laser power by a factor of 1.75.

Chapter 5 discusses challenges for the lock stability of the main IFO that arose from the significant increase of available laser power. Modifications of the frequency stabilization loop and the automatic alignment of the Michelson interferometer were needed to allow stable operation at laser power levels which are about three times higher than prior to GEO-HF. Additionally, chapter 5 displays the immense impact of the thermal lens in the beam splitter of the MI at achieved laser power levels. A system to compensate for the thermal lens is needed. Actually, such a system is in the process of being installed while this thesis is handed in. This system is not part of the described work but a follow-up work of [Wit09].

Finally, chapter 6 addresses the important aspect of the GEO 600 sensitivity at high laser power. It is shown, that at high frequencies, the sensitivity improves as expected with the square root of the laser power. However, it is also shown that a not yet understood noise source, which increases with the laser power, limits the sensitivity at medium frequencies. Since astrophysical sources appear to be more likely at medium frequencies, this laser power dependent noise forces us to operated GEO 600 at medium laser power levels on a routinely bases. Chapter 6 also provides a summary of investigations which were carried out to understand this noise. However, further effort is needed to fully understand this noise and subsequently to remove it.

2 The GEO 600 gravitational wave detector

Increasing the laser power in a *gravitational wave* (GW) detector affects many parts of the instrument. A basic understanding of the instrument of interest – which is GEO 600 in our case – is needed to understand the topics that are discussed in this thesis. In this chapter, an overview of GEO 600 and the GEO 600 upgrade program called GEO-HF is given. Here, the focus is put on crucial subsystems and the optical layout.

We will follow the path of the light on its way from its creation in the laser system to the detection *photo diode* (PD)¹. On its way it will pass all optical systems of interest. It will be distinguished between the laser and the laser bench, the input optics, the dual-recycled Michelson interferometer and the output and detection part.

This chapter starts with a sketch of the *old* laser system and the *old* input optics. During the work of this thesis, the laser system was replaced and the input optics were upgraded. In this chapter, the initial systems are described. The necessity for modifications at these systems within the GEO-HF upgrade and the new systems themselves as well as their installation process are described in chapter 4.

Further on, an introduction about the core of GEO 600, the *dual-recycled Michelson interferometer* (DRMI), is given. The DRMI received several changes in the last years. The readout method was changed and two major modifications at the signal-recycling cavity were made. These changes are summarized and the current configuration of the DRMI is described.

At the end of the light path description, an overview of the output optics is provided. They consist of suspended beam steering and focusing mirrors, an output mode cleaner and the detection photo diode. At this point, a look at the recent GEO 600 sensitivity is taken and major noise sources which limit the sensitivity are listed.

In addition, the mirror suspension systems and their local controls are described. They are important for the issues that are discussed in the following chapter.

The chapter at hand concludes with a brief overview of the GEO-HF upgrade program. GEO-HF aims at an improvement of the GEO 600 sensitivity at high frequencies. At the date of writing this thesis, January, 2014, the GEO-HF upgrade is almost completed. The only exceptions are residual commissioning work with respect to laser power increase and an improvement of the observed squeezing.

¹ Only a tiny amount of the laser light that is created in the laser system makes its way to the detection PD. Actually it is about 0.02 % in the case of GEO 600.

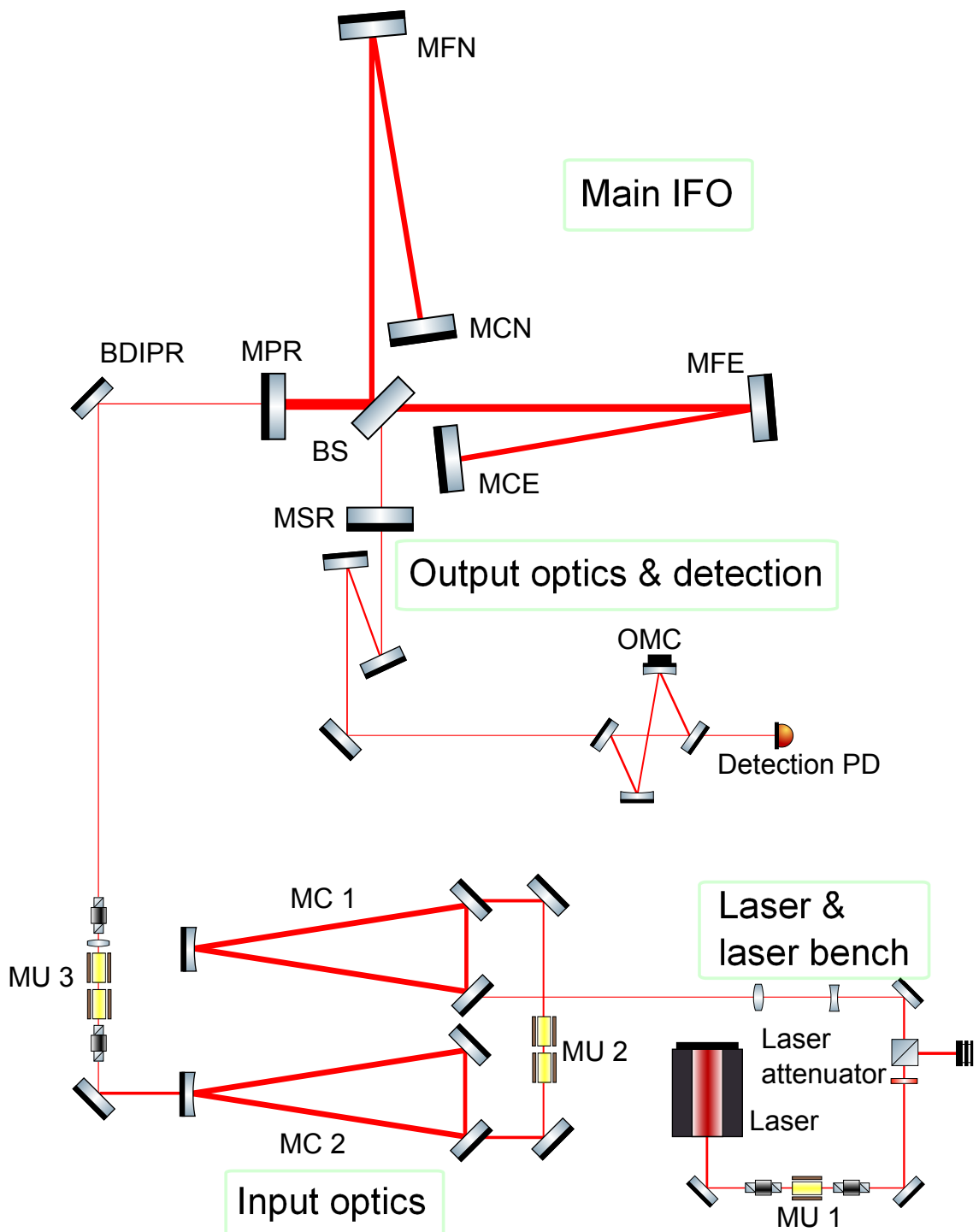


Figure 2.1: Simplified GEO 600 layout. Not to scale. The different subsystems that are shown in this figure are described in this section. For clarity, GEO 600 is split into four subsystems. These are laser & laser bench, input optics, the dual-recycled Michelson interferometer and the output & detection part. Except for the laser & laser bench, the orientation of components as shown in this figure reflects the actual arrangement of the instrument. The GEO 600 squeezer, being irrelevant for the content of this thesis is omitted.

2.1 The Laser system

A Michelson based GW detector needs a laser source that meets strict requirements for stability, noise performance and reliability. Until September 2011, these requirements were met by a 15 W laser system [Zaw02]. The major work that is described in chapter 3 was done while this system was still in use. In chapter 4.1, the replacement of this old laser system by a master amplifier system is described. This new system has a maximum output of about 35 W and it is the same model the Enhanced LIGO detectors used as a laser source. The Advanced LIGO detectors are still using this type as pre-amplifier of an 200 W laser system [Bog13]. In the following, the initial laser system will be referred to as “old laser” while the new system will be referred to as “new laser”. More detailed information about the old laser than provided here can be found in [Heu04, Fre03] while the new laser is described in chapter 4.1 and [Fre07].

The old laser is an injection locked master-slave system. This means two laser oscillators were in use. A master laser (namely a *Non-Planar-Ring-Oscillator* (NPRO)) provides a laser beam of about 1 W and an output wavelength of 1064 nm with a high stability in amplitude and frequency. This beam is optically connected to a slave laser which provides a high power beam with similar qualities in amplitude and frequency as the master laser, due to the injection locking technique. Even though this system was supposed to deliver 15 W output power [Zaw02], 12 W to 14 W were more realistic numbers for its operation in GEO 600 according to later documentations like [Fre03, Smi06].

Figure 2.2 shows the initial optical setup on the laser bench. After exiting the slave laser and amplifier, respectively, the laser beam passed several optics on an optical bench. Apart from beam steering and mode matching optics, these optical components fulfilled several crucial tasks. A *mounting unit* (MU) hosts two *Faraday Isolators* (FIs) and an *Electro-Optical Modulator* (EOM) [Goß04]. The FIs are adjusted for maximum extinction of the reverse light. The EOM is the model PM25 from Gsaenger which uses KTP as the refractive material. It is part of a resonant circuit to generate 25 MHz modulation sidebands for the locking of the first input mode cleaner. Originally, this first MU, called MU1 was meant to be suspended in vacuum similar to two more MUs as described further below. The idea of also suspending MU1 was abandoned in an early stage and it was placed instead directly on the laser bench.

Another EOM (PCML) was used as a fast actuator for the frequency control loop. After the new laser was installed the EOM was removed because a similar model is included in the 35 W laser system. Another mentionable component on the laser bench is a laser beam attenuator. It consists of a remote controllable $\lambda/2$ wave plate and a polarizing beam splitter to adjust the laser power used for operating the IFO. After this attenuator, the laser beam is sent towards the first input MC in the vacuum system. The light is s-polarized from this point on.

The laser beam attenuator fulfills an important task for the operation of GEO 600 and it is still in use since the new laser was installed. It is used to remotely adjust the laser power GEO 600 is operated with to defined values as required.

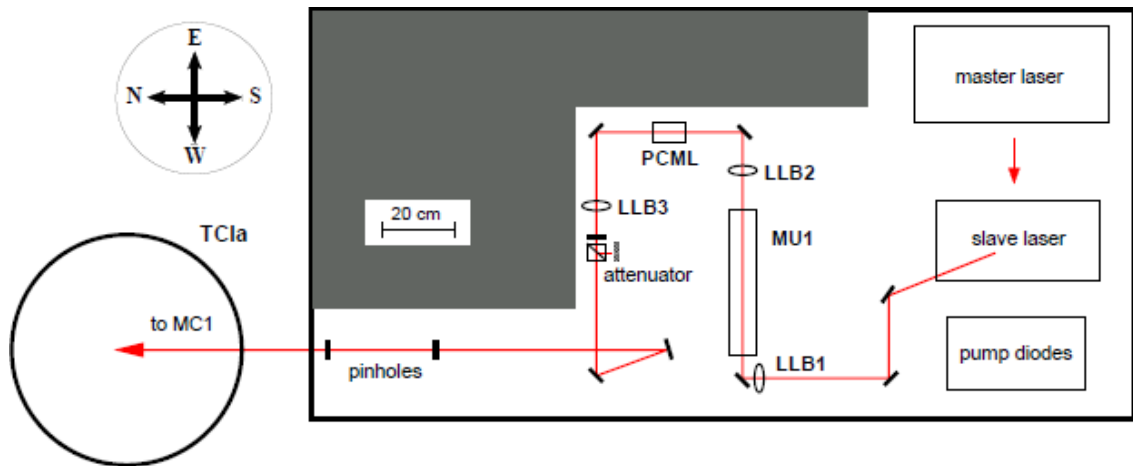


Figure 2.2: The optical setup on the laser bench while the old laser system was still in use [Fre03]. Omitted are optics between master and slave laser as well as the auxiliary reference cavity and its input optics. The latter was placed in the gray area.

Each component on the laser bench shows an optical loss up to some point. In the majority of cases, these losses are well below 1%. However, the two FIs show significantly more losses than the other elements. Each of them has a loss of about 10%. Eventually, about **8 W is the maximum power** available that could be coupled into MC1 before the new laser was installed. The new laser system and the corresponding new layout on the laser bench is described in more detail in chapter 4.1.

2.2 The in-vacuum input optics

Before the light is coupled into the main IFO it passes the *Input Optics* (IO). They are suspended in the vacuum tanks TCMA and TCMb. The key components the IO consist of are two *Mode Cleaner* (MC) cavities and two MUs. In addition, a mode matching telescope to the *Power Recycling Cavity* (PRC) is part of the IOs. Beam steering mirrors are used for the alignment into the two MCs and the IFO, respectively. The layout of the IOs is shown in figure 2.3. Detailed descriptions about the IOs are given in [Goß04, Fre03], while the corresponding suspension systems are describes in detail in [Goß04]. The IOs and their modifications with respect to the GEO-HF upgrade are the major topic of chapter 4.

2.2.1 The input mode cleaners

The MCs are two ring cavities that are similarly constructed. The main task of the MCs is to filter transverse modes of the injected laser beam [Fre03]. Above their cavity pole they also provide attenuation of laser frequency and laser amplitude noise. Furthermore, they serve as reference cavities for pre-stabilizing the laser frequency [Fre03] as described in [Fre03] and [Gro03]. Each MC consists of two partly transmissive mirrors that are used as input and output couplers, respectively, and is completed by a third high reflective mirror to form a triangular cavity. Furthermore, these mirrors are suspended as double pendulums. Each mirror is referred to by the acronym MMC1 or MMC2, supplemented by a,b or c like shown in figure 2.3¹. The round trip lengths are 8 m and 8.1 m for MC1 and MC2, respectively. In the original design both MCs had a (fairly high) finesse of about 2000. In chapter 4.3, the process of decreasing their finesses by changing the individual input and output couple mirrors is described. The optical parameters of the new and the old MCs are given there, too.

For both MCs, two of their three mirrors have flat inner surfaces while the remaining one has a concave radius of curvature of about 6.7 m which defines their spatial eigenmodes. The back surfaces are AR coated and flat except for the b mirror of MC2. It has a curved (AR coated) backside that serves as part of a mode matching telescope to the PRC. Apart from the slightly different round trip lengths, the MCs differ in the way the input and output coupler mirrors are arranged. As can be seen in figure 2.3, for MC1 the flat a and c mirrors are the partly transmissive in and out couplers respectively. In the case of MC2, the flat a mirror also serves as an input coupler while the curved b mirror is the out coupler.

With respect to a significant laser power increase, the MCs need modifications. Even

¹ The first M stands for “mirror” followed by the respective mode cleaner short cut. Both mode cleaner input mirror acronyms end with an “a”. The final letter of the other mirrors are given clockwise in alphabetical order like shown in figure 2.3.

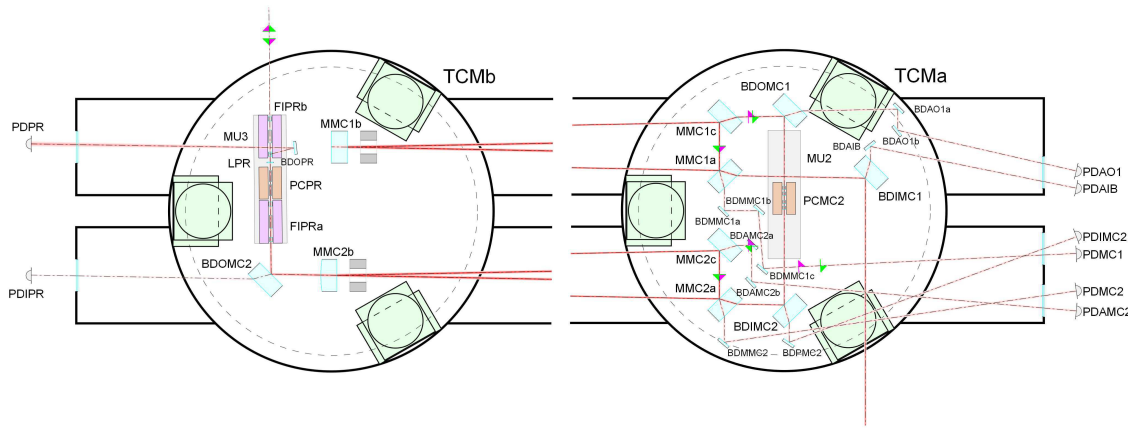


Figure 2.3: Optical layout of the input optics. The laser beam enters on the bottom right side and is directed by beam steering mirror, namely BDIMC1 into MC1. The output beam of MC1 passes two EOMs and gets directed into MC2. After leaving MC2, the beam passes two further EOMs, two FIs and a mode matching telescope. The mode matching telescope consists of the curved out couple mirror of MC2 and a lens on MU3. The beam leaves the IOs, as can be seen on the top left in this figure and is directed towards the main IFO as shown in figure 2.1. Please note, that the photo diodes that are shown in this figure are place holders for several optics and photo diodes that are positioned on breadboards outside the vacuum. These components are described in [Fre03].

though unwanted light fields were more than sufficiently suppressed by these cavities, their conservatively high finesses resulted in disadvantages. First, the light field which is stored in the MCs was so strong, that initial locking at input laser powers above 3 W was almost impossible due to radiation pressure effects. Second, the TEM_{00} mode itself got strongly attenuated. 50% of the injected fundamental mode got lost in the MCs. We will discuss both aforementioned aspects in chapter 4.3. A more detailed description of the input MCs is given in [Fre03]. Their longitudinal control is described there as well, while the aspects concerning their auto-alignment system can be found in [Gro01]. The suspension system of the IOs is explained in [Goß04].

2.2.2 The mounting units

Two more mounting units exist apart from MU1. These are MU2 and MU3 and are not placed on the laser bench as MU1 is. Their positions can be seen in figure 2.3. Both are suspended and support several optical components as described in [Goß04]. MU2 is arranged between MC1 and MC2 and carries two EOMs for imprinting modulation sidebands on the laser beam for the angular and length sensing control of MC2 and the PRC, respectively. The modulation frequency for the PRC lock is chosen such that it is resonant in MC2 to pass unhindered.

MU3 is placed behind MC2 and supports two Faraday isolators, two EOMs and a mode matching lens. A schematic drawing of MU3 is given in figure 2.4. As it is the case for MU1, the FIs are adjusted for maximum extinction of reverse light. The EOMs on MU3 generate the modulation sidebands for the angular and length sensing and control of the *Michelson Interferometer* (MI) and the *Signal Recycling Cavity* (SRC), respectively. In addition, the EOM used for the generation of the SR modulation serves as a fast actuator in the frequency stabilization loop. All EOMs on MU2 and MU3 used *Lithium Niobate* (LiNbO_3) crystals as the refractive material. This material shows strong thermal lensing effects and even gets damaged at laser powers GEO-HF is supposed to be operated at. The replacement of these LiNbO_3 EOMs by new *Rubidium Titanyle Phosphate* (RTP) EOMs that withstand much higher laser power is described in chapter 4.2.

2.2.3 The mode matching telescope onto the power-recycling cavity

The mode matching lens is part of a mode matching telescope onto the PRC and has a focal lens of 1 m. Beside the lens sitting on MU3, the mode matching telescope consists of the curved b mirror of MC2, as mentioned above. The surface of MMC2b that is directed towards MC2 is concave and has a *radius of curvature* (RoC) of about -6.8 m. Its other surface is convex and its RoC is about 35 cm. The focal length of the two lenses it consists of were not optimally chosen in the initial design of the IOs. The visibility to the PRC was only about 80% at default operating power, i.e. 2 kW impinging at the beam splitter. For higher input powers, the visibility decreased due to thermal lensing in the FIs and EOMs on MU3. The improvement of the mode matching to the PRC that was achieved during the IO optics upgrade is described in chapter 4.4.

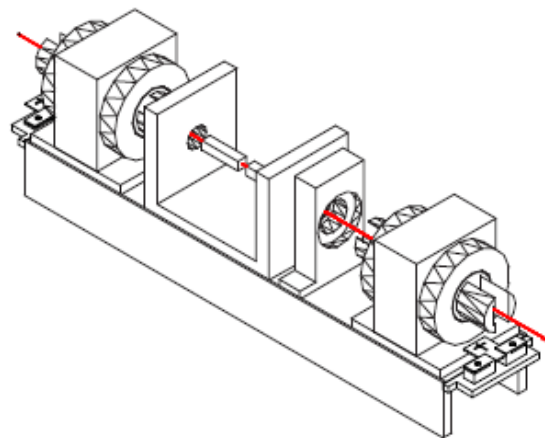


Figure 2.4: A schematic drawing of MU3, the third and final mounting unit. This platform is suspended and supports two FIs, two EOMs and a mode matching lens [Goß04].

The actual laser power that is available to get coupled into the main IFO was much smaller than the laser power injected into the first MC. For about 8 W right before MC1 only **a maximum of 4 W total laser power** could be sent towards the IFO. The major loss of about 50 % in total at the IOs are due to the MCs themselves. However, other parts contribute too like losses at the FIs in MU3 for instance. According to [Fre03] a loss of 10 % was measured for the FIs before their installation.

The laser beam that exists the IOs is directed by a beam steering mirror, namely BDIPR to the Dual-recycled Michelson interferometer.

2.3 The dual-recycled Michelson interferometer

GEO 600's core instrument is a *Dual-recycled Michelson interferometer* (DRMI) with 600 m long arms that are folded once. Due to the one-time folded arms of the *Michelson interferometer* (MI), an effective arm length of 1200 m is achieved. The term *dual-recycled* (DR) refers to the fact that two different recycling techniques are used. These are the *power-recycling* (PR) technique and the *signal-recycling* (SR) technique. The following provides an introduction to these systems and to the readout technique.

2.3.1 The Michelson interferometer

To date, all interferometric, large-scale GW detectors use a MI as their key subsystem. The MI was originally designed by Albert Michelson and Edward Morley to measure the relative motion of the earth through the aether [Mic81]. As generally known, the aether theory proved to be wrong and it was found that the speed of light is independent from the motion of the observer. Eventually, this led to Einstein's theory of *special* relativity [Ein05]. However, the MI proved to be an excellent tool to measure differential length changes in its two arms. Thus, it became *the* instrument of choice to prove the existence of one of the predictions that Einstein made in his theory of *general* relativity [Ein16, Ein18]: gravitational waves.

The upper part of figure 2.1 shows the layout of the MI for the case of GEO 600. The laser beam leaves the IOs to the north and is directed by a beam directing mirror, namely BDIPR, to the east into the MI. Beforehand, modulation SBs for the MI lock were imprinted on the laser beam by one of the EOMs that are placed on MU3. The laser beam is split into two beams of almost equal intensity by the *beam splitter* (BS). These two beams run through the north and the east arm, respectively. Both arms are folded once by the mirrors MFE and MFN in the far east station and far north station. The two end stations are separated by 600 m each from the central building that houses all other major optics. Except for the BS and the two folding mirrors, the MI comprises of the two "close" mirrors MCE and MCN. MCE and MCN serve as the end test masses. They reflect the respective beams back to the far mirrors and thereby to the BS.

The MI is adjusted such that the two light fields that return from the arms interfere almost destructively at the output port in the south: The MI is operated close to the so-called dark fringe. Furthermore, the MI is built using high quality mirrors with small losses. Thus, the light is mostly reflected to the input port which is also called the "bright port". The controlled MI behaves like a mirror for the input light.

Differential arm length fluctuations as caused by a passing GW result in a phase shift in the two interfering light fields. This phase shift results in amplitude fluctuations of the light field at the output port, the so-called dark port. A different viewpoint for this is that differential arm length fluctuations create signal SBs on the carrier light that leave the MI via the dark port. To detect the signal SBs with a PD, an optical *local oscillator* (LO)

is needed. As optical LO serves a fraction of the carrier light itself. As mentioned before, the MI is not operated at the dark fringe, but close to it. The *dark fringe offset* (DFO) allows a small amount of the laser light to leave the MI at the dark port. In the case of GEO 600, as discussed here, the amount of light is about 6 mW in default operation. The corresponding beat signal between the residual DFO induced carrier light and signal SB light is detected by a PD. A differential strain is thereby transformed into a voltage. The PD signal is finally calibrated to obtain the main detector output, “h” [Smi06].

The readout

Operating the MI close to the dark fringe and detecting the beat signal of signal SBs with the residual carrier light, as just described, is called DC readout. It was implemented in GEO 600 in September 2009 [Deg10] and routinely used since then. Before the GEO-HF upgrade started, GEO 600 used heterodyne readout as all other large scale GW detectors did. Figure 2.5 illustrates the scheme of heterodyne and DC readout. For heterodyne readout, the MI is operated at the dark fringe instead of close to it. The optical LO signal is provided by *radio frequency* (RF) SBs imprinted on the laser beam by an EOM before the DRMI. An asymmetry in the MI’s arm length, called the Schnupp asymmetry, allows the RF SBs to leave via the dark port. In the case of GEO 600, the Schnupp asymmetry is 69 mm. A RF beat signal is created between the RF SBs and signal SBs and detected by a PD. To obtain the main detector output, this signal needs to be demodulated at the corresponding RF frequency.

Heterodyne readout has the impression of being more complex than DC readout. However, heterodyne readout was expected to be more robust against technical noises [Pri12]. In years of operation, it turned out that heterodyne readout has several drawbacks. Fluctuations in the amplitude and frequency of the RF SBs coupled to the detector output, creating noise. Furthermore, the shot noise level is higher by a factor of $\sqrt{2/3}$ to $\sqrt{2}$ for heterodyne readout [Hil09] and the implementation of squeezing is more complicated [The11].

With the implementation of DC readout in GEO 600, the heterodyne technique was not fully abandoned. During lock acquisition, the IFO is first locked in heterodyne and the DFO is induced slightly later. The heterodyne lock did also prove to be a good diagnostic tool for experiments, i.e. with respect to a laser power increase, as described in chapter 5. However, the actual operation of searching for GWs uses DC readout. For the Advanced LIGO detectors, Advanced VIRGO and KAGRA the use of DC readout is foreseen [Har10, The09, Aso12]. As in GEO 600, it was also demonstrated in Enhanced LIGO [Fri12].

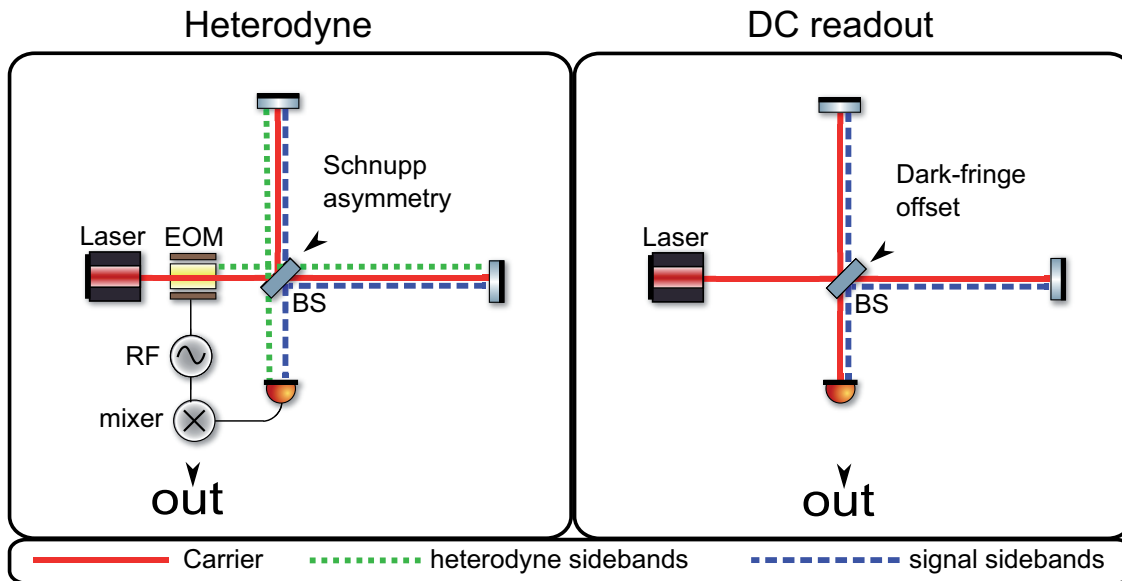


Figure 2.5: Schemata of heterodyne and DC readout.

2.3.2 Power-recycling

The PR technique was first suggested by Drever and Schilling [Dre83a] and was first experimentally employed in the Garching 30 m Prototype [Sch97]. PR benefits from the fact that a MI is operated at or close to the dark fringe. Almost 100% of the light that is sent to GEO 600's MI is reflected back towards the IOs. Because the MI behaves like a mirror one can form a cavity by placing an additional mirror, the *power-recycling mirror* (MPR), between the IOs and the MI. This cavity is called *power-recycling cavity* (PRC). We obtain a *power-recycled Michelson interferometer* (PRMI). Depending on the reflectivity of MPR and the losses within the MI, the PRMI has an additional build-up of the laser power. According to equation 1, an additional power build-up has an obvious benefit: While the shot noise increases proportional to the square root of the laser power in the IFO, the signal increases proportional to the laser power. Thus, the shot noise compared to the signal decreases with the square root of the laser power in the IFO.

The transmittance of MPR is 0.1%. If we assume that the transmittance of MPR matches roughly the losses in the MI, this allows for a theoretical power build up factor of 1000, according to equations 26 and 27 in [Miz95]. In reality, the PR factor of GEO 600 is slightly above 800, if operated in combination with signal-recycling, due to extra losses within the MI. Signal-recycling is discussed in the following paragraph.

One aspect of the PRMI is of significant importance for the topic discussed in chapter 3. The major loss channel for the injected laser light is scattering at the corresponding PRMI mirrors and residual transmittance of the mirrors themselves. Scattering is caused by tiny mirror imperfections. The losses that are caused by mirror imperfections are negligible

for the case of the MI, but become significant for the PRMI with a PR factor of almost 1000. The scattered light illuminates the tanks in which the mirrors are suspended. If the scattered light is detected by sensors such as PDs that are sensitive to this scattered light and if the PDs are used for a control loop, the performance of the corresponding loop can be disturbed. In chapter 3, we will learn that this is actually the case. Laser power fluctuations that couple via scattered light into the sensors of the main suspension local control sensors disturb the operation of these loops. This topic represents the first major challenge towards stable operation of GEO 600 with increased input laser power.

Besides the strong laser power build-up and its resulting benefit on shot noise reduction, the PRC fulfills other important tasks. It is used as the ultimate frequency reference for the laser frequency stabilization [Gro03, Fre03]. In chapter 5.1, the laser frequency stabilization is explained to understand a power up related issue that is discussed there.

In addition, the PRC has a cavity pole of about 15 Hz due to the storage time of the light within the PRMI. Therefore, laser amplitude noise gets passively filtered [Smi06].

Detailed descriptions about various aspects of the PRMI can be found in [Gro03].

2.3.3 Signal-recycling

By placing a mirror, the so-called *signal-recycling mirror* (MSR), in the output port of the MI a cavity for the signal SBs is formed. This cavity is called *signal-recycling cavity* (SRC) and was first proposed by Meers in 1988 [Mee88]. The SR technique itself was first demonstrated in 1991 [Str91]. A SRC causes a resonant enhancement of the signal SBs. Therefore, the GW signal increases with respect to shot noise, because the signal SBs contribute negligibly to the total power at the dark port. If PR and SR is used in combination it is called *dual-recycling* (DR). GEO 600 is the first kilometer scale GW detector that uses a *Dual-recycled Michelson interferometer* (DRMI) as its central instrument.

There are two major parameters, that determine the characteristics of the SRC. These parameters are the reflectivity of MSR and MSR's microscopic position. The reflectivity of MSR affects the bandwidth of the SRC. The currently installed MSR has a transmittance of 10%. This leads to a bandwidth, measured as *half width at half maximum* (HWHM) of 1100 Hz [Pri12]. The microscopic position of MSR defines the frequency of the SR resonance, f_{SR} , with respect to the carrier. For $f_{SR} = 0$ Hz, the SRC is called tuned. Since 2010, GEO 600's SRC is in this state. For $f_{SR} \neq 0$ Hz the SRC is detuned. Detuning of the SRC is used to enhance signal SBs that are separated from the carrier frequency by a given Fourier frequency, f_{sig} .

SR has a further benefit with respect to HOMs. HOMs are created within the IFO due to asymmetries that cause imperfect extinction of the two interfering beams at the BS. SR converts HOMs that exit the PRMI via the dark port back to the TEM₀₀ mode due to an effect that is called *mode healing*. Mode healing reduces the shot noise level, because it increases the light power that is stored in the PRC and decreases the amount

of HOMs that are present at the output port. HOMs at the output contribute to shot noise. Furthermore, it has to be added that the aforementioned PR factor of about 800 is only achieved if the DRMI is locked. The PR factor is about 30 % smaller if just the PRMI is locked due to missing mode healing.

In 2010, two major changes were made to GEO 600's SR configuration. Before that date, the SRC was not operated in the tuned state but in the detuned state at a detuning frequency of $f_{\text{SR}} = 550$ Hz. Additionally, the bandwidth of the SRC was reduced by installing the aforementioned MSR which has a transmittance of 10 %. The previously used mirror has a transmittance of 2 %. The reason for executing these two changes lies within the major goal of the GEO-HF upgrade, an improvement of the sensitivity at high frequencies. GEO 600 is limited by shot noise at frequencies above approximately 600 Hz. Figure 2.6 provides calculated shot noise levels of GEO 600 for different SR configurations. The advantage of tuned SR compared to detuned SR with the initial MSR lies in a wide reduction of shot noise except for a narrow band around the detuning frequency. Increasing the SR bandwidth, i.e. by decreasing the mirrors reflectivity, trades a lower shot noise level at high frequencies with a higher shot noise level at lower frequency down to DC. Because other noises dominate the sensitivity of GEO 600 at low frequencies, the disadvantage of an increased bandwidth is minimal. Both SR changes are presented in [Pri12]. A description of the mode healing effect can be found there, too. Furthermore, [Gro03] provides pioneering aspects about the implementation of the DRMI lock in GEO 600 and [Hil06] compares initial experiments that compare the SR operation in the tuned and detuned state.

Laser power impinging on the BS

In section 2.2 it is stated that a maximum of 4 W total laser power was available with the old laser to be coupled into the DRMI. This is half of the available laser power that could be sent to the IOs before their upgrade. Under normal conditions, less laser power was used. These normal conditions will further on be referred to as *default operation* of GEO 600. Default operation corresponds to about 2.6 W that are directed towards MPR. If we take imperfect mode matching and the PR factor of slightly above 800 into account **we have 2 kW laser power impinging on the BS for a power of 2.6 W that is sent to the DRMI.**

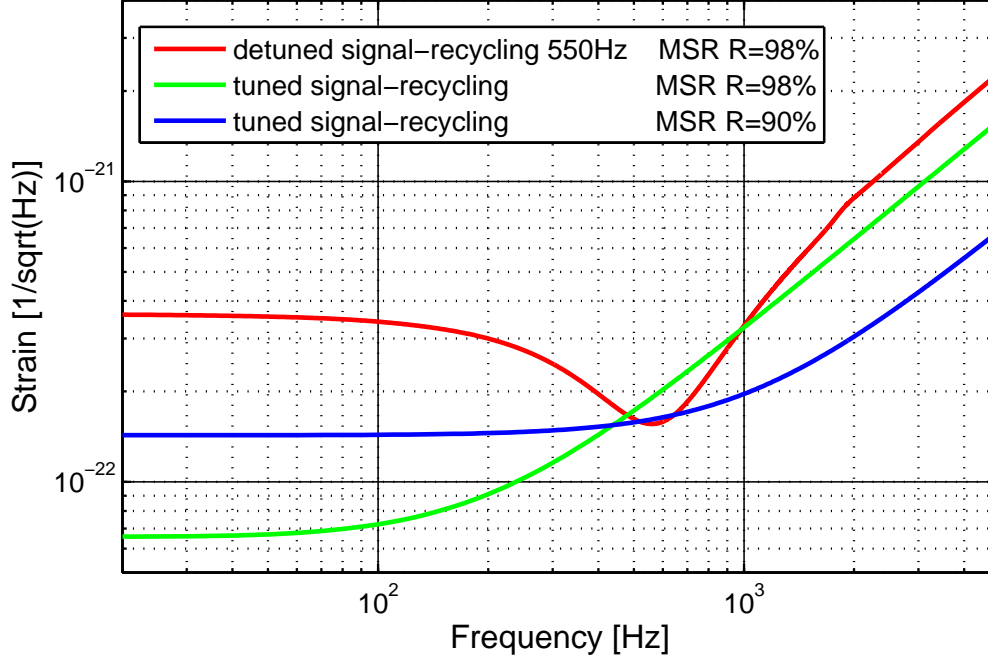


Figure 2.6: Calculated shot noise level of GEO 600 for different SR configurations [Pri12].

2.4 From output to detection

The GW signal SBs leave the DRMI at the dark port together with about 6 mW carrier light that are used as optical LO. These components represent the output beam and their beat signal is detected by a PD. In addition, the output beam is contaminated by other light fields. These fields leak out of the detector, carry no significant GW signal but contribute to shot noise. Therefore, the output beam is filtered by a cavity before detection to strongly attenuated unwanted light. This cavity is called the *output mode cleaner* (OMC). In the following, components in the final path of the light that was initially created by the laser system are described.

2.4.1 Suspended output optics

Three mirrors that are suspended as single pendulums are used to direct the output beam towards the OMC and the detection PD. These mirrors are the so-called BDO mirrors, where “BD” is commonly used as an acronym for *beam directing* mirrors and the “O” stands for *output*. The first BDO mirror, BDO1, is partially transmissive and has a

transmittance of $T = 1\%$. Since the MI SBs are present in the output beam, the beam transmitted by BDO1 is used for the MI lock and its automatic alignment.

Furthermore, the front side of BDO1 has a RoC of about 6.3 m and is part of the mode matching telescope towards the OMC. The mode matching telescope is completed by two further lenses in front of the OMC. In between these lenses a FI is placed. The remaining two mirrors are used as beam directors. Due to infrastructural constraints, three output mirrors are used while theoretically two mirrors would be sufficient.

The BDO mirrors are also important with respect to the auto alignment of the output beam onto the OMC. Actuation in four degrees of freedom is applied to the mirror level at BDO1 and BDO3.

2.4.2 The output mode cleaner

The OMC was implemented to strongly attenuate components in the output beam that contribute to shot noise but carry no extractable GW signal. Such beam components are HOMs and RF SBs and contribute about 80% of the 37 mW light power in the output beam at default operation¹ [Wit14].

The OMC is designed to attenuate these unwanted beam components by a factor of at least 100 to reduce the associated shot noise contributions by a factor of 10 or more. Carrier light and the signal SBs pass the OMC unhindered. Figure 2.1, that shows a simplified layout of GEO 600, also contains the schematics of the OMC. The OMC is a four mirror cavity with flat input and output mirrors. These two mirrors have a transmittance of 2%. The remaining two mirrors are curved and have a *anti-reflective* (AR) coating. One of these AR mirrors is mounted to a *piezo-electric actuator* (PZT) that is used as an actuator for the length control. A comprehensive description of the OMC, its implementation in GEO 600, including its control scheme and experiences with the OMC are given in [Pri12].

After passing the OMC, the remaining 6 mW output beam impinges the detection PD. The OMC adds a further degree of complexity to GEO 600 because it represents a further cavity that needs to be controlled. For several “power up” experiments that are aiming at investigating issues like the stability of the DRMI at high laser power, it is beneficial to exclude the OMC. Therefore, several aspects that are described in further chapters were performed in heterodyne lock, as an initial diagnostic tool.

¹ Default operation means that an input laser power is used that corresponds to a circulating power of 2 kW to 2.5 kW impinging on the BS if the DRMI is locked. This phrase was defined above, but with respect to the power in the output beam another fact needs to be taken into account. Heating elements, the so-called side heaters were installed at MFE. They are used to compensate for astigmatism and reduce the amount of HOMs and therefore the power in the output beam by 37% [Wit14] at default operation laser power. For this reason, prior publications such as [Pri12] state that the output beam contains only 10% carrier light power.

2.4.3 Squeezing in GEO 600

In 1981 Caves proposed to use squeezed light states at the output of GW detectors to suppress quantum noise [Cav81]. Squeezed light states are states whose uncertainty in one of its two quadratures is reduced at the expense of the other quadrature [Vah08]. GEO 600 is the first large scale, interferometric GW detector that demonstrated the successful application of squeezing [The11]. Because GEO 600 is limited by shot noise at frequencies above 600 Hz and not limited by radiation pressure noise at lower frequencies, squeezing is used to suppress shot noise. Since 2011 it is even routinely in use. To date, the level of the observed squeezing is about 3.5 dB.

Squeezing plays mostly no role for the discussed topics in this thesis and is therefore neglected in the following. The curious reader is asked to refer to publications that are describing the various aspects about the GEO squeezer. Selected examples for these publications are [Vah08, Kha11, The11, Gro13].

However, it is worthwhile to mention that squeezing is also working if GEO 600 is operated with higher laser power levels as typically used at the time the work for this thesis started. For instance, for most of the time during the joint science run of VIRGO and GEO 600 that is summarized in chapter 3.4, squeezing was applied while GEO 600 was operated permanently with the maximum laser power that was available in that time period.

2.4.4 The GEO 600 sensitivity

Depending on the frequency, different noise sources limit the GEO 600 sensitivity. In the following, a brief overview about these noises is given. Therefore, we are going to orient ourselves at the recent sensitivity of GEO 600 and the most important noises sources that couple to it. A more detailed overview of the different theoretical noise sources that are present in GEO 600 is given in [Smi06].

Figure 2.7 shows a typical, sensitivity of GEO 600 at default laser power of 2 kW impinging on the BS. In addition, this figure shows *understood* noise sources of interest during the same time. The uncorrelated sum of the understood noises is also shown. Several of these noise sources are fundamental, i.e. their origin lies in random processes. One example for such a fundamental noise is shot noise. With respect to a laser power increase, shot noise is the most interesting noise source as long as radiation pressure noise plays no role, as it is the case for GEO 600. According to formula 1 the ratio of GW signal to shot noise can be improved by increasing the laser power that circulates in the MI. Shot noise almost completely limits the sensitivity of GEO 600 above 600 Hz. It is the only obstacle that needs to be overcome to achieve the main goal of GEO-HF: an improvement of the sensitivity at high frequencies. No other noises contribute significantly at high frequencies.

At low frequencies, i.e. below 100 Hz, the sensitivity is understood equally well as it is at high frequencies. As can be seen in figure 2.7, the main contribution to the sensitivity

at low frequencies comes from MI automatic alignment feedback noise. Eventually, these noises are induced by seismic noise.

The frequency range from 100 Hz to about 600 Hz is often referred to as medium frequency range or simply “mid-frequencies”. In the medium frequency range, the sensitivity was originally expected to be limited by thermal noises, which are further examples of

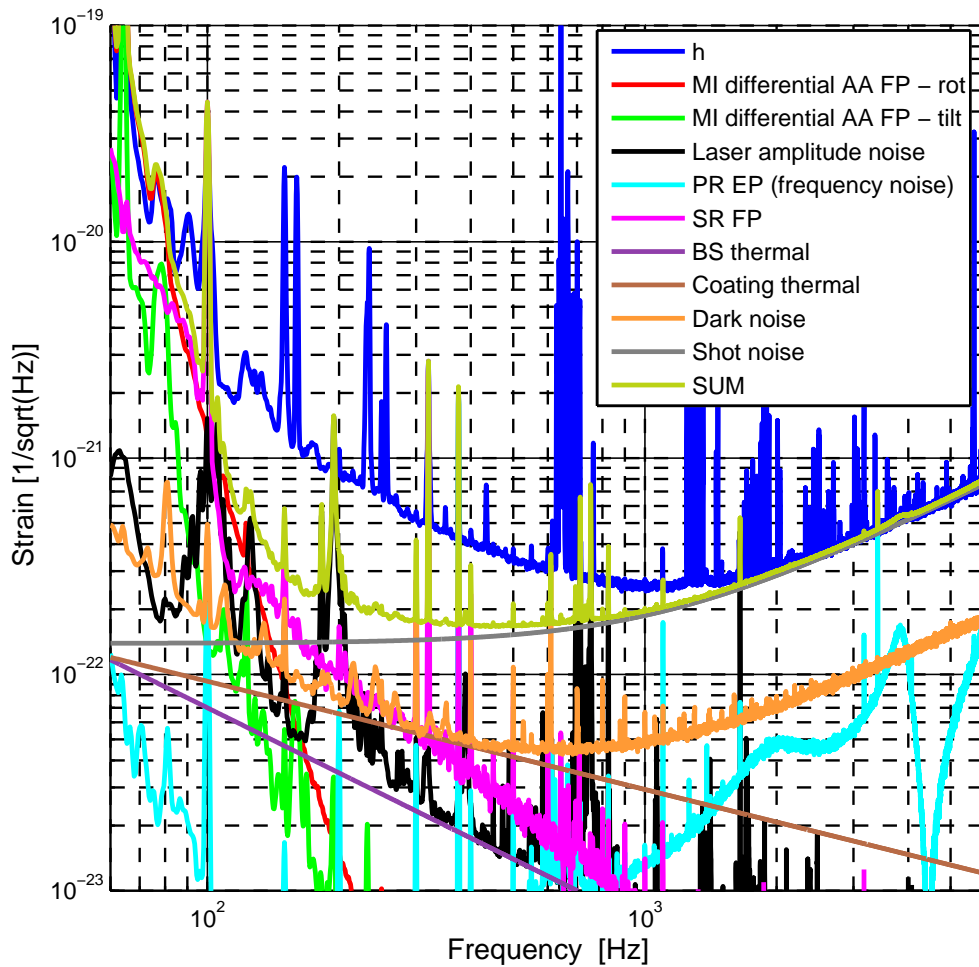


Figure 2.7: Exemplary sensitivity of GEO 600. Several projected noises are displayed to show up to which level they are limiting at certain frequencies.

fundamental noise sources. Figure 2.7 contains the predicted BS thermal noise and coating thermal noise. Both noises are at least one order of magnitude below the actual sensitivity. As can be seen, there is a gap between the sum of the noises and the sensitivity at medium frequencies. We observe a noise at medium frequencies that is not yet understood. In chapter 6, we get back to this and we will see that the noise at medium frequencies gets higher if the circulating laser power is increased. Note that it is not stated that *the* unexplained noise is laser power dependent. It is possible that we observe a not understood noise at medium frequencies that does not depend on the laser power and a second, laser power dependent component exists that starts to dominate h if the laser power is strongly increased.

2.5 The GEO 600 suspension systems and its local controls

This section gives an overview of the suspension systems used to suspend the main optics of the GEO 600 gravitational wave detector. One key system of the suspensions is the *local control* (LC). The LC is used to control the position and orientation of the upper masses of the individual suspension and therefore the mirrors itself. Furthermore, the LC actively damps the eigenmodes of the suspensions at its eigenfrequencies. The suspension LCs will play a major role in the context of laser power fluctuations coupling via stray light into the shadow sensors of the LCs as described in chapter 3. A more detailed description of the whole suspension system and the LCs can be found in [Goß04].

2.5.1 The suspensions system

The ambient seismic noise at the GEO 600 site for frequencies above 3 Hz is roughly of the form $10^{-7} \text{m}/\sqrt{\text{Hz}} \cdot [1\text{Hz}/f]^2$. A strong isolation of more than ten orders of magnitude at 50 Hz is required for the test masses to obtain the design sensitivity of GEO 600 [Goß04].

In order to meet this requirement, the main test masses are suspended as triple pendulums [Pli00, Tor00, Goß02], and the uppermost stage is actively damped by magnet-coil actuators. These magnet-coil actuators are a part of the so-called local control, whose performance is negatively influenced by laser stray light as described in chapter 3. Further isolation is provided by the use of cantilever-spring stages to damp vertical motions and by stack isolators to pre-isolate the suspension point itself [Goß04].

The mirrors belonging to the MI, i.e. MCE, MCN, MFE, MFN and the BS contain a monolithic last stage to lower the thermal noise of the suspension and the test masses themselves [Bar02, Goß04, Smi04]. That leaves MSR being the only triple suspended optic with no monolithic stage. All other relevant optics are suspended as single or double pendulums.

Other key parts of GEO 600 are also suspended as pendulums and play a minor but not negligible role with respect to the discussed topic of chapter 3.3. Reaction masses are suspended behind several optics to provide seismically-isolated platforms supporting actuators. These actuators are used to apply fast feedback signals to maintain the MI at the operating point and the cavities in resonance. In the cases of MCE, MCN and MSR, the reaction masses are even suspended as triple pendulums.

All important optics are enclosed in an *ultra-high vacuum* (UHV) system to avoid contamination of the optics by dirt and to minimize both the influence of refractive index variations of the air and acoustic coupling to the optics [Goß04]. One main disadvantage of this is the inaccessibility of all components within the UHV. Maintenance work or even large scale changes of components situated inside the UHV need a lot of effort in order to ensure cleanliness and most of all safety of in-vacuum components. A schematic drawing of a GEO 600 triple suspension is shown in figure 2.8.

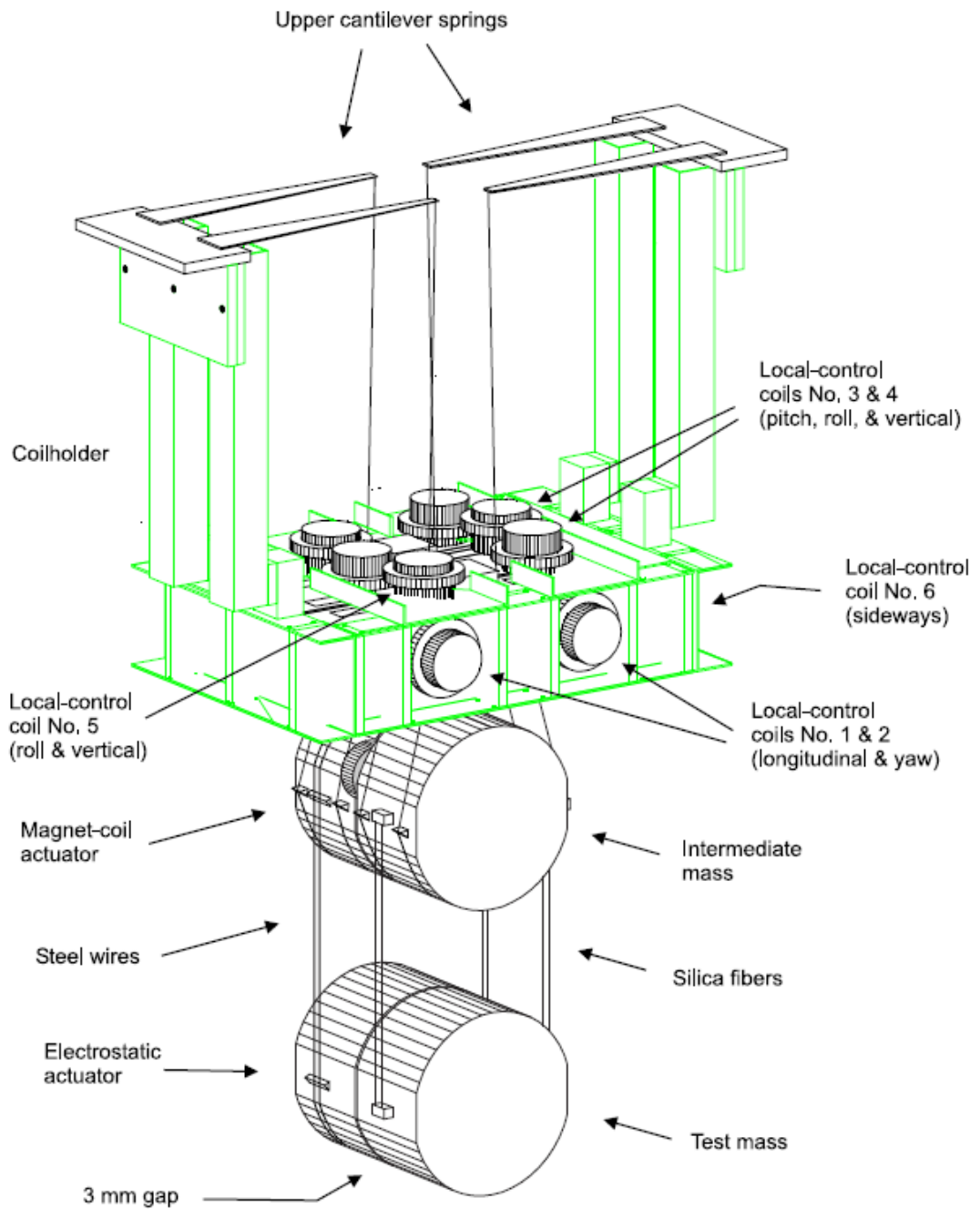


Figure 2.8: A schematic drawing of a GEO 600 triple suspension system. Actually, two suspensions are displayed. In the front, the triple suspension of the mirror is shown while right behind it one can see the triple suspension of the reaction mass. The assembly of the shadow sensors and local control coils are labeled. This drawing is taken from [Goß04].

2.5.2 The suspension local control

The local control is used to actively damp eigenmodes of the different pendulums used in GEO 600. Furthermore, the LC controls the different degrees of freedom of the suspended optics at low frequencies. In the case of the triple-suspended main optics (as well as their reaction masses) and MPR, all six degrees of freedom are controlled and actively damped. All other suspensions only possess control over rotation and tilt, thus a 4-channel LC system is in use for these.

The individual components of a single LC channel are as follows: To read out individual degrees of freedom, IR sensitive optical sensors, the so-called shadow sensors, are used. They sense the position of a metal flag attached to the upper mass, which partly blocks the light from a LED radiating in the IR range. A so-called local control circuit serves as the servo to generate a feedback signal. Depending on the number of degrees of freedom that are supposed to be controlled, the LC circuit has four or six channels. The feedback signal is applied as a current to a coil which serves, in combination with a magnet attached to the upper mass, as an actuator. Each coil is mounted on a rigid frame, together with the corresponding shadow sensor, is encapsulated in a glass housing to ensure UHV compatibility. The metal flags are attached to the individual magnets. For simplicity, a single coil/magnet actuator including the corresponding shadow sensor and LED as well as the metal flag is called a *flag*. The orientation of the six flags belonging to a GEO 600 main suspension can be seen in figure 2.8. Note that there are more than six flags visible in figure 2.8. The six flags that belong to the mirrors suspension are highlighted via the description arrows while the remaining flags belong to a reaction mass pendulum right behind the main suspension. The LC circuit includes low pass filtering above its active band of roughly 3 Hz to provide a short settling time without adding extra noise in the GW detection band. Further filter components are several notches to filter the 50 Hz of the supply voltage and other significant oscillations. It is worth mentioning that the LC circuit has two UGFs at 0.3 Hz and 3 Hz. Having no gain at DC allows for offset currents to the coils that are used for alignment purposes [Gro01]. In general all (electronic) channels of a LC circuit belonging to a single suspension are placed in a combined way in one dedicated module. Digital supervision of the analog local control servo can be done by a PC using LabVIEW [Cas00].

The shadow sensors are sensitive to IR light and are also able to detect the 1064 nm laser light with which GEO 600 is operated. Therefore, a negative influence of the LC operation due to a coupling mechanism of scattered laser light into the shadow sensors is possible. That this is not only the case but even the first major obstacle towards a significant increase of circulating light power in the main IFO will be the essential topic of chapter 3.

Figure 2.9 shows an example of a spectral density of the BS flag 1 error signal. The data was calibrated from $V/\sqrt{\text{Hz}}$ to $\text{m}/\sqrt{\text{Hz}}$. The calibration factor was obtained from a test suspension setup but it is also valid for error signals of any GEO flag. It was found that 1 V corresponds to approximately $6 \mu\text{m}$ in the case of the AC coupled error signal

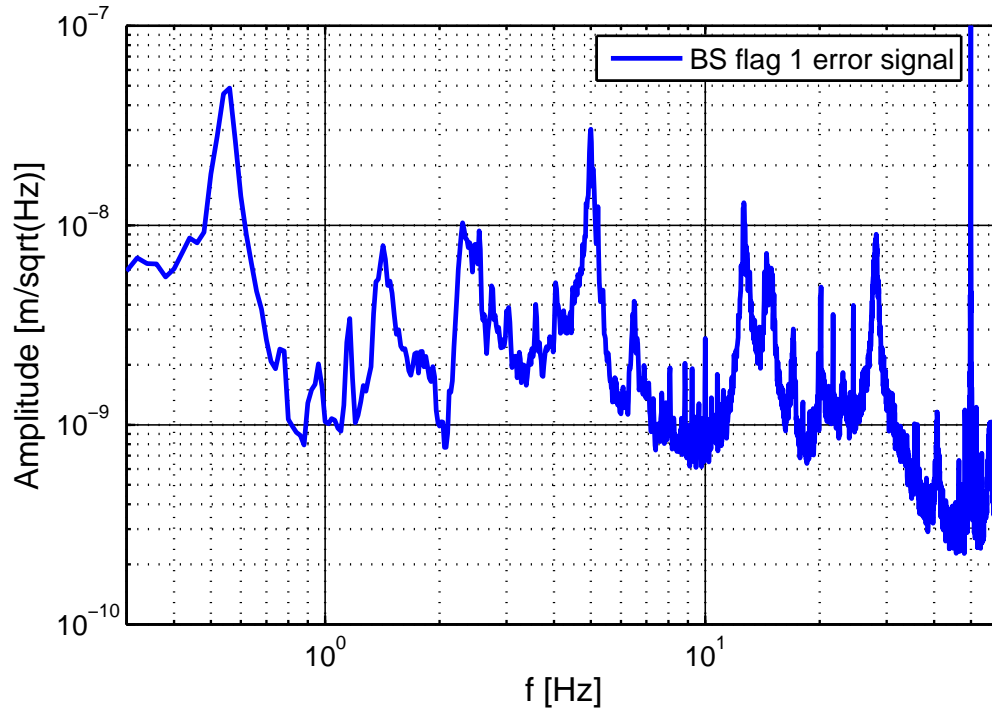


Figure 2.9: A spectral density of the BS flag 1 error signal calibrated to $\text{m}/\sqrt{\text{Hz}}$. The pronounced peaks around 1 Hz, like the one at 0.55 Hz are pendulum resonances.

monitor outputs of the LC electronics. In chapter 3.3, a description of the test suspension setup is given.

Rotation and tilt, the GEO 600 nomenclature

Just a remark at this point. In regard to the degree of freedom control of a suspension, GEO 600 nomenclature uses the phrases “rotation”, or simply “rot”, and “tilt”. If a mirror is rotated, it means that it is moved such that the normal on the mirror surface moves in the horizontal plane with respect to the beam axis. Tilting a mirror moves this normal in the vertical plane. At LIGO, people speak of “yaw” for rotation and of “pitch” for tilt. Furthermore, a rotation of a mirror around the beam axis is called “roll” like it is at LIGO.

2.6 The GEO-HF upgrade

The GEO-HF upgrade was suggested in 2005 [Dan05] and refined at later times. It aims at an improvement of the GEO 600 sensitivity at high frequencies such that the sensitivity is comparable to the transitional stages of Enhanced LIGO and Virgo+ on their way to the *Advanced* stage. At high frequencies, i.e. above 600 Hz, the sensitivity of GEO 600 is limited by shot noise. The different design aspects of GEO-HF aim at a shot noise reduction and are described in [Wil06, Lüc09, Lüc10]. In summary, the modifications GEO-HF is composed of are as follows.

- The readout technique was changed from heterodyne readout to DC readout. This change includes the installation of the OMC.
- The signal-recycling tuning was altered from detuned to tuned operation.
- By increasing the transmission of MSR, the bandwidth of the SRC was increased.
- Squeezing was implemented and is in permanent use to reduce shot noise at the dark port.
- To further reduce shot noise, the circulating laser power will be significantly increased. An increase by a factor of about three is already possible but not routinely used due to reasons that are explained in chapter 6. As part of the laser power increase a *thermal compensation system* (TCS) is in the process of being installed at the time this thesis was handed in. It will be used to compensate for the thermal lens in the BS that becomes significant at high circulating laser power [Wit09].

Figure 2.10 shows calculated shot noise curves for GEO 600 for different stages of the GEO-HF upgrade. Except for remaining commissioning work with respect to laser power increase and an improvement of the observed squeezing, the GEO-HF upgrade is completed. The majority of the aspects that GEO-HF consists of are briefly described above. A more detailed description can be found in [Pri12].

In this chapter, an introduction about the GEO 600 GW detector was given. The following chapters of this thesis cover considerable aspects about the various challenges that come along with the increase of the circulating laser power.

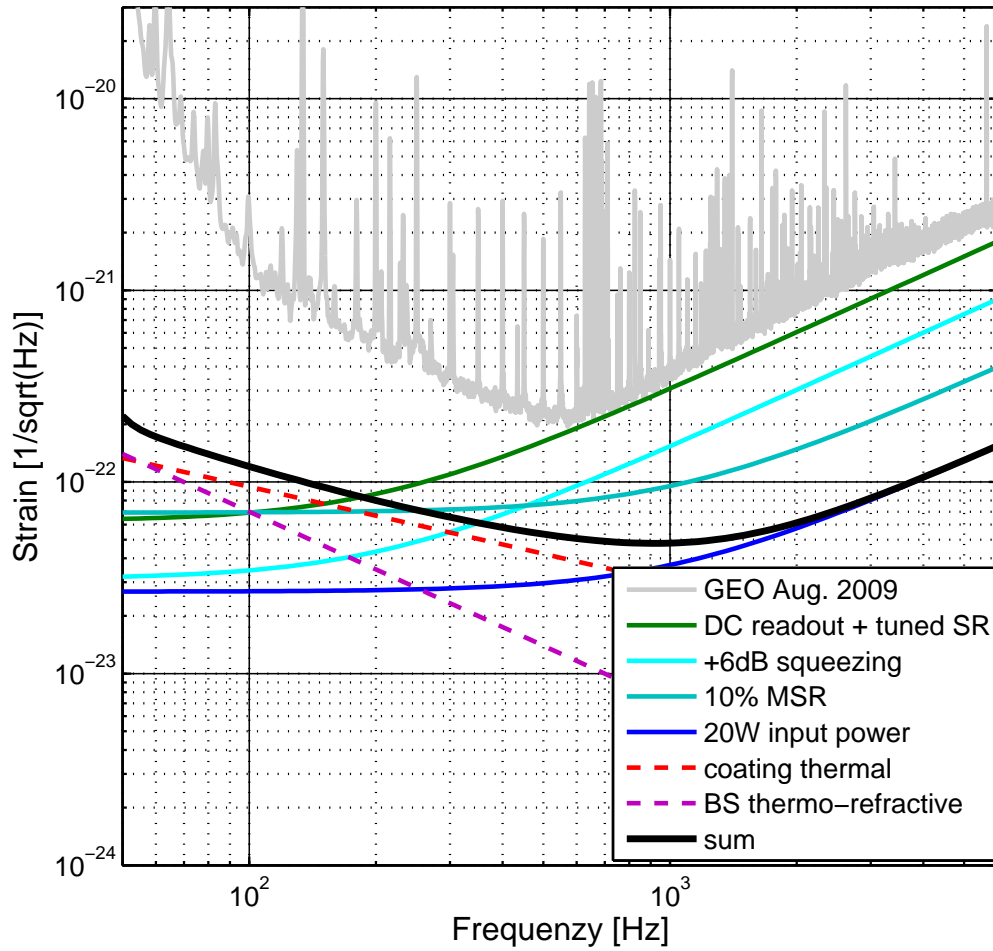


Figure 2.10: Calculated shot noise of GEO 600 over the course of the GEO-HF upgrade. The black curve that shows the sum of the noise takes only shot noise and thermal noises into account.

3 High power instabilities and the influence of laser stray light on suspension local controls

For stability reasons, GEO 600 was limited to an operational laser power of about 2 kW impinging on the *beam splitter* (BS). In this chapter, the origin for this limitation is described. It is shown that laser power fluctuations which couple via stray light to the shadow sensors of the GEO 600 main suspension local controls cause instabilities at high laser power. This effect increases as the used laser power does. It is the first major obstacle to be addressed to extend the laser power limit.

In this chapter, measurements are presented that show the significance of this stray light contamination. To eliminate the problem, a modulation-demodulation scheme for the local control systems was designed, commissioned and implemented at all main suspension local controls except for the suspension of the signal-recycling mirror. This implementation allowed for stable operation at full available laser power, while the old GEO 600 laser system was still in use. The installation of the new laser system and its accompanied increase of available laser power resulted in no further stray light induced stability issue regarding the main IFO. At the end of this chapter, the effect of stray light contamination to the various other suspension local controls is discussed. In many cases, stray light coupling plays no major role at operational powers that are within the scope of the GEO-HF upgrade. However, stray light coupling may restrict a further laser power increase above 30 W input power if no measures are taken in such cases.

3.1 Lock instabilities at high laser powers

Until September 2011, the light source of GEO 600 was a 15 W laser [Zaw02]. As described in chapter 2, roughly 8 W maximum laser power was actually available at the first mode cleaner. Before the finesse of both mode cleaners was reduced (see chapter 4), roughly 50% of the laser power was lost at the mode cleaners themselves and other input optic components like Faraday isolators. Therefore, 3.5 W were left to be coupled into the main ifo. However, under normal operating conditions just about $\frac{2}{3}$ of this laser power was used. With the PRC gain being approximately 900 this leads to a intra-cavity power of roughly 2 kW.

Why were only $\frac{2}{3}$ of the available power used? The more laser power that is put to use, the higher the signal to noise ratio gets at frequencies at which an interferometric GW detector is shot noise limited. Thus, the sensitivity to astrophysical sources emitting GWs at these frequencies is improved. However, a better sensitivity is in general of little use if it comes at the price of less stable operation of the instrument. Just this was the case until the first major challenge of the task of increasing the laser power was addressed: reducing instabilities at high laser powers.

With 2 kW circulating power, the operation of GEO 600 was sufficiently stable. In particular, this state was best understood with respect to the multitude of parameters that can potentially be tuned. Even though most control loop gains in GEO 600, which depend on the laser power are normalized by the actual laser power, at operating powers different from $\frac{2}{3}$ slight adjustments of control loop gains are beneficial. Small scale non-linear effects can always be found in a system as complex as GEO 600. One example of this is the mode matching to the PRC. Until the corresponding mode matching telescope that is described in chapter 4.4 was improved, the mode matching got worse for higher input powers. This fact was due to thermal lensing of the input optics, namely the EOMs and Faraday isolators on MU3, and leads to a non-linear power build up with respect to the input laser power. But no matter how carefully all corresponding parameters were tuned, operation at maximum laser power used to be very unstable if not impossible, particularly when there was above-average seismic noise on site.

One way to get an impression of the stability at different laser powers is to observe the circulating power in the main ifo. In a state that is less stable than another state one would expect more fluctuations in the circulating light power. In the following, let us simply talk about power fluctuations. A simple example of a cause of more power fluctuations than usual is increased seismic noise on site, i.e. due to weather conditions or nearby construction work. Another example would be a non-optimal gain of a system that is relevant to the circulating power in the main IFO. Oscillations at the UGF can occur with small or no phase margin.

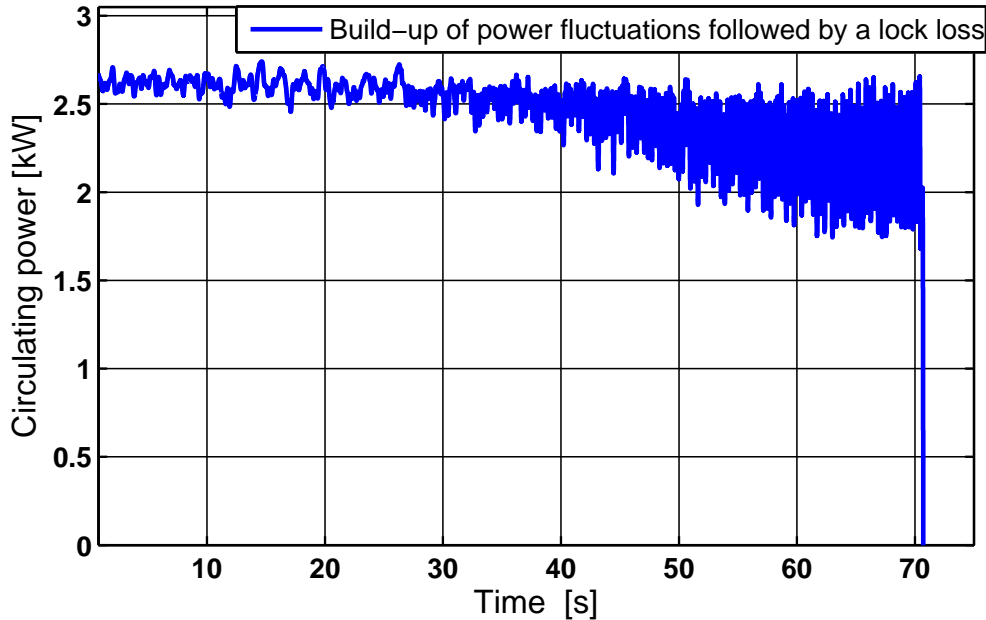


Figure 3.1: A time series plot showing the build-up of fluctuations on the circulating power in GEO 600 followed by a lock loss. The signal is recorded by a PD monitoring a pick-off beam of the AR coating of the BS. A drop of this signal to zero indicates a lock loss. The higher the circulating power the more often this kind of lock loss occurs. At a circulating power above 3 kW, a stable lock for more than a few minutes is almost impossible to obtain.

3.1.1 A typical lock loss while using high laser power

In the case of GEO 600, another issue resulted in an increase of power fluctuations. For input laser powers above 2 W the amount of power fluctuations largely increased, while at the same time the stability decreased. As noted above, operation at maximum input power was either only barely possible or not possible at all. The circulating power is recorded using a PD (“PDBS”) monitoring a pick-off beam of the AR coating of the BS. In figure 3.1, a time series of PDBS is plotted during an operational power of 2.6 kW at the BS. The input power has just been increased before the start time of this plot. From second 30 on, one can see fluctuations building up and eventually leading to a lock loss after second 70.

The amount of lock losses that look like the one shown in figure 3.1 did significantly increase for higher laser powers. To get a better understanding of how the amount of power fluctuations is influenced by the laser power we can have a look at a spectral density instead of a times series. Thereby, we can study whether the fluctuations occur at

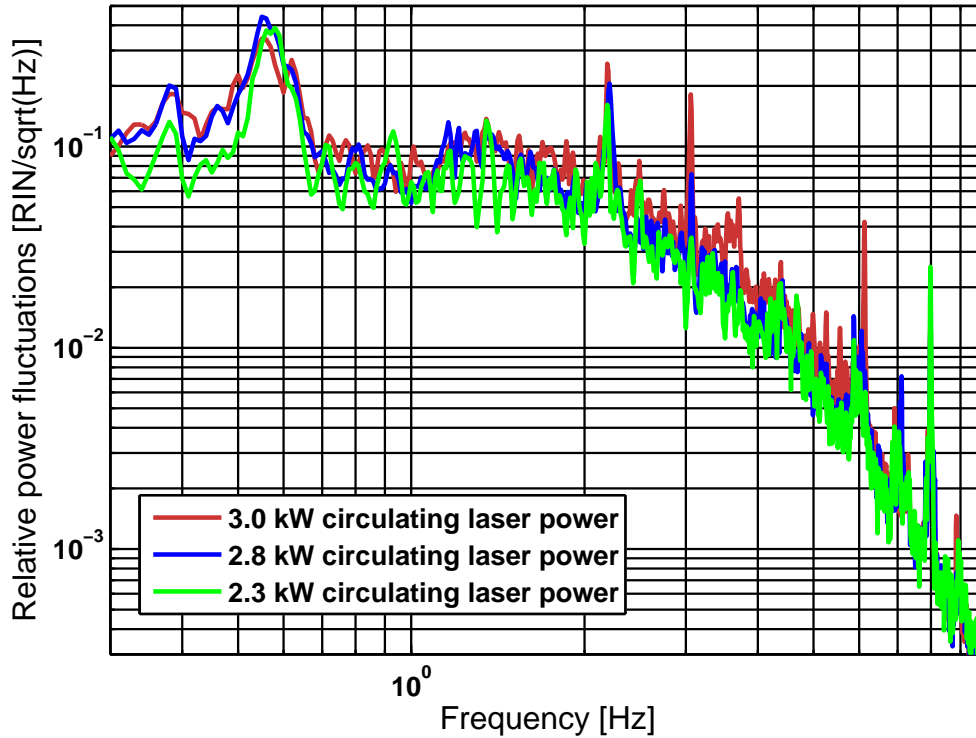


Figure 3.2: Spectral density of the circulating power for different input powers. All three cases are normalized by the corresponding mean value of the circulating power to get a direct comparison of relative power fluctuations. Note the strong build-up of oscillations for 3kW circulating laser power. The two peaks which increase the most with higher input power are at 3.1 Hz and 6.2 Hz. It is striking that the second peak is at exactly twice the frequency of the first peak.

certain frequencies. Figure 3.2 shows spectral densities of PDBS while GEO 600 was in heterodyne lock. Each curve is for a different laser power and each curve is normalized by the respective DC value. The data used for this plot was taken at a time with low and constant seismic conditions. Therefore, the seismic had no major influence on the amount of laser power fluctuations at the different reference times shown in this figure. As can be seen in figure 3.2, power fluctuations strongly build up as the maximum input laser power is reached. Furthermore, the build up of the power fluctuations shows a strongly non-linear behavior. This can best be seen by comparing the amplitudes of the oscillations at 3.1 Hz and 6.2 Hz in the figure for different input laser powers. These two peaks at 3.1 Hz and 6.2 Hz helped to justify a hypothesis described below that actually explains the

origin of these power dependent power fluctuations.

3.2 Stray light coupling to the main suspension local controls

In this section, we will learn about a process that caused fluctuations of the circulating power in GEO 600's main interferometer to build up with increased input laser power: Stray light coupling to the main suspensions local control shadow sensors. This effect of scattered light that disturbs the operation of suspension local controls. Furthermore, it was the major obstacle towards an operation of GEO 600 at significantly higher laser power.

In addition, this section provides a quantitative measure of the amount of stray light that is present at the shadow sensors of each individual main suspension LC.

3.2.1 Influence of laser stray light to the operation of a local control

As described in chapter 2, an important loss channel of a PRMI with a big PR factor operated at or near the dark fringe is scattering. In the case of GEO 600 it is even the dominant loss channel. Therefore, most of the laser light coupled into the PRC ends up as scattered light inside the vacuum system. This scattered light is partly reflected on the surfaces of the different components inside the individual vacuum tanks and the inner surfaces of the tanks themselves. A small fraction will find its way to the shadow sensors of the LCs.

That scattered light can easily reach the upper mass can be seen in figure 2.8 in chapter 2. It shows the schematics of a triple suspension system including the corresponding LC flag assembly. It is not clear in figure 2.8 that the scattered light can also easily reach the shadow sensors. This gets obvious by looking at the photograph of the upper part of a suspension model as shown in the figure 3.3. The assembly of all six flags around the upper mass is visible. Scattered light can easily reach the areas between the metal flags and the shadow sensors that are encapsulated inside the glass housing.

As described in chapter 2, the shadow sensors are operated with infrared light and are also sensitive to scattered light from inside the IFO. Therefore, fluctuations on the circulating power in GEO 600 itself can show up in LC error signals if a sufficiently strong coupling exists.

In figure 3.2, intra-cavity power spectral densities for different input powers are shown. It is obvious that the circulating power fluctuates the most at frequencies where the suspensions move the most, i.e. at frequencies at which the active band of the LC electronics is. A fluctuation in the circulating power at such frequencies with a sufficiently large amplitude could show up not only in a LC error signal, but also result in a disturbance of the loop's performance. Such a fluctuation of the circulating power could find its way via scattering as stray light to the shadow sensors of the LC. It would be misinterpreted



Figure 3.3: A photograph of the flag assembly at a GEO like suspension model. Metal flags attached to the upper mass stick into the glass housing of the coils. There is sufficient space between a flags and the corresponding glass housing for scattered light to enter.. Because the shadow sensors are encapsulated inside the glass, the scattered light can eventually reach them.

as a movement of the upper-most mass. Accordingly, feedback at the same frequency would be applied to compensate for this fake movement. This results in a movement of the upper-most mass itself that is only marginally damped or not damped at all by the suspension on its way to the mirror. The mirror would shake at the same frequency and thus modulates the intra-cavity power at the fundamental frequency and at twice the frequency. The peaks at 3.1 Hz and 6.2 Hz in figure 3.2 can be explained by this mechanism.

If the just described coupling mechanism exists, it should be possible to see fluctuations like they occur in the circulating power in some or at least one of the many shadow sensor signals belonging to the main suspension LCs. Anticipating the results presented in section 3.2.3, there are several cases that show strong contamination of laser stray light coupling. These cases actually show fluctuations that grow in a similar way at the same time as the circulating power does in figure 3.1. Figure 3.4 exemplarily shows this for the first shadow sensor belonging to the BS LC (“BS flag 1”). Similarities between figure 3.1 and figure 3.4 are obvious. Fluctuations are building up from second 30 on until at second 70 a lock loss occurs.

The information given so far indicates that coupling of laser power fluctuations to the shadow sensors of GEO 600 main suspension LCs is an issue. Potentially, it is even the essential show stopper for a significant increase of operational laser power. To determine how much of a problem scattered light and its coupling to the sensors of the LCs actually is, we measured its amount for all flags of all of GEO 600’s main suspensions. The technique used for this purpose is a noise projection and its details are explained below. These

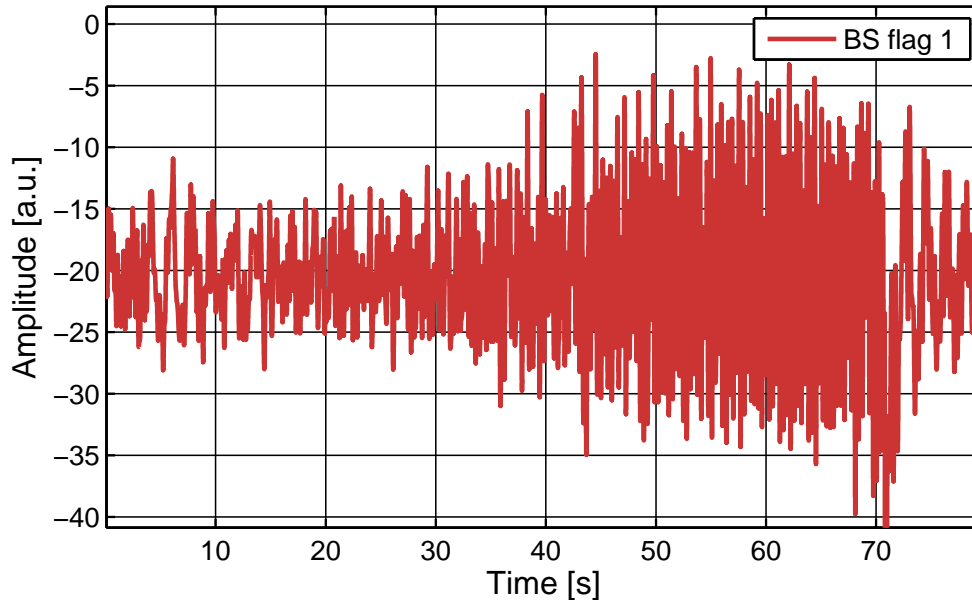


Figure 3.4: A time series that shows the BS flag 1 signal during the exact same time as figure 3.1 which shows the circulating power in the IFO. At second 30 one can clearly see strong fluctuations building up. At second 70 these fluctuations stop. This is exactly the same time at which the lock loss occurs as can be seen in figure 3.1. Note that the data is low pass filtered for clarity to suppress a large 50 Hz line that is present in LC signals. Additionally, the seismic is fairly constant during the observation time and cannot explain the sudden acceleration.

projections have shown the significance of stray light coupling to the shadow sensors of the LCs. Actually at all but the MSR suspension the stray light coupling is sufficiently strong to disturb the detector's operation.

3.2.2 Determining the amount of stray light contamination

In the following, the measurement principle is described which was used to determine the amount of laser stray light contamination for all LC error signals. It is a noise projection that uses a single frequency injection to measure its coupling constant. The assumption is made that the stray light coupling to the shadow sensor signals is flat in frequency. This is a reasonable assumption since there are no obvious processes thinkable causing a frequency dependent coupling.

To do the projection, the amplitude of the input light and therefore the intra-cavity

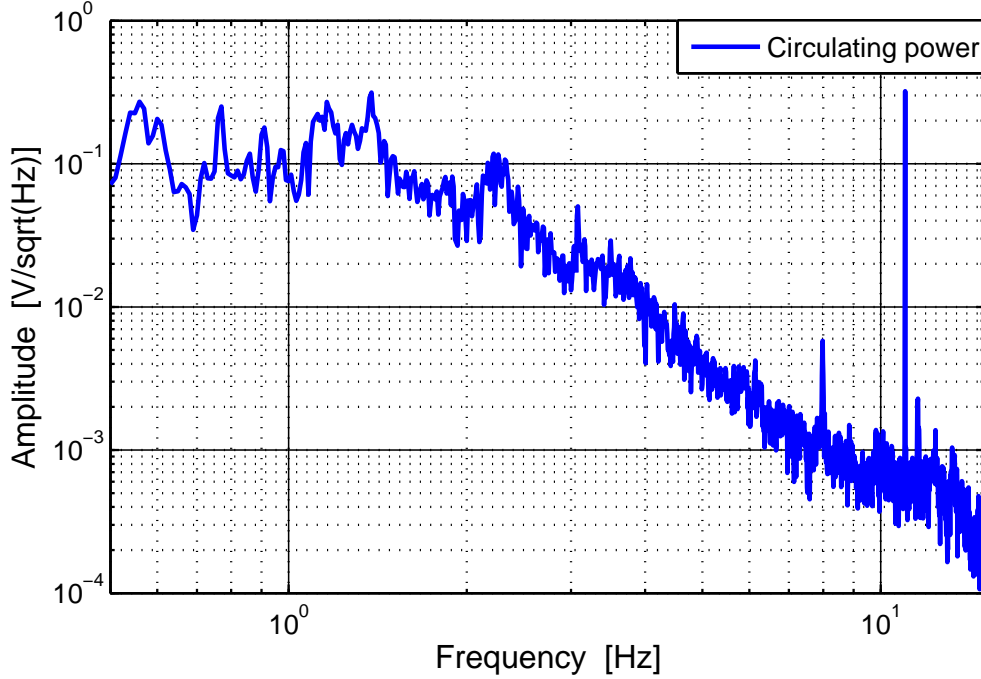


Figure 3.5: Spectral density of the circulating power in the main IFO at $\frac{2}{3}$ of the available laser power. This corresponds to roughly 2 kW impinging on the BS. The laser amplitude is modulated at 11 Hz. The modulation is applied to mark the injected laser light in order to determine the amount of stray light coupling to the LC error signals.

power is modulated at a fixed frequency. The modulation frequency is chosen slightly above the unity gain frequency of the LC. As actuator for the modulation serves the current of the GEO 600 slave laser diodes.¹ The amplitude is chosen such that not only the corresponding modulation peak in an intra-cavity power spectral density is dominated at the modulation frequency but also the LC error signal spectral density themselves, the latter being the case for many but not all of the various LC error signals. An upper limit of the modulation's amplitude is set by the constraint to allow a stable lock of the detector during the measurement. A modulation amplitude of 2% to 3% of the circulating DC laser power proved to be a good choice. (To modulate the circulating power by 1.6% of its DC mean, a signal of 100 mVpp needs to be injected to the appropriate electronics

¹ Since the new laser system was installed, an AOM is used as actuator for such measurements. Its actual purpose is to be an actuator in the amplitude stabilization loop. However, while these measurements were done the old laser system was still in use. Its diode currents were used as actuator of the amplitude stabilization loop and for stray light measurements.

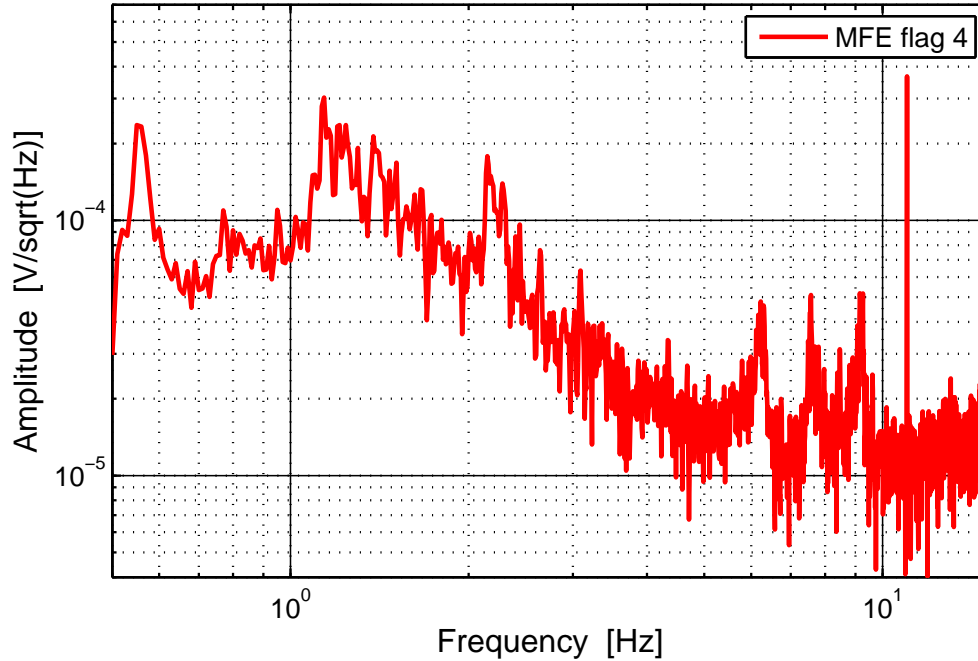


Figure 3.6: Spectral density of the MFE flag 4 error signal for the very same time as the plot shown in figure 3.5. At 11 Hz a strong coupling of the modulated laser power is visible. In this case the coupling peak is more than one order of magnitude above the surrounding noise floor. The error signal is almost completely dominated by stray light from within the IFO at 11 Hz.

input.)

Depending on the suspension the projection was done for, a modulation frequency of about 10 Hz or slightly above was chosen. In figure 3.6, the spectral density of a typical LC error signal is shown. A good choice for a modulation frequency in this example is 11 Hz (or near to that). A higher surrounding noise floor like at 7.5 Hz or at 9 Hz would result in a less precise measurement. Higher modulation frequencies seem to have the advantage of having a higher SNR for the coupling peak in the corresponding flag signal. However, selecting a frequency close to the control bandwidth of the LCs allows for (visual) clearer results.

Figure 3.5 shows the spectral density of the intra-cavity power while the current of the slave laser diodes was modulated at 11 Hz with an amplitude that corresponds to 1.6% of the mean of the circulating power. Furthermore, figure 3.6 shows the corresponding spectral density of MFE flag 4 error signal during the same time. In figure 3.6, a fairly large coupling is visible at 11 Hz. The “coupling peak” is more than one order of magnitude

higher than the noise floor that surrounds it. This means that the error signal of MFE flag 4 is dominated by the 11 Hz modulation imprinted on the input laser beam. It is dominated by laser stray light coupling at 11 Hz and it has to be dominated by the coupling peak to get a valid projection.

At the modulation frequency f_{mod} , we can calculate the ratio r_{proj} of the modulation peak amplitude in the spectral density of the circulating power $P_{\text{power}}(f_{\text{mod}})$ and the peak amplitude of the spectral density of MFE error signal $P_{\text{flag}}(f_{\text{mod}})$. We call this ratio,

$$r_{\text{proj}} = \frac{P_{\text{power}}(f_{\text{mod}})}{P_{\text{flag}}(f_{\text{mod}})} \quad (3.1)$$

the projection factor. It provides a measure of the amount of stray light contamination.

The projection factor r_{proj} is the key to the stray light projection explained here. The projection is done by multiplying the flag spectral density at all frequencies f with the corresponding projection factor. We get

$$P_{\text{flagproj}}(f) = r_{\text{proj}} \cdot P_{\text{flag}}(f), \quad (3.2)$$

the projected spectral density of the flag error signal.

Furthermore, we can display the projected spectral density of the flag error signal $r_{\text{proj}} \cdot P_{\text{flag}}(f)$ and the circulating power spectral density $P_{\text{power}}(f)$ in the same plot. This is shown in figure 3.7 for the case of MFE flag 4. In this figure, the projected flag error signal $r_{\text{proj}} \cdot P_{\text{flag}}(f_{\text{mod}})$ and the circulating power spectral density $P_{\text{power}}(f)$ have not only an equal value at $f_{\text{mod}} = 11$ Hz but also at frequencies up to 4 Hz. The spectral density of the MFE flag 4 error signal is obviously dominated by laser stray light coupling at these frequencies. It does not show the actual movement of the uppermost mass for the corresponding degree of freedom anymore. Even if the flag spectral density comes close to the spectral density of the circulating power, the LC error signal is contaminated by a significant amount of laser stray light. It needs to be pointed out that this special case, shown in figure 3.7 is one of the most dramatic findings during the investigation of stray light coupling to the LC shadow sensors. Therefore, it is a good example to illustrate the technique used to determine the amount of laser stray light at the main suspensions. However, at most other suspensions the stray light contamination is not significantly less.

If the coupling peak is small but still visible in the flag spectral density one can still do a less accurate projection. In this case, one can calculate a projection factor r_{proj} but keep in mind that its value is less reliable. The real projection factor will probably differ. Therefore, if the coupling peak is small but still visible, the projection provides an upper limit for the amount of stray light contamination.

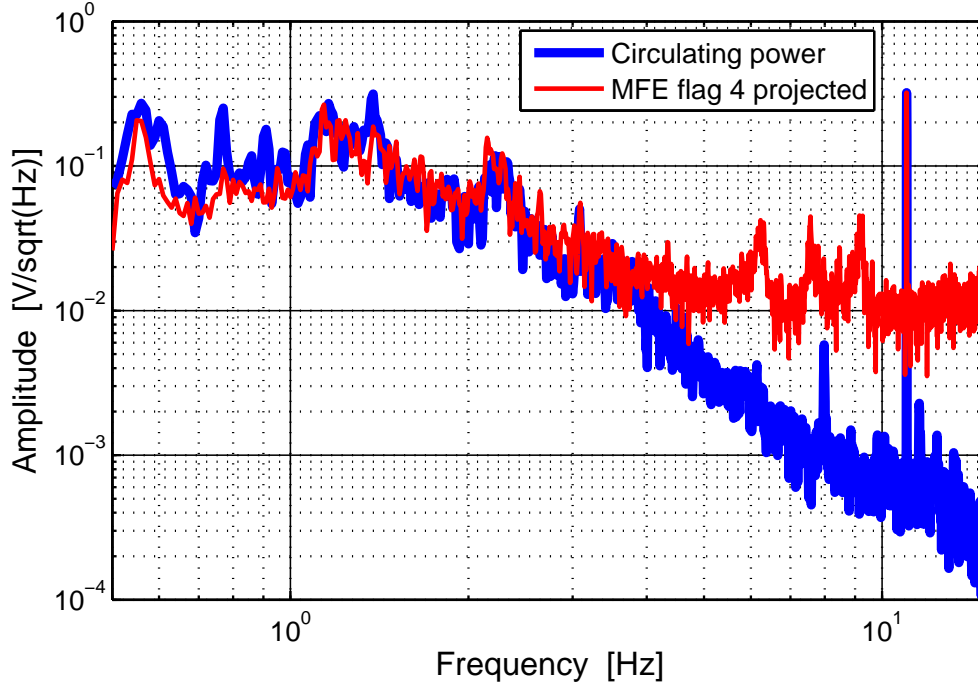


Figure 3.7: An exemplary laser stray light projection, shown for the case of the error signal of MFE flag 4. At 11 Hz, the frequency this projection was made for, the spectral density of the error signal is clearly dominated by laser stray light coupling. Therefore, this projection shows that the error signal is also dominated at frequencies from DC to 4 Hz, even though only $\frac{2}{3}$ of the available input laser power are in use. This implies definite disturbance of the control of the corresponding degree of freedom.

Projection factor and coupling factor

A trite remark at this point: Of course it does not matter whether the flag spectral density is multiplied by the projection factor or whether the circulating power spectral density is multiplied by the inverse of the projection factor. The results are the same. An advantage of the inverse of the projection factor, from now on called coupling factor $c_{\text{couple}} = r_{\text{proj}}^{-1}$ is that it provides a number that is proportional to the amount of stray light contamination. For an individual LC one can directly compare the amount of stray light contamination at the individual flags in a quantitative way by comparing coupling factors. The larger the coupling factor the larger the stray light coupling.¹ Furthermore, assuming equal gain for

¹ One could also compare the projection factors. But in that case a smaller value would mean a larger coupling. Confusion would be granted.

all main suspension LC error signals, it is possible to compare flag signals belonging to different suspensions. Exact equal gain can of course not be granted, but this assumption can be used as an approximation for the GEO 600 main suspension LC systems.

3.2.3 Amount of laser stray light at all main suspensions of GEO 600

With the noise projection method explained in section 3.2.2, the amount of stray light coupling to all shadow sensors of all main suspension LCs was measured. These investigations have shown that for all main suspension LCs, except for the one that belongs to MSR, contamination of the error signals by laser stray light is an issue to be dealt with.

The fact that the MSR suspension LC shows significantly less stray light contamination than all other LCs that belong to the dual-recycled Michelson interferometer main suspensions has a trivial reason. It is placed at the dark port and is not part of the power-recycled Michelson interferometer. Its corresponding vacuum tank's only connection to the remaining main IFO vacuum cluster is an aperture which has a diameter of about 8 cm.

In figure 3.8, a whole set of projections for all six error signals of the BS LC is shown. All remaining projections of the other main suspensions can be found in appendix A. The corresponding coupling factors for the BS and all other main suspensions can be found in table 3.1. One can see in figure 3.8 that the error signals of BS flag 1 and flag 2 are dominated by the coupling of laser stray light at frequencies up to 2 Hz. For significantly higher circulating laser powers, as planned in the GEO-HF upgrade, the same will be the case for the remaining four error signals.

Even at the initial GEO 600 operational power, optimal damping of the corresponding rotation degree of freedom cannot be provided for this particular case. A strong oscillation at a pendulum resonance, excited for example by a seismic event, would modulate the circulating power and therefore the stray light inside of all tanks belonging to the main IFO.

Suspension	coupling factors $c_{\text{couple}} \cdot 10^{-4}$ [a.u.]					
	Flag 1	Flag 2	Flag 3	Flag 4	Flag 5	Flag 6
MPR	8.55	2.95	1.90	2.18	11.25	4.02
BS	17.61	16.92	4.56	3.84	2.86	11.35
MCE	11.33	9.07	1.20	1.26	0.83*	1.68
MCN	3.65	1.38	1.00*	1.36	5.91	5.83
MFE	12.69	14.05	4.40	12.50	6.32*	6.55*
MFN	2.06	2.22	5.08	3.35	5.38	9.47
MSR	none	1.67*	1.25*	none	none	none

Table 3.1: Coupling factors for all main suspension local controls. If we assume equal gain at all LCs, we see that at most LCs an equally high coupling exists as in the case of the BS LC. Numbers marked with * are upper limits.

The local controls will sense these fluctuations. The resulting feedback which is applied to the uppermost mass will enhance the fluctuations even further. If more laser power is used, the amount of stray light illuminating the vacuum tanks gets higher. Therefore, the amount of laser power fluctuations increases with increasing operational power, just as shown in figure 3.2 in section 3.2.1. At the same time the likelihood increases that lock losses as shown in figure 3.1 happen. The major aspect of a decreased stability of GEO 600 for high laser power operation is explained by the mechanism of laser power fluctuations coupling as stray light into the shadow sensors of the GEO 600 main suspension local controls. The results of the stray light coupling measurements that are summarized in table 3.1 imply that at almost all main suspension LCs stray light coupling limits an operation of GEO 600 with significant higher laser power. In the following section, a solution for this problem is provided that does not require any hardware change inside the vacuum system.

A further glance on the exemplary lock loss

By comparing the measured coupling factors of the main suspension LCs in table 3.1, it is obvious that the stray light contamination is highest for the rotation and longitudinal degrees of freedom (i.e. flags 1 and 2 serve for both rotation and longitudinal damping). This is even more obvious by comparing all stray light projections shown in appendix A. This means that stray light introduced fluctuations should in particular be visible in the rotation alignment signals and the spot position signals. This is actually the case as shown in figure 3.9. The upper plot of this figure shows the circulating power as shown in figure 3.1, and for clarity it is zoomed in to seconds 25 to 75. The other two plots of figure 3.9 show the spot positions on MFE and MFN for rotation and tilt, respectively, at the same time. In both cases, the plots show a strong increase in fluctuations belonging to rotation at the same time the fluctuations on the circulating power are building up. In tilt the effect is only marginal. This is a nice agreement with the results of the stray light projections that were just discussed.

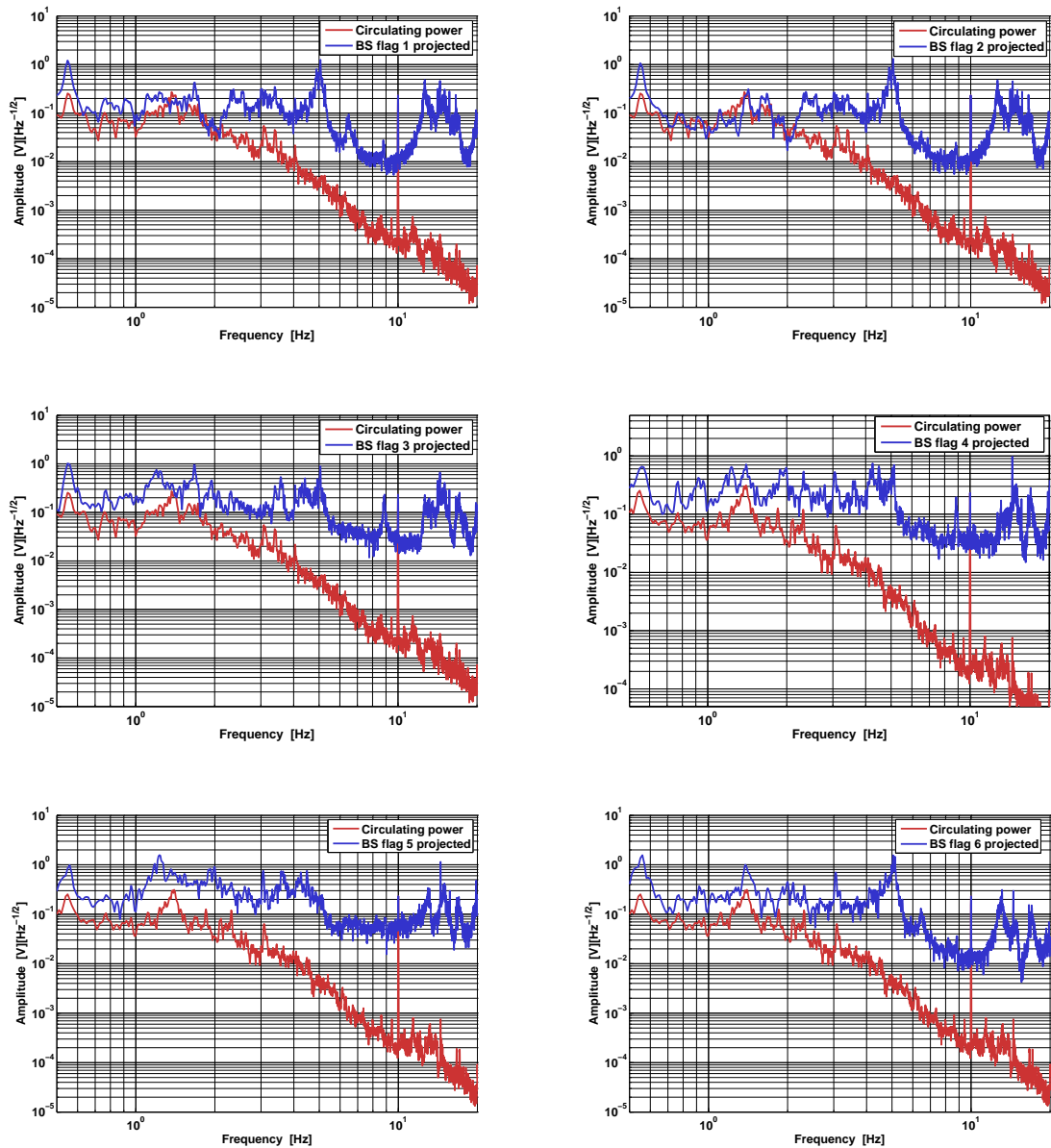


Figure 3.8: Laser stray light projection for all six BS flags at $\frac{2}{3}$ of the available input laser power. The laser amplitude modulation is applied at 10 Hz. All traces are showing 5 minutes of data. For flag 1 and 2 the error signals are clearly dominated by laser stray light around 1 Hz. Both flags control the rotation and longitudinal degrees of freedom. Thus, there will be a disturbance of optimal damping of the upper most mass in rotation and longitudinal degrees of freedom. The error signals belonging to the remaining four flags still show stray light contamination to some degree. One can act on the assumption that for higher circulating power these flags would limit a stable operation.

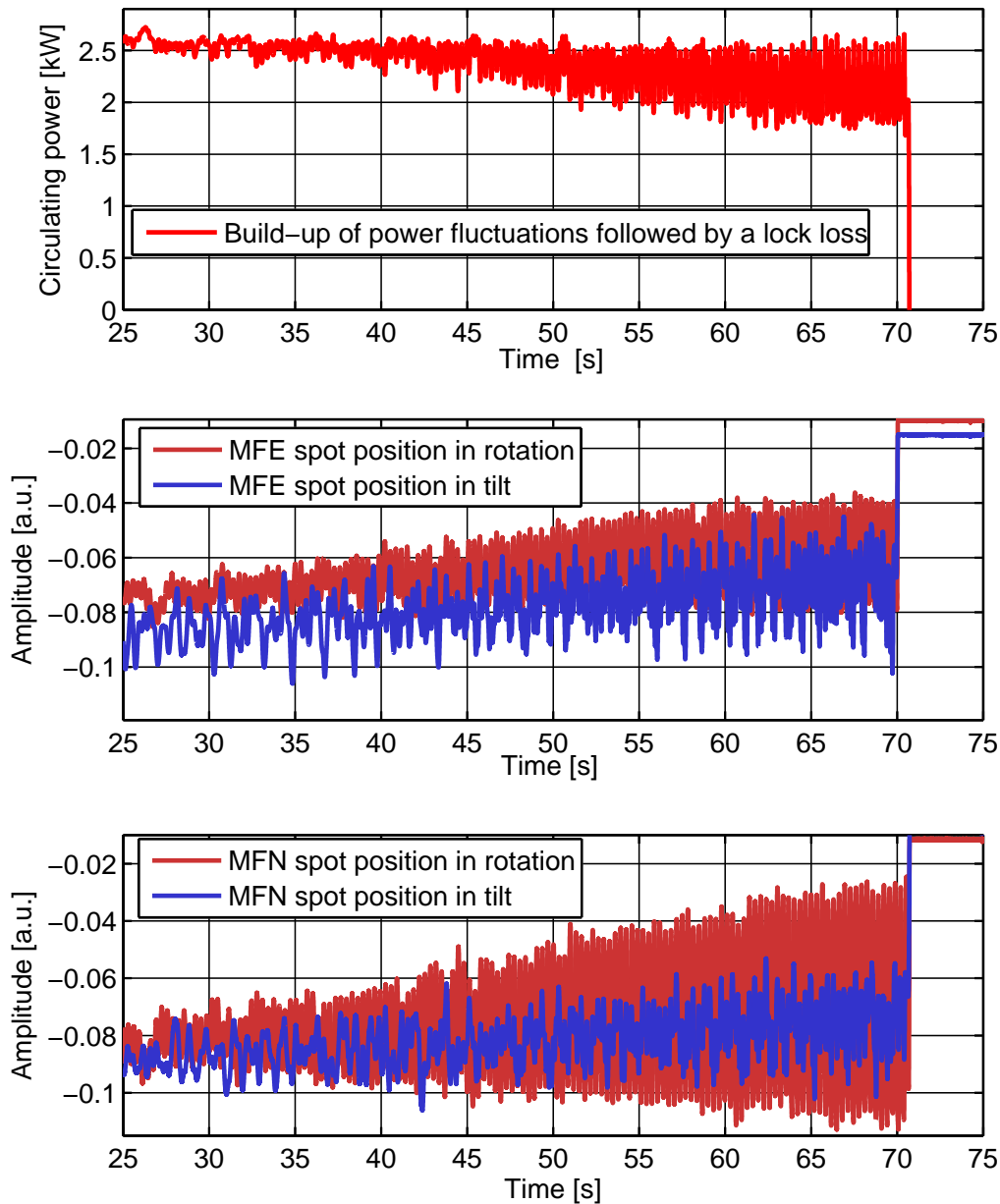


Figure 3.9: A further glance on an exemplary lock loss. The upper plot of this figure shows the circulating power while a stray light induced power fluctuation builds up and finally results in a lock loss after 70s. It uses the same data as figure 3.1, and is zoomed in for clarity. The plot in the middle and the plot on the bottom show spot position signals on MFE and MFN in rotation and tilt, respectively. It is obvious that the spot position signals show a significant higher build up of fluctuations in rotation. This matches with the previous results that more scattered light couples into the flags that are used for the rotation control of the upper masses.

3.3 A modulation-demodulation scheme for the local controls

What can we do to reduce or even get rid of the laser stray light coupling and allow for a stable operation with higher circulating light power? An obvious way to reduce the amount of stray light coupling would be to block it on its way to the flags such that it does not contaminate the LC error signals anymore. For example, this could be done by installing baffles in the tanks that are housing the corresponding suspensions.¹

Another option is an exchange of all shadow sensors by new ones that are not sensitive to infrared light. For this case, all LEDs would need to be replaced by a type that is radiating at a significantly different wavelength from the main laser. Preferable would be a far shorter wavelength and new sensors that are insensitive to 1064 nm light. Furthermore, shadow sensors and LEDs as well as the coils are combined encapsulated in glass. To switch to a different wavelength the flags need to be redesigned, built and replaced.

For both options, i.e. stray light blocking and flag replacement, the vacuum tanks that belong to the main interferometer would have to be opened up. Two major arguments speak against this, neglecting the corresponding work time needed for now. First, we would have significant large down times of GEO 600. A major goal of the GEO-HF upgrade is to allow for as much astrowatch time as possible. The second and probably more important argument is the large risk that lies in opening the tanks of the central cluster and in particular the needed work at the suspension systems. Breaking a monolithic suspension or even flooding the 600 m long vacuum tubes are two examples of the potential risks. Regarding these infrastructural restrictions, another approach including a smaller risk and consuming a minimum of science time is preferable. We decided to use a modulation-demodulation scheme on the flag readout system for the suspension local controls.

3.3.1 Basic idea and requirements

As shown in chapter 3.2, the major amount of laser power fluctuations that couple as scattered light into the shadow sensors of the LCs lies in the active frequency band of the LC electronics. To filter out the scattered light that is sensed by the shadow sensors, the LEDs, operated at DC, will need to be modulated with a sufficiently high modulation frequency. Thus, the part of the error signal that mostly contains scattered light information and the error signal that shows the actual movement of the upper mass will be well separated in frequency by the modulation frequency. The required DC error signal,

¹ In 2012 and 2013 several baffles were actually installed to reduce scattered light in the tanks. Although, the baffles were not installed to reduce stray light coupling to the suspension LC shadow sensors, we made use of the shadow sensors sensitivity to scattered light to get a measure of its reduction due to the installed baffles. It turned out that the amount of scattered light detected by the shadow sensors decreased just by a factor of two to three. With respect to scattered light coupling to the LC's shadow sensors, this decrease is not sufficient to handle laser power levels as planned for GEO-HF.

that senses the pure movement of the upper mass, can be obtained by demodulating the PD photocurrent. This modulation step shifts the stray light contaminated part to AC. To remove the stray light part low pass filtering of the demodulated error signal should be applied. This is the working principle of the modulation-demodulation scheme that we implemented for the GEO 600 LCs.

Requirements

Operating the GEO 600 LCs with a modulation-demodulation scheme will necessitate an extension of the LC electronics. Ideally, the existing LC electronics remain unchanged but get extended by a second module. This second module will have to carry out the modulation and demodulation tasks, and can be easily placed into the LC operation chain. Such an additional module will have to meet several requirements to not influence the LC performance in a negative way.

No extra noise should be introduced into the GEO 600 detection band, as it was already demanded for the LC electronics themselves in chapter 2.5.1. Also, such a module should be compact, robust and work reliably. Compactness is preferable due to space limitations on the GEO 600 site. Robustness and reliability are necessary for continued data taking periods. Disturbances of the LC operation that shake a suspension or even result in a lock loss cannot be tolerated. Furthermore, one needs to keep an eye on the stability of the LC loop and an appropriate oscillator needs to be found. It is desirable to choose a modulation frequency outside of the GEO 600 detection band as long as the existing LEDs are capable of operating at a corresponding AC frequency over many years.

3.3.2 The Modulation Drive

We developed a six channel modulation-demodulation scheme for the GEO 600 main suspension LCs. To make it as simple and practical as possible it is an additional electronic module that converts the DC readout of the LC that belongs to a single suspension to an AC readout. This module is called *Modulation Drive* (MD). In the process of testing and optimizing the MD several changes were implemented until the MD reached its final layout and was ready to be installed at the LCs. The working scheme of the MD is outlined in figure 3.10 and described below, whereas the experiments that lead to its final layout are presented in section 3.3.3. The circuit diagram is given in appendix C. Although the MD is developed as six channel solution for the main suspension LCs, it can also be used for the four channel LCs of the other suspensions. Two channels are simply not used in that case.

It turned out that an external *Local Oscillator* (LO) is preferable to an on board LO for the MD. As described in section 3.3.3, using an external LO has two major advantages: First, commercial on-board LO chips (which were tested) showed a worse noise perfor-

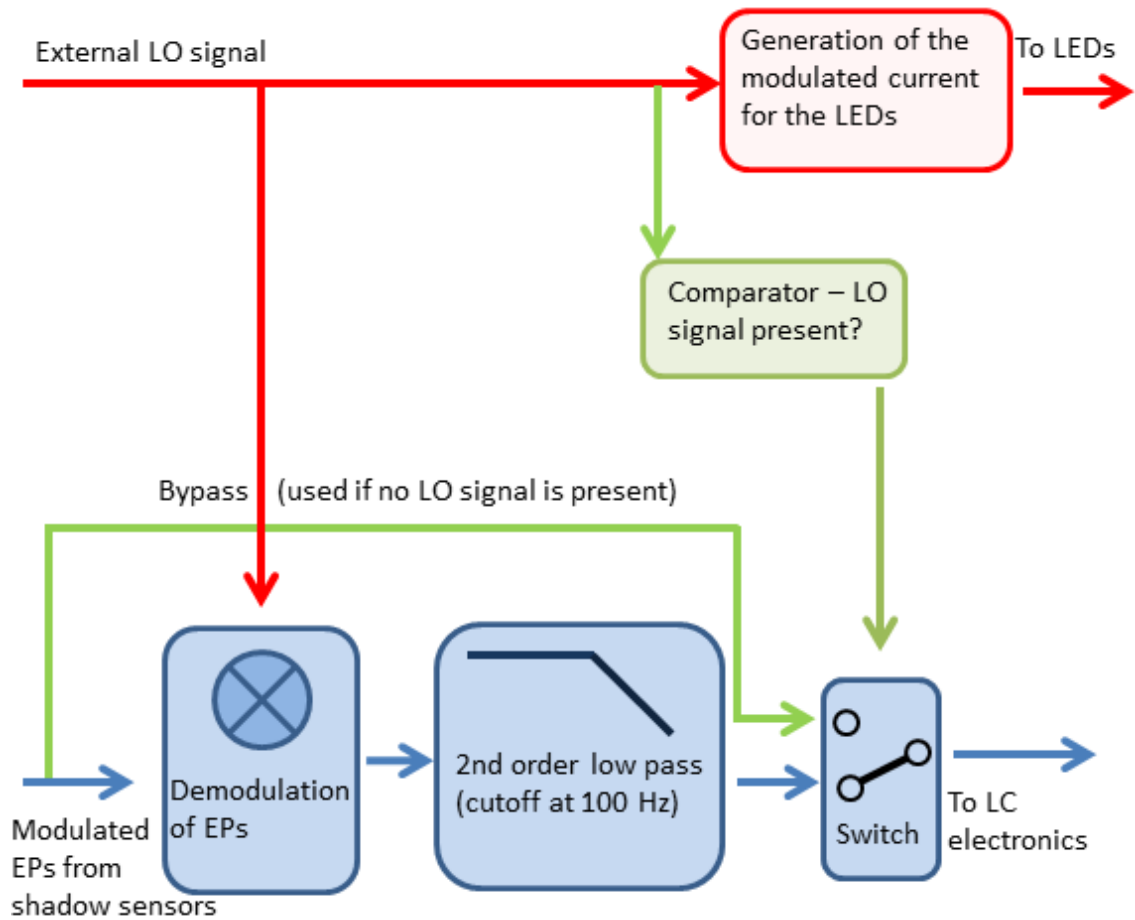


Figure 3.10: MD scheme in its final version. An external LO signal is used to generate a modulated current to drive the LEDs. The modulated error signals (EPs) are received and mixed down to DC in a further modulation step. Low pass filtering of the signals strongly attenuates the stray light contaminated part. If no external LO signal is applied, the LEDs are operated at DC and the error signals bypass the demodulation step.

mance than external LO sources. Second, the MD’s circuit becomes simpler by using an external LO source and the LO frequency can be remotely controlled if necessary.

LO and MD power supply

The LO is provided by an additional module that uses a microcontroller to generate the signal. As described below, it was shown that the noise performance of such a microcontroller generated signal is equally good as the one generated by a commercial function

generator. Because only a single fixed frequency is needed that does not need to be changed regularly, the flexibility of a function generator is not needed, and an integrated version was expected to be more fail-safe.

Furthermore, we integrated a GEO-like power supply on the microcontroller board. The circuit diagram of the MD's power supply and of the LO source microcontroller board is provided in appendix C.

Anticipating the results below, three of these local oscillator and MD power supply modules are used for GEO 600. One of these modules is used to supply the LO signal and the electrical power to each MD at the far end stations. The third module supplies just the LO signal for five MDs installed at the LCs in the central building.

Modulating the LEDs

The MD differentially receives the electric LO signal to decrease its susceptibility to electromagnetic noise compared to the use of a single wire. Since the LC LEDs can easily withstand being operated with AC currents of several kHz on long timescales¹, a modulation frequency of about 10 kHz is used to have the modulation outside of the GEO 600 detection band. As amplitude of the LO signal, received by the MD, 6 V_{pp} are needed. The LO signal is converted to a current that drives the LEDs which are connected in series for an individual suspension LC. To convert the LO signal, a current driver consisting of an operational amplifier and a transistor is used that is connected in series with the LEDs. The transistor is also used to allow operation of four and six LEDs, respectively, such that the MD can be used for the four channel and the six channel LCs. A fuse in this chain ensures that the LEDs do not get damaged, i.e. by a short cut that would result in 15 V over the LEDs instead of 6 V. LED protection is particularly important because a broken LED cannot be replaced without opening the corresponding vacuum tank. By driving the LEDs with the AC current, the whole error signal that are detected by the individual shadow sensors get shifted to the modulation frequency and are thereby separated from the DC stray light parts.

Getting the stray light free error signals

In default operation, the LC error signals are received as a current by the LC electronics and are converted into feedback signals. If a MD is installed at a LC, the modulated error signals are first received by the MD using a current to voltage converter. Each channel

¹ The original datasheet of the LEDs could not be found anymore. We just know that they were obtained from Siemens or Infineon. However, a similar model using the same chip is the sfh484 LED. Its datasheet contains information that implies that a long scale modulated operation does not harm the LEDs as long the modulated RMS current is equal to the actual DC current.

gets mixed down with the LO signal by an “AD630” (see appendix C). The AD630 is a commercial modulator/demodulator from “Analog Devices”. Each demodulated error signal gets filtered by a two pole lowpass with a cut off frequency of 100 Hz to suppress the stray light component. Using a far smaller cut off frequency would result in a significant loss of phase margin within the active band of the LC electronics that is between 0.3 Hz and 3 Hz. Finally, a voltage to current converter is used to emit the demodulated error signals as a current. This is needed since the LC electronics expect an input current as signal from the shadow sensors. Due to that the LC electronics can remain unchanged if a MD is installed.

A simple bypass

A final feature of the MD was not described so far. If need be the MD can simply be bypassed by switching off the external LO signal. The MD detects if an appropriate LO signal is present. If not, it bypasses the demodulation path and simply emits the error signals as currents at the correct level. The possibility to bypass the MD turned out to be very practical in the testing and optimization phase of the MD as well as during problems at the far suspension LCs, which are described in appendix C.2.

However, the major reason to install this bypass was to be safe against a loss of the LO signal.¹

3.3.3 Primary tests at the test suspension

To extend a GEO 600 local control by a modulation drive, it needs to be checked for its functionality first. To minimize risks for an actual GEO suspension system, all MDs that have been installed in GEO 600 are tested beforehand at a test suspension setup. Figure 3.11 provides a photograph of the test suspension. These tests include checks for functionality of the corresponding module, level adjustment of the individual channels and other minor tests. In addition to risk reduction, initial testing at the test suspension ensures maximum science time, since no subsystem of the main IFO is needed for experiments that can be done at a test system. Also, the major part of experiments that were carried out during the process of developing the MD to its final layout happened at the test suspension. These tests include finding an appropriate modulator to minimize the noise that is introduced by the modulation-demodulation process. After the basic functionality of a MD module or a new MD type was shown, further experiments were carried out at the LC of the power-recycling mirror suspension as described in the next section.

¹ It should be added that for safety reasons, all corresponding LC gains need to be set to zero while pulling the LO signal. This is to avoid getting error signal jumps into the feedback loops.

The test suspension

The test suspension is a duplicate of a GEO 600 triple suspension system including a six channel LC. However, it has some differences compared to an actual GEO 600 triple suspension. One important difference is, that the test suspension is not mounted on a pre-isolation system, the so called stacks which are noted in chapter 2.5.1. For details about the stacks and the whole GEO 600 suspension system see [Goß04]. Furthermore, the test suspension is not placed in vacuum, and uses thicker wires to suspend metal dummy mirrors. These differences result in a stronger movement of the pendulum stages as compared to a GEO 600 suspension. Stronger movement of the upper mass results in an increased signal strength in the LC error signals compared to the LC error signals of the main suspensions for instance.

For a noise comparison of LC error signals in default operation to the operation with installed MD, this needs to be taken into account. In particular, if such a comparison of LC error signals is aiming at investigating possible extra noise, that arises from the modulation-demodulation process. A noise analysis within the active band is particularly difficult. Corresponding results at frequencies of a few Hz and below could only be obtained at the actual GEO suspension LCs.

MD testing at the test suspension LC

Noise, added to the LC electronic signals by the MD, should be as small as possible. Within the active band of the LC it should even not exist. One major task of a LC is to damp pendulum resonances. Noise induced by the MD to flag signals at pendulum resonance frequencies could excite these resonances. The result would be undesired movement of the mirror that eventually disturb the detector's performance. In the worst case, lock losses could occur. To investigate the noise performance of a LC operated with MD experiments at the test suspension were done. Most of these experiments were focused on minimizing additional noise, introduced by a MD, and on determining which LO signal source is most applicable for low noise operation of LCs with a MD.

Such experiments were done, while operating the test suspension LC with a MD using different modulation sources. The LC error signals were recorded right after the current to voltage converter on the LC electronics board, that receives them. To record the signals a HP 35670A spectrum analyzer was used. Figure 3.12 shows error signals of the test suspension LC flag 1. Different LO sources are in use in the displayed cases to drive the MD. All modulators were operated at a frequency of 5 kHz.

The blue trace shows a spectral density of the LC flag 1 error signal for default operation, i.e. no MD installed. The light green trace shows the flag 1 error signal while a MD is installed using a commercial on board modulator, namely a XR2206 monolithic function generator from EXAR as LO. Because we found that the XR2206 LO signal has fairly high amplitude noise, an additional amplitude stabilization loop was used to further stabilize



Figure 3.11: The GEO 600 test suspension. This is a duplicate of a GEO-like triple suspension including a six channel local control system. Initial experiments with the MD were performed at this test setup.

its LO signal. Amplitude stabilization of the LO signal provided by the XR2206 results in a broad band reduction of noise in the demodulated flag signal. This is shown in the dark green curve. Furthermore, the black curves shows the demodulated error signal for using a self build Wien bridge oscillator as LO of the MD. Obviously, using this LO results in the noisiest of the displayed cases. Finally, an Agilent 33250A function generator was

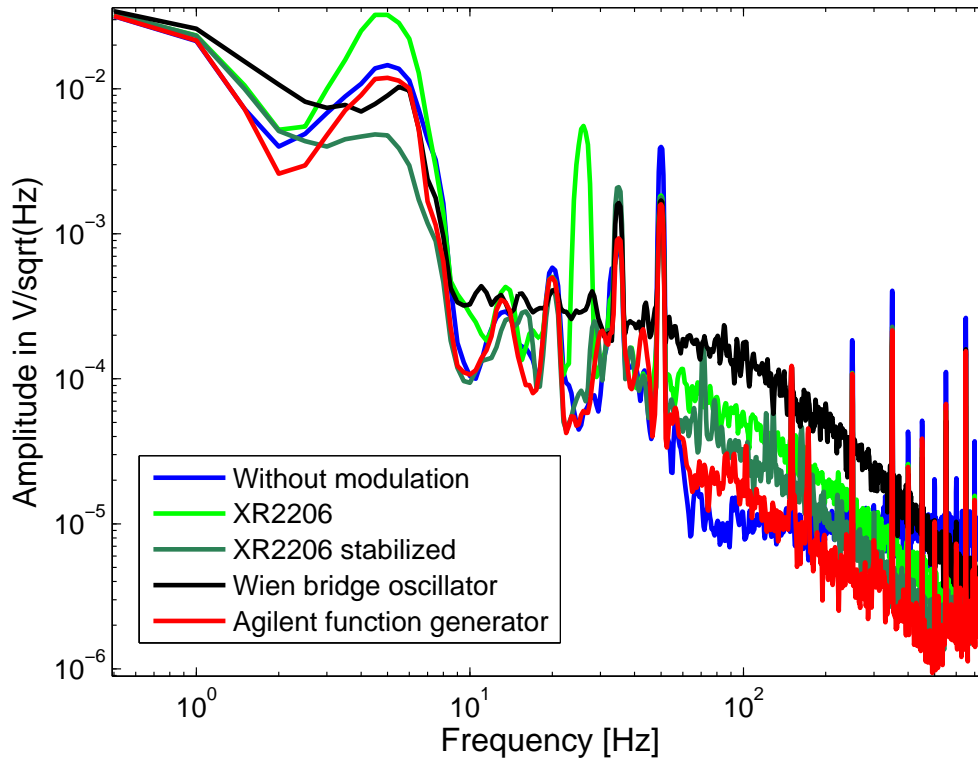


Figure 3.12: Error point spectral densities showing the test suspension LC flag 1 signal operated with MD using different LO signals. These spectral densities are compared to the case without modulation (blue trace). Note that the measurements get less reliable the lower the frequency gets due to a missing pre-isolation system at the test suspension.

used as LO source for the MD. This is shown in the red curve and represents the best result. For all cases in which a LC is extended by a MD, the error signal noise gets below the DC case for frequencies between 100 Hz and 500 Hz. This is due to the 100 Hz double low pass that is a part of the MD.

The test suspension LC shadow sensors sense stronger movement of the uppermost mass than they would at an actual GEO 600 suspension. Therefore, no direct information about small noise contributions that are caused by the individual modulators can be obtained below approximately 10 Hz. For these experiments it was ensured that no unnecessary disturbances occurred, like other people doing physical work nearby. Otherwise, the data would be dominated by movements of the upper mass up to even higher frequencies. Reliable information at lower frequencies needed to be obtained by measurements done directly at a GEO 600 suspension. These are presented in the next section.

Regarding the results shown in figure 3.12, the best choice would be to use a commercial,

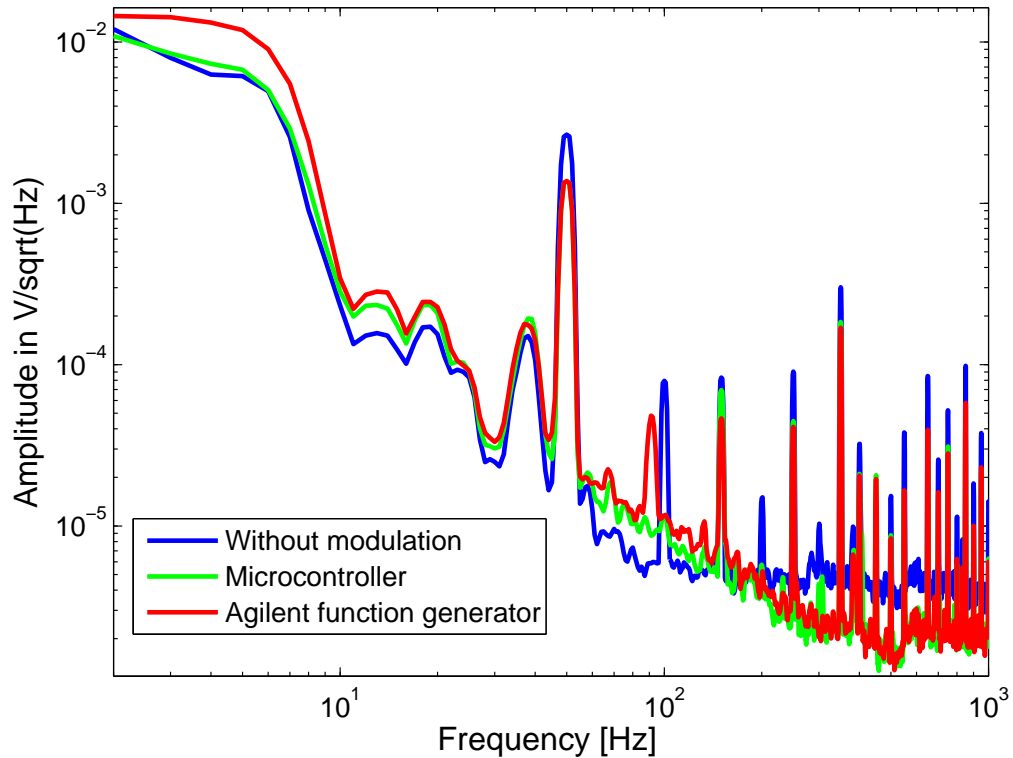


Figure 3.13: Error point spectral densities showing the test suspension LC flag 1 signal, operated with MD, using an Agilent function generator and a self made microcontroller circuit as source for the LO signals, respectively. These spectral densities are compared to the case without modulation (blue trace). The microcontroller circuit is equally well suited as LO source for the MD as the Agilent function generator.

external function generator, as it adds the least noise which is preferable. At least three function generators would be needed, one of them serving as modulation source for MD(s) in each building.¹ Some effort was taken to either improve the performance of the XR2206 or to find another solution that can compete with the Agilent function generator. The best possible performance achieved by using the XR2206 is already shown in figure 3.12. The mentioned amplitude stabilization feedback loop was commissioned for quite a while but still results did not reach the level of an Agilent function generator.

Later on, we investigated the possibility of using a LO signal generated by a microcontroller circuit as described above. It showed a comparable or even slightly better noise

¹ MDs are needed at suspension LCs that are placed in three different buildings: the central building and the two far end stations.

performance than the commercial Agilent function generators that are available on site. A comparison of the test suspension LC error signals being operated with MD using the microcontroller signal, the Agilent function generators and the case without modulation is given in figure 3.13. This measurement shows that the microcontroller circuit and the Agilent function generators are equally well suited as LO sources for the MD with respect to the amount of noise added to the demodulated LC error signals.

A disadvantage of a microcontroller circuit as LO for the MD is that to change the signal's frequency it needs to be reprogrammed. This involves some effort and cannot be done on the fly like it works for commercial function generators. However, a fixed modulation frequency is needed for operating a LC with MD. Therefore, the application of a microcontroller circuit as LO source suggests itself.

Being confident with the microcontroller as LO source we decided to abandon the idea of an on board solution and go for an external LO source. This resulted in the final layout of the MD as shown in appendix C. Additionally, the idea of the aforementioned bypass that is active when no LO signal is detected, was implemented.

Feedback noise at the test suspension LC

No matter which local oscillator is used for the modulation-demodulation process some extra noise is added to the demodulated shadow sensor signals of the test suspension LC. Depending on the type of LO that is used, the extra noise starts to show up at 10 Hz or above. The LC electronics should provide additional attenuation to this extra noise since it low pass filters the shadow sensor signals above its active band. As described in chapter 2.5.1, the active band of the LC electronics ends at 3 Hz. To investigate how much MD induced noise remains in the feedback to the LC coils, further experiments were done at the test suspension system. Figure 3.14 shows a similar measurement as shown in figure 3.12. For clarity all measured signals were low pass filtered at 100 Hz using a Stanford Research SR560 pre-amplifier to attenuate the high amplitude part at several 10 Hz and below. Spectral densities of the test suspension LC flag 1 error signal in operation with MD using the XR2206 and the Agilent function generator as LO are compared with the case without modulation. Furthermore, the noise of the LC electronics at the same measurement point is shown for the case that no shadow sensor signal is connected to the LC electronics.

The second plot in figure 3.14 shows the same cases, but for the flag 1 feedback signals instead of the error signals. Compared to the DC case extra noise from the modulation-demodulation process is still present in the feedback. But for the Agilent function generator as LO source it is still only present in a narrow frequency band. Above 100 Hz to 150 Hz it is even below the noise for DC operation of the LC. Due to the filtering of the LC electronics, the noise is far less problematic than it used to be in the demodulated error signals. It is time to investigate the operation of a GEO 600 main suspension LC with MD. An experiment that is meant to investigate potential coupling of MD induced

feedback noise to the strain sensitivity of GEO 600 is described further below.

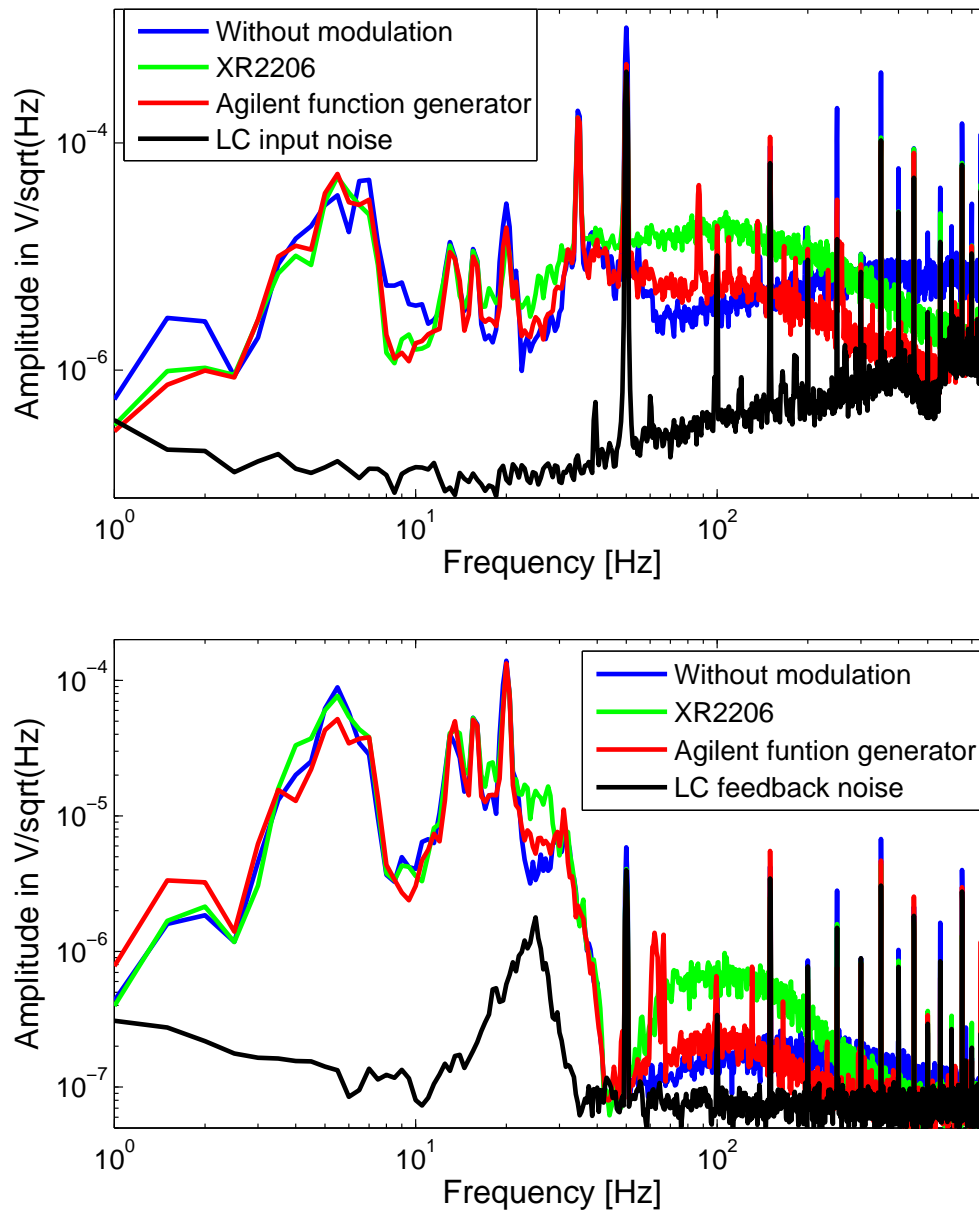


Figure 3.14: Top plot: Error point spectral densities showing the test suspension LC flag 1 signal operated with MD using different LO signals compared to the case without modulation and to the case that no shadow sensor signal at all is connected to the LC electronics. Except that the signal is low pass filtered for clarity, this measurement is comparable to the one shown in figure 3.12.

Bottom plot: Same as for the first plot, but all traces show spectral densities of the feedback signals instead of the error signals.

Note that a 100 Hz low pass filter is applied for clarity for all measurements in both plots. Because the performance when using the microcontroller as LO source to the case of the an Agilent function generator is comparable as shown in figure 3.13, only the latter is shown.

3.3.4 MD testing at the local control of the power-recycling suspensions

The results obtained by testing the MD at the test suspension LC are promising. By using an appropriate external LO for the MD only marginal additional noise is added to the flag signals of the LC at the test suspension setup. To investigate the performance of an actual GEO main suspension being operated with MD, it was first tested at the LC of the *power-recycling mirror* (MPR). Because the MPR suspension has no monolithic stage, but a six channel LC, it serves well for experiments testing the MD within GEO 600. This is due to the fact, that the steel wires of the MPR suspension are more robust than the monolithic fibers at other GEO suspensions. This is an advantage if unexpected effects like an oscillation occurs. Such an oscillation with a high amplitude would more likely

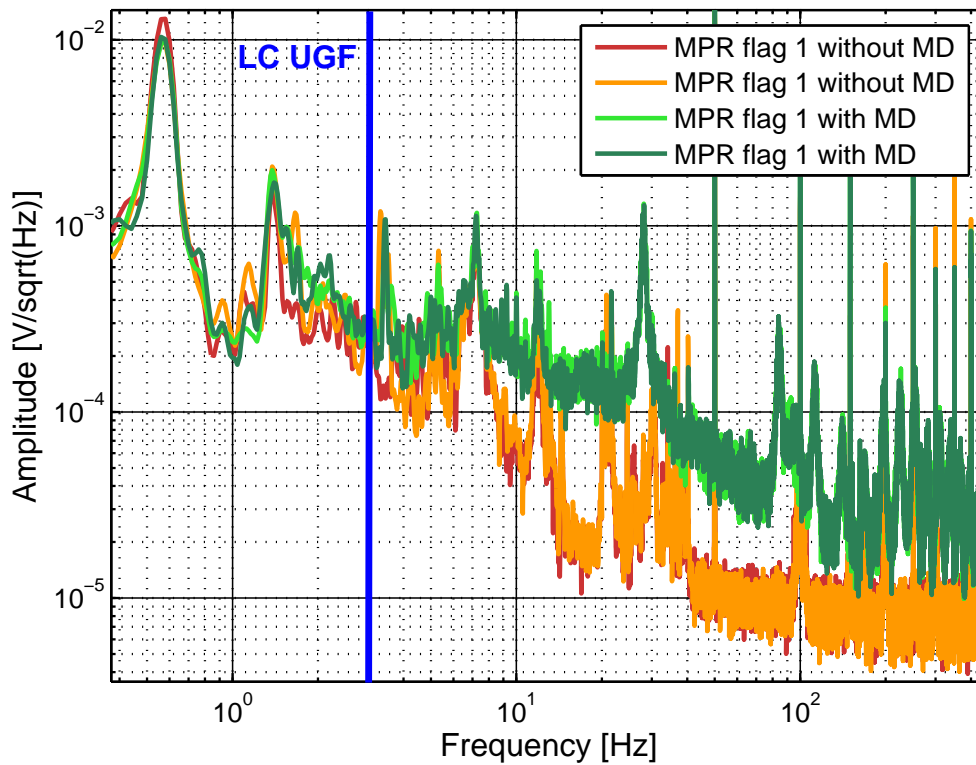


Figure 3.15: Error signal spectral densities of the MPR suspension LC flag 1 with and without MD. A significant amount of extra noise is added to the error signal above the LC's upper UGF if operated with MD. The upper UGF is highlighted in blue. The remaining five flags of the MPR LC show comparable results. Therefore, they are omitted here.

result in breaking a monolithic fiber than a steel wire of the MPR suspension.

Figure 3.15 shows two spectral densities of MPR flag 1 for default operation measured at different times (red and orange) and two spectral densities for operation with MD also measured at different times (light green and dark green). For the latter case, a microcontroller circuit that provides a 10 kHz LO signal, is used.

It is obvious, that significantly more noise is added by the modulation-demodulated process to the MPR flag 1 error signal compared to the default case. In the amount as shown in figure 3.15, this was not expected considering the results obtained at the test suspension LC. This noise seems to have two components. A broad band noise is added, that starts above the upper UGF of the LC electronics and goes below the noise in the default operation case at 400 Hz. Slightly below 20 Hz the difference of the noise is highest being almost 10 times higher for the operation with MD. Furthermore, we see large peaks at several frequencies, for example at 28 Hz or at 82 Hz.

A part of the investigation to minimize the extra noise in LC error-point signals was described in section 3.3.3 as part of finding an appropriate LO for the modulation process. If the MD uses modulators like the XR2206 as LO, the additional noise in the MPR suspension LC error signals are even worse. This is not shown in figure 3.15. It shows already

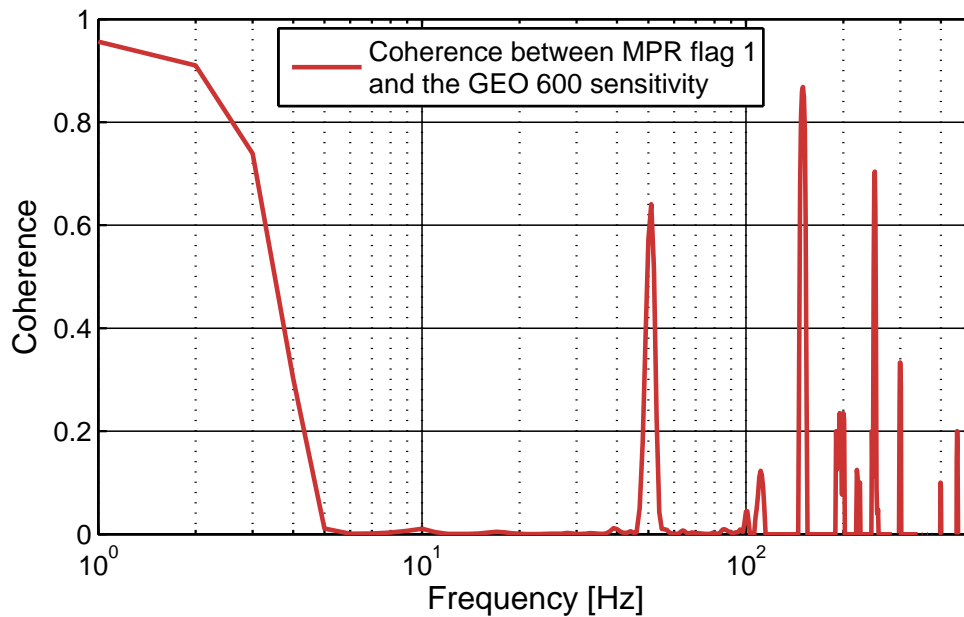


Figure 3.16: Coherence between the error signal of the MPR suspension LC flag 1 with MD and the GEO 600 sensitivity. Even though a significant amount of extra noise is added to the MPR flag1 error signal as shown in figure 3.15, a clear coherence to the sensitivity is not visible.

the results with an optimized modulation-demodulation scheme, but this additional noise looks worse than it actually is for the GEO 600 sensitivity.

First of all, the additional noise is not necessarily displacement noise of the upper mass. It is only visible if the LC is operated with MD. Thus, it can well be sensing noise and the default sensing noise of the LC gets worse if operated with MD. In addition, it was shown, that the peak-like structures at 28 Hz or at 82 Hz have a connection to a lab-view controller. If the cycle duration of this controller is changed, the frequency at which these peaks occur changes, too.

Even though the error point is more noisy above the UGF of the LC, this noise is attenuated towards the individual mirrors. As said before, the LC electronics provide further filtering of this noise above 3 Hz. Figure 3.14 has shown this. Additionally, the suspensions themselves provide filtering to residual feedback noise. Depending on the suspension an MD is installed at one or more pendulum stages provide significant further attenuation. Still, it is important to investigate if it couples to the strain sensitivity of GEO 600.

To do so we can calculate the coherence between error-point signal for the discussed case of the MPR LC operated with MD and the GEO 600 sensitivity for a data series sampled at the same time. This is shown in figure 3.16. Noise characteristics that are added by the MD show no coherence with the sensitivity. Clear coherence can only be found below several Hz and at 50 Hz and its harmonics. The latter couples via various other ways to the sensitivity.

However, a movement of the power-recycling mirror couples less into the sensitivity than a comparable movement of a mirror would that belongs to the Michelson interferometer. A shaking power recycling mirror primary affects the circulating power of the power recycled Michelson interferometer. Individual movement of a “Michelson” mirror results in differential noise and therefore directly affects the sensitivity. The effect of noise in LC error signal of a mirror that belongs to the Michelson Interferometer to the sensitivity of GEO 600 is investigated in the next section.

3.3.5 Local control noise projected to the GEO 600 sensitivity

The example of the MPR LC shows that a significant amount of noise is added to a LC error signal over a wide frequency range if operated with MD. In the following we will study in how far this noise couples to the main detector output, h , in the case of a Michelson mirror. A strong coupling to h is not tolerable, in particular at frequencies above 100 Hz, where the main detection band starts.

To investigate in how far the extra LC noise affects the sensitivity, the LC noise was projected to h . For this experiment, a sine wave was injected into the feed back signal of flag 3 of the MCN LC. The amplitude was chosen such that a significant movement of the upper mass gets detected, i.e. is visible in the flag error signal. Subsequently, it was checked if a coupling to h is visible at the injection frequency. This was repeated for

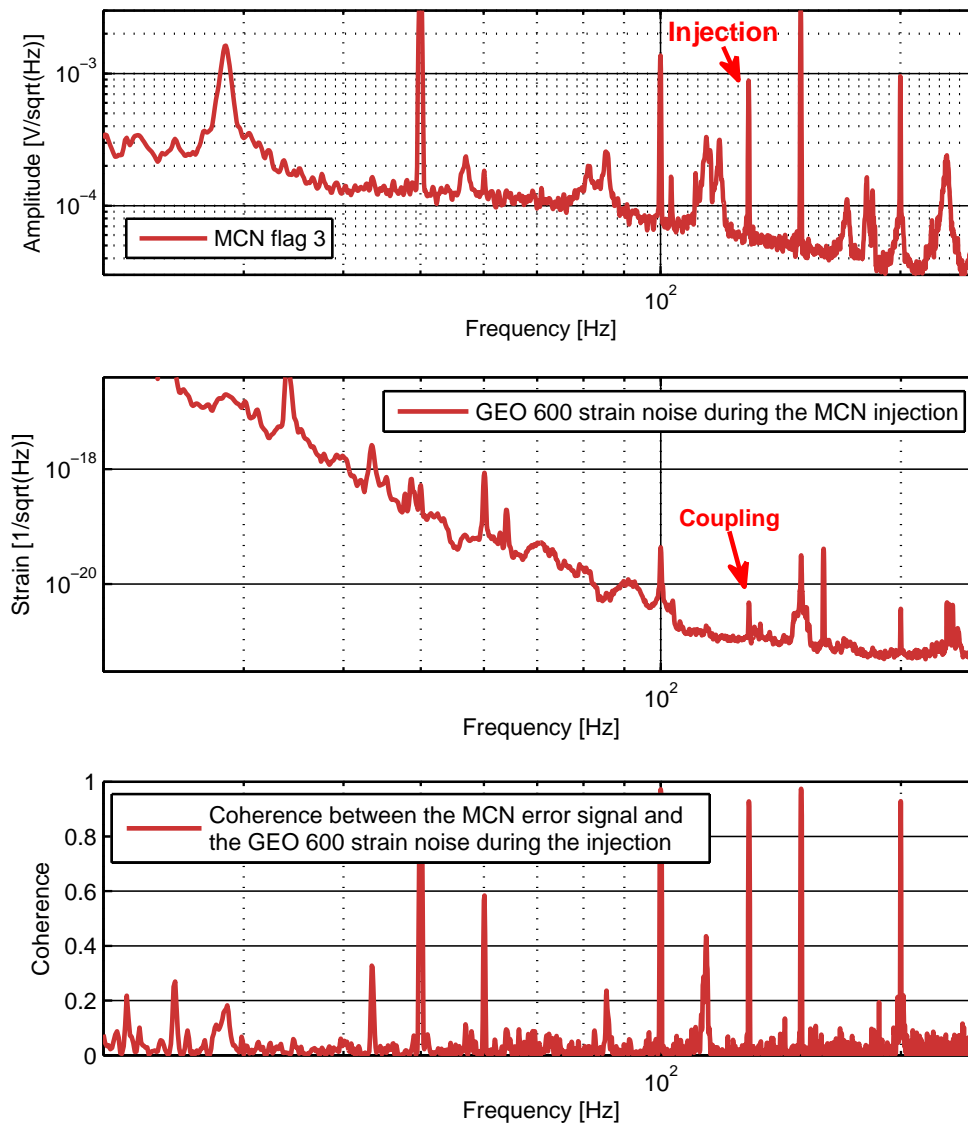


Figure 3.17: A noise injection at 129 Hz to the LC feedback in tilt of the MCN suspension and its effect on h . The plot on top shows a spectral density of the MCN flag 3 error signal. The movement at 129 Hz is clearly visible in the error signal. The plot in the middle shows the sensitivity at the same time. The injected line couples clearly to h . Also note the tiny structure at 115 Hz in h . They are part of the MD-induced extra noise. At the bottom of this figure, the coherence between the error signal and h is shown. The coherence is distinct at 129 Hz but also at other frequencies, at which the error signal shows pronounced features. A noteworthy coherence over a wide frequency band is not visible.

several different frequencies between 37 Hz and 208 Hz.

Figure 3.17 provides three different plots and shows the effect of an injection at 129 Hz. The plot on top shows the spectral density of the MCN flag 3 error signal. The injection at 129 Hz is clearly visible in the error signal. In the plot in the middle of the figure, the sensitivity is shown at the same time. The injected signal is visible in h . Furthermore, one can see a tiny bump at roughly 115 Hz. This bump in h could be caused by the corresponding noise structure in the error signal of the shown MCN flag.

A potential coupling to h gets stressed by the coherence plot at the bottom of figure 3.17. A significant coherence is not only visible at 129 Hz and at 50 Hz as well as its harmonics, but also at 115 Hz. In addition, less pronounced coherence can be found at other frequencies such as at 85 Hz that also show high noise in the flag signal. To determine the impact of the noise in the MCN error signal at much different frequencies to h as shown in figure 3.17 one needs to consider the attenuation which is provided by the suspension. Two further suspension stages separate the MCN mirror from the upper mass. Thus, the movement of the upper mass gets attenuated by $1/f^4$. However, the

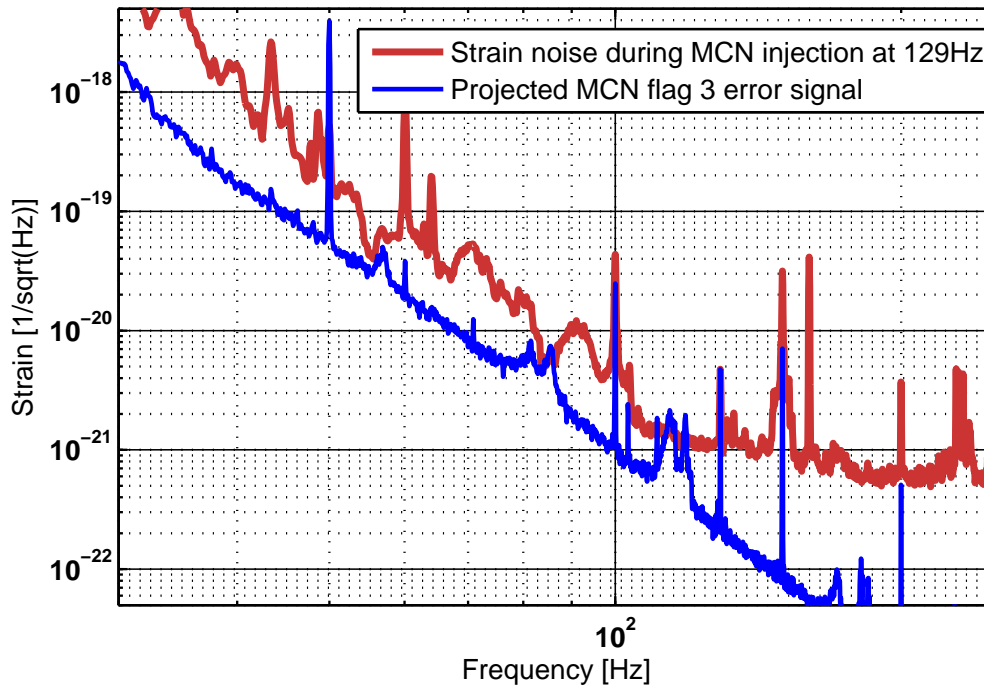


Figure 3.18: The displacement noise of the MCN flag 3 error signal projected to h . Note that this measurement delivers just an upper limit for coupling of displacement noise.

analysis of this experiment for the other used injection frequencies suggest rather an $1/f^5$ shape for its coupling to the sensitivity. This experimentally obtained shape was used to project the LC noise to h. Figure 3.18 shows the result. This figure implies that a coupling of LC noise to h exists for MCN but only in a not negligible amount at noise structures around 100 Hz. It has to be clarified at this point that figure 3.18 should be treated as an upper limit because there might be other, not yet known couplings like electrical pickup in the system. It is not entirely known that the noise floor measured in the flag is really displacement noise. It could well be sensing noise as it is added by the modulation-demodulation process.

The suspensions of the MI mirrors can be considered as identical systems. Thus, one can expect similar results for the remaining MI mirrors. If the result shown in figure 3.18 would not be an upper limit and the displacement noise of all upper masses of suspensions belonging to the Michelson would be statistically independent the effect on h would be larger.

In summary, the extra noise which is caused by the modulation-demodulation process maximally couples by a minor amount into the sensitivity. An upper limit of its coupling was provided which shows the highest impact around 100 Hz but also shows no significant broad band coupling at these frequencies or any other. The latter is important due to the broad band increase of noise in flag error signals if operated with MD. The highest impact of the extra noise in the LCs to h is at 115 Hz. There, a narrow structure seems to couple to h and causes a bump which is slightly visible in the surrounding noise floor.

At present, other noise sources limit the sensitivity of GEO 600 in the discussed frequency range. These are MIAA and SR longitudinal feedback noise below 100 Hz as well as an unexplained noise from 100 Hz to several 100 Hz. As soon as these noises are significantly reduced, a further investigation of the potential coupling of LC displacement noise to h will be useful. In the mean time, this small amount of extra noise in h is tolerable, compared to the immense benefit of being able to operate GEO 600 at higher laser power, as shown in the following sections.

3.3.6 Modulation Drive implementation at the GEO 600 main suspensions

According to the results presented in section 3.2, all main suspension LCs, except the one belonging to the signal-recycling mirror, will need to be operated with MDs. Otherwise, the laser powers that are planned in the GEO-HF upgrade will not be achievable due to the stray light coupling to the shadow sensors of the LCs. Therefore, MDs have been installed at all these LCs to get rid of the stray light contamination.

After the initial MD tests and a permanent MD installation at the MPR LC, the BS LC was the first LC belonging to a triple suspension to be permanently operated with MD. A reduction of fluctuations of the circulating power in the IFO was directly visible.

After the BS LC, Modulation Drives were installed at the remaining main suspension LCs in the central cluster of GEO 600. Namely, these are the LCs belonging to MCE and MCN. All four MDs in the central cluster receive their LO signal from a single microcontroller module that is programmed to deliver the modulation signal at 10 kHz. Later on, the BDIPR suspension LC was also equipped with a MD as described in section 3.5.1. BDIPR is the mirror directing the input beam towards MPR and thereby to the main IFO.

The remaining far mirror suspension LCs (belonging to MFE and MFN), were operated with a MD shortly after. Further investigations to minimize extra noise have been necessary for these two. This effort is described in appendix C.2.

The benefit of operating the LCs with MD is best visible by observing LC error signals of flags that show a strong contamination with scattered light from the main IFO. Corresponding to the results discussed in section 3.2, BS flag 1 is an example with a lot of stray light contamination.

Figure 3.19 shows two spectral densities of the BS LC flag 1 error signal. The frequency axis is chosen such that the active band of the LC electronics and the frequencies slightly above it are displayed. The blue trace shows operation with MD, whereas the red trace shows default operation. For both, GEO 600 was in full lock with 3 kW impinging on the BS. At both times, the data was taken, the seismic conditions were very low. Otherwise full power operation would not be possible without working MDs. If operated with a MD, the spectral density of flag 1 has the same shape as if no stray light coupling would exist. Without MD a significant amount of additional noise is dominating the flag spectral density from 0.7 Hz to 4 Hz. All this extra noise is actually stray light that contaminates the error signal. Extra noise introduced by the MD at frequencies above the LCs active band was discussed extensively in the last section. However, figure 3.19 does not only justify the installation of MDs at GEO 600 LCs but shows its necessity. Within the active band of the LC no extra noise is visible in the LC signal while operated with MD compared to default operation.

By observing the circulating power in the IFO after the installation of MDs at the aforementioned LCs, a decrease of fluctuations on the circulating power is expected. Figure 3.20 confirms this. It compares spectral densities of the circulating power at full laser

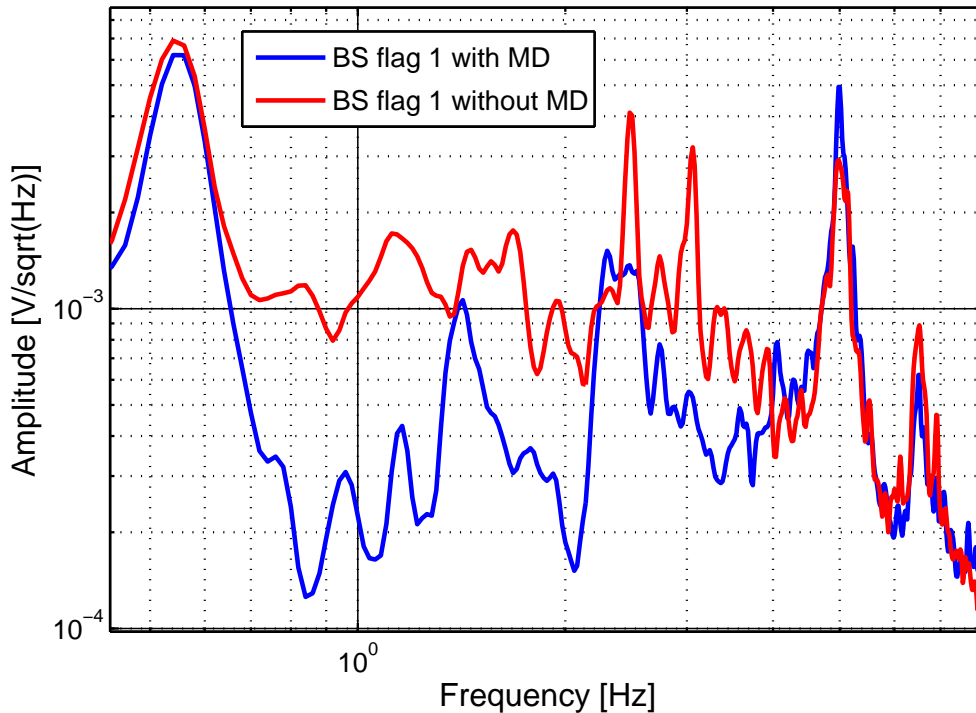


Figure 3.19: Error point spectral densities of BS flag 1 with and without MD. GEO 600 was operated with 3 kW impinging on the BS. The seismic was almost identical low during both corresponding times. Note the large difference of both signals between 0.7 Hz and 4 Hz. The difference is caused by laser stray light contamination.

power.¹ The red trace shows the case without working MDs, i.e. all MDs are bypassed. The green trace shows the case, for which all MDs are active. They filter the scattered light from within the IFO. Therefore, the scattered light cannot induce disturbances to the LC operation as described in section 3.2.1. This results in a circulating power that is much more quiet.

With the significant reduction of fluctuations on the circulating power, the stability at high laser power increased significantly. For 3 kW impinging on the BS it is even comparable to the stability at the default power of 2 kW. The corresponding sensitivity of GEO 600 at full laser power is shown and discussed in the next section.

¹ Note, that this measurement was done while the old laser system was still in use. Thus, maximum laser power corresponds to about 3 kW which are circulating in the IFO.

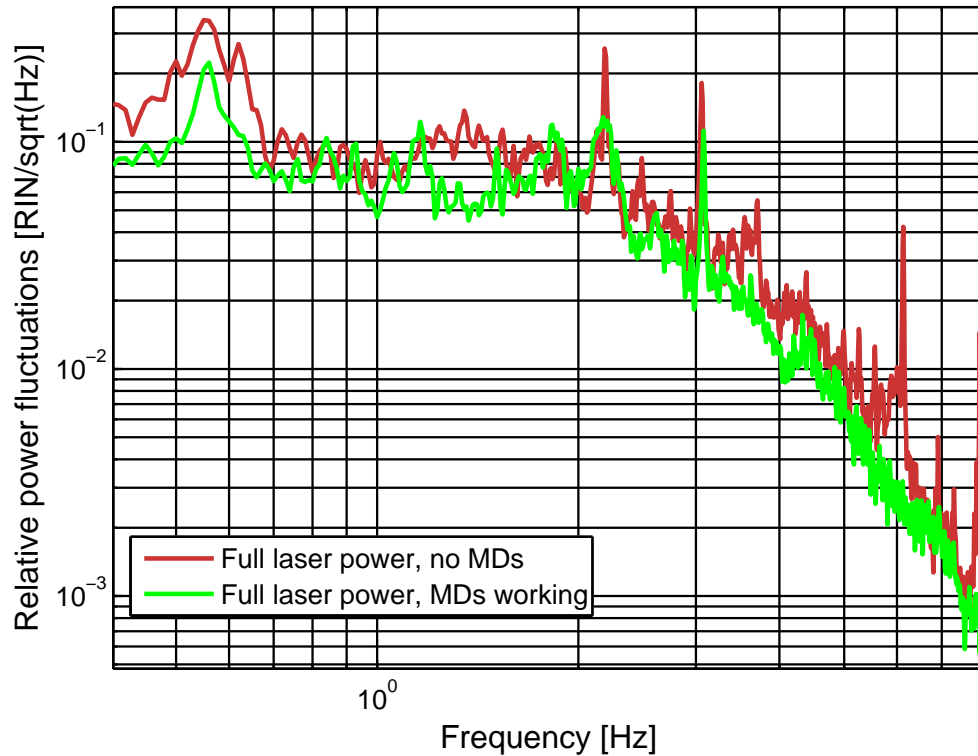


Figure 3.20: Relative power fluctuations of the circulating power in the IFO with and without MD installed at the main suspension LC electronics. Both traces are for full available input laser power, with the old laser system.

3.3.7 Sensitivity at full laser power

Implementing MDs at almost all main suspension LCs successfully removed problems due to the laser stray light coupling to the corresponding shadow sensors. Therefore, stable operation at full available laser power became possible, while the old laser system was still in use.

However, the most important question remains. How does the GEO 600 sensitivity look like at full operational laser power? Figure 3.21 gives an answer to this question. It compares the GEO 600 sensitivity for 2 kW and 3 kW laser power impinging on the BS. As can be seen, the sensitivity improves at high frequencies for high laser power, while it stays constant at low frequencies. The actual improvement is about 22% which corresponds to a factor of $\sqrt{3/2}$, as expected according to formula 1. This improvement in sensitivity due to the use of full laser power, in combination with the possibility to operate GEO 600 stably at this high power levels lead to an operation at full laser power over the whole VIRGO GEO 600 science run in Summer 2011. The next section is dedicated to the Virgo

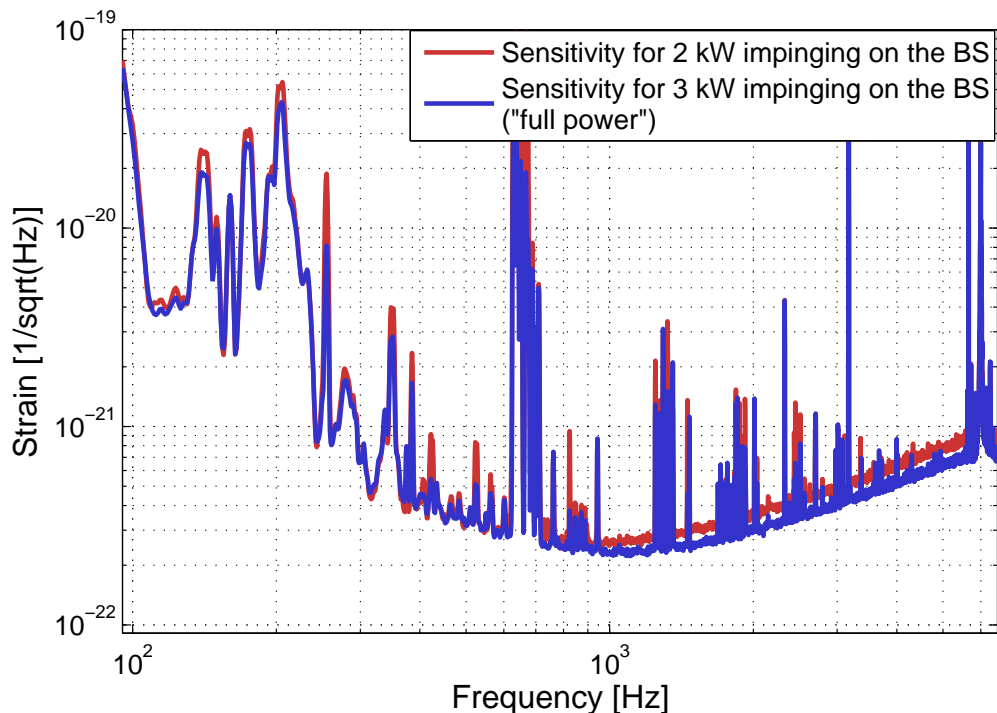


Figure 3.21: GEO 600 sensitivity in April 2011 for 2 kW and 3 kW impinging on the BS. The latter being the maximum possible operational laser power, due to being laser power limited, at that time. The sensitivity improvement at high frequencies is about 22 % as one would expect regarding the corresponding circulating power levels.

GEO 600 science run.

Being able to use $\frac{3}{2}$ times more power and therefore having a sensitivity at high frequencies that is improved by a factor of $\sqrt{3/2}$, results in a higher astrophysical reach of GEO 600. Because space is three dimensional, the amount of potential detection candidates increases by the cube of the sensitivity improvement. With full laser power we are able to detect 1.84 times more GW wave sources at high frequencies as we have been before the installation of the MDs at the main suspension LCs.

At this point the task of operating GEO 600 with full available laser power is completed - at least until the installation of the new laser system that is described in chapter 4.1.

With the new and higher available laser power, new challenges apart from stray light coupling will arise. The following chapters of this thesis will deal with many of them. Among these challenges is a laser power dependent noise at medium frequencies, i.e. at about 100 Hz to 1 kHz. This noise was not visible before more laser power was available and additional noise sources between 100 Hz and 1 kHz were removed. Therefore, it is

not visible in figure 3.21. The laser power dependent noise at medium frequencies is the major topic of chapter 6.

But the stray light story is not fully told. With respect to more available laser power as foreseen in the GEO-HF upgrade, there are more suspension LCs that can potentially cause problems due to stray light coupling. In section 3.5, these issues are discussed. Prior to that we will get an overview about a joint science run of VIRGO and GEO 600. This science run started short after the date GEO 600 was finally laser power limited.

3.4 Laser power limited operation during the VIRGO GEO 600 science run

A joint science run of the VIRGO GW detector and GEO 600 started in June 2011 that lasted for three months. Two major breakthroughs at the GEO 600 instrument resulted in an increased sensitivity at high frequencies just before the science run. These were the routinely use of squeezing and the routinely use of full available laser power. The latter is described in the last section. Due to these improvements, the GEO 600 sensitivity surpassed the sensitivity of VIRGO at high frequencies.

At this point, we present aspects about the VIRGO GEO 600 science run.

3.4.1 A reminder: the upgrade of the output mirror suspensions

A further major change which was done right before the science run resulted in an improved sensitivity at a frequency range of several ten Hz to several hundred Hz. It is mentioned at this point to explain the differences in the sensitivity of GEO 600 during the science run and the sensitivity shown in figure 3.21. This change was the upgrade of the output mirror suspensions (BDO suspensions) that was triggered by noise in the region of 80 Hz to 300 Hz. The major contribution to this so-called “200 Hz forest” turned out to be due to resonances in the BDO suspensions. Those resonances caused additional beam jitter of the output beam. After the installation of the OMC, this additional beam jitter resulted in a considerable increase of noise in the region from 80 Hz to 300 Hz. To reduce this coupling, it was decided to upgrade the BDO suspensions. The BDO suspension upgrade is described in [Pri12]. It significantly reduced the “200 Hz forest”. Figure 3.22 shows the GEO 600 sensitivity for full laser power before and after the BDO suspension upgrade.

Later on, it turned out that the sensitivity in a range of several ten to several hundred Hz only stays constant for high laser power operation because it was limited by other noise sources. After the BDO suspension upgrade and a further “mid-frequency cleanup” it became obvious that we observe a laser power dependent, unexplained mid-frequency noise. This issue is discussed in chapter 6. However, in the state GEO 600 was in May 2011 and during the run in summer 2011, everything spoke for a full power operation, i.e. operating with 3 kW instead of 2 kW being incident at the BS.

3.4.2 Sensitivity and stability during the science run

Figure 3.23 shows a comparison of typical VIRGO and GEO 600 sensitivities during the joint science run in 2011. At low frequencies, GEO 600 cannot compete sensitivity wise with VIRGO. This is mainly due to several differences in the layout of the two instruments, starting with the five times longer arm length of VIRGO. Another major difference that

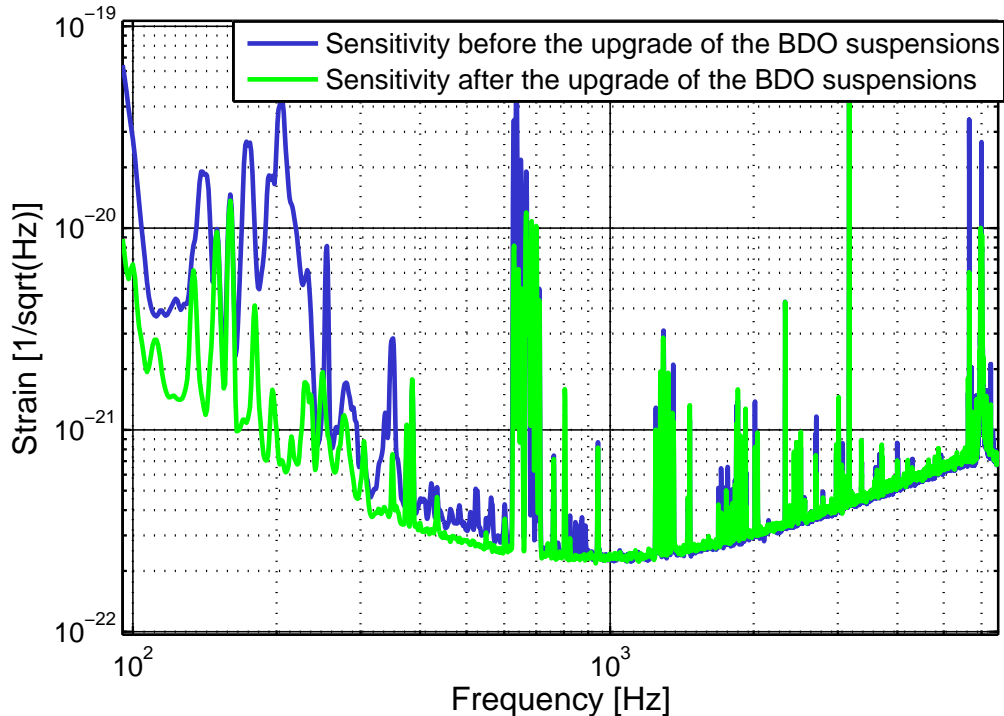


Figure 3.22: Sensitivity before and after the BDO suspension upgrade. At both times a laser power of 3 kW is impinging on the BS.

allows such an excellent low frequency sensitivity for Virgo is the super attenuator suspension system [Bra02]. Their test masses are suspended as fivefold pendulums allowing a better seismic isolation.

At several hundred Hz and above things start to look different. Between 700 Hz and 800 Hz the GEO 600 sensitivity, during the science run, is only a factor of two worse than the VIRGO sensitivity. At 2 kHz and above the GEO 600 sensitivity is even slightly better than the one of VIRGO.

Another important issue, besides the sensitivity of GEO 600, is its stability during the science run. In the months of June, July and August, we achieved a duty cycle of 82.3%. The longest lock during that time was almost 60 h. Thus, the operation at full laser power during the run showed no negative effect on the lock stability.

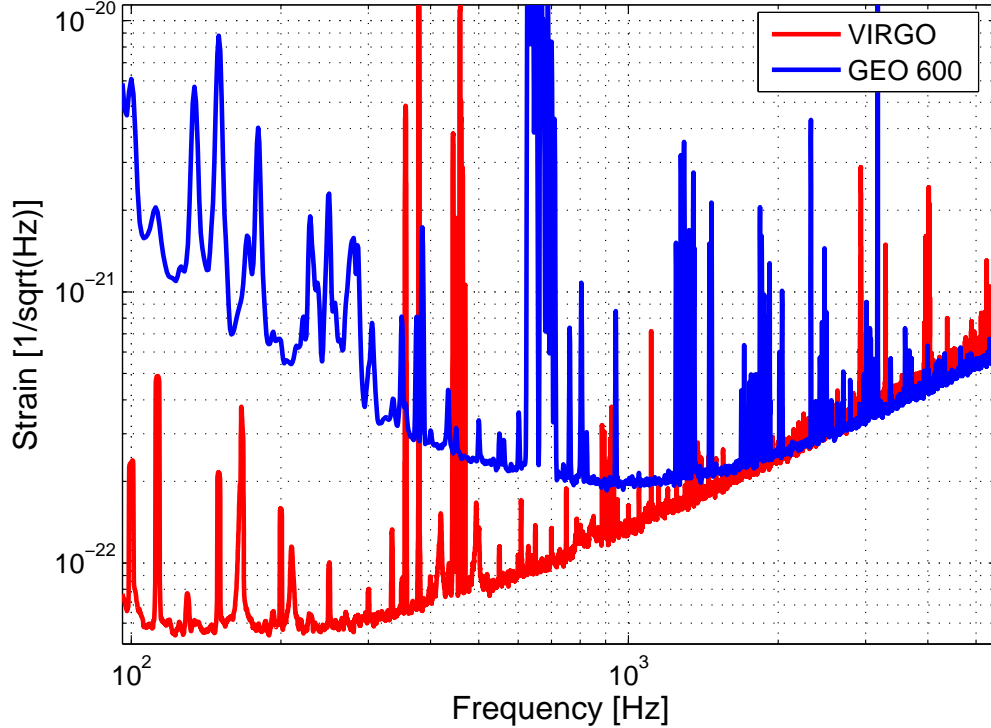


Figure 3.23: Typical sensitivities of VIRGO and GEO 600 during the joint run in summer 2011. GEO 600 is operated at full available laser power. In addition about 2.5 dB squeezing are applied. The sensitivity of GEO 600 matches the VIRGO sensitivity at high frequencies.

3.4.3 Scientific focus of the science run from a GEO 600 perspective

At low frequencies one has to admit that a joint science run between these two GW detectors makes not much sense. Only a signal of huge SNR that is found in VIRGO data can also be found in GEO 600 data at low frequencies such that a detection claim is justified. For signals at higher frequencies the science run makes sense, due to comparable sensitivity at 1 kHz and above. Examples for such signals are burst-like GWs that are emitted by sources like magnetars and certain supernovae types [Yak10]. Also binary systems are interesting in this context. During the early inspiral phase of binary coalescence events between black holes and/or neutron stars GWs would be expected to have a low frequency. But for merger and ringdown phases, in which GWs could be emitted at frequencies where VIRGO and GEO 600 have comparable sensitivity, crucial insights into the corresponding physics could possibly be obtained. Furthermore, the simultaneous detection in the later phase would validate potential low frequency signals in the VIRGO data.

3.5 Stray light coupling to local controls of the remaining suspensions

The installation of MDs at all but the MSR main suspension local controls allowed for stable operation with roughly 3 kW impinging on the BS. At that time, until the new laser was installed GEO 600 was laser power limited. Still there are many other suspensions at GEO 600 that use similar or identical local control systems. Thirteen suspensions alone are located on the input optic side, five of them supporting beam steering mirrors, six belonging to MC1 and MC2, respectively and two that suspend MU2 and MU3. On the output side of the IFO, three mirrors are suspended and used as beam steering mirrors that align the output beam onto the detection PD or rather the OMC. These candidates could possibly be affected by the influence of laser stray light coupling to their LC shadow sensors. Therefore, it was necessary to determine the amount of laser stray light and to decide on how to proceed if a significant stray light contamination is detected. It was found that in many cases, the influence of scattered light coupling is rather small and will not limit the operation up to laser power levels as planned for GEO-HF. However, there were two exceptions found for which stray light coupling will limit at some point. In one of these cases, a MD was already installed, in the other case measures to reduce the coupling will be necessary as soon as the circulating power in the DRMI exceeds a value of about 10 kW.

3.5.1 Stray light at the BDIPR LC and resulting MD installation

The first candidate we will focus on is the LC of the BDIPR suspension. BDIPR is the mirror that directs the input beam into the PRC. It is located in the same tank as MPR. Since the MPR LC shadow sensors show a strong contamination of stray light, it seems likely that also the BDIPR shadow sensors do. Stray light projections have shown that this is the case. Up to date, the BDIPR LC is the only example besides the main suspensions LCs at which a MD installation was necessary.

Amount of stray light contamination at the BDIPR LC

The amount of stray light that couples into the shadow sensors of BDIPR was measured using the same noise projection technique as described in section 3.2.2. A major difference between the BDIPR LC and the main suspension LCs is that only four flags are used to control the degrees of freedom of the upper mass. Two of them control rotation and the other two tilt. Furthermore, the BDIPR LC error signals have no default (low noise) monitor output. Instead error signal monitors can be activated using a matrix switch in a LabVIEW control program. These monitor outputs provide signals which are noisier than the signals of the default monitors of the main suspension LC error signals. Therefore, this leads to a less precise measurement as the projections shown in section 3.2.3.

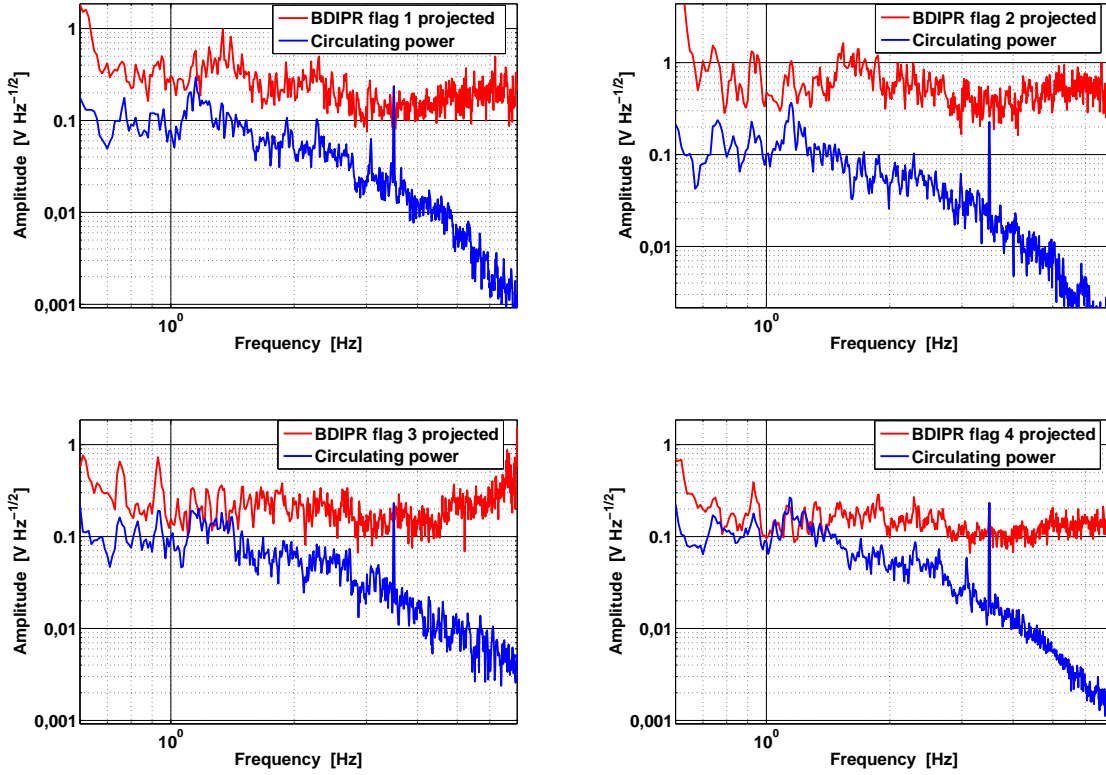


Figure 3.24: Laser stray light projection for all four BDIPR flags. GEO 600 was operated with 2.5 kW being incident at the BS during the experiment. The laser amplitude modulation is applied at 3.5 Hz. All traces show 5 minutes of data. Except for flag 2 stray light contamination is visible. In the case of flag 4 stray light even dominates the error signal's spectral density around 1 Hz. Please note that the calibration to $m/\sqrt{\text{Hz}}$ that is provided in 2.5 is not applicable in the shown case due to a different recording of the data.

For the projections at the BDIPR LC, an amplitude modulation at 3.5 Hz was chosen and a modulation amplitude that corresponds to 0.8% of the mean of circulating power in the IFO was used. It was applied to the AOM that is used as actuator of the laser amplitude stabilization. This slight difference to the method described in section 3.2.2 is due to the fact that the new laser system was already in use at the time the projection was made. The new laser system uses an AOM instead of the slave laser current as actuator for amplitude stabilization. A description about the new laser system is given in chapter 4.1.

Figure 3.24 shows the projections for the BDIPR LC. Stray light contamination is clearly detectable in all but one of the four shadow sensor signals. They suggest that the alignment onto the PRC is disturbed by the effect of stray light coupling into BDIPR's

shadow sensors at frequencies of about 1 Hz. Even though a strong influence on alignment fluctuations of the IFO is not detectable at low operational laser power, a negative influence on the GEO 600 operation is obvious at laser powers planned to be used for GEO-HF.

MD implementation at the BDIPR LC

In anticipation of a disturbance of the alignment onto PRC, a MD was installed at the BDIPR LC in spring 2012. Even though BDIPR only possesses a four channel LC, a default MD was installed. Just the first four channels are used. The local oscillator is the same used for all other MDs that are in operation except for the far mirror suspensions. With BDIPR only hanging at a double suspension it needed to be assured that no extra noise below 10 Hz is introduced to the LC EPs as it was observed in the cases of MCE and MCN. As described above, BDIPR flag signals are not recorded by default. For that reason they were recorded over several days before and after the actual MD installation. The individual error signals were compared for both cases and within the limits of the monitoring method no extra noise below 13 Hz was found.

At that time, the GEO 600 operation was limited to maximum of 3.5 kW impinging on the BS due to the restrictions set by the old input optics. Therefore, no further results were obtained that show an improvement of the GEO 600 operation due to the BDIPR MD. With a dedicated investigation that would have used plenty time on this very maximal laser power and several on/off toggling of the corresponding MD in addition this may have been possible. However, it was not expected that any information obtained this way would have justified the effort and the associated loss of science time. In regard to the case of stray light coupling into the shadow sensors of the BDIPR LC we consider the results of the corresponding stray light projections as sufficient to justify the MD implementation.

3.5.2 Stray light at the BDO suspension local controls

The BDO mirrors are used as a beam steering telescope onto the OMC and thus onto the detection PD. Stray light coupling to their LC systems would cause disturbances of the alignment onto the OMC. The performance of the OMC AA could be negatively influenced. Even additional noise in the GEO 600 sensitivity is thinkable. The latter being caused by similar beam jitter effects like caused by resonances of the BDO suspensions as described in [Pri12]. Undesired misalignment of the output beam onto the OMC has an effect on the transmitted carrier light power. Such changes of the transmitted carrier light power are compensated by an adjustment of the dark fringe offset. Thus, stray light coupling to a BDO LC can have an indirect influence on the IFO.

While almost all of the injected light into the main IFO ends up as stray light in the main cluster, TCOa and TCOb, the tanks housing the BDO optics are well separated. A hole of about 8 cm diameter situated between the vacuum tanks TCC and TCOa optically

connects the two areas to allow the dark port beam to exit towards detection. Therefore, a significant amount of stray light contamination is not expected in TCOa and TCOb. An exception for this is BDO1. It is situated on one axis with the BS and the connecting hole between TCC and TCOa. Furthermore, the flags and thus the shadow sensors of the BDO mirrors are attached at the mirror level. A stray light projection for the BDO1 LC error signals appears to be useful.

Stray light projection for BDO1

The BDO mirrors are controlled by a four channel LC system. Flag 1 and 2 are used to control tilt and longitudinal movement and flag 3 and 4 are used to control rotation. Due to the reasoning given above a stray light projection for the shadow sensors of the BDO1 LC was done. Figure 3.25 shows the corresponding results.

GEO 600 was operated at 2 kW impinging on the BS. The laser power was modulated at 12 Hz with an amplitude that corresponds to 1.6 % of the IFO circulating DC power. It was applied to the usual adding point in the power stabilization loop.

Flag 1 clearly shows a coupling of laser power fluctuations. The coupling at the remaining three flags is four to five times smaller. But even for flag 1 it is not as strong as it is at many main suspension flags. Still it is not negligible at laser power levels that are available with the new laser system. For usual operational laser powers, i.e. 2 kW impinging on the BS, and the maximum laser power before the IO upgrade, i.e. about 3.5 kW, a MD installation is not needed. As shown in section 3.3 of this chapter, it would introduce extra noise to the flag signals above 10 Hz. Unlike at the other suspensions at which MDs were installed, this noise could hurt the operation. Because the flags are attached to the mirror, this noise would directly result in beam jitter.

In chapters 5 and 6, various aspects and experiments at laser powers as far as 8 kW impinging on the BS are described. Even at such high laser power levels no indication was found that signalize a significant influence of stray light coupling to any BDO LC. However, the results shown in figure 3.25 suggest to keep in mind that stray light coupling to the BDO1 LC is a potential candidate to be a further show stopper of the power up process. Of course, a MD can be installed at the BDO1 LC. But the LCs act on the mirror level. Therefore, it is possible that the MD produces too much noise and eventually disturbs the alignment onto the OMC. In this case, one must either think of optimizing the MD scheme to reduce the noise or just block the stray light physically at flag 1.

3.5.3 Stray light coupling at the old input optics local controls

Before the input optics upgrade was done that is described in chapter 4, about 50 % of the laser power sent to MC1 was lost on its way to the main IFO. The major part of these losses were caused in the high finesse input mode cleaners, as described in chapter

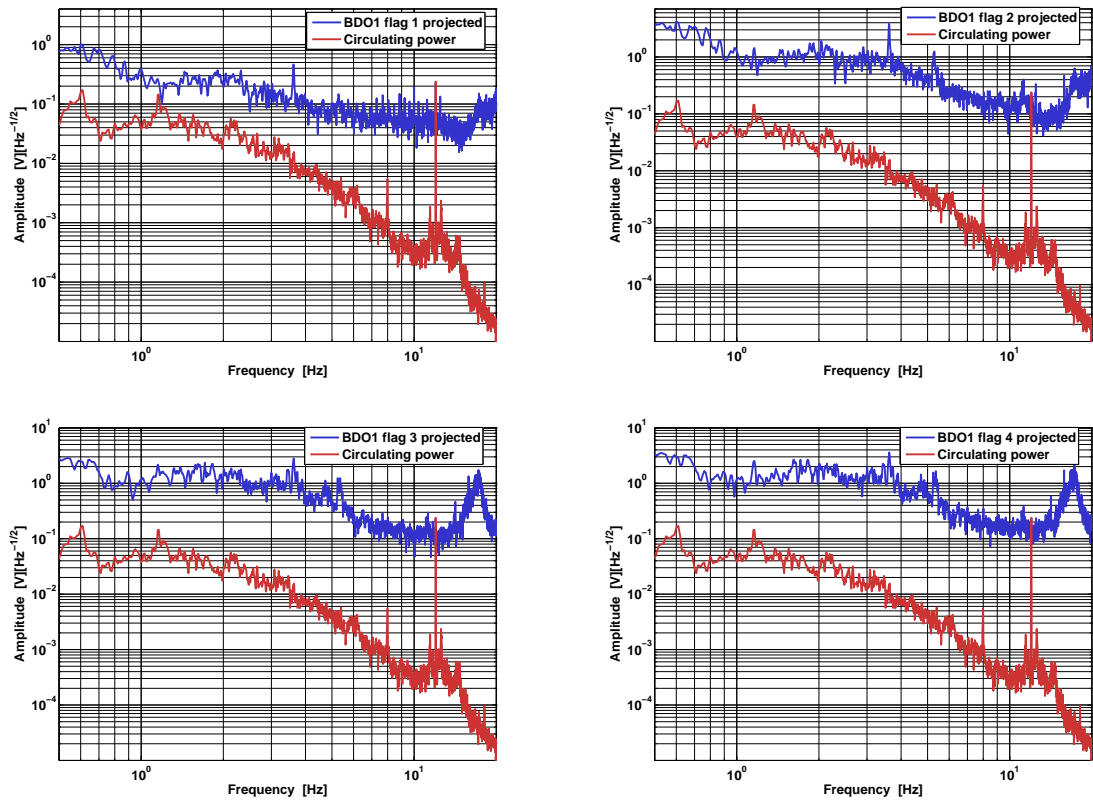


Figure 3.25: Laser stray light projection for all four BDO flags. GEO 600 was operated with 2 kW impinging on the BS during the experiment. The laser amplitude modulation is applied at 12 Hz. All traces use 5 minutes of data. Only flag 1 shows stray light contamination in an amount, that will cause problems at significantly higher laser power.

2. Most of that light ends up as stray light in TCMA and TCMB, the vacuum tanks housing the IOs (namely the MCs themselves, several beam steering mirrors and the two mounting units). This means that before the IO upgrade was finished, nearly the same amount of light got lost as stray light in those tanks as got lost in the PRC.

All twelve suspensions in TCMA and TCMB use four channel local control systems. And all their shadow sensors are sensitive to the stray light that is illuminating the tanks. A negative influence of laser power fluctuations coupling as stray light to the shadow sensors of the corresponding LCs seems likely. Thus, experiments were done for all flags of all LCs belonging to suspensions in TCMA and TCMB to determine the amount of laser stray light coupling to the corresponding shadow sensors.

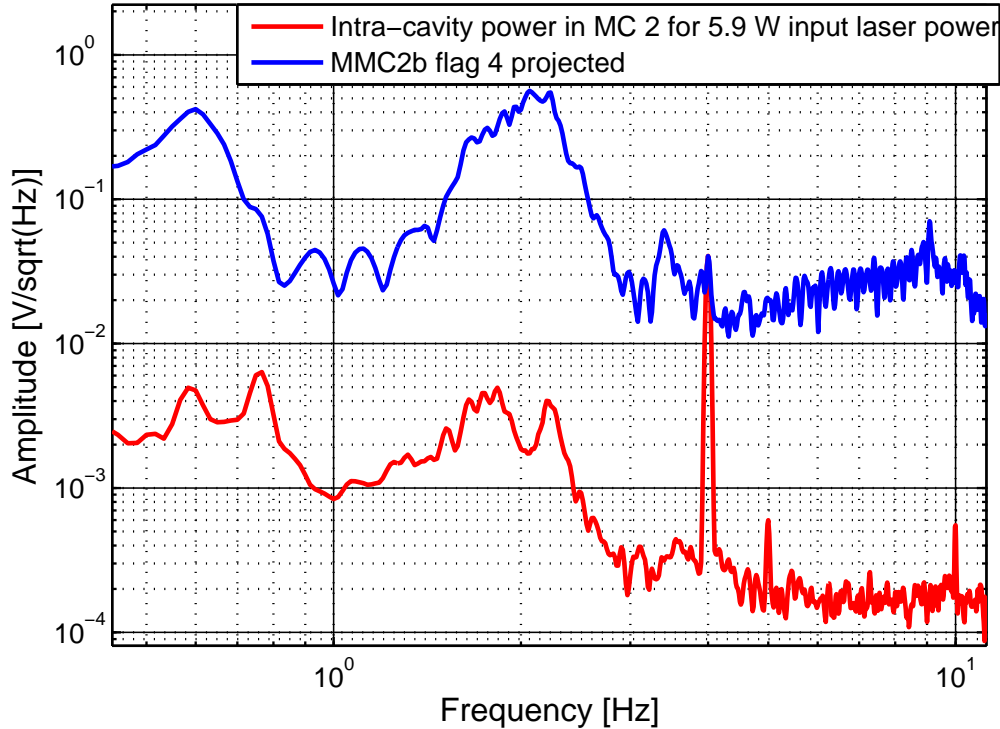


Figure 3.26: Stray light projection for MMC1b flag 4. Coupling of stray light is barely visible in the displayed case. It is far from limiting. There is no other case of stray light coupling to shadow sensors at the IO side that shows a significant stronger coupling as shown here.

Stray light contamination at the old input optics LCs

To record the error signals of the LC systems that are in use at the IO suspensions, the same restrictions as described for the BDIPR apply, i.e. that no default error signal monitor output exists. Furthermore, there are two cavities on the input optic side both sharing the same two vacuum tanks. These two cavities are supposed to be the major sources of scattered light. Only the MC 2 circulating power is monitored. Therefore, the MC 2 circulating power was used to do the stray light measurements at the IO LCs, assuming the MC 1 circulating power to have a similar spectral shape. Still, sufficiently accurate results were obtained to evaluate the stray light contamination.

The stray light contamination at all flags of all suspensions on the input optics side was measured while the old MCs were still in use. For all these experiments, an input laser power of 5.6 W to MC 1 was used. This value corresponds to the default power at

which GEO was operated at during that time. Even though the fact that about 50% of the laser light gets lost in the corresponding two vacuum tanks, the contamination turned out to be small compared to the suspension LCs of the PRC. In many cases, a coupling could not even be detected. At several other flags, a rather small coupling was found, like shown in figure 3.26. This figure shows an exemplary stray light projection for flag 4 of the MMC1b suspension. Actually, this projection delivers only an upper limit for the stray light contamination because the coupling peak is barely distinguishable from the noise that surrounds it. In return, the effect of scattered light originating from the first MC is not included. But assuming the MC 1 circulating power to fluctuate two to three times as much as the MC 2 power at frequencies below 3 Hz, stray light contamination is far from limiting in this case.

There is no flag signal on the IO side that shows significant more stray light coupling compared to the example given in figure 3.26. Furthermore, a laser input power to MC 1 that is above 10 W was not used before the IO upgrade described in chapter 4 due to the damage threshold of the old LiNbO₃ EOMs used for imprinting modulation SBs. No cause of action needed to be taken to deal with stray light coupling to the shadow sensors of the IO suspension LC. The post IO upgrade situation will be discussed in chapter 4.3. To anticipate the essence: After the reduction of the finesses of the two MCs, the stray light contamination on the IO side decreased as expected. As long as no further laser upgrade beyond the current 35 W system is planned, the coupling of laser power fluctuations to the shadow sensors of the IO suspension LC is negligible. It will not limit the stability of the detector from the IO perspective.

3.5.4 The effect of stray light coupling to the LCs of the reaction masses

The main displacement actuator of the Michelson interferometer, the *electrostatic drive* (ESD), may allow for an indirect coupling of stray light. The ESDs are used to apply feedback on the mirror level via an electrical force. Movements of the reaction mass as caused by stray light coupling to their LCs could modulate the effective electrical force and thus disturb the performance of the system. This possibility was investigated and it was found, that this coupling plays no important role because the arrangement of the ESDs in GEO 600 does not allow for a significant coupling. In appendix B, a brief consideration about this mechanism is provided.

4 The upgrade of the GEO 600 input optics

In the previous chapter, it is described how laser power fluctuations coupled as scattered light into the shadow sensors of the suspension local controls. This coupling prevented a stable operation of GEO 600 at laser power levels which are significantly above 2 kW. The discussed investigation and subsequent installation of a modulation-demodulation scheme for the suspension local control electronics removed these instabilities. GEO 600 could be stably operated with maximum available laser power. Ultimately, this progress intensified the necessity for further parts of the GEO-HF upgrade: The installation of a new laser system and an upgrade of the *Input Optics* (IO). The IO upgrade, affects the two input mode cleaners, all in vacuum *Electro-Optical Modulators* (EOMs) for imprinting modulation side bands to the main laser beam and the mode matching telescope towards the power recycling cavity. These aspects are the major topic of the chapter at hand.

Foremost, this chapter starts with a description of the new laser system. Its installation and the accompanied increase of available laser power strengthened the need for the IO upgrade.

The second section of this chapter discusses the first part of the IO upgrade: A replacement of four EOMs that are used as phase modulators to create modulation *sidebands* (SBs) of the laser light. These SBs serve as reference against which cavity length and angle changes are measured for control purposes. The initial *Lithium Niobate* (LiNbO_3) EOMs needed replacement due to poor thermal properties with respect to a significant increase of laser power. EOMs using *Rubidium Titanyle Phosphate* (RTP) as refractive material have better thermal properties than LiNbO_3 and were therefore installed. In particular, RTP withstands higher laser power.

Further on, aspects of the modifications that were done at the input *mode cleaners* (MCs) are described. The finesse of both mode cleaners was reduced from about 2000 to 300 for two reasons. A smaller finesse of the individual cavities decreases radiation pressure effects. Furthermore, the new MCs attenuate less TEM_{00} carrier light due to reduced scattering losses. The throughput of the two MCs is significantly increased from about 50 % to 73 % in total.

Finally, a change at the mode matching telescope onto the power-recycling cavity is discussed. In its initial design, about 20 % of the light that is sent to the IFO was reflected by the power-recycling mirror at low laser power. Due to thermal lensing on components in the beam path between the second MC and the power-recycling cavity, the mode matching got worse at higher laser power. At present, the mode matching is better by a factor of almost three at low laser power and gets slightly better at higher laser power.

In summary, the IO upgrade aims at an improvement of the IOs efficiency with respect to a significant increase of the transmitted laser power and an increase in its robustness against an operation at high laser power in general. Due to the stronger laser system, 2.5 times more light is available to be sent to MC1. The RTP EOMs allow to use this higher power without getting permanently damaged. Finally, the modifications at the MCs and the PRC mode matching telescope resulted in a further factor of 1.75 more power that can be coupled into the main IFO.

4.1 A 35 W laser for GEO 600

The installation of a new and more powerful laser was a fixed objective of the GEO-HF upgrade plan. This new laser system was developed to be used in both enhanced LIGO detectors and for GEO 600 in context of the GEO-HF upgrade. It is often referred to as “Frontend”. Both advanced LIGO detectors still use the Frontend as pre-amplifier for their 200 W laser system [Bog13].

In the case of GEO 600, the installation of the Frontend happened in October 2011, right after the joined science run of Virgo and GEO 600. Its installation was mainly executed by members of the AEI laser group. However, as essential part of the GEO 600 GW detector, the Frontend and the new setup on the main laser bench are described here. The accompanied increase in available laser power necessitates the major amount of the work that is described in the following parts of this thesis and further stresses the importance of the discussed matters in the previous chapter.

4.1.1 The Frontend

GEO 600’s new laser source is a master amplifier system that provides up to 35 W. It was developed for the efficient amplification of single frequency, linearly polarized, fundamental mode lasers for the application in GW detectors [Fre07]. The setup of the amplifier system using a NPRO as seed source is shown in figure 4.1.

NPROs were already used as master laser in first generation GW detector’s laser systems due to their high stability in amplitude and frequency. By injection-locking or amplification their power was amplified to levels of 10 W to 20 W [Wil00, Sav98, Bon02]. GEO 600 used a master-slave configuration as initial system (see chapter 2 for a brief description and further references).

As can be seen in figure 4.1 the NPRO beam passes polarizing optics, a FI and a mode matching telescope before it is injected into the actual amplifier. The polarizing optics are in place to convert the residual circular polarized light of the NPRO to linear polarization. The actual amplifier consists of four amplifier stages made of *Neodymium doped Yttrium Orthovanadate* (Nd:YVO₄). Each crystal is pumped with light from a fiber-coupled laser that delivers a maximum output power of 45 W. The mirrors sketched in figure 4.1 between the pump optics and the Nd:YVO₄ crystals are dichroic to separate the pump light and the actual 1064 nm laser light. By this four stage amplifier system, the initial (maximum) 2 W NPRO beam can be amplified up to 35 W. The highest output power measured for the GEO 600 system on site was about 33 W. For more details about the new laser see [Fre07].

The optical layout of the Frontend

The optical layout of the Frontend as it is implemented as laser source of GEO 600 is shown in figure 4.2. Two major differences to the basic design of the amplifier given in

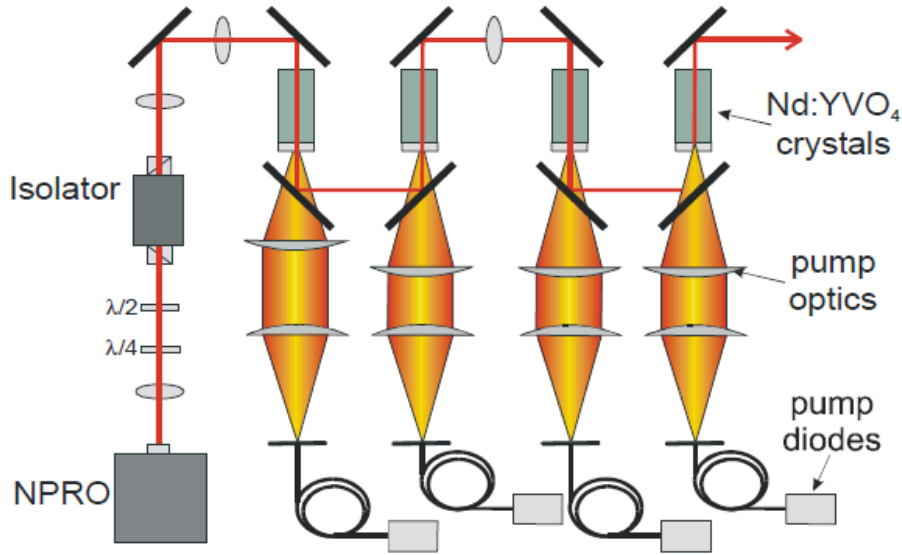


Figure 4.1: The principal setup of the four stage amplifier with a NPRO as seed source [Fre07].

figure 4.1 are included in GEO’s Frontend. It is extended by actuators for the frequency and amplitude stabilization loops of GEO 600.

A more detailed description of its optical components, is as follows: A commercial NPRO is used as seed laser providing a circular polarized beam. This beam passes polarizing optics (namely a $\lambda/4$ plate, a $\lambda/2$ plate and a polarizing beam splitter) to convert circular polarized light to s-pol light. The s-pol beam passes an EOM (“FE_EOM”) and shortly after an *Acousto-Optical Modulator* (AOM, “FE_AOM” in figure 4.2). The EOM is used as actuator for the frequency stabilization loop while the AOM serves as actuator for the amplitude stabilization loop. Further on its way to the amplifier the NPRO beam passes a shutter and an FI, the latter to extinct reverse light. A mode matching telescope (consisting of the two lenses “FE_L3” and “FE_L4”) comes next and is used to adjust the geometric properties of the beam to the required shape of the amplifier stage. Finally it is directed to the actual amplifier itself that is described above. In transmission of the second to last beam directing mirror (“FE_M4”), a PD (“NPRO Monitor Diode”) serves as a monitor of the seed beam power. After the four amplifier stages the 35 W beam leaves the Frontend through a window. This window blocks remaining (scattered) pump light while it is AR coated for 1064 nm light. The beam leaving the Frontend continues its way to the MCs via an optical bench as described in the following section.

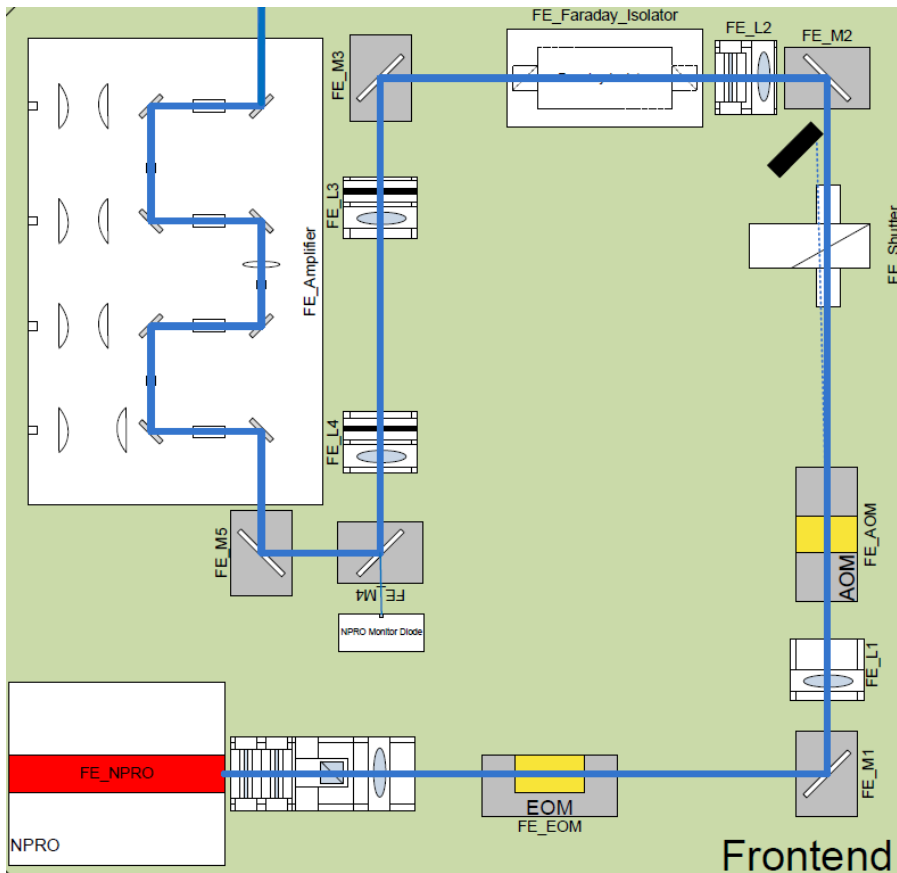


Figure 4.2: Optical layout of the Frontend as implemented at the GEO 600 site [Bog11].

4.1.2 The optical layout on the laser bench

Before being coupled into the first MC, the beam passes several optics on an optical bench, the so called laser bench. The layout of the laser bench and the purpose of the different components placed on it are described in this section. The main tasks that are fulfilled on the laser bench are imprinting of phase modulation for the locking of MC1, tunable laser power attenuation, extinction of reverse light and mode matching to the first MC. Furthermore, in and out of loop detectors for the first amplitude stabilization loop and a path for the squeezing reference light can be found as well as a (not used) triangular pre-mode cleaner. The full layout of the new laser bench setup is given in figure 4.3. It contains some changes compared to the old configuration that was shown in chapter 2 (figure 2.2).

The beam leaving the Frontend is directed towards MU1 and passes two lenses (LLB1 and LLB2) to match the beam size for the small apertures inside MU1 (i.e. 8 mm cross section). On its way to MU1, it additionally passes a first attenuation unit consisting of a

$\lambda/2$ wave plate (WPLB1) and a thin film polarizer (TFPLB1). Unlike the automated laser attenuator unit described in chapter 2, it can only be tuned manually. Its original purpose was to prevent the full laser power to accidentally be send towards the IOs. As described in chapter 4.2, the old LiNbO_3 EOMs on MU2 and MU3 could be operated safely only up to laser powers of about 10 W. Since their replacement happened more than a year after the new laser was installed, it needed to be ensured that they were not accidentally exposed to higher powers. TFPLB1 lets the p-pol light pass and sends the s-pol light to a beam dump. The attenuation unit is still in place to date. It can for example be used to measure the laser power or to attenuate the beam for alignment purposes. The polarization of the main beam is converted back to s-pol via WPLB2 directly in front of MU1.

MU1 stayed unchanged compared to the old set up consisting of two FIs and an EOM. These components are used for extinction of reverse light and applying 25 MHz modulation side bands for MC1 locking respectively, as explained in chapter 2. It must be noted that the FIs cause the highest power loss on the way to MC1. Each FI shows a loss of about 10%. To date, this significant loss does not limit us. However, as soon as a laser power limited operation of GEO 600 is achieved again, these FIs should be replaced.

After passing MU1 the beam passes the automated laser attention unit consisting of the automated $\lambda/2$ wave plate WPLB3 and the thin film polarizer TFPLB2, that was already mentioned in chapter 2. S-pol light passes TFPLB2 while p-pol light gets send to a beam dump. WPLB3 can be controlled remotely using Labview to set the desired input power to the IOs and thereby to the main IFO. Both beam dumps belonging to the first manual and second automated attenuation unit are designed to easily handle the total laser power provided by the Frontend.

Finally, the beam passes a mode matching telescope consisting of LLB3 and LLB4 to match the internal mode of MC1 and is sent to the vacuum system and thereby MC1 itself. Mostly limited by losses at the two FIs, a maximum of 19 W can be coupled into MC1 now. This is about 2.4 times the power that was available with the old laser system.

There are three more beam paths that do not directly belong to the just described path that directs the beam towards the in vacuum IOs:

The beam directing mirror BDLB03 has a transmission of 1% to let some light pass. This light is used as reference for the main laser GEO 600 squeezer for the phase lock to the main GEO laser. It passes polarizing and mode matching optics and is coupled into an optical fiber to send it to the main squeezing laser.

Right behind MU1 another partly transmissive mirror (BDLB04) lets 1% of the light pass that is directly split again at a beam splitter (BDLB11). In transmission, a triangular pre-mode cleaner is set up. However, the pre-mode cleaner is not in use.

The beam reflected by BDLB11 is send to the in and out-of-loop photo diodes (PDLB1 and PDLB2) of the first amplitude stabilization loop.

4.1.3 The need to limit the laser power until November 2012

The Frontend was installed and operating in October 2011. But until November 2012 we had to limit the maximum input power to MC1 to 10 W. (Which are still about 2 W more than used before.) The reason for that is to protect the four in vacuum EOMs on MU2 and MU3. They could not withstand significantly higher laser power as was shown by [Kwe11]. Therefore, experiments at higher input laser power were considered to exhibit too much of a risk for the old EOMs without having a replacement in hand. Chapter 4.2 is dedicated to their replacement by RTP EOMs. These new EOMs finally allowed experiments at laser powers above 10 W input power.

To ensure no accidental exposure of the old EOMs, more than half of the laser power provided by the Frontend was dumped via the first laser attenuation unit on the laser bench that is described above. The amount of laser power that was dumped, was chosen such that a maximum of 10 W was available to be sent towards the first mode cleaner.

The following sections of this chapter describe the different modifications at the in-vacuum input optics that ultimately allowed to provide significantly more laser power to be coupled into the main IFO. Various aspects about the operation of GEO 600 with much higher input laser powers as used to this point are described in chapters 5 and 6.

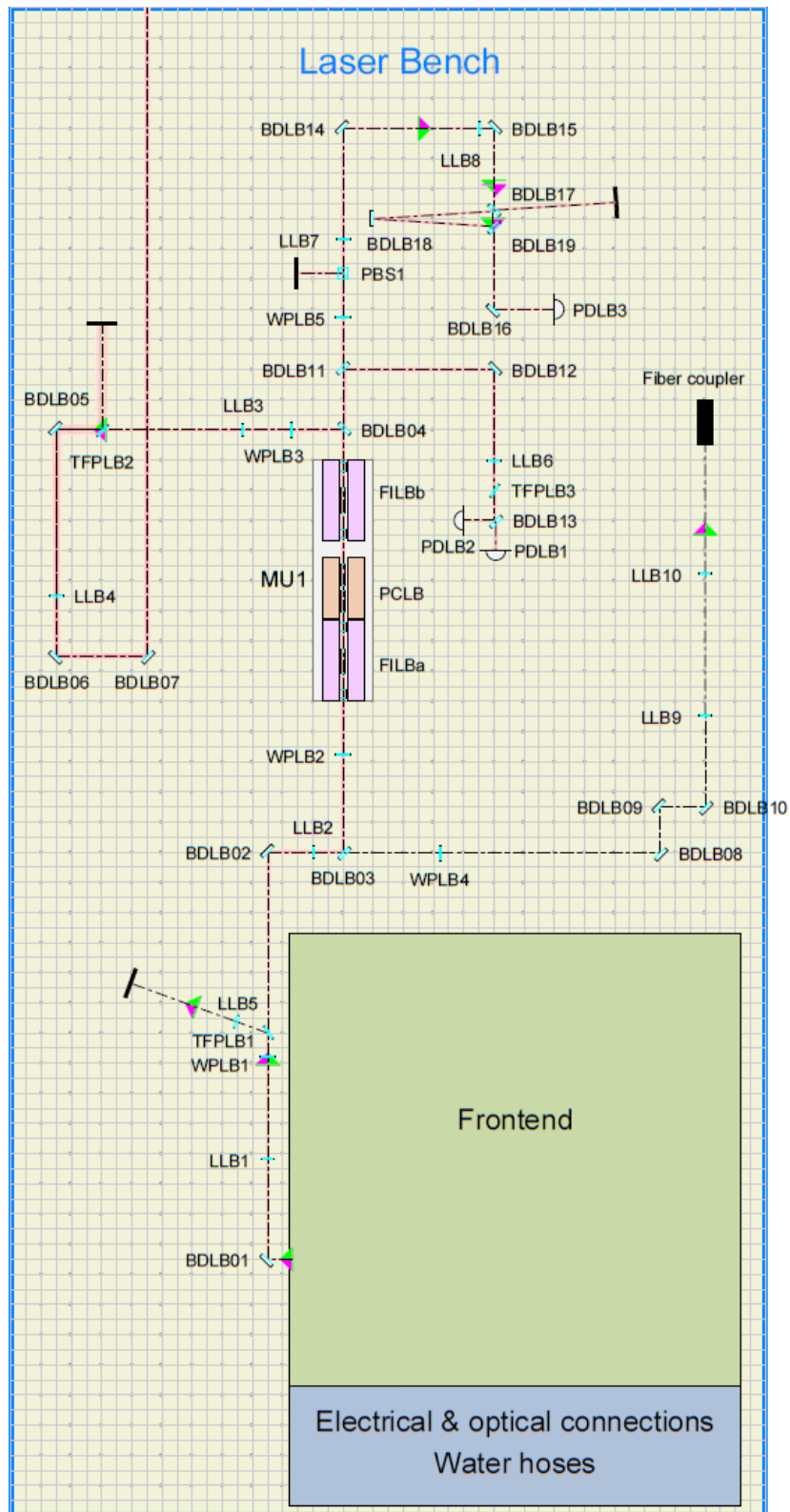


Figure 4.3: The new optical setup on the laser bench [Bog11]. The layout of the Frontend is omitted and can be seen in figure 4.2.

4.2 The new RTP EOMs

Phase modulation of the laser light at *radio-frequencies* (RF) is necessary for the angular and length sensing and control of an interferometric GW detector. *Electro-Optical Modulators* (EOMs) are used as phase modulators to create modulation *sidebands* (SBs) of the laser light. These SBs serve as a reference against which cavity length and angle changes can be measured. In the case of GEO 600, RF SBs at five different frequencies are needed. Therefore, five modulators are used to generate these SBs.

As described in chapter 2, the five modulators are placed on so-called *Mounting Units* (MU) at three different positions. The first one sits on MU1 that is placed on the laser bench. The remaining four EOMs are located inside the vacuum system. Two of these EOMs are sitting on MU2 and the remaining two on MU3, respectively. Figure 2.3 shows their locations.

The major topic of this section is the replacement of the four EOMs that are placed inside the vacuum system. Their replacement was necessary with respect to the laser power increase. All four original EOMs used LiNbO_3 crystals as the refractive material. This material is known to show stronger thermal lensing compared to other materials like RTP. Furthermore, it was shown that LiNbO_3 crystals as used in GEO 600 get permanently damaged if exposed to the laser powers anticipated for GEO-HF [Kwe11]. A permanent damage is not tolerable. In particular, it is not tolerable if an operation of these EOMs is foreseen over years and the EOMs are placed within the vacuum system.

Therefore, the LiNbO_3 modulators needed to be replaced. The new EOMs use RTP as the refractive material. RTP shows less thermal lensing and can withstand significantly higher laser powers.

The EOM on MU1 is omitted from the discussed topic in this section. This is due to the fact that because it is placed on the laser bench, it is easily accessible should a replacement become necessary in the future. A potential damage of this EOM due to the exposure of laser power that is available with the new laser is not expected (since KTP is used and not LiNbO_3). Furthermore, under normal operating conditions, the laser power is constant at the crystal. Thermal lensing effects can therefore be compensated by the mode matching telescope towards MC1.

We start this section with a brief summary about basic concepts that are needed for the following discussed matter. This is succeeded by a description of the old LiNbO_3 EOMs and their positioning within the optical layout. The latter will explain the need for careful planing of their replacement. In particular, we want to keep the same modulation frequencies and the positions of the EOMs within the optical layout. Further on in this chapter, a comparison of the (thermal) properties of LiNbO_3 and RTP as the refractive material for EOMs is given. A description about how the decision was made to use certain crystal geometries with respect to their availability and actual need for GEO-HF follows. This section continues with describing the process of matching a RF signal to such an EOM in a resonant circuit. Afterward, the results that were obtained in the testing process of the new modulators are presented. The achieved modulation depths with the RTP EOMs are

given compared to a GEO 600-like LiNbO₃ EOM. Selected further information related to this topic can be found in appendix D.

4.2.1 EOM basics

Before we start describing the replacement of the old LiNbO₃ EOMs by the new RTP EOMs, we briefly summarize some basics to support the main topic of this chapter. We set the focus on phase modulation of carrier light in general, the need for phase modulation in interferometric GW detectors and on how phase modulation of the light is realized.

Why do we need phase modulation of the carrier light?

Properly aligned interfering beams are essential for any interferometric GW detector [Gro03]. A proper power build-up in a cavity depends on the angle between its eigenmode and the beam injected into the cavity. To grant an optimized alignment on long time scales, GEO 600 uses automatic alignment systems for the MI and its different cavities. A description about the auto alignment systems in GEO 600 is given in [Gro03].

Differential wave front sensing is the central method of an automatic alignment system [Gro03]. It is used to measure the angle between a cavity eigenmode and the beam injected into this cavity. This allows one to obtain an error signal that can be used to generate feed back to a mirror of the cavity. Thereby, the angle between the cavity eigenmode and the beam injected into the cavity can be minimized. Phase modulation of the carrier light is needed for differential wave front sensing to generate an error signal in the first place. Detailed explanations of the differential wave front sensing method are given in [Mor94, Hei99].

Phase modulation

Differential wave front sensing and automatic alignment are no central topics of this thesis. But testing and implementation of new electro-optical phase modulators are. EOMs can be used to phase modulate a light field. The material an EOM (crystal) is made of, changes its refractive index n if an electric field is applied to it. If the electric field is modulated with a frequency Ω , the refractive index is modulated. Therefore, an EOM is capable of phase modulating a beam of light that is sent through it.

The following overview about phase modulation orientates on the descriptions given in [Doo12]. Mathematically speaking, the carrier light field $E_0 e^{i\omega t}$ with frequency ω and amplitude E_0 is multiplied with a time-dependent phase factor $e^{i\Gamma \sin(\Omega t)}$, where Γ is the modulation index. With the Jacobi-Anger expression,

$$e^{iz \sin(\theta)} = \sum_{n=-\infty}^{\infty} J_n(z) e^{in\theta}, \quad (4.1)$$

where J_n are the Bessel functions, we get:

$$\begin{aligned} E_0 e^{i\omega t} \cdot e^{i\Gamma \sin(\Omega t)} &= E_0 e^{i\omega t} \cdot \sum_{n=-\infty}^{\infty} J_n(\Gamma) e^{in\Omega} \\ &= E_0 J_0(\Gamma) e^{i\omega t} + E_0 J_1(\Gamma) e^{i(\omega+\Omega)t} + E_0 J_{-1}(\Gamma) e^{i(\omega-\Omega)t} + \mathcal{O}(\Gamma^2). \end{aligned} \quad (4.2)$$

The modulation indices Γ and therefore the power in the SBs we are dealing with are small compared to the carrier as can be seen in section 4.2.6. For small arguments, the Bessel functions can be written as

$$J_n(z) = \frac{1}{n!} \left(\frac{z}{2}\right)^n. \quad (4.3)$$

Furthermore, for Bessel functions with $n \in \mathbb{Z}$ the relation $J_{-n}(z) = J_n(-z)$ holds. Therefore, we can write 4.2 as

$$E_0 e^{i\omega t} \cdot e^{i\Gamma \sin(\Omega t)} = E_0 e^{-i\omega t} \pm E_0 \left(\frac{\Gamma}{2}\right) e^{i(\omega \pm \Omega)t} + \mathcal{O}(\Gamma^2). \quad (4.4)$$

This means, if we neglect terms of higher order $\mathcal{O}(\Gamma^2)$, we get two SBs with frequencies of $(\omega + \Omega)$ and $(\omega - \Omega)$. SBs of higher order can be neglected for our application since the amplitude of the Bessel function decays with higher $|n|$.

In section 4.2.6 modulation index measurements of the new RTP EOMs are described. For these measurements, a linearly polarized laser beam is sent through the EOM. An RF-voltage is applied to the EOM and therefore generates modulation SBs on the carrier light. To obtain the different modulation indices, the power in the carrier and in the first order SBs was measured. If the power in the carrier is $P_0 \propto E_0^2$ and the power in one of the two (first order) SBs is $P_1 \propto (E_0 \Gamma/2)^2$ we can calculate the modulation index by

$$\Gamma = 2 \cdot \sqrt{\frac{P_1}{P_0}}, \quad (4.5)$$

for modulation SBs that are small compared to the carrier.

Phase shift

The phase shift that an EOM induces to a light field depends on the voltage applied to the crystal as well as the material properties of the crystal. It can be described by the following formula [Sal04, Gro06]:

$$\Delta\phi = \Gamma = \frac{\pi L}{\lambda} r_{33} n_z^3 \frac{U_z}{d}. \quad (4.6)$$

Here λ is the wavelength of the laser light, r_{33} the electro optical coefficient, n_z the refractive index and U_z the electrical field in z direction. Furthermore, L is the crystal length and d the separation of the electrodes, i.e. the height of the crystal. Equation 4.6 will be needed to compare the achievable modulation depth with the new EOMs to the old LiNbO₃ EOM type. Corresponding material properties of RTP and LiNbO₃ are given in table 4.2.

4.2.2 The old LiNbO₃ EOMs of GEO 600

As described in chapter 2, four LiNbO₃ EOMs were used to generate modulation SBs on the carrier light for angular and length sensing and control of different cavities. The corresponding suspended platforms, namely MU2 and MU3 that support these EOMs are also described in chapter 2. Figure 2.4 provides a schematic drawing of MU3 while the actual positions of MU2 and MU3 can be found in the optical layout of the the IOs that is given in figure 2.3.

Each of the two in-vacuum mounting units supports one module that consists of two EOMs. Figure 4.4 shows a photograph of a spare module as it could be found on MU2 and MU3 respectively before they were replaced by the new EOM modules. The base of this module is a macor block¹. Its base is 50×93 mm² and its height is 13 mm. Four holes are used to fix the macor base to the respective mounting unit. The drilling distances are 40 mm by 80 mm.

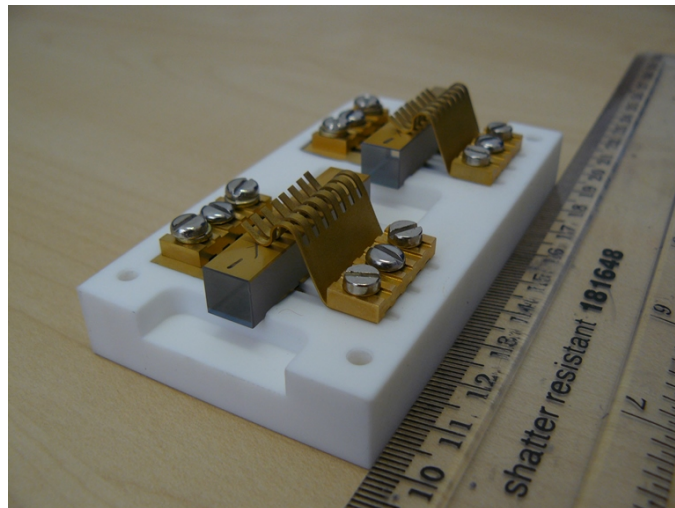


Figure 4.4: A module carrying two LiNbO₃ EOMs.

¹ Macor is a machinable glass-ceramic that is ultra-high vacuum compatible.

The macor block supports two LiNbO_3 crystal that are the central part of the two EOMs. Both crystals are countersunk by 1 mm. The crystals dimensions are $8 \times 8 \times 35 \text{ mm}^3$. The $8 \times 8 \text{ mm}^2$ front and back surfaces of the crystals are AR coated. The top and bottom sides of the crystals have a gold coating to form a capacitor that in turn allows for an electric field in the crystal if a voltage is applied to the capacitor. Gold coated clamps are holding the crystals on the macor block and serve as an electrical connection. The clamps are attached to the macor block via three threaded bolts. The gold coated bottom sides of the crystals are also electrically connected to the individual golden structure that can be seen on the left hand side of figure 4.4. (This is not obvious from the picture.) The golden structures on the left hand side are attached to the macor block by three respective bolts, too.

One bolt on each side of an individual EOM is used to attach one wire end of a twisted pair cable to the capacitor plates. The twisted pair cable is 140 cm long and electrically connects the EOM to a vacuum feed-through. Outside of the vacuum, the RF source, an RF amplifier and a matching circuit can be found. These components are described in section 4.2.5.

The two EOMs on MU2 are used to generate the modulation SBs for the locking of MC2 and the PRC while the remaining RF SBs for the MI and the SRC lock are generated by the two EOMs on MU3. Table 4.1 provides the corresponding values for the RF frequencies and power. In addition, the corresponding signal voltages are given as measured before the corresponding matching circuits. Note that the RF frequency for the PRC lock is 37.1 MHz. This corresponds to one free spectral range of MC2. Therefore, the PRC SBs can pass MC2 unhindered. Details on how to deliver the electrical RF signal to the EOMs can be found in appendix D.2.

The maximum RF power that can be applied to one EOM is limited. As mentioned before, the EOMs are in vacuum and sitting on a macor block. Possibilities to dispose heat from the crystals are therefore limited. The highest RF power that we consider safe to dissipate at one EOM is 2 W (33 dBm). This corresponds to a voltage of 10 V_{rms} of the signal *before* the corresponding matching circuit for such a 50Ω system if the matching would be perfect and no further losses occur.

This limit has no significance for the old LiNbO_3 EOMs simply because the highest applied voltage before any matching circuit is 4.25 V_{rms}. But it sets an important restriction on the decision of what kind of RTP EOMs to install with respect to their availability as described further below.

The need for in-vacuum SB generation

The arrangement of the GEO 600 IOs is an example of the infrastructural constraints compared to its larger cousins LIGO and VIRGO. Space limitations on the site resulted in the necessity to implement input mode cleaners with a shorter round trip length as those used in LIGO and Virgo. To assure sufficient filtering, two MCs are used. Short MCs were easier to implement within the given infrastructure restriction on the GEO

	MC2	PRC	SRC	MI
Frequency in MHz	13.0	37.1	9.0	14.9
RF power in mW (before matching circuit)	80	245	149	361
Amplitude in V _{rms} (before matching circuit)	2.0	3.5	2.73	4.25

Table 4.1: RF frequencies, powers and voltages before the corresponding matching circuits of the LiNbO₃ EOMs. The corresponding values for the new EOMs can be found in table 4.3. Note that the voltages across the crystals is different to these values due to resonant enhancement by the matching process.

site. In addition, two MCs instead of one MC has the advantage that more HOMs are suppressed if the round trip length of the light in the two MCs is different.

Therefore, imprinting of modulation SBs could not be realized before the MCs (except for the 15 MHz SBs for the MC1 lock). The free spectral ranges of MC1 and MC2 are 37.5 MHz and 37.1 MHz respectively. These numbers prohibit imprinting of four different RF SBs as needed for MC2, the PRC, the SRC and the MI lock on the carrier light before the first MC that would reach the main IFO and MC2, respectively. Even the generation of the SRC and MI lock SB in addition to the PRC RF signal between the two MCs would be technically challenging. Frequencies of about 74 MHz and 111 MHz might be needed.

Therefore, the four EOMs that are the topic of this section can be found on MU2 and MU3. In turn, the given positioning of the in-vacuum EOMs demands careful planning in regard to the GEO-HF upgrade. The new modulators need to work reliably after their installation. A potential need to open the vacuum again is not only labor-intensive but represents an unwanted risk for in-vacuum components.

4.2.3 Thermal properties of LiNbO₃ and RTP

Studies of the thermal properties of RTP and LiNbO₃ have shown that RTP is better suited for the applications with high laser power than LiNbO₃ [Sal04, Gro06]. Table 4.2 provides a comparison of selected properties of RTP and LiNbO₃. Particularly important are the more than two times higher damage threshold of RTP and its ten times lower absorption for 1064 nm light. Therefore, RTP should be able to withstand at least 20 times higher laser power. (The company Raicol even quotes a damage threshold for the uncoated RTP crystals of 1 GW/cm² according to [Gro06].) In addition, a lower dn/dT in combination with the ten times lower absorption of 1064 nm light implies a significantly lower thermal lensing effect. These are promising features for the application as material for EOMs in second generation GW observatories. Enhanced LIGO already made use of RTP EOMs for their IO system. Advanced LIGO uses the very same EOMs Enhanced LIGO used [Doo11, Gro06].

	units	LiNbO ₃	RTP
damage threshold	MW/cm ² (10 ns, 1064 nm)	280	≥ 600 (AR coated)
absorption coeff. at 1064 nm	ppm/cm	≤ 5000	≤ 500
n_z at 1064nm	none	2.16	1.82
r_{33}	pm/V	30.8	39.6
r_{23}	pm/V	8.6	17.1
r_{13}	pm/V	8.6	12.5
electro-optic coeff. ($n_z^3 r_{33}$)	pm/V	306	239
dn_y/dT	10 ⁻⁶ /K	5.4	2.79
dn_z/dT	10 ⁻⁶ /K	37.9	9.24

Table 4.2: A comparison of selected properties of LiNbO₃ and RTP [Gro06].

There is another important fact about LiNbO₃ besides its worse thermal properties compared to RTP. It was shown that LiNbO₃ crystals can get permanently damaged if exposed to GEO-HF laser power levels using comparable beam parameters [Kwe11]. For LiNbO₃ crystals this effect of a changed refractive index was shown first, but other materials are also affected [Pei99]. Even though the change in refractive index can partly be annealed by heating the crystal [Yao04] it is problematic for in-vacuum EOMs that are supposed to be operated at high laser powers over years.

In the course of the thermal measurements done by [Kwe11] a GEO-like spare LiNbO₃ EOM as shown in figure 4.4 was exposed to a TEM₀₀ laser beam that had comparable beam parameters as at MU3 (i.e. a beam diameter of 1 mm at the crystal). The laser power was constantly ramped up to 40 W and back to zero for many times over 28 hours. In the end, a permanent structure was imprinted to the crystal that resulted in the loss of several percent of the TEM₀₀ light to higher order modes at low laser power. The corresponding result can be found in appendix D. One can assume that if the EOM would have been exposed for longer times to such high laser power the amount of light that would be converted to modes of higher order would further increase. Therefore, LiNbO₃ EOMs are not suitable for an application as phase modulators in GEO-HF.

This information about the potential destruction of LiNbO₃ crystals if exposed to high laser power densities is even more important for GEO 600 than the knowledge that RTP shows less thermal lensing. Pure thermal lensing could be compensated by thermal compensation plates that have a negative dn/dT for instance. Such a compensation is not foreseen for GEO-HF. The optimization of the mode matching telescope that is described in section 4.4 improved the mode matching to the PRC sufficiently. However, a permanent damage of EOMs that are placed within the vacuum system can not easily be fixed. Therefore, the decision was made to replace the existing LiNbO₃ EOM crystals by RTP EOMs.

The new RTP EOMs that are described further below were all tested for high laser

power operation by members of the AEI Laser group as described in [Bog13]. In the course of these measurements, it turned out that the thermal lensing effect of the RTP EOMs that are sitting on the new modules is higher than expected. In particular, the type that was installed on MU3 shows a thermal lens of almost the same order of magnitude as the Faraday Isolators on MU3 do. However, a thermal degeneration at laser powers up to 30 W with beam parameters as can be found at MU3 was not observed. Results from [Bog13] and [Kwe11] about the thermal lensing measurements of RTP EOMs used for GEO 600 and other optical components of interest are given in appendix D. In particular, values for the actual measured thermal lenses of the corresponding EOMs are provided.

4.2.4 The new RTP EOMs

A simple replacement of the LiNbO_3 EOM crystals by RTP crystals of the same dimensions would be the easiest approach with respect to the IO upgrade. In this case, a similar modulation depth can be expected for the same applied voltage according to equation 4.6 and the material properties that were given in table 4.2. This is due to the fact that the ratio of the electro-optic coefficients $r_{33}n_z^3$ for RTP and for LiNbO_3 is 239/306. For the same voltage applied to the new crystals we would get about 0.8 times smaller SBs. This can easily be recovered by applying slightly more RF power to the new crystals.

The new RTP EOMs options

It turned out that RTP crystals that have the same physical dimensions as the old LiNbO_3 crystals are not available (i.e. $8 \times 8 \times 35 \text{ mm}^3$), according to the manufacturer. Two options for the dimensions of RTP crystals were most promising for us. The first option would be to use crystals with dimensions of $8 \times 8 \times 10 \text{ mm}^3$. According to the manufacturer, RTP crystals with an aperture of $8 \times 8 \text{ mm}^2$ can only be produced up to a length of 10 mm. Such short crystals would result in a significantly smaller modulation depth for the same applied voltage. As a second alternative, crystals with dimensions of $6 \times 6 \times 35 \text{ mm}^3$ were offered to us.

We learned above that the RF power dissipated by a crystal is limited to roughly 2 W due to poor thermal conduction. That leads to the question of what modulation depth we can achieve with the respective two new options compared to the old $8 \times 8 \times 35 \text{ mm}^3$ LiNbO_3 crystals. To answer this question we insert the corresponding values in equation 4.6 and get for the ratio between a $8 \times 8 \times 10 \text{ mm}^3$ RTP crystal and a $8 \times 8 \times 35 \text{ mm}^3$ LiNbO_3 crystal:

$$\Gamma_{RTP_{short}} : \Gamma_{LiNbO_3} = 1 : 4.48 \quad (4.7)$$

This means, by using just one RTP crystal of this size we need to recover a factor of

4.5. According to the used RF modulation amplitudes for the $8 \times 8 \times 35 \text{ mm}^3$ LiNbO₃ that were given in table 4.1 this is only possible for the MC2 modulation if we do not want to apply more than 2 W to one crystal.

By comparing the $6 \times 6 \times 35 \text{ mm}^3$ RTP crystal with the old $8 \times 8 \times 35 \text{ mm}^3$ LiNbO₃ we end up with:

$$\Gamma_{RTP_{long}} : \Gamma_{LiNbO_3} = 1 : 1.04 \quad (4.8)$$

We get almost exactly the same modulation index as we currently operate with. The realization of sufficiently large modulation SBs seems to be no problem with $6 \times 6 \times 35 \text{ mm}^3$ RTP crystals.

However, an aperture of $6 \times 6 \text{ mm}^2$ results in a smaller ratio of aperture to beam diameter at MU3 as usually is used in GEO 600 (i.e. 1 to 6)¹. This could be tolerated because the ratio of EOM aperture to beam diameter being $\frac{6}{1.019} = 5.89 w$ is just marginal below 6. In the original configuration of the components on MU3 this ratio was not set by the EOM but by the first FI. It has an aperture of $8 \times 8 \text{ mm}^2$. Therefore, we had the smallest ratio between beam diameter at a component and any aperture of components on MU3 of 1 to 6.5. Here, the beam diameter is largest at the first FI and has a value of 1.23 mm.

The new EOMs

We acquired both types of RTP crystals for the new EOMs. On MU2 we decided to install one unit with two EOMs, each consisting of *two* $8 \times 8 \times 10 \text{ mm}^3$ RTP crystals. By using two of these short crystals instead of one, a factor of two with respect to achievable SB strength is recovered. This is sufficient for the corresponding need on MU2. Furthermore, we decided to install a unit with two $6 \times 6 \times 35 \text{ mm}^3$ RTP crystals on MU3. This choice allows for similar high modulation index by applying similar RF powers as before. Only a small amount of margin to align the laser beam through MU3 is lost. If it would have turned out that the $6 \times 6 \times 35 \text{ mm}^3$ EOM aperture caused unforeseen problems we could still use the other EOM type.

Figures 4.5 and 4.6 show the two types of RTP EOM units that were finally installed. Figure 4.5 shows a unit with two EOMs, each consisting of two $8 \times 8 \times 10 \text{ mm}^3$ RTP crystals. Such a module was installed on MU2. The dimensions of the macor block that is holding the two EOMs are the same as for the old LiNbO₃ EOMs to assure compatibility with the mounting unit design. The new module can simply be clamped on the same spot where the old EOM was sitting.

Figure 4.6 shows an unit with two EOMs, each consisting of one $6 \times 6 \times 35 \text{ mm}^3$ RTP

¹ A ratio of 1 to 6 between an aperture and the corresponding beam diameter at this aperture assures that a negligible amount of the beam is cut off if the beam is properly centered. Furthermore, alignment tasks are easier, the bigger this ratio.

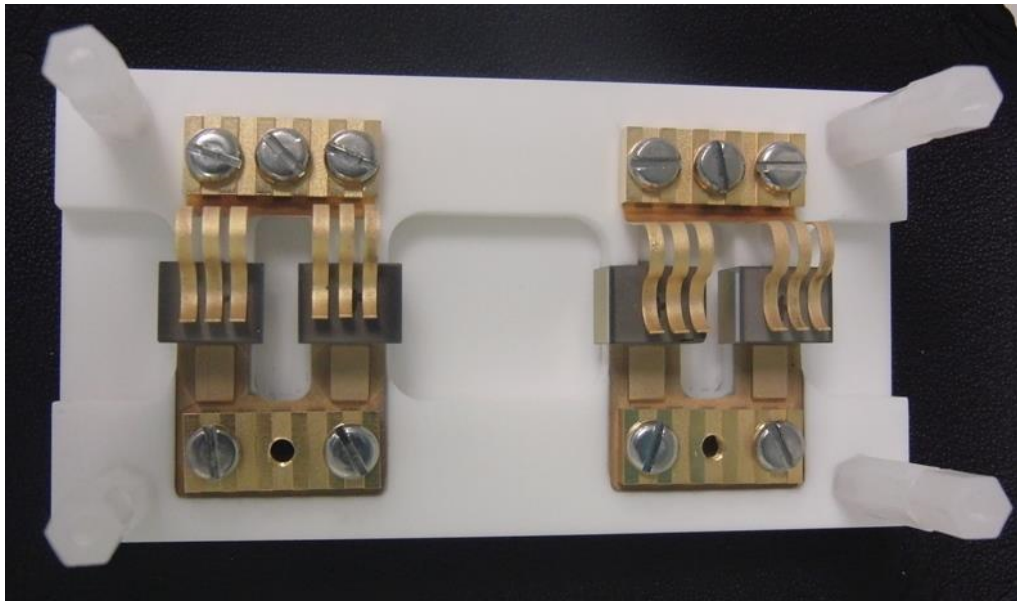


Figure 4.5: A module carrying two RTP EOMs consisting of two crystals that have dimensions of $8 \times 8 \times 10 \text{ mm}^3$. This module was installed on MU2 and serves for the generation of the MC2 and PRC SBs.

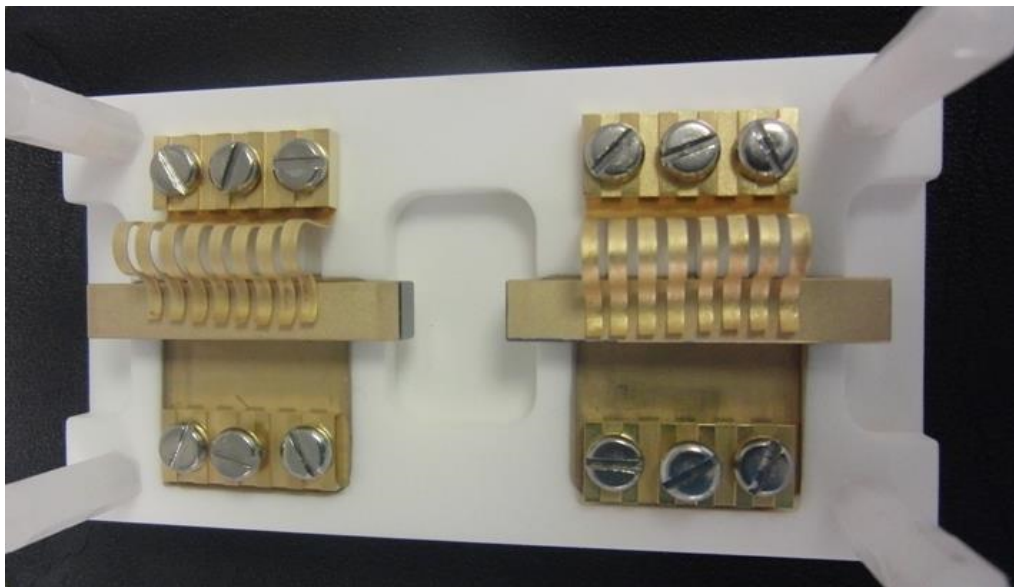


Figure 4.6: A module carrying two RTP EOMs that have dimensions of $6 \times 6 \times 35 \text{ mm}^3$. This module was installed on MU3 and serves for the generation of the MI and SRC SBs.

crystal. This type was installed on MU3. To allow a simple exchange of the MU3 modulators, the dimensions of the macor block are slightly different. It is 1 mm higher to still have the laser beam axis right in the middle of the crystals. Thereby, a replacement is as simple as it is for MU2.

4.2.5 RF matching of GEO 600 EOMs

Each EOM in GEO 600 that is used to generate modulation SBs on the carrier light for angular and length sensing and control of different cavities is part of a resonant impedance matching circuit. This matching circuit serves to match the input impedance of a RF source to the output impedance of the load, i.e. the EOM. Thereby, the matching circuit maximizes the power transfer to the load and minimizes reflections from the load, respectively. Additionally, the amplitude of the RF voltage gets transformed to higher values on the EOM side of the impedance matching circuit, as required to create sufficiently strong modulation SBs on the laser beam.

RF matching of the GEO EOMs to the RF sources is an important task for the generation of modulation SBs. Therefore, its principle is explained in appendix D.2.

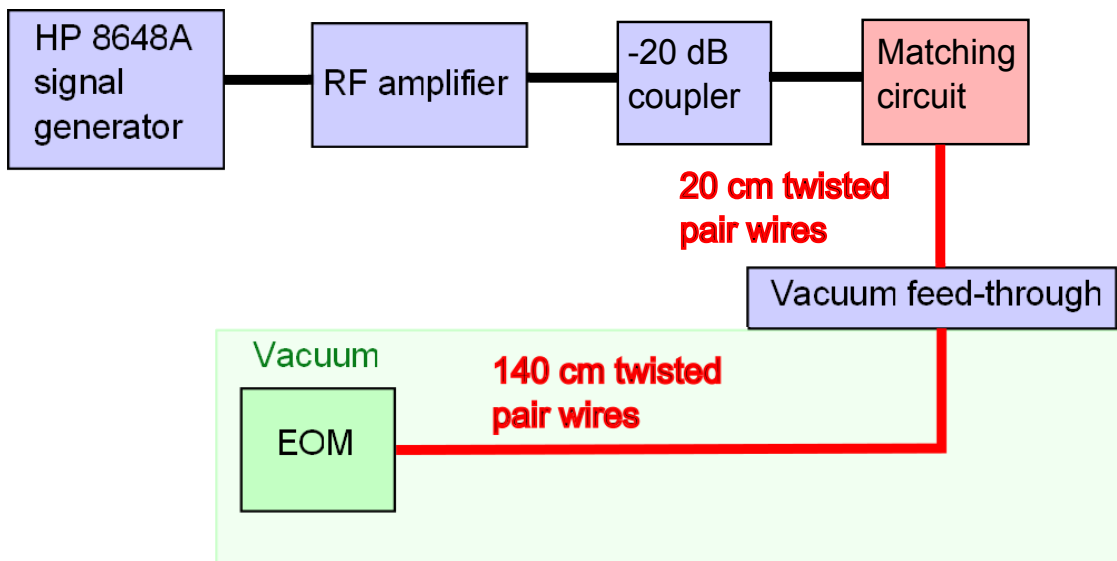


Figure 4.7: RF matching test setup for the impedance matching of the EOMs.

4.2.6 Initial experimental tests of the new RTP EOMs

All purchased RTP EOM units were experimentally tested to verify that they are capable of generating the expected modulation depth to a laser beam. These tests were carried

out at the Physics and Astronomy department of the University of Glasgow and mainly consisted of two parts. First, both types were tested as part of a resonant matching circuit as described in appendix D.2. The purpose of these matching tests were to confirm that an RF signal is applied to the individual EOMs and is not mainly back-reflected at any point of the matching chain. For each of the needed four RF frequencies an individual matching circuit was built. These matching circuits are working for both of the new EOM types. As a second test, it was confirmed that all EOMs produce SBs with (nearly) the expected modulation depth to a linear polarized TEM₀₀ laser beam if an RF signal is applied to them using the aforementioned matching circuits. In the following, we are going to summarize these experiments and their results.

Besides the experimental verification that expected modulation depths are achievable, a second type of experiment was performed with them. These additional tests were thermal lensing experiments. Their purpose was to determine the thermal lens of the individual modules and to confirm that GEO-HF laser power levels do not cause permanent damage. The thermal lensing experiments were part of the work of [Bog13]. Selected results that are important for the discussed matter are summarized in appendix D.

Matching results

Both EOM types were electrically tested as part of a resonant matching circuit. This effort was supported by Gavin Newton from the University of Glasgow. Details about these matching circuits are given in appendix D.2. Figure 4.7 shows the corresponding test setup. The purpose of these tests is to minimize the reflected RF power of the matching circuit with respect to the total applied RF power at the required frequency. Furthermore, the resonant matching circuit transforms the input voltage of the RF signal to approximately ten times higher values at the load, i.e. the EOM.

For each of the four required modulation frequencies a separate matching circuit was built. Subsequently, these matching circuits were used for the optical measurement of the modulation depth. For all four matching circuits, the reflected RF power could be minimized to at least -20 dB of the overall RF power. In the case of the 9 MHz SR modulation even -23 dB were achieved. Furthermore, each matching circuit is built to be applicable for each of the new EOMs, independent of the type (i.e. consisting of a $6 \times 6 \times 35 \text{ mm}^3$ crystal or two times a $8 \times 8 \times 10 \text{ mm}^3$ crystal). The EOMs have a slightly different capacity which is in the order of 10 pF. A trim capacitor (25 pF to 75 pF) is parallel connected into the matching box for the corresponding adjustment. For details about the matching principle see appendix D.

Modulation depth results

To ultimately show that we can obtain sufficiently strong modulation SBs with the new EOMs we did optical measurements. For these experiments, the new EOMs were individually used in a test setup to generate modulation SBs on a laser beam. For a given RF power and voltage, respectively, the modulation depth of the first SBs was determined. To do so, the power in one of the first SBs and the carrier was measured. Formula 4.5 was used to calculate the corresponding modulation depth.

The corresponding test setup is shown in figure 4.8 in a simplified version¹. A NPRO serves as a laser source to have 1064 nm carrier light as used for GEO 600. Because a s-polarized laser beam is needed, polarizing optics are in place. After the beam is properly

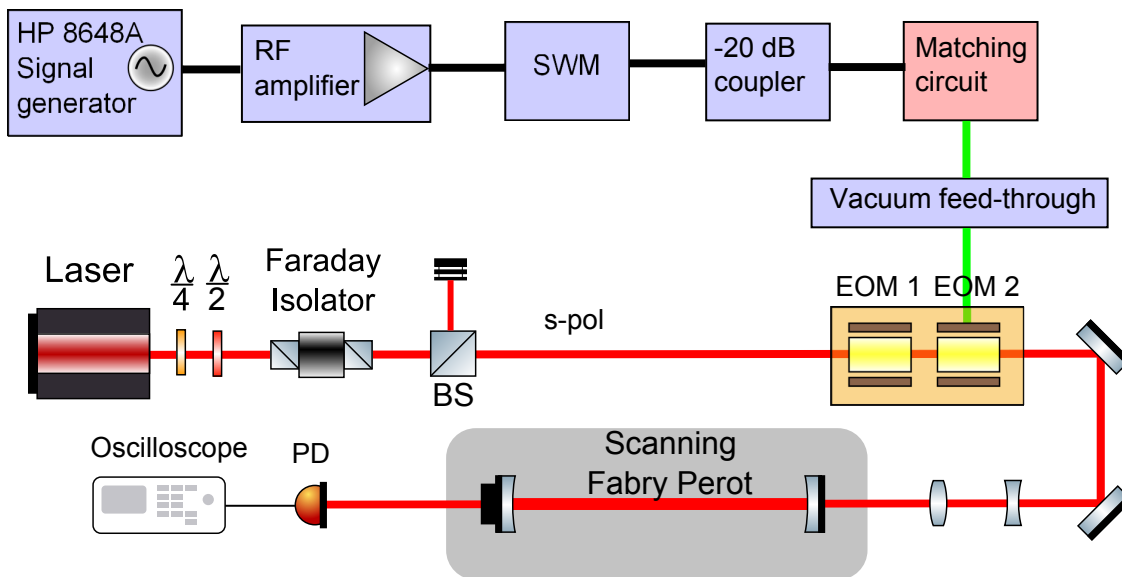


Figure 4.8: Optical setup for the measurement of the achievable modulation depth with the new EOMs. A s-polarized laser beam passes an EOM module. A RF signal is applied to one of the *two* EOMs on the module. The phase modulated beam is coupled into a scanning Fabry Perot interferometer. Its transmission is monitored by a PD to determine the modulation index by measuring the power in the carrier and the first order SBs, respectively. The electrical part of this setup is included in this figure for completeness. It is the same as shown in figure 4.7, except for an additional *standing wave meter* (SWM).

¹ These measurements were done in the 10m Prototype lab of Institute of Gravitational Research of the University of Glasgow. The measurement setup was placed right in between the optical setup of the main optical bench belonging to the Prototype experiment. Therefore, in the presented layout several components are neglected that were only used to adapt beam properties for the modulation depth measurement or that were needed to implement the test setup into the existing Prototype setup without disturbing ongoing work that is not related to the discussed matter.

polarized, it is sent through one of the new EOM units. One of the two EOMs of a single unit is electrically connected to an RF source while the other EOM on the unit is not connected. The beam passes both EOMs on the unit and is directed to a scanning Fabry-Perot cavity. An oscilloscope monitors the transmission of the (aligned) scanning Fabry-Perot cavity which is detected by a PD.

The RF signal is applied to the EOM via the same matching circuits as used and built for the initial matching optimization test. A *standing wave meter* (SWM) was additionally included in the electrical chain to check the matching and to measure the applied RF power. If the matching was worse than it was during the electrical tests it could easily be restored by slight adjustments at the aforementioned trim capacitor of the matching circuit.

In the course of these measurements, all EOMs were tested for at least one of the required modulation frequencies. Most EOMs were tested for at least two frequencies. Additionally, the tests were done for different RF powers between 0.2 W up to 2 W measured by the SWM. The results were reproducible and consistent for the different RF frequencies and RF powers. This means we measured the same modulation depth for two different frequencies at the same RF power for an EOM of one type. Furthermore, the measured modulation depths scaled with the square root of the RF power as it should according to equation 4.5.

The achieved modulation depth Γ for the two new EOM types for an RF power of 0.5 W (2 W) measured at the SWM are as follows:

- RTP, EOM consists of one crystal with $6 \times 6 \times 35 \text{ mm}^3$ EOM: $\Gamma = 0.25$ ($\Gamma = 0.5$)
- RTP, EOM consists of two crystals with $8 \times 8 \times 10 \text{ mm}^3$ EOM: $\Gamma = 0.17$ ($\Gamma = 0.33$)

We can compare this to a similar measurement of the modulation depth that was done with an $8 \times 8 \times 35 \text{ mm}^3$ LiNbO₃ EOM for an RF power of 0.5 W:

- LiNbO₃ , EOM consists of one crystal with $8 \times 8 \times 35 \text{ mm}^3$ EOM: $\Gamma = 0.32$

The calculated ratios 4.2.4 and 4.2.4 of achievable modulation depth of the two types of new RTP EOMs to the old LiNbO₃ EOMs were $m_{RTP_{2-short}} : m_{LiNbO_3} = 1 : 2.24$ ¹ and $m_{RTP_{long}} : m_{LiNbO_3} = 1 : 1.04$. If we take the modulation depth result for the LiNbO₃ EOM as basis, we get about 20 % higher modulation index as expected from the new EOMs that consist of two short crystals. For the long and thin crystals we get a lower modulation index than expected. Because Γ is just 28 % smaller than that for the old LiNbO₃ EOM used as reference, it is sufficient to achieve the required modulation for the SRC and MI SBs on MU3. The RF signal amplitudes will only need small adjustments according to these results.

1 The ratio was calculated in section 4.2.4 for one crystal. Here we take into account that the EOM consists of two crystals.

It must be noted that the RF matching setup for the modulation depth measurement of the LiNbO_3 EOM differed slightly from the setup for the new GEO 600 EOMs. This setup was built for the use in the 10 m AEI Prototype reference cavity. The major difference is that the length of the twisted pair wires between the matching circuit and the EOM is shorter. These wires are just 15 cm long instead of 140 cm. Potentially, less power gets lost due to RF radiation between the matching circuit and the EOM. We did a corresponding test with the same optical setup as shown in figure 4.8. However, this measurement as part of preparation work for the installation of the 10 m AEI Prototype reference cavity is not part of this thesis. The modulation index result of the LiNbO_3 EOM is given to have a comparison with the corresponding results of the RTP EOMs.

With equation 4.6 we can calculate the voltage across the different crystals for the obtained modulation indices. For a $6 \times 6 \times 35 \text{ mm}^3$ RTP EOM and a modulation index of $\Gamma = 0.25$ we get $U_z = 61 \text{ V}$. This result can be checked with the voltage conversion which the matching box provides (see appendix D.2). The voltage at the load, i.e. the EOM can be written as $U_z \approx U_2 = U_1 \cdot N_2/N_1$ for the case of small losses. The ratio of the used turns of the coil is $N_2/N_1 \approx 13$. Because a modulation index of $\Gamma = 0.25$ was measured for a RF power of 0.5 W which corresponds to 5 V at the 50Ω input side, we end up with $U_z = 65 \text{ V}$.

In the case of an EOM that consists of two crystals with $8 \times 8 \times 10 \text{ mm}^3$ EOM and a modulation index of $\Gamma = 0.17$ we get $U_z = 41 \text{ V}$. For completeness, $U_z = 81 \text{ V}$ is the result for the $8 \times 8 \times 35 \text{ mm}^3$ LiNbO_3 EOM and a modulation index of $\Gamma = 0.32$.

4.2.7 Implementation in GEO 600

As mentioned before, we need the strongest modulation index for the SB modulation of the MI lock, generated on MU3. Therefore, we installed one unit of $6 \times 6 \times 35 \text{ mm}^3$ EOMs on MU3. Because the $8 \times 8 \times 10 \text{ mm}^3$ EOMs provide sufficiently strong SBs for a given RF power, to fulfill the requirements for MU2, such a module was installed there.² The latter allows for a higher SB amplitude for the same applied RF power as for the short crystals. The matching results that were presented in the previous section did not show indications to prefer one unit of one type to the other. To decide, which units to install, we have chosen the modules with the lowest thermal lensing effect according to the results summarized in appendix D. The installation of the EOMs was pretty much straightforward. We took the corresponding MU out of the suspension and replaced the LiNbO_3 EOM unit by the RTP one. Each unit was pre-aligned by carefully superposing its axis with the axis defined by the MU. Figure 4.9 gives an impression of this. It shows the central part of MU3 with one EOM unit that is attached to its base. After the EOMs were put on the respective MU and they were electrically connected to the matching setup,

² The identification numbers are “M866” for the unit on MU2 and “M865” for the unit on MU3. The remaining units “M864”, “M867” and “M868” are safely stored.

	MC2	PRC	SRC	MI
Frequency in MHz	13.0	37.1	9.0	14.9
RF power in W (before matching circuit)	160 mW	410 mW	720 mW	320 mW (20 mW)
Amplitude in Vrms (before matching circuit)	2.8 V	4.5 V	6 V	4 V (1 V)

Table 4.3: RF frequencies, powers and voltages before the corresponding matching circuits of the new RTP EOMs.

the matching itself was tested. In all four cases, the matching could be easily optimized by tuning the trim capacitor of the corresponding matching circuit.

In addition to the replacement of the EOMs on the two mounting units, we exchanged two vacuum feed-throughs. They are part of the electrical chain as shown in figure 4.7.

The new values of the RF amplitudes are given in table 4.3. Note that the values which are provided in table 4.3 are the values as used at the time this thesis was handed in. The applied RF power for the SR lock was for instance significantly increased to obtain a higher SNR for the corresponding error signal. For the MI lock, two numbers are given. 4 V are currently applied during lock acquisition while only 1 V are applied during DC lock.

After the whole IO upgrade work that took place in the vacuum tanks was done we could lock the different cavities without having mentionable trouble (except for time consuming alignment work, as expected). The following section describes the next main part of the IO upgrade, the replacement of the input and output mirrors of the mode cleaners.

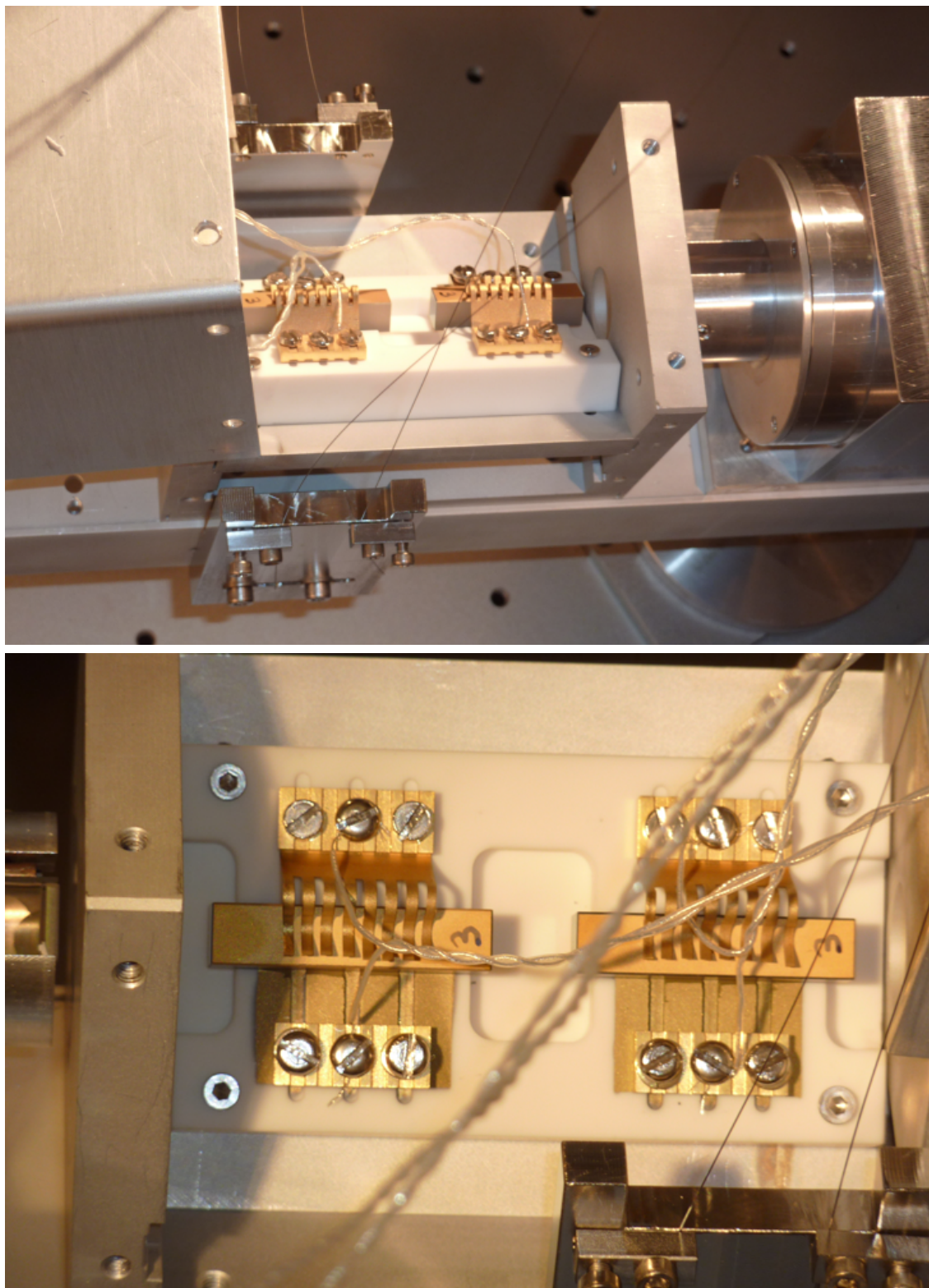


Figure 4.9: An EOM unit on MU3 during the replacement. MU3 was sitting on a stand while this pictures were taken.

4.3 The new input mode cleaners

GEO 600 uses two consecutive input *Mode Cleaners* (MCs) to filter unwanted light fields such as higher order spacial modes from the input beam before it enters the main IFO. In their original design, each MC had a finesse of about 2000. This value was conservatively chosen. While the MCs provided more filtering than necessary, two important disadvantages were present. A large amount of carrier light was lost due to scattering into the vacuum tanks. In addition, radiation pressure effects were close to limiting due to the strong light fields associated with such a high finesse.

In the section at hand, the process of reducing the finessees of MC1 and MC2 is described. This was done by replacing the initial input and output mirrors that have a transmittance of 0.15 % by new mirrors that have a higher transmittance of 1 %. As a direct visible result, the transmission of carrier light was increased by about 50 %. Furthermore, this section provides information about the new mirrors and the performance of the new MCs at high power operation is shown. The initial design of the MCs is described in chapter 2.2.

4.3.1 The need for a finesse reduction of the mode cleaners

The main IFO of GEO 600 is operated with TEM₀₀ light. To filter out residual light in the input beam that consists of higher order modes two mode cleaner cavities are in place. The expression mode cleaner cavity refers to the fact that a cavity provides a filter effect [Fre03].

Two Hermite-Gauss modes that have a different mode number experience a different phase change while passing the same distance. This is due to the fact, that their Guoy phase depends on their mode numbers. Therefore, a cavity can be designed such that it is resonant to a particular Hermite-Gauss mode, like the TEM₀₀, while other modes are mostly reflected. This is exactly how MC1 and MC2 are designed. A detailed description about the mode cleaning effect and optical cavities in general is for example provided in [Pri12] and [Fre03].

As was described in chapter 2, the two mode cleaners had a comparatively high finesse of about 2000 in their initial design. This high finesse granted that unwanted light fields were more suppressed than needed. Harmfully, in sum about 50 % of the TEM₀₀ light got lost at the IOs. A significant amount of this loss happened in MC1 and MC2 and was scattered into the vacuum tanks. An increase of the transmitted laser power through the MCs would provide more laser power that could be coupled into the main IFO.

In addition, the light fields that built up in the old MCs while being locked were strong enough that radiation pressure forces became significant. Initial locking of the cavities used to be very difficult due to the radiation pressure effect. Even for small input laser power this was the case. The force F_{rad} of an electromagnetic field that is reflected by a loss-less mirror is $F_{\text{rad}} = P/c$ [Sau94]. Here, P is the light power and c the speed of

light. If a 3 W laser beam is injected into a locked cavity that has a finesse of 2000, a light power of almost 2 kW circulates within the cavity. Thus, the radiation pressure force is of the order of 1 mN after the light field builds up.

To compensate for the impact of this force, the MCs are locked at low input power. Slightly later, the laser power is increased and the forces that are applied by the alignment actuators counteract the radiation pressure force. At laser powers levels, such as those available with the new laser, it would likely be more challenging to keep the lock. However, if maintaining the lock at input laser powers above 10 W would have been possible, could not been shown due to the aforementioned laser power limit that was set by the LiNbO₃ EOMs.

To increase the transmission of the two consecutive input MCs and to prevent radiation pressure effects at laser power levels that are available with the new laser, it was decided to decrease their finesse. Thereby, no changes of the optical layout were planned. The optical layout of the MCs and their design is explained in chapter 2.2. Figure 2.3 provides a schematic drawing of the MCs themselves and the optics that surround them. To reduce the finesesses of each MC a replacement of their input and output mirrors is necessary. The initial transmittance $T = 1 - R$ of the old mirrors was 0.15 % which corresponds to a finesse $\mathcal{F} = \pi\sqrt{R}/(1 - R)$ of about 2000.¹ Here, R is the reflectivity of the mirror. To achieve a finesse of 300 instead of 2000 we need mirrors that have a transmittance of 1 %.

4.3.2 The new input and output mirrors

In the following, the coating specifications of the old MC mirrors with respect to their transmittance are summarized. Furthermore, the specifications of the new MC mirrors that were ordered are defined and the measured values of the actual new mirrors are provided.

Initial MC mirror specifications

Each MC mirror consists of a cylindrical substrate which is coated on its front and back side. The height is 5 cm and their diameter is 10 cm. The substrates are made of fused silica (“Suprasil 1”) and weight about 860 g. The new mirrors have to have the same dimension and weight because the MC suspensions are made for mirrors of that size. Thus, no modifications at the suspension systems are necessary if the dimensions do not change.

The surfaces of the original input and output mirrors that face the inside of the individual MCs are HR coated and have a transmittance of 0.15 % at the respective angle of

¹ Because one mirror in each mode cleaner has a Transmittance of almost zero, we can use the Finesse formula for a Fabry-Perot cavity.

Mirror	MMC1a	MMC1b	MMC1c	MMC2a	MMC2b	MMC2c
Transmittance [ppm]	1778	35	1606	1532	1360	114

Table 4.4: Specified transmittance of the old MC mirrors [Fre03]. The high reflective mirrors MMC1b and MMC2c are still in place.

incidence. The transmittance of the individual third mirrors are in the order of 10 ppm to 100 ppm. These two mirrors were not exchanged. Table 4.4 summarizes these values as provided by the manufacturer according to [Fre03]. The back sides of the input and output mirrors are AR coated. Furthermore, the surfaces of all mirrors that needed replacement are flat except for MMC2b. This fact is important for the polishing process that proceeds the coating process.

The specifications of the new MC mirrors

To obtain mirrors with new coatings as required for GEO-HF, we have to specify the properties of the coatings. An adequate number of substrates that have the correct dimension already existed. These substrates needed to be polished first because only one of them had an appropriate coating that could be used again. This single exception was the old MMC2b spare which has an AR coating on its convex curved surface that reflects slightly less than 0.08 %. In the following, the specifications of the new mirrors are given.

The laser beam impinges on three of the four input and output mirrors at an angle of incidence of 44.3° . These mirrors are MMC1a, MMC1c and MMC2a. The remaining mirror, namely MMC2b, is hit at an angle of about 1.1° . For these respective angles, the HR coated surfaces of the new mirrors need to transmit 1 % s-pol light at a wavelength of 1064 nm. In particular, the transmittance of the two mirrors that belong to one cavity need to be as equal as possible. For the desired transmittance of 1 % an absolute error of 0.05 % would result in a reflection of about 3 % of the incoming light. An absolute error of 0.05 % was granted by the manufacturer.

Apart from the HR coating on the front sides, reflections on the backsides have to be minimized. Thus, the back surfaces of the new mirrors require AR coatings. We decided on a value of the AR coating to ensure $< 0.05\%$ reflectivity. This would result in < 10 mW residual reflected light if a 20 W beam impinges on the AR coating. Table 4.5 summarizes the coating specifications for the new mirrors.

We ordered five new mirrors with the described specifications. Four of these mirrors were specified to have a transmittance of 1 % at an angle of incidence of 44.3° as required for MMC1a, MMC1b and MMC2a. One of these mirrors was acquired to be a spare. The remaining fifth mirror is meant to replace MMC2b. For the MMC2b replacement, the decision was made to acquire no spare.

	MMC2b	all other mirrors
Transmittance of HR coating	1 % at 1.1°	1 % at 44.3°
Reflectivity of AR coating	<0.05 % at 0°	<0.05 % at 44.3°

Table 4.5: Specified properties of the new MC mirrors.

Experimental check-up of the new MC mirrors specifications

The HR and AR coatings of the new mirrors were experimentally checked.¹ Table 4.6 summarizes the results of these measurements. The mirror labeling that is used in this table reflects how they were finally installed.

As can be seen in table 4.6, the HR coatings are good with respect to the desired transmittance. However, the AR coatings are worse than specified and during the coating process dirt must have found its way *underneath* the coating.² Still, the decision was made to install the mirrors.

Positioning of the new mirrors within the optical layout

All values for the transmittance are close 1 % and do not differ more than 0.06 % from each other. Because the measured transmittance values for the HR coatings were the major argument for the order, the mirrors were finally installed. Since two mirrors show the same transmittance of 1.01 % at an angle of incidence of 44.3°, these two were used as the input and output mirrors of MC1. As mentioned before, only one output mirror for MC2 was ordered. It shows a transmittance of 1.03 % at 1.1°. To complete MC2, we have two remaining mirrors that have very similar transmittance at 44.3° as required for the input mirror. Even though the transmittance of the spare at 44.3° is slightly closer to the transmittance of MMC2b at 1.1°, we took the other mirror. The major reason for this choice is the visually higher quality of both coated surfaces, i.e. it has less dust underneath its coatings than the spare mirror has, and it has a smaller residual reflection on its AR side compared to the spare.

¹ The setup used for these measurements is as follows: A commercial NPRO was used as laser source. Polarizing optics were in place to provide s-pol light for the test. The beam impinged on the respective coating at the respective angles of incidence. The power in the transmitted beam of the HR coating and the residual reflected power of the AR coatings was measured. Both a PD and a power-meter were used to double check the results. All measurements were done in a clean room to ensure the cleanliness of the mirrors.

² Apart from the worse than specified AR coatings the coatings themselves showed flaws. When we examined the surfaces with a microscope, we found a significant amount of dust underneath the coatings. Furthermore, some kind of thin lubricating film was found underneath some coatings. However, the manufacturer agreed to provide a new set of mirrors at no charge that fulfill the specifications and are flawless. Therefore, the mirrors can be replaced if it turns out to be necessary in the future.

	MMC1a	MMC1c	MMC2a	MMC2b	spare
Specified values:					
T of HR coating	1.0 %	1.0 %	1.0 %	1.0 %	1.0 %
R of AR coating	0.05 %	0.05 %	0.05 %	< 0.08 %	0.05 %
Measured values:					
T of HR coating	1.01 %	1.01 %	1.07 %	1.03 %	1.06 %
R of AR coating	0.16 %	0.14 %	0.21 %	<0.08 %	0.39 %

Table 4.6: Specified and measured transmittance T of the HR coatings and residual reflection R of the AR coatings. The transmittance of the HR coatings match sufficiently well while all AR coatings except for the one of MMC2b are significantly worse than specified. The new MMC2b is actually the initial MMC2b spare and only its HR side was overworked.

The AR coating residual reflections are not as specified. For the installed mirrors, the AR reflex is three to four times higher than wanted. In the case of the spare mirror the AR reflection is even worse. To compensate for this we decided to install specially designed beam dumps at appropriate spots inside of the vacuum tanks.

Besides this experimental check of the coatings, the RoC of MMC2b's concave surface was measured to be 6.62 m which is sufficiently close to the specified value of 6.72 m.

4.3.3 The new mode cleaners in operation

The actual mirror replacement was demanding but could be executed without mentionable difficulties. To date, the new MCs have not shown evidence that radiation pressure does limit their performance. However, they have not yet been operated at more than 2/3 of the available 18 W of laser power which could be injected into MC1. The following discusses the throughput increase of the MCs for carrier light. Subsequently, the performance of the new MCs up to 2/3 of the available laser power is discussed. Finally, a brief discussion about the reduced stray light contamination of the IO suspension shadow sensors follows.

Throughput of the IOs

The reduction of the finesses of the MCs did allow to increase their throughput for carrier light. The throughput is defined as ratio between the transmitted laser power and the injected laser power. It was measured for both MCs. These measurements have to include the particular MU behind the respective MC. The transmitted power of MC1 in lock can only be measured in reflection of MMC2a if MC2 is unlocked while the transmitted power of MC2 in lock can only be measured in reflection of MPR if the PRC is unlocked. The

three beams whose power was measured are the ones that are sent to the PDs that are labeled “PDMC1”, “PDMC2” and “PDPR” in figure 2.3.

The overall throughput of the new IOs is 81 % if we exclude the visibility of MC1 that is slightly above 90 % since the laser replacement. Including the visibility of MC1 leads to a throughput of 73 %. Thereby, the individual throughput of MC1 is 82 % and the throughput of MC2 is 90 %. Please note that the reflected beam of MPR passes two FIs, one of them twice before its power can be measured. Thus, the actual throughput of MC2 is higher than of 90 %. With respect to the degree of pollution underneath the coatings, this is an astonishing result.

The performance of the MC AA at different laser powers

The new MCs have to show satisfying performance at high laser power levels compared to the default, low power state. To investigate if this is the case, they were operated at different laser power levels and their AA error signals were compared. The highest laser power that has been used corresponds to 12 W input laser power into MC1. This is about 2/3 of the currently available laser power.

Figures 4.10 and 4.11 provide examples of one of the AA error signal spectral densities of MC1 and MC2, respectively. Each figure shows an error signal for three different laser power levels which correspond to input powers to MC1 of 3 W, 6 W and 12 W.

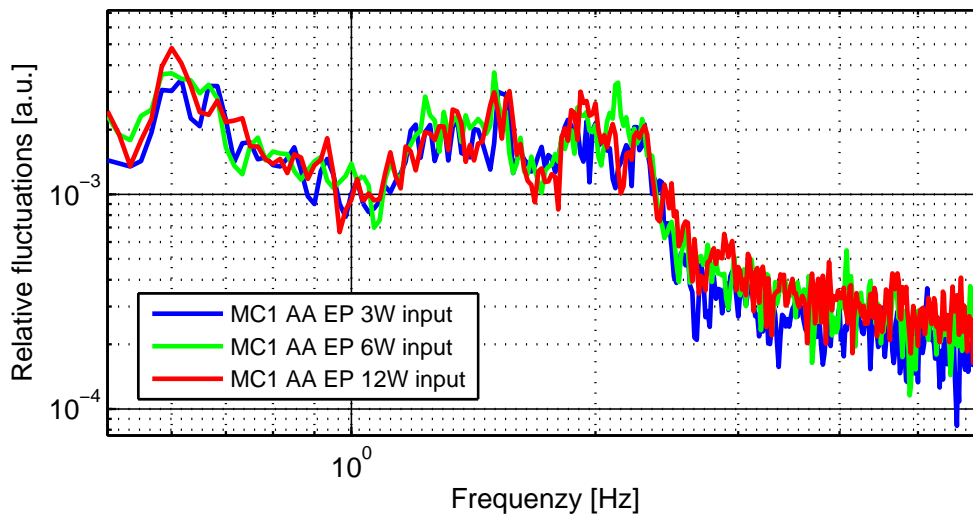


Figure 4.10: Spectral densities of one of the MC1 automatic alignment error signal for three different input laser powers as depicted in the legend. This case shows the error signal of the a and c mirror in tilt.

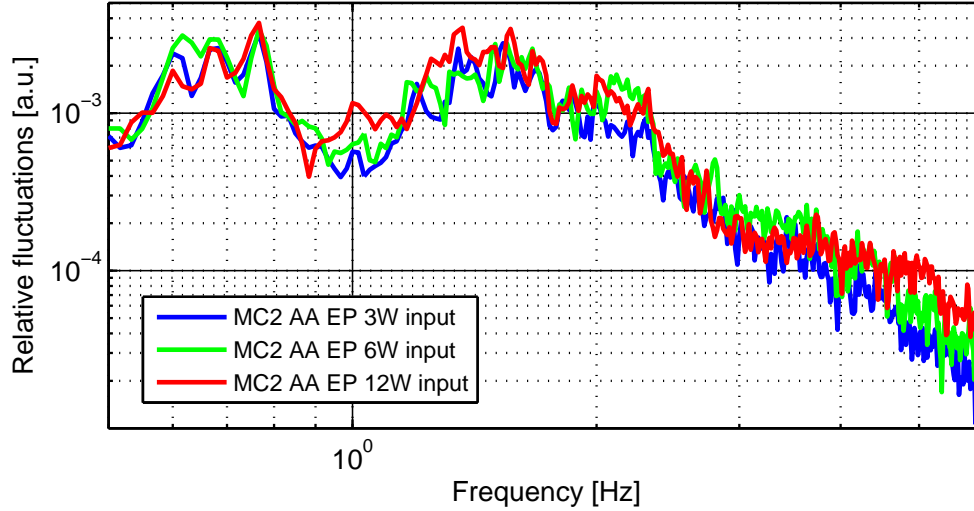


Figure 4.11: Spectral densities of one of the MC2 automatic alignment error signal for three different input laser powers as depicted in the legend. This case shows again the signal of the a and c mirror in tilt. The time at which this measurement was done is identical to the measurement shown in figure 4.10.

Furthermore, the data is normalized by the respective input laser power and the seismic conditions on site were fairly equal for each measurement. As can be seen in figure 4.10, the AA signals for MC1 show a comparable amount of fluctuations for the different cases. Thus, no undesired effects can be reported from the perspective of the MC1 AA.

As can be seen in figure 4.11, the AA signals in MC2 show a slight increase of fluctuations at some frequencies with increasing laser power. However, measurements up to 12 W input power were only performed at two occasions and it has yet to be seen if this slight increase of fluctuations in the MC2 AA is reproducible. If it is reproducible and the fluctuations further increase for higher laser powers, additional investigations could become useful. Fluctuations in the MC2 AA which grow with laser power will propagate to the main IFO and enhance fluctuations in it and thus affect the lock stability of the IFO.

Measurements at higher input laser powers will require modifications to the optical setup in the beam paths of the corresponding pick-off beams on the optical benches that surround the MCs as denoted in figure 2.3. Such modifications will soon be necessary in order to provide more laser power for the injection into the PRC for experiments at higher laser power levels as are discussed in the next chapter.

Stray light coupling at the new input optics LCs

Before IO upgrade was done, stray light coupling to the shadow sensors of the LCs on the IO side was measurable. However, this effect was not limiting the IOs operation up to laser power levels that were considered safe before the IO upgrade. In chapter 3.5.3 the corresponding measurements are described.

After the installation work of the new IOs was completed, stray light coupling experiments were done again for selected flag signals that showed a measurable amount of stray light coupling before the upgrade. For laser power levels that are comparable to the experiments described in chapter 3.5.3 stray light coupling is not detectable anymore. This result further proves that less scattered laser light is illuminating the inside of the IO tanks.

Measurements of stray light coupling to the IO LC shadow sensors at or close to maximum laser power were not performed. The aforementioned experiments at low laser power sufficiently prove that stray light coupling at the IOs will not cause problems at recently available laser powers. For laser power levels that are significantly beyond the scope of the current laser system, more detailed stray light measurements are recommended. Before considering installing a new laser system, stray light measurements at the IOs should be performed at the highest possible input laser power to obtain valid estimates towards post GEO-HF power levels.

However, before the discussion of the laser power increase at GEO 600 returns back to the main IFO in the next chapter, a small but efficient modification of the mode matching telescope towards the PRC is described.

4.4 Improvement of the PR mode matching

The spatial mode of the laser beam that is sent from MC2 to the main IFO needs to be matched with the mode of the PRC. For this purpose a mode matching telescope is in place. It consists of the aforementioned output mirror of MC2 (MMC2b) and a lens that sits on MU3. Both surfaces of MMC2b are curved with radii of curvature of 6.8 m and 0.34 m, respectively. The lens that was formerly used on MU3 has a focal length of 1 m.

In the past, the mode matching onto the PRC was far from being optimal. If GEO 600 was in DR lock at low laser power, i.e. at powers of about 1.5 kW impinging on the BS about 16 % of the injected light was reflected due to the not optimal mode matching. This reflected light is lost and cannot contribute to the power buildup in the IFO.

In addition to this initial bad mode matching, thermal lensing of components on the IO side resulted in an even worse mode matching in operation at higher laser power. The main contributions of this thermal lensing effects at the IO side were caused by two FIs and two LiNbO₃ EOMs that were sitting on MU3.¹ With respect to a laser power increase this situation needed to be improved.

Figures 4.12 and 4.13 show the dependence of the mode matching onto the PRC on the laser power for different operational powers. In figure 4.12, the circulating laser power in the IFO is plotted while being in full DR lock and compared to the laser power reflected by MPR at the same time. On the left side of the figure, GEO 600 was operated with 1.5 kW impinging on the BS. This corresponds to the default lock acquisition power of GEO 600. The reflected power at that time corresponds to 16 % of the total power sent towards MPR. As can be seen, the laser power was increased three times during the displayed time frame, reaching 3.4 kW impinging on the BS in the end. With each power step, the power reflected by MPR increased in a disproportional way due to the aforementioned thermal lensing effects. At the lowest displayed laser power 300 mW are reflected by MPR while at the highest displayed laser power 1.5 W are reflected. At the highest laser power 1.5 W of the light that is sent to the PRC is reflected. This corresponds to 29 % of the total laser power that is sent to MPR.

Figure 4.13 emphasizes the effect of the laser power depended mode matching. It shows the ratio of the reflected laser power to the laser power that is coupled into the IFO. The latter is obtained from the circulating power assuming a constant power buildup in the IFO for different input powers. In particular, the thermal lens of the IFO's *beam splitter* (BS) is neglected. Note that figure 4.13 neither shows the visibility of the PRC nor 1 minus the visibility.

The just shown disproportionately high decrease of the PRC mode matching with increased laser power as well as the initially bad mode matching needed to be improved

¹ According to [Kwe11] the thermal lens of the FIs and the LiNbO₃ EOMs on MU3 are of the same order of magnitude. Because the only other components in the beam path are MMC2b (made from fused silica) and a BK7 lens. The latter is placed on MU3.

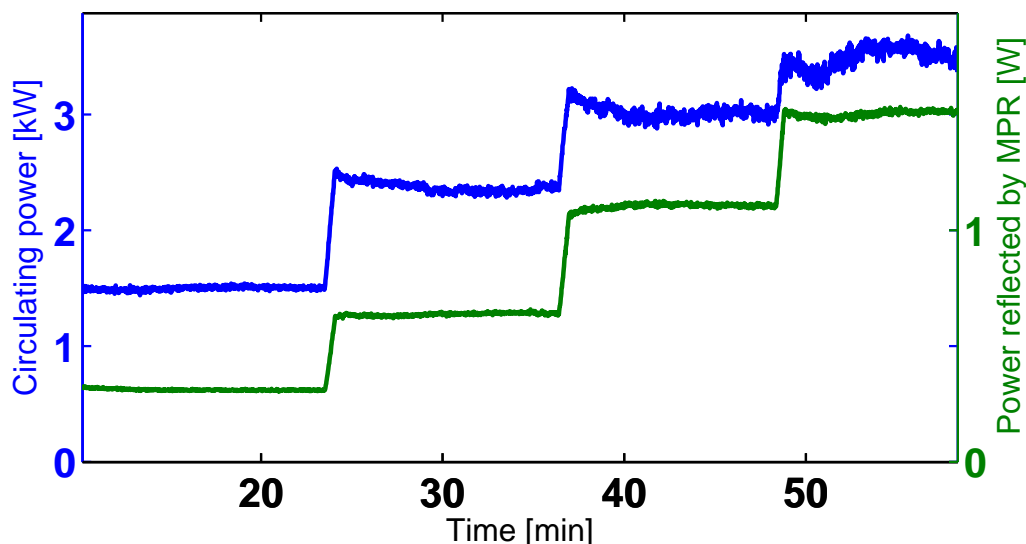


Figure 4.12: Circulating laser power in the IFO in kW (blue trace) versus laser power reflected by MPR in W (green trace) while the IFO is in full DR lock *before* the IO upgrade. This plot shows the mode matching onto the PRC situation before the mode matching lens on MU3 was replaced. The laser power injected to the IFO was increased three times during the displayed time. In the beginning, 1.5 kW are impinging on the BS while 0.3 mW are reflected by MPR. After minute 50, the highest laser power that could be used before the IO upgrade is reached. At that time about 3.4 kW are impinging on the BS while 1.5 W are reflected by MPR. This corresponds to a input laser power of 10 W towards MC1.

with respect to a laser power increase.

While we were working inside of the tanks TCMA and TCMB during the actual input optic upgrade was a good chance to improve the mode matching. Finesse simulations suggested to replace the $f = 1$ m mode matching lens on MU3 by one with a focal length that is higher. According to that a focal length of about 1.8 m would be optimal for low power operation.¹

However, a slightly higher focal length was chosen. With respect to higher operational powers in the future, it is preferable to have the optimal mode matching at higher input powers instead of just about 2 W at MU3. We decided to go for a slightly higher focal length of 2 m and thus move the optimal mode matching to higher input power.

The new mode matching lens that was installed in MU3 was bought from Melles Griot. It is plan convex (as the old lens was) and has a focal length of $f = 2$ m. The material

¹ Note that the numbers for the thermal lenses of the FIs and EOMs show some variance depending in which reference document one consults. A value of 1.8 m as optimal focal length for the new lens corresponds to results that were close to what we actually observe in the experiment.

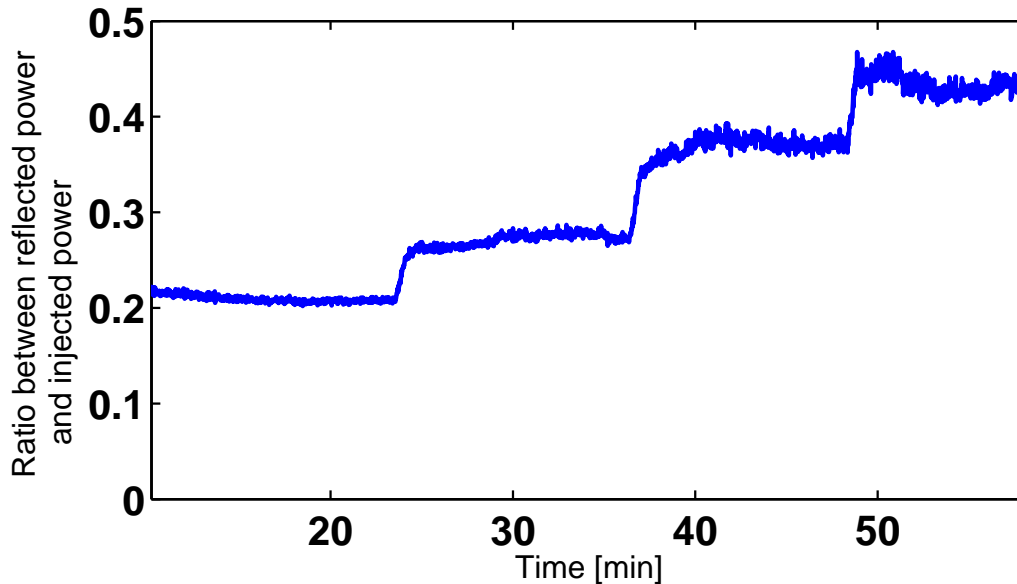


Figure 4.13: Laser power reflected by MPR divided by the power injected into the IFO while the IFO is in full DR lock *before* the IO upgrade. To calculate the ratio, the data from figure 4.12 is used. Therefore, it shows the same time and is meant to emphasize the significant effect of the laser power dependent mode matching to the PRC before the IO update.

it is made of is BK7 and both sides of the lens are AR coated. The AR coating of the new BK7 lens was measured (using a s-pol beam) to reflect 0.04% on the plan side and 0.06% on the convex side for an angle of incidence of 2.4° . This is about two times better than the AR coating of the old BK7 $f = 1$ m mode matching lens. The AR coating of the old lens was checked in a reference measurement. It was also shown that the AR reflex increases for bigger angles. Due to space limitation of the used setup, an accurate measurement for smaller angles was not possible. A lens made from fused silica would show less thermal lensing. One exemplar was available but its AR coatings were bad. They showed about 1% reflexion on each side for angles close to 0° . Because on MU3 the FIs will clearly dominate the thermal lensing effect, we decided to use a BK7 lens with good AR coating instead.

Significant better mode matching to the PRC

After the IO upgrade was successfully completed, a similar measurement as shown in figures 4.12 and 4.13 was done to show the improvement of the mode matching to the PRC in dependance of laser power. This is shown in figures 4.14 and 4.15.

Due to the improved mode matching, the reflected power is lower by a factor of almost

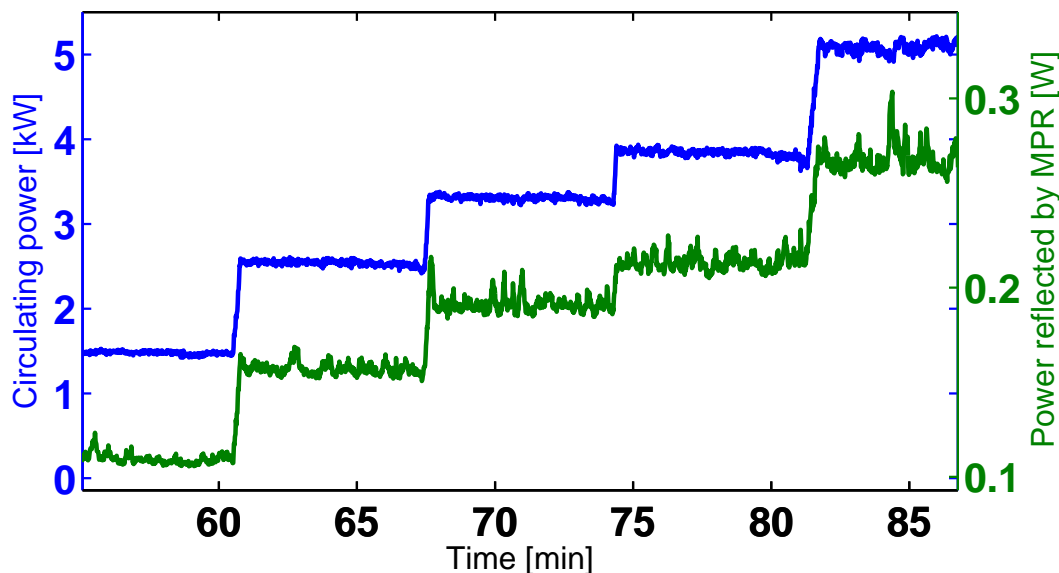


Figure 4.14: Circulating laser power in the IFO in kW (blue trace) versus laser power reflected by MPR in W (green trace) while the IFO is in full DR lock *after* the IO upgrade. The mode matching onto the PRC improved significantly after the replacement of the lens on MU3. Instead of four different laser power states, five are shown. The first four correspond to the same input laser powers sent towards the PRC as shown in figure 4.12. In the 5th power state, a even higher input power is used that results in 5 kW impinging on the BS. Still, just 270 mW are reflected by MPR.

3 at low laser power state than it has been before the IO upgrade. In total, 7% of the the laser power that is sent to the PRC is reflected at low power (the power used for lock acquisition). For this experiment, the laser power was increased in four steps. The first three steps correspond to input laser powers as used for the experiment shown in figures 4.12 and 4.13. Due to the better mode matching, one can see that more power is impinging on the BS. In the last step, GEO 600 was operated with a power that corresponds to 5 kW impinging on the BS. Still, less laser power is reflected by MPR as has been at low power before the IO upgrade. Furthermore, the ratio between reflected power by MPR divided by the power sent into the IFO is smallest here. Over all, these results show the significant improvement of the mode matching to the PRC. In combination with the modifications that were done at the MCs, 0.57 times less input laser power to MC1 is necessary to have 1.5 kW laser power circulating in the locked DRMI.

The next chapter addresses challenges for the operation of the DRMI which arise if it is operated at significantly higher laser power levels as were available before the IO upgrade.

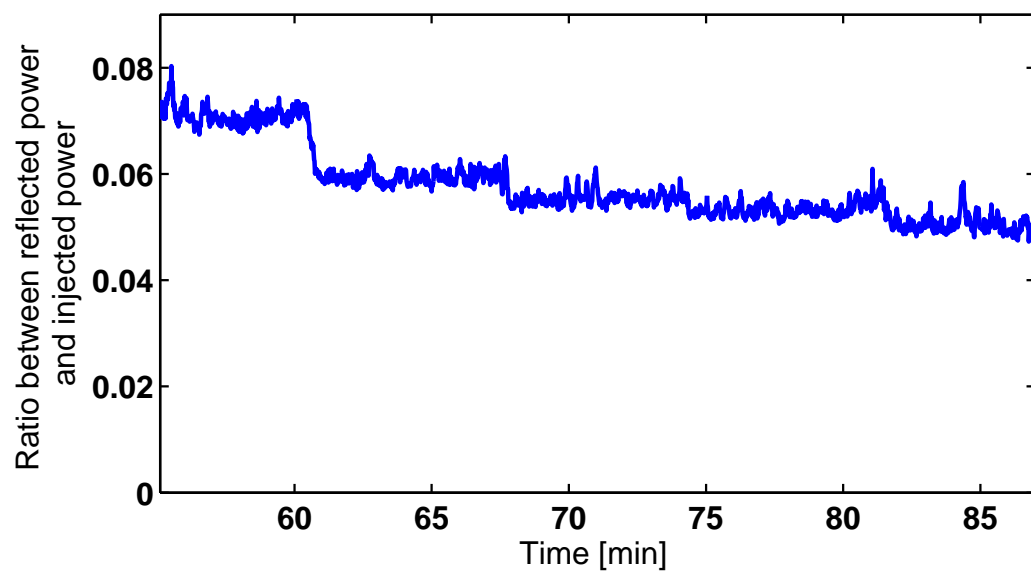


Figure 4.15: Laser power reflected by MPR divided by the injected power into the IFO while the IFO is in full DR lock *after* the IO upgrade. The initial mode matching at low laser power improved by a lot. For higher input powers the mode matching gets slightly better.

5 Towards higher laser power levels

In chapter 3, the work is described that allowed for a stable operation of GEO 600 with significantly more laser power than 2 kW impinging on the *beam splitter* (BS). As a result, GEO 600 was laser power limited with the maximum being at 3 kW. The installation of the new and stronger laser system, that is described in chapter 4.1 increased the available laser power by a factor of 2.5. As foreseen, this high increase in available laser power necessitated the upgrade of the *input optics* (IOs). In particular, the *Lithium Niobate* (LiNbO_3) EOMs that were used before the IO upgrade set a limit to the maximum usable laser power due to their damage threshold. This threshold corresponded to about 3.5 kW impinging on the BS.

The IO upgrade, as part of the GEO-HF upgrade, is the major topic of chapter 4. A planned result of the IO upgrade was a further increase of laser power due to a higher transmission of the two input *mode cleaners* (MCs) and an improvement at the mode matching telescope towards the *power-recycling cavity* (PRC). In combination, these two modifications at the IOs increased the available laser power which can be sent to the PRC by a factor of 1.75. At present, about 4.5 times more laser power is available as compared to before the GEO-HF upgrade started. Compared to the default laser power of GEO 600 before its upgrade, this even corresponds to a factor of more than 6.

To make use of 4.5 times more laser power a variety of new challenges need to be addressed. The chapter at hand discusses modifications at different subsystems of GEO 600 that allowed for a further extension of the current limit of usable laser power. Thereby, we will focus on one of two particularly important issues with respect to an extension of this limit, the stability of the lock. The other important aspect, the sensitivity at high laser power is discussed in the following chapter.

The current limit of usable laser power cannot be defined by an exact value. The highest circulating laser power that was ever measured in GEO 600, but only for several seconds, is roughly 8 kW. First experiences were obtained while the *dual-recycled Michelson interferometer* (DRMI) was locked in heterodyne for several ten minutes with 6 kW to 7 kW impinging on the BS. The highest power in full DC lock was about 5.5 kW. This lock lasted for 20 min. In fact, at such high power levels, the stability decreases.

Already before the installation of modulation drives at the main suspensions local controls, a detector lock on minute scales at 3 kW was possible if the level of seismic noise was exceptionally low on site. To date, issues other than stray light coupling to the suspension local control shadow sensors limit the stability. The following chapter also points out examples that possibly cause the current limit of usable laser power and proposes further possibilities for improvements.

This section starts by displaying which obstacles prevented the extension of the the current laser power limit and subsequently delivers the implemented solutions. Two major examples which are described are modifications of the laser frequency stabilization loop and the *automatic alignment* of the MI. Subsequently, the performance of the *signal-recycling automatic alignment* (SRAA) at high power is discussed. It was found that the operating point of the SRAA depends on the laser power. Maintaining the optimal operation point is important for the stability of the DRMI.

At the end of this chapter, the most important issue that needs to be addressed at the achieved laser power levels is discussed: thermal lensing at the BS. Its impact on the laser power increase was already investigated by simulations in [Wit09]. Even though the BS thermal lens poses important consequences for an operation of GEO 600 at very high laser power, it plays only a minor role for prior discussed topics in this thesis. However, the thermal lens at the BS will become more significant for higher circulating laser powers in the IFO, as discussed in the chapter at hand. Thus, its effect for increasing laser power is shown and the need for a compensation is clear by looking at the corresponding results. If no measures are taken to compensate for the thermal lens in the BS, about 600 mW of light in HOMs contaminates the dark port if the DRMI is operated at 6 kW and the BS reaches thermal equilibrium. This corresponds to about 8% of the light that is injected into the PRC at the same time. This effect can be considered as the major limiting factor at current power levels, as explained below.

To partially compensate for the effect of the BS thermal lens, the so-called ring heater [Lüc04] at the east folding mirror, namely MFE, can be used [Wit12]. Initial experience with this system to counteract for the thermal lensing effect were obtained and it is explained why this is necessary to operate the DRMI beyond 6 kW.

Furthermore, it has to be mentioned, that the installation of a *thermal compensation system* (TCS) at the BS is ongoing while this thesis is handed in. Its design is based on a prototype system that is described in [Wit09]. Subsequent laser power increase commissioning work beyond the scope of this thesis will strongly benefit from it.

5.1 Modifying the frequency stabilization loop

In this section, the first major challenge after the IO upgrade is described which prevented operation of the DRMI at a significantly higher level of circulating laser power than had been possible before the IO upgrade. It is shown that the loop chain which is used to stabilize the frequency of the GEO laser needs modification with respect to power up. Partially, this was already foreseen, but detailed measurements at different parts of the frequency stabilization loop showed the need for a further small but mandatory change. Ultimately, the presented investigation led to a replacement of the servo module that is used for the MC2 lock. The replacement and the further changes allowed for an operation of the IFO at much higher laser power. The modifications of the frequency stabilization loop in combination with the topics which are discussed in sections 5.2 and 5.3 can be considered as the most important achievements that allowed for a more stable operation up to 6 kW circulating power in heterodyne lock and in DC lock.

Furthermore, the investigation that is discussed in this section is a prime example of the commissioning efforts that are necessary to extend the laser power limit of an interferometric GW detector.

5.1.1 The frequency stabilization loop

The issue that is described in the following benefits from a basic knowledge of the laser frequency stabilization loop chain of GEO 600. The laser frequency stabilization of GEO 600 is described in [Fre03] and [Gro03]. Based on the latter, an overview about the frequency stabilization loop is given at this point with some focus on important aspects for the discussed matter of this section.

There are two main reasons to stabilize the frequency of the GEO 600 laser system. First, coupling of laser frequency noise into the detector output signal in its measurement band gets minimized. Second, rms frequency noise at all frequencies gets minimized by it, too. The latter makes lock acquisition of the power-recycling cavity easier.

Figure 5.1 provides a schematic overview of the PR lock and the associated frequency stabilization chain of GEO600. The ultimate frequency reference for the laser light is the PRC. To lock the PRC, the laser frequency is adjusted to the longitudinally uncontrolled PRC. Thereby, a frequency stabilization chain is formed, because with MC1 and MC2, two further cavities (and their lengths) need to be controlled for this lock. The corresponding feedback is not simply applied to an actuator at the laser. As can be seen in figure 5.1, feedback is applied to different actuators, depending on the signal's frequency components.

Initially, with all three aforementioned cavities unlocked, the locking sequence starts with the lock of MC1. MC1 is locked with the Pound-Drever-Hall injection lock technique [Dre83b]. It serves as the frequency reference for the laser as long as only MC1 is locked. Also MC2 is locked with the Pound-Drever-Hall technique and replaces MC1 as frequency reference for the laser if locked. As can be seen in figure 5.1, the error signal of MC2 is

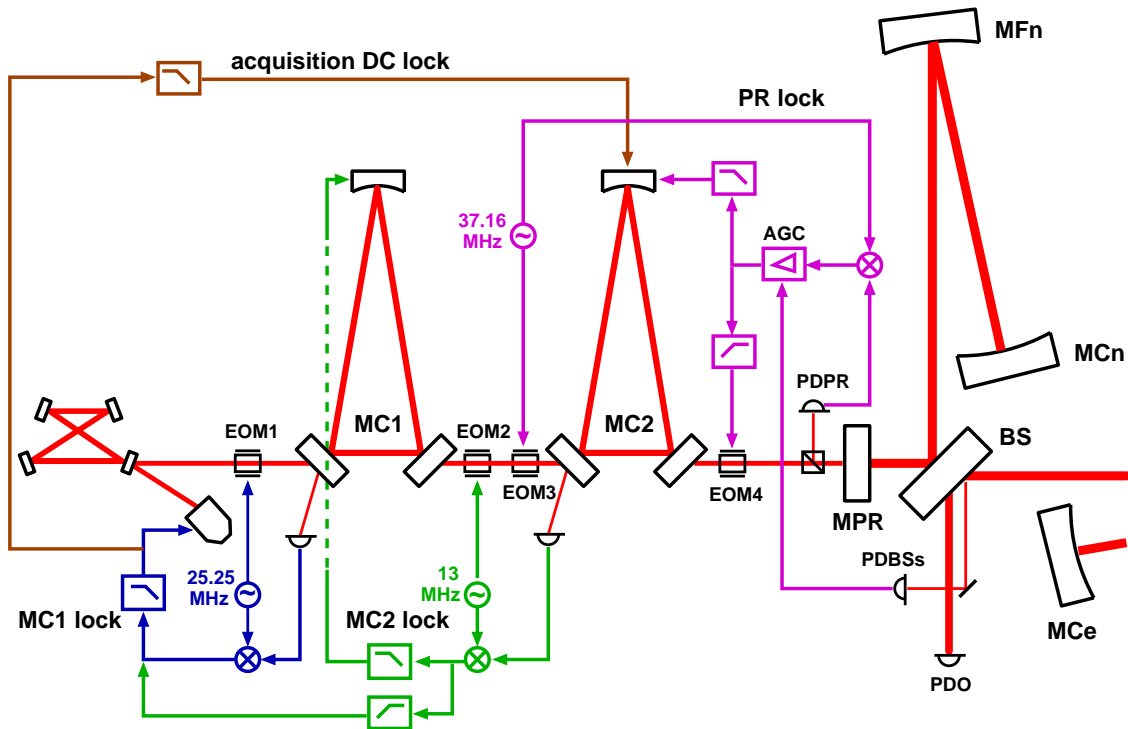


Figure 5.1: A schematic overview of the power-recycling lock and the associated frequency stabilization of GEO600 [Gro03].

split in frequency. The frequency band from DC to 1 kHz is applied to the length of MC1 after passing an appropriate servo. Signal components above 1 kHz get added to the MC1 error signal and therefore to an actuator at the laser after passing a different servo. This actuator is an EOM and a PZT. Later on, we will refer to these two paths as slow path and fast path, respectively. The sum of the slow path and the fast path will be referred to as the full loop of MC2. The UGF of the full loop is at about 20 kHz.¹

The error signal of the PRC is obtained by demodulating the signal of the photo diode that is labeled “PDPR” with the PR modulation frequency. Again, the loop is split into a slow path and into a fast path. The slow part of the feedback is applied to the MC2 length while the fast part is applied to “EOM4”. Their crossover frequency is at about 1.5 kHz. This crossover is important for the discussion below.

An uncontrolled Michelson interferometer leads to a variable finesse of the PRC. The light which is reflected by MPR varies in time. Thus, the optical gain of the PRC varies proportional to the stored light power in the cavity. To compensate for this, the PR error

¹ As a side note, the EOMs used to generate the SBs for the locking of MC2 and the PRC are the two RTP EOMs on MU2 that are part of the discussed matter in chapter 4.2.

signal can be divided by the light power to increase the loops stability. The light power is measured by the photo diode “PDBS”. The information of the light power is needed for *automatic gain control* (AGC), a feature that is not used anymore. The Pound-Drever-Hall locking of the PRC can happen largely independently from the Michelson lock.

5.1.2 Gain peaking and a double gain normalization

Lock losses which arose from the discussed matter were first observed when we tried to operate the DRMI in heterodyne lock beyond a laser power of 4 kW impinging on the BS. Up to approximately that power the lock could be maintained. But slightly above that power the IFO lost lock. Carefully watching the various control monitors of the system while a lock loss happens often provides useful indications about the reason of a lock loss. Typical reasons are oscillations in a control loop or a sufficiently strong seismic event. However, no evidence was visible on any control screen.

By analyzing data from these lock losses, we observed oscillations with comparatively small amplitude at roughly 1.5 kHz on the power circulating in the IFO. At the same frequency, an oscillation that has a small amplitude is *always* visible in the *power* stabilization loop error signal. Its amplitude increases with laser power while its frequency decreases slightly. It showed the characteristics of gain peaking.

Gain peaking at a frequency of about 1.5 kHz led us to further investigate the *frequency* stabilization loop. This loop has a crossover at this frequency. It is the crossover of the EOM path and the MC2 path which is described in 5.1.1. In figure 5.1, the corresponding split of the loop can be seen in the purple part of the schematics.

Figure 5.2 shows spectra of the PR error signal for different laser powers. It is clearly visible how the gain peaking increases with the laser power while the peak frequency which is actually the crossover frequency decreases. The fact that the cross over frequency goes down means that as the power increases, the mode cleaner path of the frequency actuation reduces in strength compared to the EOM path. To understand this, the information provided above about the frequency stabilization loop becomes useful.

Let us further follow the schematic overview of the frequency stabilization loop in figure 5.1. While the MC2 length follows the length of the PRC, the corresponding MC2 length changes get detected by the PD in reflection of MC2. After demodulation, the error signal is split again and fed back to the MC1 length and the EOM at the laser, respectively. Thereby, the fast part of the MC2 EP gets added to the MC1 EP. Both error signals of MC1 and MC2 are normalized by the actual laser power before being converted to feedback by the corresponding servos. For the MC2 error signal this gain normalization happens before the path is split, i.e. right behind the green mixer symbol in figure 5.1. This means that the gain of the slow path gets two times normalized by the actual laser power. A so-called “double gain normalization” exists. Due to this double gain normalization, the cross over frequency of the frequency stabilization loop decreases with increasing laser power.

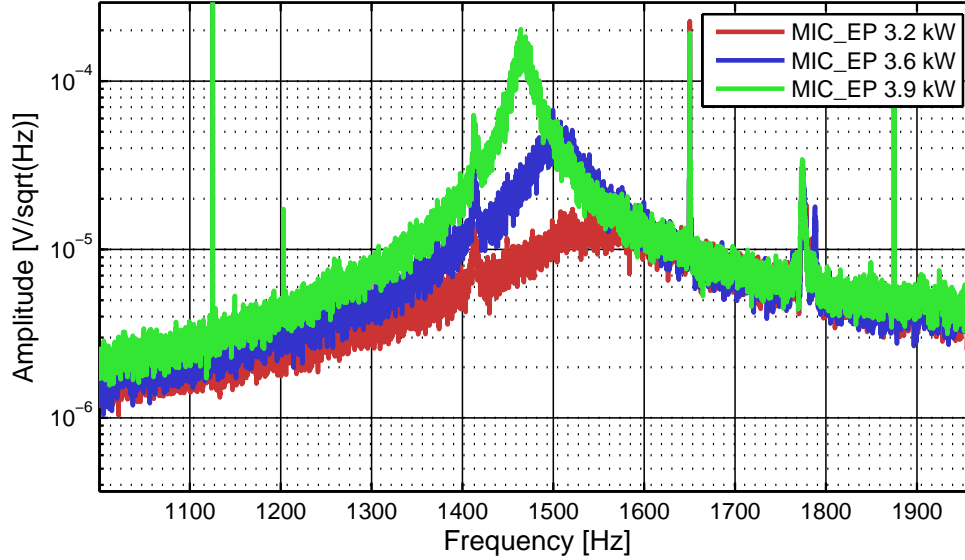


Figure 5.2: Gain peaking in the longitudinal error signal of the PRC. The cross over frequency decreases as the power increases is caused by the fact that the mode cleaner path of the frequency actuation reduces in strength compared to the EOM path.

To remove this problem of a double gain normalization, the layout of the corresponding servo needed to be changed. Due to reasons explained further below, we replaced the corresponding electronics by a new module in the end.

5.1.3 Further investigations at the frequency stabilization loop

The process of building, commissioning and installing a new frequency loop electronics servo is time-consuming. A medium-term solution to allow for a operation of GEO 600 at higher laser power was necessary to allow for operation with more than 4 kW.

To compensate for the laser power dependent crossover frequency of the frequency loop, the MC2 overall gain can be set manually. However, a manual change of frequency loop gains on the MC side, i.e. without physically changing the electronics, is only possible for two cases. These are the adjustment of the overall gain of the MC1 lock and the adjustment of the overall gain of the loop path belonging to the MC2 lock. The latter is applied before the signal is split into a slow and a fast path.

By increasing the MC2 overall gain according to the laser power, the crossover frequency of the PR split path can be kept constant. It turned out that this is only marginally possible. Otherwise, we ran into another instability. This new instability could be understood

by further investigations of the frequency loop part belonging to MC2.

Figure 5.3 provides an in-loop measurement of the MC2 loop at frequencies above 5 kHz. The slow and fast path as well as the full loop shape are shown. At the displayed frequencies, the slow path should not matter. However, at 18 kHz, gain peaking is visible in the slow path, i.e. the magnitude of the slow path transfer-function reaches one in the displayed figure. This peak increases with increasing MC2 overall gain. On the other hand, the gain of the fast loop and therefore the gain of the full loop decreases with increasing laser power at the displayed frequencies and above. If the value of the slow loop at 18 kHz reaches the value of the fast loop we run into instability.

To compensate for this, we implemented additional filters in the slow path of the MC2 locking servo. A 18 kHz notch filter is used to suppress the gain peaking at 18 kHz. An additional 10 kHz first order lowpass is used to allow for a further roll off of the signal at high frequencies. The signal of the slow path was flat above 10 kHz before its implementation. Potential further instabilities were therefore expected. For the measurement shown in figure 5.3 the 10 kHz low pass is already included.

This medium term fix led us strongly increase the laser power circulating in the DRMI in heterodyne lock up to levels of about 6 kW. To further increase the power, the topics discussed in following sections are needed. Foremost, investigations are presented that

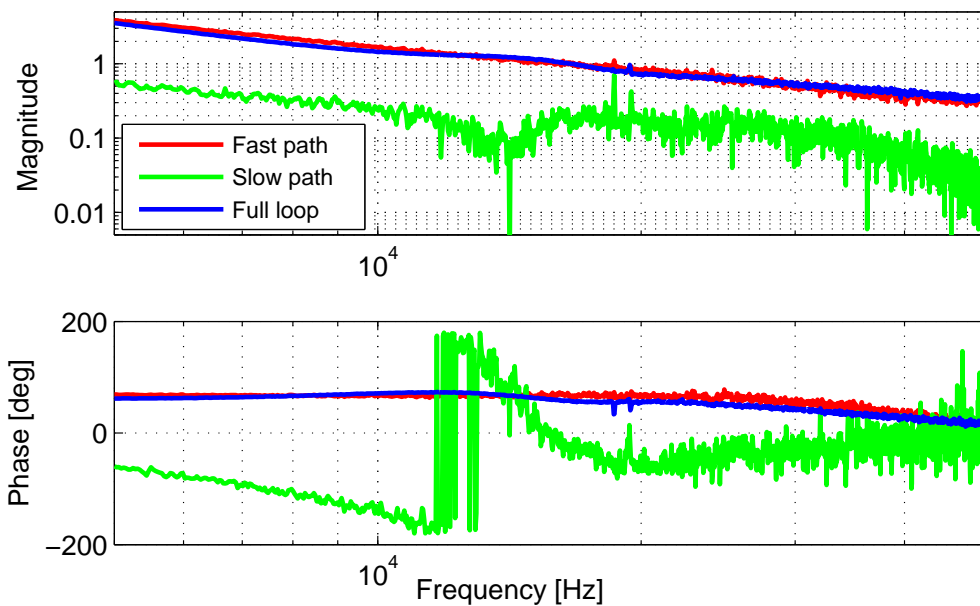


Figure 5.3: An in loop measurement of the MC2 lock that is part of the frequency stabilization loop. It shows the slow path, the fast path and the full loop at frequencies above 5 kHz. Gain peaking at 18 kHz is visible in the slow path. The gain peaking gets stronger if the laser power is increased. Eventually the loop gets instable due to it.

allowed to improve the stability in DC lock.

5.1.4 New frequency stabilization loop electronics

Eventually, we replaced the frequency loop electronics belonging to the MC2 locking part. This replacement was foreseen, but the actual date for the replacement happened earlier than planned. A major initial reason for the replacement is aging electronics. Furthermore, the new model includes the removal of the double gain normalization problem. A gain control for the MC2 lock is moved behind the point where the loop splits. Finally, the new module has a more compact design. It leaves space in the MC electronics rack for another module if needed. Currently, this space is used for a further module that contains the 18 kHz notch filter and the 10 kHz lowpass to compensate for the shown gain peaking. It has plenty space for additional components if need be. Due to the comparable minor changes in the frequency loop electronics of MC2 that were necessary to solve the initial stability issue, the new electronics layout is not given here.

5.2 High power instabilities in the Michelson automatic alignment

In the previous section, a modification of the frequency stabilization loop is described. This modification played an important role in allowing a stable lock of the DRMI at circulating laser powers that are about two times higher than the maximum power level before the IO upgrade. However, a locked DRMI at significantly higher laser power was only possible in heterodyne lock. In DC lock, the stability was not as good as the stability of the heterodyne lock. The search for GWs takes place in DC lock. Thus, studying the reason of the poor stability in DC lock at high power is of high importance. Investigations have shown that instabilities in the tilt degree of freedom in *Michelson interferometer automatic alignment* (MIAA) built up at high power, when GEO was in DC lock. In heterodyne lock, these instabilities do not occur. The following describes this problem and its solution.

In addition, this investigation led to two further facts besides its fix. The decision was made to run the MIAA routinely on CDS to have a higher degree of flexibility and the instability in the MIAA that is described below might be caused by a coupling from the longitudinal degree of freedom to the tilt degree of freedom via the OMC. The latter is only an hypothesis and needs further investigations.

5.2.1 Gain peaking in the MIAA in DC lock

After the modifications in the frequency stabilization loop were done, first experiences in heterodyne lock were obtained at laser power levels up to 6 kW impinging on the BS. Before this, the operation at 4 kW was hardly stable. However, similar attempts in DC lock to operate at comparable laser power levels were not successful. Lock losses were frequent beyond 3.5 kW circulating power and an operation at 4 kW was impossible.

Just before these lock losses at high laser power occurred, strong oscillations in the MIAA error signals, in particular in tilt, were building up and were clearly visible on the corresponding labVIEW control monitors. These oscillations happened at frequencies between 9 Hz and 10 Hz. A non-optimal gain normalization with laser power in the MIAA is a possible explanation, but neither the MIAA rotation nor tilt loop have an UGF there in default operation. Furthermore, these oscillations did not occur in heterodyne lock at any laser power level.

If the gain of the MIAA tilt loop was lowered in DC lock at high laser power, these oscillations could be reduced, but the gain reduction led eventually to oscillations at 3.5 Hz. At this frequency, the phase of the MIAA tilt loop crosses 0° in default operation. Obviously, the gain margin of the tilt loop reduces with increasing laser power in DC lock. Therefore, the loop shape of the MIAA tilt loop was measured at different laser powers in heterodyne and DC lock. Figures 5.4 and 5.5 show the results.

Figure 5.4 shows a measurement of the MIAA tilt loop shape in heterodyne lock for two different laser power levels. These measurements use a swept sine wave injection. It

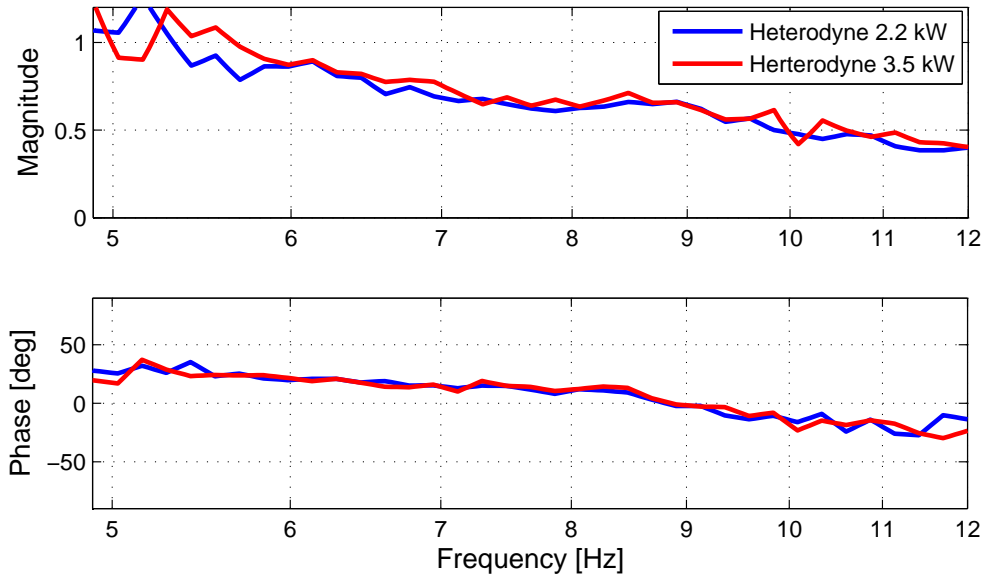


Figure 5.4: A measurement of the MIAA tilt loop in heterodyne lock at two different values for the circulating laser power in the IFO as depicted in the legend. Unlike in DC lock, as shown in figure 5.5, no noticeable problems were expected nor detected. Figure 5.5 shows a similar measurement in DC lock.

only shows the measurement for frequencies above 5 Hz, i.e. where the UGF of the loop is, to 12 Hz. This choice becomes clear if this figure is compared with figure 5.5. However, the loop shape is not affected by the amount of laser power that circulates in the IFO if the IFO is in heterodyne lock.

In DC lock this is different. Figure 5.5 shows a similar measurement of the MIAA tilt loop in DC lock for three different laser power levels. The loop shape could only be measured up to a maximum power of 3 kW and the overall gain of the loop is slightly lowered compared to the measurement in heterodyne lock. Otherwise, the lock could not be maintained when the injected signal crossed the 9 Hz region. Still, this measurement provides enough information to explain the lower stability of the DC lock compared to the heterodyne lock.

As can be seen in figure 5.5, just above 9 Hz, where the phase margin of the loop reaches zero, gain peaking is visible. This gain peaking increases with higher laser power and happens at the same frequency as the oscillation build up in the IFO right before the aforementioned high power, DC lock losses. One can imagine that this gain peaking further increases at higher power and prohibits a loop measurement above 3 kW. More importantly, the measurement has shown that this laser power dependent gain peaking is the reason for the poor stability in DC lock at high laser power. A solution for the power dependent gain peaking is provided below.

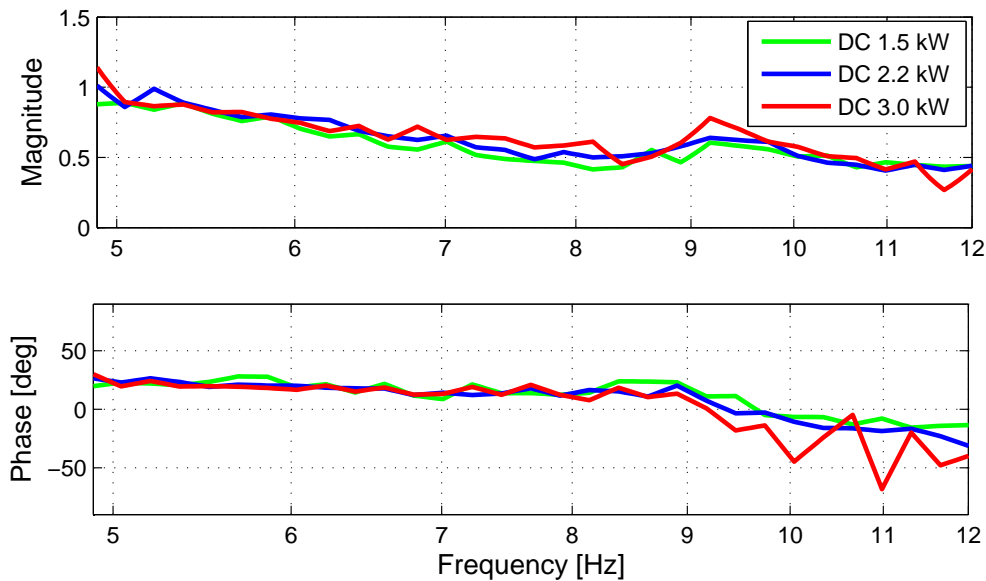


Figure 5.5: A measurement of MIAA tilt loop in DC lock at three circulating laser powers as depicted in the legend. Just above 9 Hz where the phase drops below zero, gain peaking occurs if the circulating laser power is increased.

5.2.2 A possible reason for gain peaking in the MIAA

The reason for the gain peaking to occur in the first place is an open question. However, there is a hypothesis that led to a cure for the gain peaking. At this point this hypothesis is outlined and subsequently described how it directed the way to allow for an increase in DC lock stability at high laser power.

Longitudinal to tilt coupling?

The suspension point of MI mirrors at GEO 600 is not optimally chosen. It is about 7 mm off of the center of mass. Thus, a longitudinal actuation on a mirror causes a small but significant tilting. To compensate for this, the longitudinal feedback signal is filtered and added to the MIAA feedback in tilt. We refer to this as longitudinal to tilt feed forward. The current shape of this filter is shown in figure 5.7 as used for the application at MCN.

The hypothesis with respect to this is as follows: In heterodyne lock, this system seems to work reliably at any laser power. In DC lock, this is different. Two main differences between heterodyne lock and DC lock exist which are needed for this hypothesis. The DC

lock in GEO 600 requires an additional controlled cavity, the OMC.¹ Furthermore, DC operation requires the signal which is detected by the HPD in transmission of the OMC. The MI differential is locked to this signal. If the OMC transmitted power fluctuates, the DFO gets accordingly adjusted by applying longitudinal feedback to the MI mirrors. In addition, part of this feedback is added to the MIAA in tilt by the longitudinal to tilt feed forward. In its initial configuration, the longitudinal to tilt feed forward had non-negligible gain around 9 Hz as shown in figure 5.6. This is the frequency gain peaking in the MIAA happens at high power as shown above in figure 5.5.

It was studied whether the gain of the longitudinal to tilt “feed forward” affects the gain peaking in the MIAA tilt loop. Therefore, similar measurements as shown in figures 5.4 and 5.5 were done. These experiments have shown that the feed forward signal that is added to the MIAA tilt signal for MCN affects the gain peaking. The gain peaking increases if the feed forward gain gets larger and the gain peaking is reduced if the feed forward gain is decreased. It even vanishes if the feed forward is switched off. This result motivated further study of the shape of the MIAA longitudinal to tilt feed forward at MCN. The following shows how a change in the longitudinal to tilt feed forward shape as applied to MCN removed the high power instabilities in the MIAA.

5.2.3 Changing the feed forward loop shape

To remove the gain peaking, a modification to the longitudinal to tilt feed forward at MCN was done. Figure 5.6 shows its initial shape. Note the maximum of the amplitude close to 10 Hz, close to the gain peaking frequency. Figure 5.7 shows the new shape of the longitudinal to tilt feed forward as now applied to MCN. The new shape was realized by replacing a low pass filter with a cutoff frequency of about 9 Hz by a notch filter at about 22 Hz. After this change, an operation of the DRMI in DC lock at a laser power level of more than 4 kW circulating in the IFO was possible. The important aspect of the sensitivity at such high laser power is addressed in chapter 6. A further measurement of the MIAA tilt loop shape in DC lock as previously shown in figure 5.5 was redone at laser power levels of 2.2 kW and 3.5 kW. Figure 5.8 shows the result. The gain peaking is successfully removed. Note that the modification of the longitudinal to tilt feed forward to MCN resulted in a small loss of phase margin. It was traded against a stable operation at high laser power.

One further consequence of the discussed investigation besides the stability improvement at high laser power was to implement the longitudinal to tilt feed forward into the CDS system to increase its flexibility. Further changes of the loop shape, if necessary, are easier to implement.

1 In general, DC operation does not require an OMC but it is beneficial to use an OMC due to various aspects as described in [Pri12].

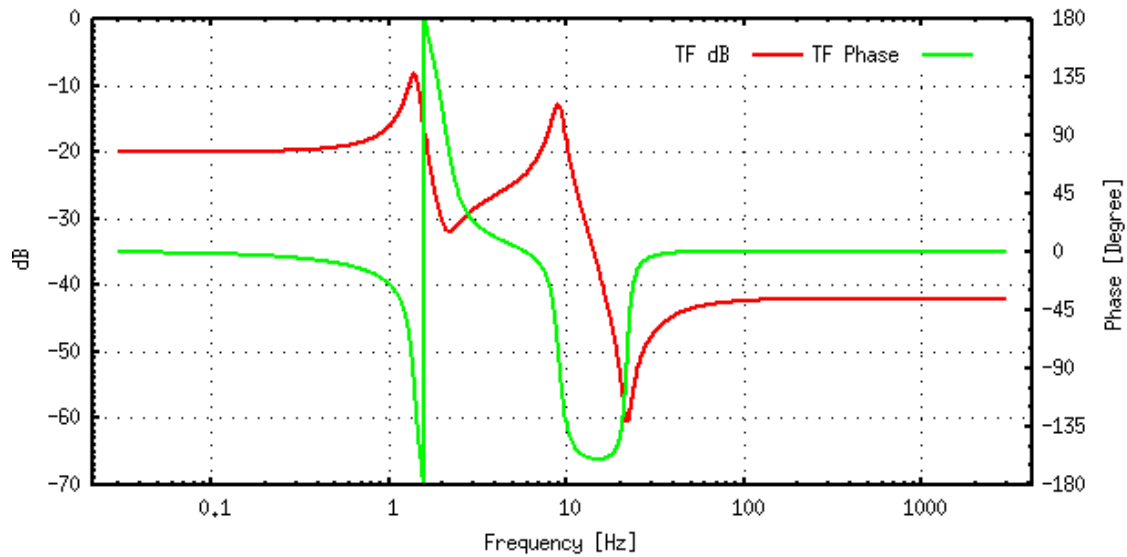


Figure 5.6: The old shape of the MIAA longitudinal to tilt feed forward at MCN.

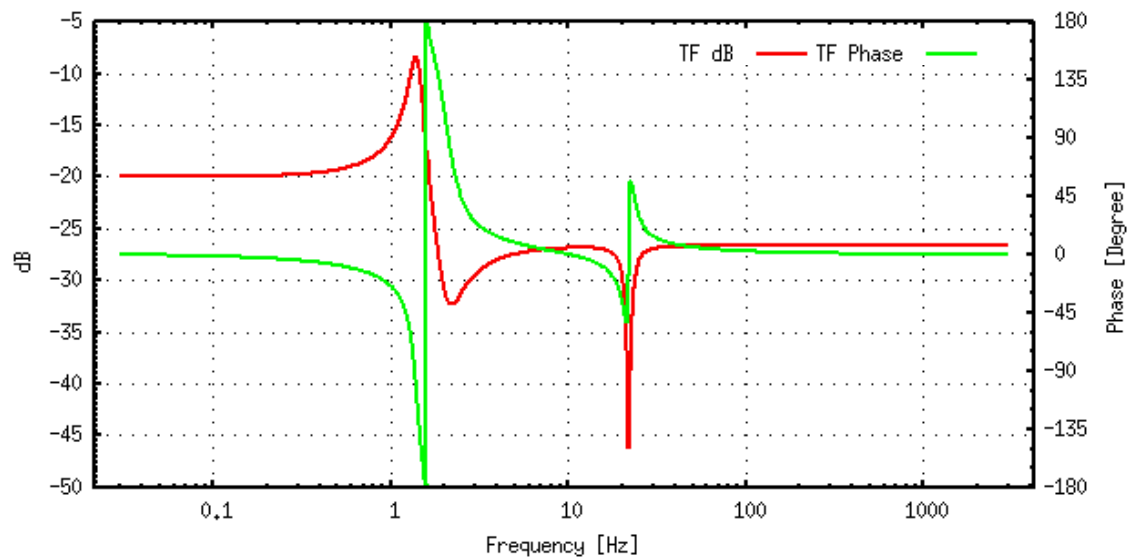


Figure 5.7: The new shape of the MIAA longitudinal to tilt feed forward at MCN.

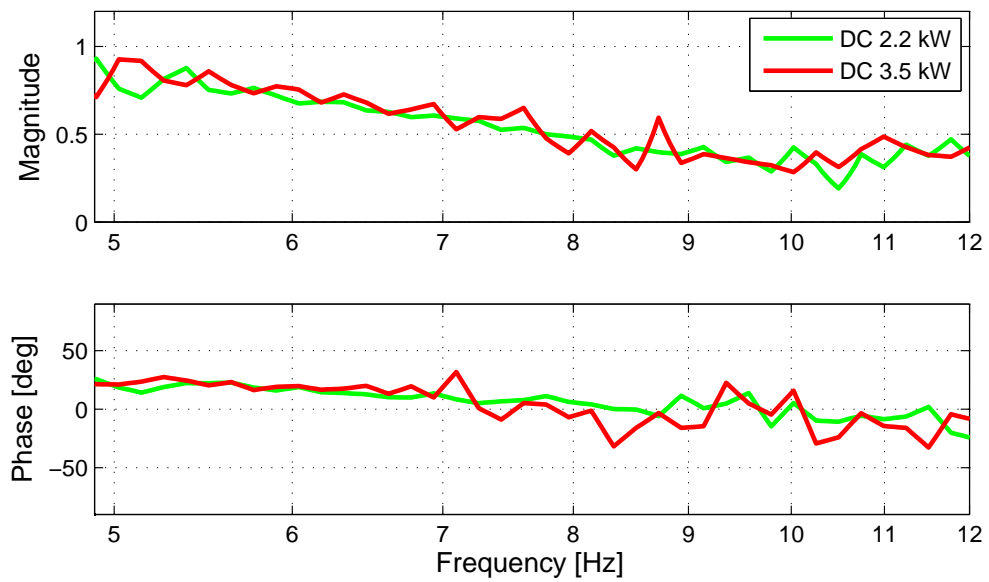


Figure 5.8: A measurement of MIAA tilt loop in DC lock at 2.2 kW and at 3.5 kW impinging on the BS. This measurement was done after the shape of the MIAA longitudinal to tilt feed forward at MCN was changed. The gain peaking is gone.

5.3 Signal-recycling automatic alignment and power up in GEO 600

In this section, the performance of the *signal-recycling automatic alignment* (SRAA) at high laser power is discussed. The operating point of SRAA needs adjustment at different laser power levels. Otherwise, the lock stability decreases and lock instabilities become more frequent.

This section starts by describing the effect of the alignment of the signal-recycling mirror on the circulating laser power. Offsets in rotation and tilt degree of freedom can be used to adjust the operating point of the SRAA. These offsets change in a reproducible way if the laser power is changed. Thus, the optimal operating point of the SRAA changes. This explains the need for changing the offsets at high laser power. Furthermore, this section provides a brief proposal for an automated control of the SRAA operating point that will be beneficial with respect to further power up commissioning work.

5.3.1 The effect of the alignment of the signal-recycling mirror on the circulating power

The error signals for the AA of cavities in GEO 600 are obtained by differential wave front sensing on a *quadrant photo diode* (QPD). Drifts of the beam position on the corresponding QPD are usually centered by automated beam steering mirrors. The SRAA is the only example of an automatic alignment system of a cavity in GEO 600 that does not use automatic beam centering on its QPD. Thus, the beam position on the QPD can drift which leads to offsets in the SRAA.

These offsets have an unwanted influence on the performance of the SRAA. If the beam on the QPD is not centered well, the AA does not hold MSR at the optimal operating point. To compensate for these offsets, digital offsets are added in the corresponding servo. They can be comfortably adjusted via LabVIEW.

At default operation, beam drifts such as those caused by tidal forces, do not significantly influence the performance of the SRAA. An adjustment of the SRAA offsets is only occasionally necessary.

This is different if default operation is interrupted to perform power up experiments. If the circulating power in the IFO is doubled, spot positions show drifts on minute time scales which are of the same magnitude as caused by tidal forces during several hours. Such drifts are most likely caused by thermal lensing effects such as those existing in the BS. However, their origin was not yet investigated in detail.

The focus of this chapter is an increased stability for operation at high laser power. A misaligned SRC is disadvantageous for the stability. This can be seen in figure 5.9. It shows two power normalized spectral densities of the circulating laser power in the PRC while operated with 3.6 kW impinging on the BS for two different MSR alignments.

The blue trace shows the normalized spectral density of the circulating power while the SRAA offsets are chosen to be close to its optimum. The red trace shows the same, except

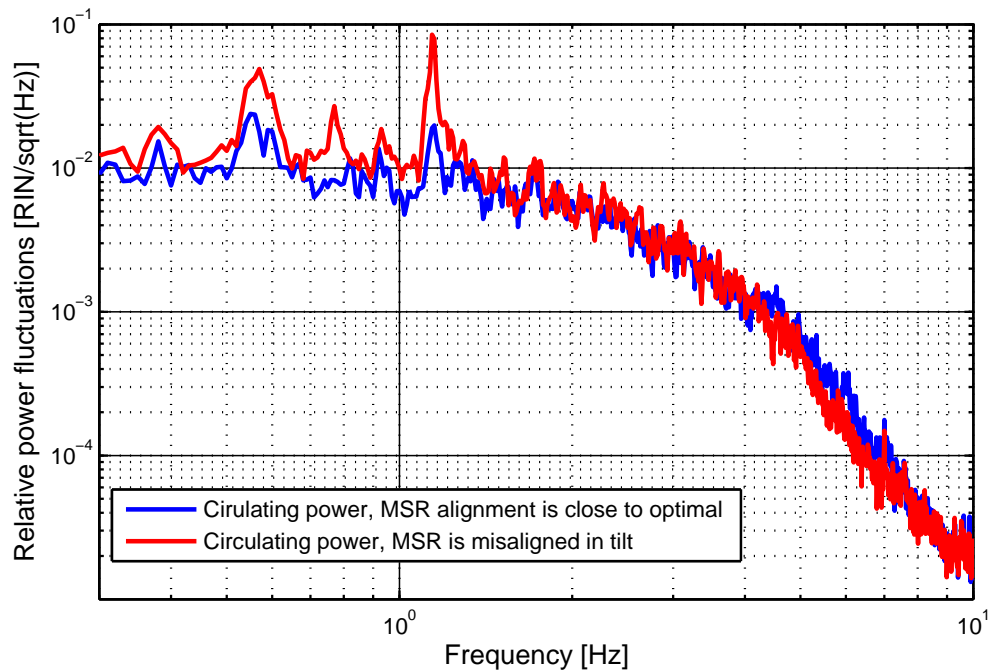


Figure 5.9: The effect of MSR alignment on the amount of fluctuations in the circulating laser power. Two spectral densities of circulating power are compared: close-to-optimal MSR alignment and a state in which MSR is intentionally misaligned in tilt. The effect of a misalignment in rotation is similar as the shown case.

for the fact that the SRAA tilt offset was intentionally set to a wrong value. Therefore, the SRAA does not keep MSR at its optimal operation point. MSR is not ideally adjusted to the axis of the output beam, i.e. it is misaligned.

As can be seen in figure 5.9 the effect on the circulating laser power is as follows. In the well aligned case, which is shown in blue, fluctuations on the circulating laser power are rather small, i.e. like they nominally are. If MSR is misaligned, which is shown in red, stronger fluctuations around 1 Hz exist. In particular, at suspension resonances, i.e. 0.55 Hz and 1.2 Hz for instance, the power fluctuations have a higher amplitude. The seismic conditions on site were comparable during both displayed times. Thus, the influence of the seismic is marginal for the displayed measurement.

A likely explanation for this increase of fluctuations is a reduced mode healing effect. As described in chapter 2.3, the SR cavity partially converts HOMs which are caused for example by mirror imperfections back to the TEM₀₀ mode. Residual movements of the suspended mirrors cause fluctuations around the operating point of the SRAA and thus around the state at which the mode healing effect is optimal. This effect degenerates if MSR is misaligned because residual mirror movements now cause fluctuations around a

non-optimal operating point. The circulating power in the PRC fluctuates more and the average value of the stored light power is decreased. For GEO 600 in its current configuration, it is possible to reduce the circulating laser power by about 10 % by intentionally mis-aligning MSR and still hold the lock of the DRMI. Thereby, the stability of the lock is significantly reduced and the circulating laser power fluctuates a lot. This effect is present for both low power and for high power operation.

5.3.2 SRAA offset adjustment at high laser power

As mentioned before, the SRAA uses digital offsets to compensate for movements of the spot position on the SR QPD. To compensate for spot movements that occur between significantly different operating laser powers, these offsets need adjustment. The need for these adjustments increases with the laser power in a non-linear way, but they are reproducible.¹

To date, these adjustments happen partially automatically. We defined two different states at which LabVIEW sets the necessary offsets. The first state is default operation, i.e. 2.2kW impinging on the BS. The second state is usually defined for a power level of 3.6kW. If a threshold is crossed that lies in between these two power levels, the offsets are changed.

However, in the recent commissioning state with respect to power up, a careful setting of the SRAA offsets is mandatory for power levels that strongly differ from the two states that were mentioned above.

Suggestions for improvement

Future commissioning of GEO 600 will benefit from a reduction or preferably a removal of the dependance of laser power to SRAA offsets. Therefore, the next step would be to implement automatic spot position centering of the beam that impinges on the SR QPD to compensate for drifts. Possibly, this is all that is needed to remove the dependance of laser power to SRAA offsets.

However, if the dependance remains, the implementation of two control loop is conceivable. Such loops could keep the two SRAA offsets in rotation and tilt at their optimal values. An application of the dither technique for the SRAA offsets as is already used for the OMC AA [Pri12] might be a helpful tool with respect to an automated offset control. The DC value of the circulating laser power can be used as an error signal while the MSR alignment is modulated. A different option for the error signal is the relative amount

¹ For instance, if the laser power is increased from 2.2kW to 6 kW, the adjustment of these offsets as set via LabVIEW is as follows: The tilt offset needs to be increased by 30 % to 40 % and the rotation offset needs to be decreased by roughly 25 %.

of fluctuations on the circulating power in a limited frequency band such as around suspension resonances. The (not band pass filtered) relative amount of fluctuations of the circulating power already exists in the LabVIEW system.

5.4 A trivial consequence of the laser power increase: PD saturation

A trivial consequence of the laser power increase is potential saturation of the many PDs used for sensing and control as well as monitoring of the various subsystems. The adjustment of power on these PDs is mostly done such that it is optimal for a defined input laser power level. For example, this means that a high SNR for a corresponding PD signal is obtained as generally desired for the control of cavities. However, for higher laser power, saturation will happen at some point. Therefore, it is useful to have an overview of these PDs and their DC level for a defined detector state.

Two important examples of saturation need to be mentioned at this point. These are the PD that is used for the initial MI lock and automatic alignment of the MI and the HPD, the final detection PD which is used for the MI lock in DC operation.

The power on the PD for the MI lock and automatic alignment increases non-linearly with the laser power if no measures are taken to compensate for the BS thermal lens. As described in section 5.6, it saturates for a dark port power of 800 mW. This level is reached if three times the default laser power is used and the BS thermal lens is not compensated.

Furthermore, the HPD itself saturates if about 4.5 kW are circulating in the DC locked IFO and the DFO is at default. The corresponding electronics of this PD are adjusted such that they are optimal for default operation of GEO 600. For power up experiments in DC lock, the DFO has to be lowered above a power of 4.5 kW. Actually, it is useful to decrease the DFO beforehand such that the light level detected by the HPD corresponds to default operation. This corresponds to about 6 mW impinging on it. The reason for this are occasional oscillations in the MIAA.¹ Such oscillations cause fluctuations in the carrier light power at the dark port. If these fluctuations are strong enough, the IFO loses lock.

¹ A dependence of these oscillations on the circulating power is not likely. They occur at any laser power. In some cases, they are preceded by pronounced seismic event like caused by a passing tractor.

5.5 Power fluctuations at high laser power

In the previous sections of this chapter, several aspects are discussed that allowed an increase of the laser power limit after the IO upgrade. At this point, we take a look at the amount of fluctuations on the circulating power at high laser power compared to low laser power. Figure 5.10 is provided for this purpose. It shows spectral densities of the circulating power for 2 kW, 5 kW and 6 kW. All cases are normalized by their respective DC values. As can be seen, the amount of relative fluctuation increases slightly with the laser power. Note in particular the slight increase of fluctuation around 1 Hz. It indicates non-optimal alignment of MSR as shown in figure 5.9. The higher amount of fluctuations above 3 Hz for the case of the 6 kW reference was not yet studied. Over all, further investigations are needed to reduce fluctuations at such high laser power levels to an amount as present at low and medium power levels, i.e. up to about 4 kW at which the lock is comparable stable as it is at 2 kW.

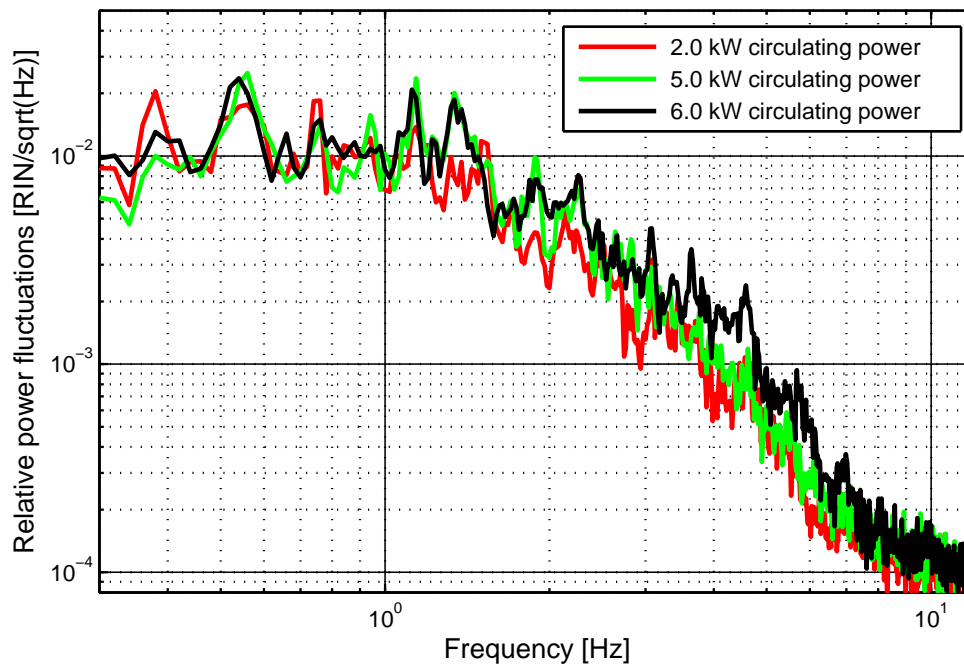


Figure 5.10: Relative intensity noise of the circulating laser power at different laser powers up to 6 kW.

5.6 The thermal lens in the beam splitter

GEO 600 does not use Fabry-Perot cavities in its arms and has a high PR gain of about 850. Thus, the full circulating power in the PRC impinges on the BS. The BS is made of fused silica and has a cylindrical shape. It has a thickness of 8 cm and a diameter of 26 cm. An important feature of the BS material is that it shows very low absorption at 1064 nm. The absorption was measured to be about 0.25 ppm/cm [Hil06]. Newer measurements suggest that the absorption is close to 0.4 ppm/cm as noted in [Wit09]. Due to the high laser power that impinges on the BS a non-negligible amount of light gets absorbed. In addition to the comparably small beam radius of about 1 cm at the BS, a significant thermal lensing effect is present and visible. In [Wit09] this effect is estimated and its impact for GEO-HF laser power levels is studied. There, it was found that the thermal lens has a focal length of about 6 km for a circulating power of 2.7 kW and will be of the order of 1 km for 20 kW.¹

One major consequence of the BS thermal lens is a reduction of the power build-up in the PRC with increasing circulating laser power. This is caused by the mode mismatch of the two arms which in turn is caused by the thermal lens that mostly has an effect on the light in the east arm of the MI. The mode mismatch converts TEM₀₀ into HOMs, in particular into the LG₁₀ mode. These HOMs experience different resonance conditions in the PRC compared to the TEM₀₀ mode due to their different gouy phases. A significant amount leave the IFO via the dark port and contaminate the output beam.

With respect to the laser power increase, the BS thermal lens needs to be compensated. Therefore, the investigations that are described in [Wit09] were followed up by its author and will lead to the installation of a *thermal compensation system* (TCS) for the BS. The installation is being planned at the time this thesis is handed in. This particular TCS will not be discussed in this thesis because it is not part of the described work. However, it will be an important tool to further push the current laser power limit of GEO 600 that was achieved due to the discussed topics in this thesis. A previous design of the TCS and various considerations about it are provided in [Wit09].

In addition to a TCS at the BS, there is another option for compensating for the BS thermal lens [Wit12]. The ROC of the MI folding mirror in the east arm, namely MFE, can be adjusted. A ring heater is placed behind MFE [Lüc04]. This heater is used to partly compensate for a mismatch in the ROC of the MI mirrors by creating a thermal gradient inside of MFE. A further increase of this thermal gradient in MFE can be used to partly compensate for the thermal lensing effect in the BS [Wit12]. However, the MFE ring heater induces a large amount of astigmatism which produces HOMs [Wit14]. To compensate for this astigmatism, heating elements, the so-called side heaters, were installed at MFE. This effort and its reduction of astigmatic effects is discussed in [Wit14].

¹ For this overview, the fact is neglected that different beam waists in the horizontal and vertical direction at the BS need to be considered. [Wit09] uses 1.2 cm for the horizontal direction and 1.0 cm for the vertical direction and an absorption of 0.5 ppm/cm.

The described matter in this section aims at a presentation of the effect that is caused by the thermal lens in the BS and to show how significant its impact is at the achieved laser power levels. First experiences of a partial compensation of the BS thermal lens by using the MFE ring heater is presented in the following section.

5.6.1 Observation of the beam splitter thermal lens

Before the GEO-HF upgrade started, GEO 600 was routinely operated with about 2 kW impinging on the BS. At this power level, the BS thermal lens has a focal length which is close to 10 km. Due to the various aspects that are discussed in this thesis, it is possible to operate GEO 600 at almost three times higher laser power levels without further measures to compensate for the BS thermal lens. However, the effect of the BS thermal lens becomes more and more pronounced the higher the circulating laser power.

A method of observing the thermal lens in the BS is to operate the DRMI at different laser power levels and observe the light power at the dark port while no means are undertaken to compensate for the thermal lens. In particular, the settings of the MFE heaters are such that the dark port power is minimized at default operation, i.e. for 2.2 kW impinging on the BS in DC lock. Figure 5.11 visualizes the effect of the BS thermal lens for power levels between 1.5 kW and 6 kW impinging on the BS. The DRMI is in *heterodyne* lock and no DFO is applied. Three different plots are shown. The plot on top of figure 5.11 shows the power that circulates in the IFO. It is measured by the PD that senses a pick-off beam of the BS AR coating. The other two plots show different representations of the light power at the dark port. The dark port power is measured by the PD that is used as the sensor of the MIAA. It is placed in transmission of BDO1, as described in chapter 2.4. Since no DFO is applied, the dark port beam contains mostly of HOMs and of an insignificant amount of modulation SBs. The plot in the middle shows the dark port power in mW and the plot at the bottom the change of the dark port power normalized by the circulating power in the IFO. The latter is calibrated such that its value is one for default operation, i.e. 2.2 kW laser power impinging on the BS in *DC lock*.¹

For the measurement which is shown figure 5.11, the laser power was increased in four steps. A fifth attempt to further increase the power was undertaken at the end. Eventually, this attempt resulted in a lock loss. Its reason is given further below. At the beginning, the circulating power is 1.5 kW and 28 mW light power are present at the dark port. The relative amount of dark port power is larger than one. Shortly after, the power is increased to about 3.7 kW. This power increase takes roughly 1 min. During this time,

¹ If locked in DC with 2.2 kW circulating power, an additional 6 mW are present at the dark port. The settings of the MFE side heaters and the ring heater are optimized such that the total dark port power is minimized. This minimum is 37 mW for default power [Wit14]. In this configuration, the value of the normalized dark port power is one if displayed like shown in the bottom plot of figure 5.11.

the relative amount of dark port power gets briefly lower than one because the state is crossed for which the MFE heaters settings are optimized.² After the first power up is done, the dark port power needs about 10 min to settle. It settles at 120 mW and the relative power in the dark port is above two. Also note, how the circulating power slightly drops while the dark port power settles. At this point, the necessity for a TCS is already clear.

However, three further power increase steps followed in the experiment that is shown in figure 5.11. Each step shows a similar behavior, while the thermal lens increases with the circulating power. Close to the end, 5.5 kW are impinging on the BS for about five minutes and the relative dark port power reaches a factor of 8 higher value than its minimum is. The total dark port power is 700 mW. This is about 10 % of the light that is sent into the IFO.

At the very end of the experiment, it was attempted to further increase the power, which led to a lock loss. Shortly before the lock loss, 6 kW are impinging on the BS and more than 800 mW of light, mostly HOMs, leave at the dark port. The reason for the lock loss was found. It was due to an instability in the frequency loop as explained in section 5.1. At the time this experiment was done, the new module which belongs to the MC2 lock was not yet implemented and the primary solution was not yet fully optimized.³

But even with a high power compatible frequency loop configuration, higher power levels would not be possible without further modifications. It was found that just above a dark port power of 800 mW, the PD used for the MIAA saturates due to the large amount of HOMs. However, an attenuation of the pick-off beam is not the preferable solution. Instead, a partial compensation of the BS thermal lens by using the MFE heater system was chosen.

Ultimately, the goal will be to fully compensate for the BS thermal lens. The experiment that was just discussed shows the need for such a compensation. While for default operation, just about 30 mW light in HOMs leave the dark port, more than 800 mW of HOM are present for a circulating laser power that is “just” three times higher. All this light is lost with respect to the main purpose of GEO 600, the detection of gravitational waves. This huge amount of junk light can cause a further, more important impact. Even though an OMC is used to filter the dark port beam, HOMs can have an impact on noise in h by coupling to the OMC transmitted power via alignment fluctuations.

2 Actually, the default state is not exactly crossed, because the BS is not in thermal equilibrium within the short moment at which 2.2 kW are impinging on it.

3 A slight increase of the MC2 overall gain would have been most likely sufficient to avoid this lock loss.

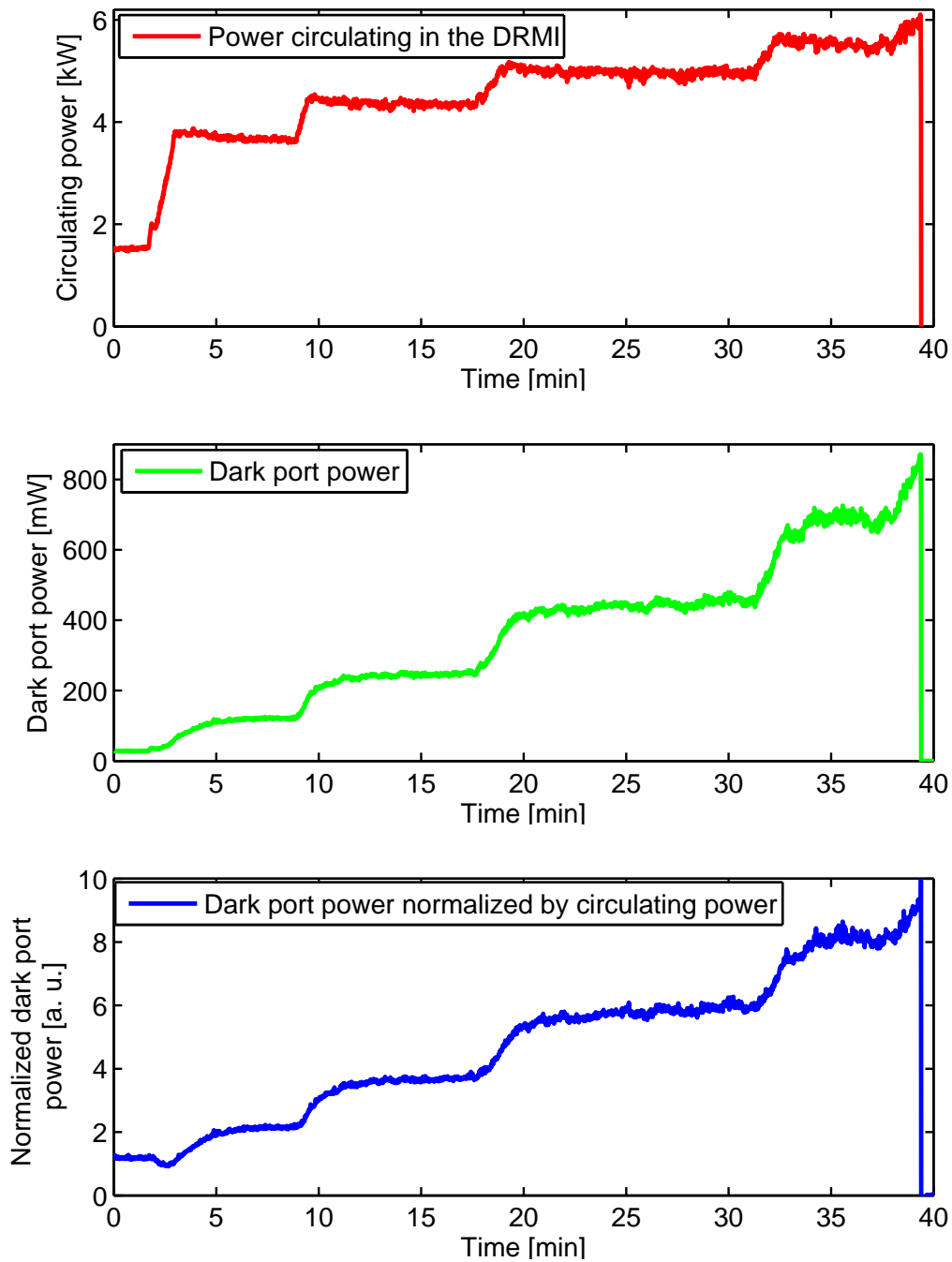


Figure 5.11: The change of the dark port power, caused by the BS thermal lens at different laser power levels. The top plot in this figure shows the laser power circulating in the DRMI. In the middle, the dark port power is displayed in mW. The plot at the bottom of this figure shows the dark port power normalized by the circulating power. The data is calibrated such that the normalized dark port power is 1 in a.u. for operation at default power. All plots show data from the same time while the DRMI was in heterodyne lock until shortly before minute 40 when a lock loss occurred.

5.7 Partial thermal compensation and first indications for a cold locking issue

First experiences were obtained at laser power levels beyond 6 kW circulating in the DRMI in heterodyne lock. To increase the circulating power above 6 kW all power up related measures that are discussed before this point in the thesis at hand are mandatory. In addition, the BS thermal lens needs to be at least partially compensated. The MFE heater system [Wit14, Lüc04] is used for this, because the TCS at the BS was not yet installed. It is expected that further experiments will strongly benefit from the TCS. The following provides preliminary observations while partially compensating for the BS thermal lens with the MFE ring heater. Its application is increasingly necessary at laser power levels above roughly 6 kW.

Additionally, a first indication for an issue is reported which is possibly related to so-called “cold locking”. Cold locking refers to the fact that obstacles occur if the lock is tried to acquire while components are not in thermal equilibrium. This can either be due to a thermal lens itself which did not fully decay or a thermal lens which did already decay but a thermal compensation system is set to high power operation.

5.7.1 Laser power increase with a partially compensated thermal lens

To partially compensate for the thermal lens in the BS at higher laser power levels, the MFE ring heater can be used [Wit12]. By applying a higher heating power, the thermal gradient in MFE is increased and thus its ROC is lowered. Therefore, the amount of light that gets converted into the LG₁₀ is decreased for an operation at higher laser power levels.

Figure 5.12 displays the effect of an increased power of the MFE ring heater on the amount of HOMs at the dark port. In the upper plot of this figure, the circulating power in the PRMI is shown while it is in DC lock. The bottom plot shows the relative amount of light at the dark port at the same time. The experiment is the same as that shown in figure 5.11 except for the fact that the MFE ring heater setting is optimized for an operation at high laser power, i.e. 3.7 kW for this example.

At the beginning of the displayed time, about 1.5 kW are circulating in the DRMI. Subsequently, the laser power was increased in four steps. After the second step a power level of 3.7 kW is reached for which the ring heater setting is optimized. (The ring heater setting was changed about half an hour before the time at which this plot starts. Half an hour corresponds approximately to the time constant of this system.) In this state, the light power at the dark port is only 74 mW instead of 120 mW as shown in figure 5.11 for a comparable power level and no partial thermal compensation.¹ A further reduction of

¹ Note that 6 mW of the 74 mW is carrier light due to DC operation. One would expect about 10 mW of carrier light in DC lock at that power. However, the DFO was reduced for this experiment to increase the stability for reasons that were explained in section 5.6.

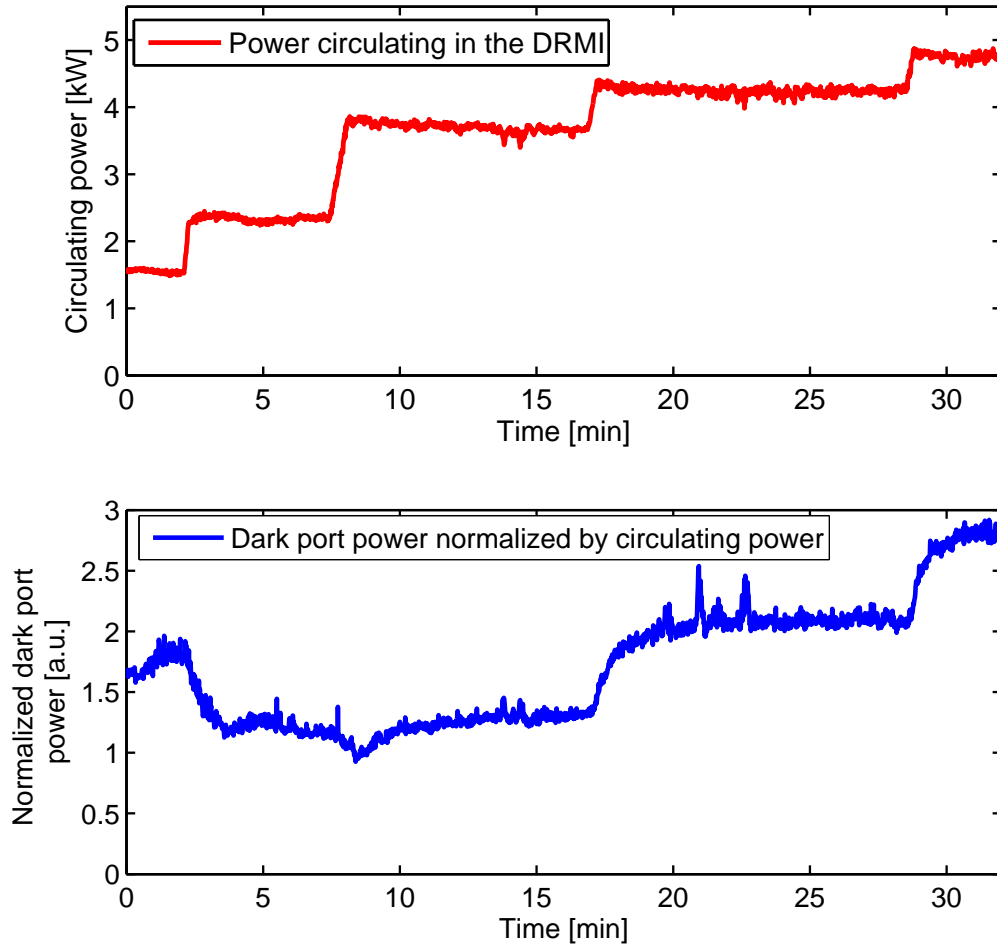


Figure 5.12: Reduction of the dark port power by partially compensating for the BS thermal lens with help of the MFE ring heater. The upper plots shows the circulating power in the PRMI that is locked in DC. The bottom plot shows the relative dark port power as defined in the previous section. The ring heater is set to a setting that was found close to optimal for a circulating power of 3.7 kW. At this power the relative dark port power is reduced by a factor of roughly 1.75. To be compared with figure 5.11.

this power by the use of the MFE side heaters to compensate for astigmatism is likely possible considering the results that are provided in [Wit14]. Furthermore, it is visible that the relative dark port power does still slightly increase within the first few minutes in which this laser power level is set. A closer look even shows that after 3.7 kW is reached, the relative dark port power decreases for about 30 seconds and then increases again. This indicates that further optimization is feasible.

After reaching with 3.7 kW circulating power, the laser power is increased in two additional steps. The relative dark port power increases as one would expect. However, due to partial compensation of the BS thermal lens, the dark port power is significantly smaller than that shown in the previous section. At the end of the displayed time in figure 5.12, a power of almost 5 kW circulates in the PRC and the relative dark port power reaches a value of 3. At a comparable power level without partial thermal compensation, this value is 2 times larger, as shown in figure 5.11.

The significant reduction of the amount of HOMs at the dark port due to the partial thermal compensation has an obvious side effect. A saturation of the PD that is used for the MI RF lock and MIAA will happen with a partial thermal compensation as shown above at higher power levels. Therefore, first experiences could be obtained while the DRMI was locked for several ten minutes with almost 7 kW impinging on the BS. If we assume not partial but optimal thermal compensation as planned for in the near future, this PD will not saturate until the IFO is operated with 40 kW circulating power.

5.7.2 First indications for cold locking issues

We made first observations that show obstacles if trying to re-lock after a lock loss at high laser power. In particular, this was observed if the MFE ring heater was used prior to the lock loss to partially compensate for the BS thermal lens at a high laser power level. These observed difficulties of re-locking can be separated into two aspects.

The first aspect is obvious, considering the fact that locking is only possible if the ROC of MFE is adapted as described in [Lüc04]. If the MFE ring heater power is increased for a power up experiment, the ROC of MFE differs from the default value. If the lock is not quickly restored, the BS thermal lens decays and thus the ROC mismatch in the MI arms increases. This results in an unfavorable effect on the longitudinal control signal [Lüc04]. The BS thermal lens and the heater induced MFE ROC time constants are different from each other. The time constant of the BS is much smaller. Therefore, it is at times necessary to wait for MFE to cool down for a time. This is one example why the TCS at the BS will have advantages.

The second aspect that we observe when the MFE ring heater power is increased for a power up experiment happens during the lock acquisition of the OMC.¹ Usually, if the OMC is locked on the carrier and the alignment of the output beam onto the OMC is optimal, the HPD detects 6 mW carrier light.

In the case of lock acquisition while the MFE ring heater power is increased and the BS thermal lens did already decay, the HPD detects significantly less power. For instance, if

¹ Currently, the lock acquisition for DC lock is as follows, if the input mode cleaners are already locked: The DRMI locks at low laser power, i.e. 1.5 kW, in heterodyne with no DFO induced. Slightly later, the laser power is increased to the chosen value. Then, the DFO is applied and within the next minute, the OMC gets locked on the carrier light. Thus, the mode cleaned output beam hits the HPD from now on.

the heater setting is optimized for an operation at 3.7 kW, the ROC of MFE is reduced and roughly half the expected amount of carrier light hits the HPD. We found that this is not due to mis-alignment of the output beam onto the OMC. By changing the applied DFO in small steps in this state, the dark port power changes as if the an offset is on top of the DFO. Except for this DFO “offset”, the shape of the carrier light as a function of actually applied DFO looks like it usually does. To minimize the carrier light, the DFO has to be set to a negative value for instance. It appears that this effect is caused due to the mis-match of the two light fields in the MI arms.

Furthermore, if we observe the dark port power in this state, while the BS thermal lens builds up, the detected power on the HPD reaches its nominal value within the next ten minutes. This is approximately the time constant of the BS thermal lens. While it builds up, the mis-match of the light fields in the two MI arms is minimized again.

Finesse simulations reproduce this experimental result and show that this effect increases with decreasing ROC of MFE, as needed for higher laser power. For the described case, the lock acquisition of the OMC is not significantly disturbed if the BS lens has already partly built up. However, it can be foreseen that the lock acquisition will be increasingly affected the more the ROC of MFE is reduced. Thus, measures need to be taken as long as the BS thermal lens is compensated with the ring heater. An easy approach is to wait for the BS thermal lens to build up since this takes only several minutes after the needed laser power level is reached. To avoid waiting for a few minutes, a more sophisticated approach would be needed, such as pre-heating the BS. Ultimately, once the TCS at the BS is installed, such measures will likely not be necessary.

5.8 The current limit and how to beat it

The topics discussed in this chapter as well as in chapter 3 are the reasons why GEO 600 can be operated at significantly higher laser power limits than before the GEO-HF upgrade started.

Figure 5.13 shows the laser power circulating in the DRMI which was locked in heterodyne during quick power up. It was performed in a fast way to partially avoid the effect of the BS thermal lens and to not be dependent on the MFE heaters. The power is increased and reaches 6 kW after two minutes. The BS thermal lens starts to build up and the aforementioned offsets of the MSR alignment need adjustment. Thus the value for the circulating laser power does not stay constant within the next minute. The MSR offsets are quickly adjusted between 2.5 min and 3 min. Its effect is not clear in this figure. From minute three on, the laser power is further increased to 8 kW until an instability occurs and the lock gets lost short before 4 min are over. The lock loss is most likely caused by a saturation on the PD for the MI lock. Just when the PD ran into saturation, the lock loss occurred. However, figure 5.13 shows the highest laser power that was ever stored in the PRC of GEO 600. The previous sections of this chapter explained how such high laser power levels became possible and suggestions are made for further improvements.

As mentioned before, the process of extending the current laser power limit will benefit from the installation of the TCS at the BS. The effect of the BS thermal lens is shown in this chapter. An example for its successful partial compensation is provided, too. The BS thermal lens is the prime example for foreseen difficulties with respect to a laser power increase. Besides thermal lensing issues, this chapter illustrates other solvable tasks

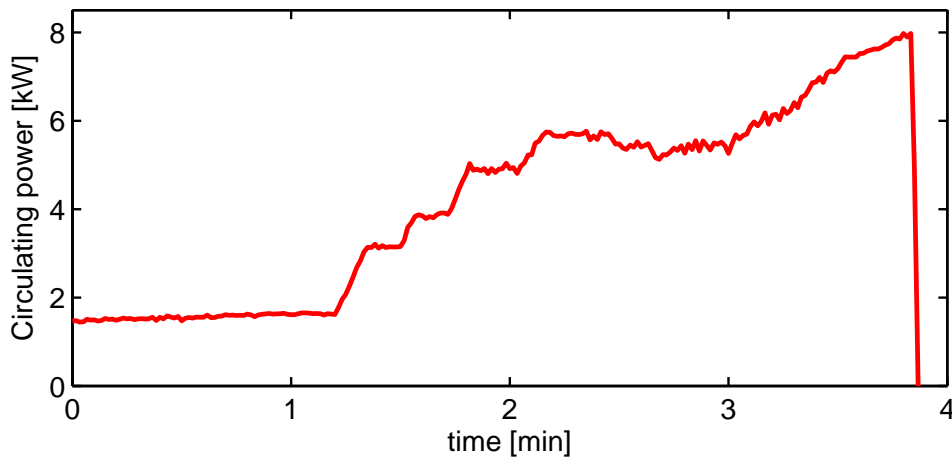


Figure 5.13: Circulating laser power in the PRMI in heterodyne lock during a fast power up experiment. This plot shows the highest laser power level that was to date impinging on the BS: 8 kW.

which will be needed in the future to further increase the laser power. One example is an optimization of the SRAA at high laser power. Also simple steps like further attenuation of pick-off beams will be necessary. Other obstacles can not yet be foreseen. However, I am convinced that the previously used approach to extend the current laser power limit will be profitable in the future: Increase the laser power until the IFO runs into an instability. Study the reason of this instability and subsequently find a solution and implement it.

However, the most important aspect needs to be addressed with respect to the laser power increase. This is the sensitivity at high circulating power in the PRC. The following chapter is dedicated to it.

6 The sensitivity of GEO 600 at high laser power

In the previous chapter, several achievements are described that allowed for a more stable operation of GEO 600 at high laser power. Furthermore, the current laser power limit is displayed and suggestions are made to further extend this limit. Thereby, the focus is set on stability issues while the aspect of the sensitivity of GEO 600 is mostly neglected.

The chapter at hand catches up with the sensitivity aspect at high laser power. Emphasis is set to a laser power dependent noise at medium frequencies, i.e. at about 100 Hz to 1 kHz. This noise became first evident after a reduction of other noises at these medium frequencies and after the increase of available laser power due to the installation of the new laser.

In the following, we will describe how the noise at medium frequencies manifests itself. Furthermore, experiments are depicted that were carried out to investigate the origin of this noise. At this point it must be clarified that, to date the origin or *origins* of this noise could not be discovered. The investigations that are listed below can be used as a guideline of what potential origins of the noise at medium frequencies were excluded so far. In addition, suggestions are made for which direction further research could be directed to understand and eliminate the discussed noise.

Ultimately, the laser power dependent noise at medium frequencies is the major reason for not routinely operating GEO 600 with significantly higher laser power. While for a higher laser power operation of the IFO the shot noise is reduced as expected, the simultaneous increase of noise at medium frequencies negates this improvement. To really benefit from a stable operation at high laser power, the open question of the laser power dependent noise at medium frequencies needs to be addressed and answered.

6.1 Laser power dependent noise at medium frequencies

Figure 3.21 in chapter 3.3.7 shows the sensitivity of GEO 600 for two different laser power levels after the installation of modulation drives at several suspension local controls. These installations allowed for a stable operation of GEO 600 at significantly higher laser power. At that time, there was no negative effect of high power operation visible. The sensitivity improved as expected when the laser power was increased.

However, the frequency range from roughly 100 Hz to several 100 Hz was strongly contaminated by a noise we used to call “200 Hz forest”. In chapter 3.4, a brief description of the 200 Hz forest and its removal is given. A more detailed explanation can be found in [Pri12]. The removal of the 200 Hz forest as well as other and less pronounced features at frequencies up to 1 kHz allowed for a clearer view on underlying noises. At the same time, the amount of available laser power increased due to the installation of the new laser system that is described in chapter 4.1.

These prior two improvements exposed an underlying noise in the medium frequency range, i.e. at frequencies from about 100 Hz to 1 kHz. This noise manifests itself to be dependent on the laser power. Its level grows while the power increases. In the following, this noise will simply be referred to as “mid-frequency noise”. One can assume that the mid-frequency noise is not restricted to medium frequencies. But at different frequencies other noises simply dominate the sensitivity. Particularly, the major limiting noises at low frequencies are feedback noise of the MIAA as well as SR feedback noise and at high frequencies it is shot noise. There are also various lines and relatively narrow band structures in the few hundred Hz regime. We will not be concerned here with these structures but instead focus on the broad noise floor that is visible between these structures.

Figure 6.1 shows typical sensitivities of GEO 600 at different laser powers up to 3.5 kW impinging on the BS. A value of 3.5 kW corresponds to the maximum laser power that was considered safe after the new laser was installed but *before* the upgrade of the input optics was completed. As mentioned before, the laser power dependent noise at medium frequencies was observed first during that time. Therefore, we start this discussion with sensitivity data as given in figure 6.1 from that time.

First of all, the benefit of operation at higher power can be seen in figure 6.1. The sensitivity is shot noise limited above several hundred Hz. Thus, it improves with the square root of the power at high frequencies. Further below a more detailed look at the sensitivity at high frequencies is provided. But at medium frequencies, the sensitivity gets worse if higher laser power is used.

Besides its dependance on laser power, a further characteristic of the mid-frequency noise is recognizable in figure 6.1. It seems to have a $1/f$ shape. The $1/f$ shape becomes more apparent the higher the circulating power in the IFO is. This means, with increasing power it dominates the sensitivity more at medium frequencies. Thereby, the frequency at which the sensitivity is best gets shifted to higher frequencies as well as the minimum frequency at which the sensitivity is dominated by shot noise.

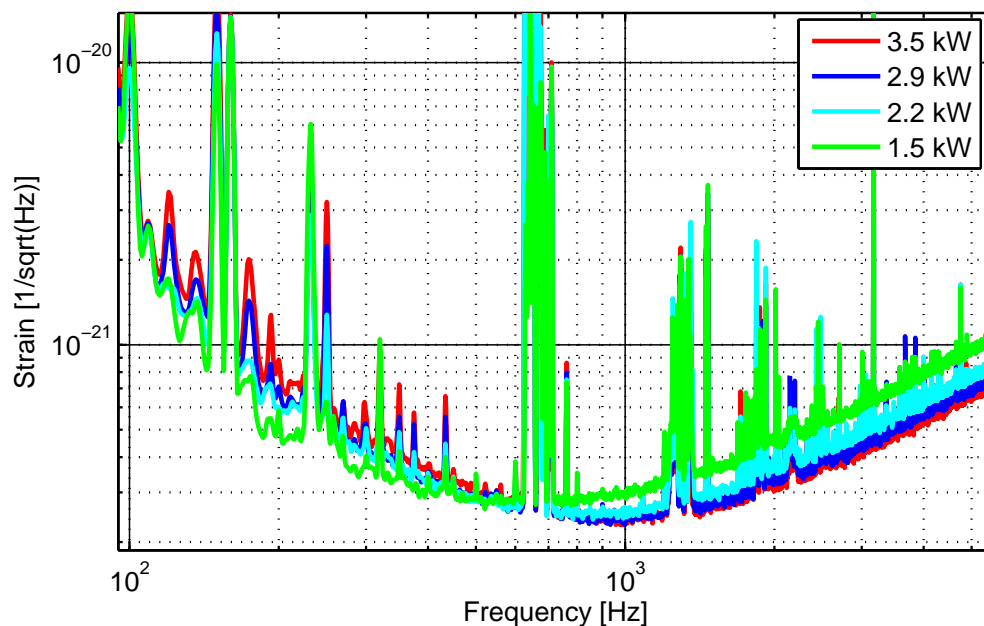


Figure 6.1: Typical sensitivities of GEO 600 in the first half of 2012 at different laser powers impinging on the BS as given in the legend. At high frequencies, the sensitivity improves as expected if more laser power is used. In turn, the sensitivity decreases at medium frequencies. This is the effect we call “mid-frequency noise”.

6.1.1 A closer look into the mid-frequency noise

Let us have a more detailed look into the mid-frequency noise. Figure 6.2 is provided for this purpose. It shows typical sensitivities of GEO 600 at different laser powers up to 4.8 kW impinging on the BS. Note that the DFO needs to be reduced at such high laser power.¹ By comparing figure 6.1 and figure 6.2 one can obtain a better impression of the

¹ The dark fringe offset is independent of the laser power at which the IFO is operated at. However, the power on the detection PD increases proportional with the power in the IFO if the DFO is kept constant. Thus, more optical LO light is present at the dark port and the detection PD saturates at some point. In the current configuration, this happens if the circulating laser power in the DRMI is in the order of 4.5 kW. In addition, occasionally occurring fluctuations which are caused by instabilities in the MIAA and which are independent from the laser power cause fluctuations of the carrier light at the dark port. Brief saturation on the detection PD can happen if the DFO is too high. Eventually, this results in a lock loss. A sufficient reduction of the DFO at higher power prevents these lock losses.

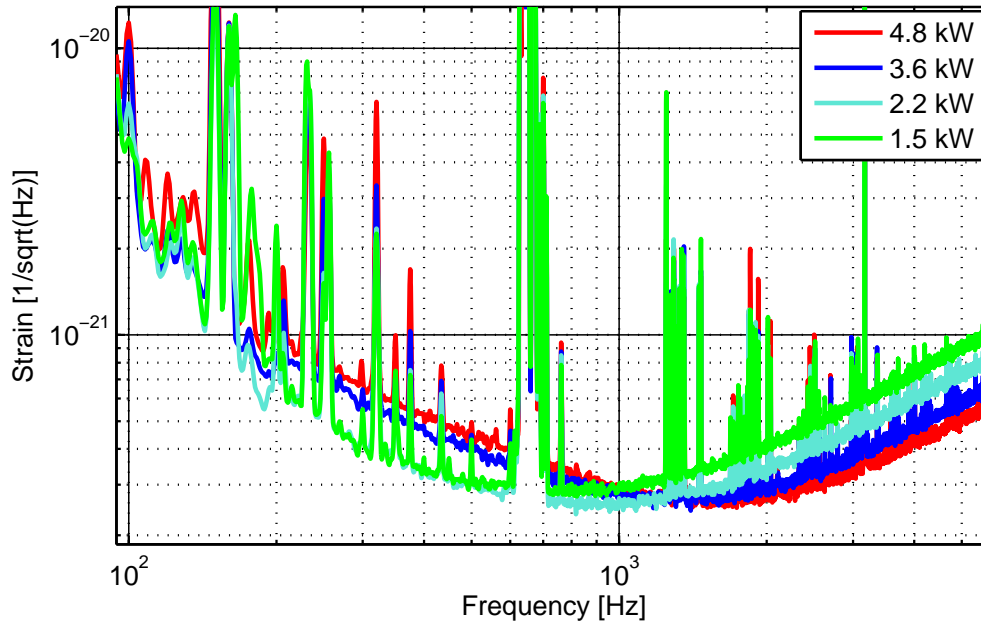


Figure 6.2: Typical sensitivities of GEO 600 in the second half of 2013 at different laser powers impinging on the BS as given in the legend. The laser power dependent increase of noise at medium frequencies is still obvious as it was in figure 6.1. Due to the completed upgrade of the IOs more laser power became available. One sensitivity here results from using a much higher laser power than what was shown in the previous figure. This figure is also shown in comparison to demonstrate that the mid-frequency noise is not always at the same level.

characteristics of the mid-frequency noise.

The tendency that the mid-frequency noise increases with the laser power is clearly visible in both plots. In addition, the $1/f$ like shape is more obvious and gets stressed by the 4.8 kW reference that is shown in figure 6.2. Also note, that the mid-frequency noise does not necessarily increase proportionally with the laser power. In figure 6.1, the noise level at medium frequencies is almost identical for 2.2 kW and 2.9 kW while in figure 6.2 the same statement is true for the references at 1.5 kW and 2.1 kW. It appears that the mid-frequency noise is not stationary.

6.1.2 The reason for not routinely using higher laser power

The laser power dependent noise at medium frequencies is the major reason for not routinely operating GEO 600 at significantly higher laser power. Any improvement of the

sensitivity at high frequencies due to higher laser power is overshadowed by the simultaneously rising mid-frequency noise. As long as the mid-frequency noise issue is neither solved nor even fully understood we will not routinely run GEO 600 at the power levels made capable by the work in this thesis. Instead, we will use a power level which maximizes the astrophysical use of GEO 600. This is the case for a circulating power that is between 2 kW and 2.5 kW. At such laser power levels, the mid-frequency noise is not too pronounced.

A low level of noise at medium frequencies is desirable because more astrophysical sources for GWs are expected at lower frequencies. The latter aspect is briefly discussed in chapter 3.4 with respect to the VIRGO GEO 600 science run in 2011.

6.1.3 The sensitivity at high frequencies

Before the mid-frequency noise will be further discussed, the obvious advantage of operating an interferometric GW detector at high laser power is shown at this point. Figure 6.3 is provided for this purpose. It shows three spectral ratios of the GEO 600 sensitivity

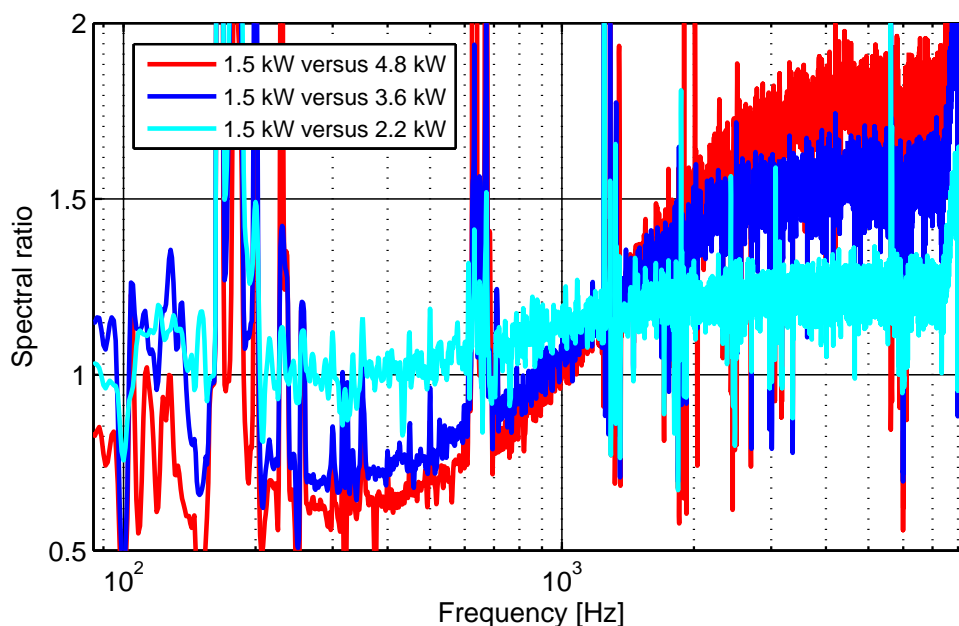


Figure 6.3: Spectral ratios of the sensitivity at three different power levels compared to low power as shown in the legend. The expected sensitivity improvements are 1.21, 1.55 and 1.79, respectively.

at different circulating laser powers compared to a level of 1.5 kW as labeled in its legend. This figure uses the same data as figure 6.2 does. As can be seen, the improvement of the sensitivity at high frequencies in the three cases matches well with the square root of the corresponding circulating power ratio. With respect to a further extension of the current laser power limit, this is good news because no unexpected noises seem to limit the shot noise limited region so far. In Addition, this is good news with respect to the routine use of squeezing. Because GEO 600 is shot noise limited at high frequencies, squeezing can also be used to decrease the shot noise level if high laser power is used. Occasionally, the IFO is operated with 3.6 kW circulating power over nights or weekends to observe aspects like stability for instance. Generally, squeezing is additionally applied during these times and shows a comparable shot noise reduction as it does at default power.

However, the mid-frequency noise has an increasing effect on the shot noise dominated region, i.e. it diminishes this region. At low laser power, GEO 600 is shot noise limited above 600 Hz. The green trace in figure 6.3 stresses this since an sensitivity improvement is visible above 600 Hz. For higher laser powers, the mid-frequency noise starts to dominate more. By displaying spectral ratios, this effect gets further stressed. The following will present a summary of investigations that were carried out so far. The ultimate goal of follow up research will be to understand and remove the laser power dependent mid-frequency noise such that the sensitivity stays constant below 600 Hz if the power is increased.

6.2 A summary of mid-frequency noise investigations

Several possible origins of the laser power dependent noise at medium frequencies were investigated so far. One main result is that some of these potential candidates can be excluded as a cause of the mid-frequency noise. Other investigations are still in an early stage and did not lead to clear results. A summary of these initial experiments is given below. The summary can be used as an overview and a guideline for further investigations. It might help to decide, in which direction future work should be directed.

6.2.1 A first step

After the existence of the mid-frequency noise became clear, it was investigated if obvious differences in length and alignment sensing and control channels of GEO 600 occur at different laser power levels. Therefore, all those channels were searched to check if a direct effect on power dependent noise at medium frequencies is detectable. None of these signals shows a comparable change at different laser powers to the one observed in the sensitivity. This effort was repeated after the IO upgrade when operation at higher laser power levels than 3.5 kW became possible. Again, no noteworthy effects were observed. Thus, we exclude a direct coupling from any of these cases.

6.2.2 Saturation effects

The performance of a control loop can be disturbed if a saturation is existent on a PD that is used as sensor for the loop. Furthermore, a saturation can occur throughout the whole electronic chain of the loop. The following lists examples, for which saturation effects are possible. The listed examples were investigated as a possible cause of the mid-frequency noise. Subsequently, some of these examples could be excluded as its origin. For other examples, an influence on the mid-frequency noise seems unlikely but further investigation might be useful.

Attenuation of pickup beams

To exclude PD saturation as the cause for the mid-frequency noise, the corresponding pick-off beams to PDs that seem to be likely candidates were attenuated and the influence to the noise level at medium frequencies was investigated. These pick-off beams belong to the in-loop PD of the second power stabilization loop, the PD that belongs to the PR control and the PD that belongs to the SR control. To check for an influence on the mid-frequency noise, the laser power was toggled multiple times in DC lock while these PD pick-off beams were attenuated. The sensitivity at different power levels was subsequently compared to the case of non extra pick-off beam attenuation. For all three

cases, the attenuation did not show an effect on the mid-frequency noise. Thus, saturation in the corresponding loops can be excluded as cause of the mid-frequency noise.

However, one should consider saturation effects for further investigations. If a saturation occurs, it can lead to falsified results. In particular, if the in-loop PD of the second power stabilization loop runs into saturation, laser amplitude noise increases and shows a similar shape as the mid-frequency noise.

Influence of the DFO

Initial investigations were carried out to examine if the size of the DFO influences the mid-frequency noise. In particular, these investigations seem to make sense with respect to saturation on the HPD. As mentioned before, such saturation occurs occasionally due to fluctuations on the dark port power that are caused by the before mentioned instabilities in the MIAA. These MIAA instabilities seem to occur independent of the used laser power level, but if they have an influence on the mid-frequency noise, this influence would grow with increasing average power on the HPD.

For these experiments, the DFO was set to different values at a given operational laser power and the sensitivity was compared in dependence of the DFO. This experiment was repeated at different laser powers. However, the noise at medium frequencies seems to show no influence on the DFO. An influence of the the DFO on the discussed noise seems unlikely by now. However, it is worthwhile to check again for an influence of the DFO as soon as DC lock at higher laser powers becomes possible.

ESD bias

The *electrostatic drives* (ESD) are the main displacement actuator of the MI and are explained in detail in [Gro03]. The ESDs are used to apply fast feedback on the mirror level via an electrical force between the MI mirror and a suspended reaction mass. Electrodes are attached on the reaction masses and the far MI mirrors for this purpose. The electrical force consists of a high DC voltage (the bias) and the high frequency part of the actual MI feedback which bandwidth overlaps with the mid-frequencies in h. The strength of the applied electrical force depends on the the distance between the reaction mass and the corresponding mirror while the distance can be changed by the bias value.

To check for a connection connection between the fast MI feedback and mid-frequency noise, the ESD bias was toggled while the applied MI feedback force was kept constant via its gain. Again, no influence on the mid-frequency noise was detected.

MI SB reduction

The amplitude of the MI SBs increases as the laser power does. To check for (RF) saturation effects the amplitude of the MI SBs was reduced up to a factor of three. Thus the power in the SBs was decreased by a factor of nine. No effect on the mid-frequency noise was observed during these experiments.

6.2.3 Influence of the LG₁₀ mode in the output beam

At an early stage of the mid-frequency investigation it was studied if the amount of LG₁₀ light at the output port influences the noise at medium frequencies. As was shown in chapter 5, the light power in the output beam increases more than linearly with the circulating power in the IFO as long as no measures are taken to compensate for the thermal lens in the BS. The thermal lens in the BS mostly affects the LG₁₀ mode. The LG₁₀ eventually leaves via the dark port and contaminates the output beam. Even though the OMC is designed to strongly attenuate such unwanted light fields at the dark port before detection [Pri12], it was considered worthwhile to exclude an influence of the LG₁₀.

The investigation which is described in the following only aimed at investigating an influence of the LG₁₀ mode. It must be clarified at this point that an effect of HOMs in general on the mid-frequency noise is neither shown nor disproved. In [Pri12], a detailed analysis of the HOM content in the output beam is given.

At the time this investigation took place, the MFE side heaters and the reflector for the MFE ring heater [Wit14] were not installed. Thus, the BS thermal lens could not be compensated for at laser power levels above approximately 2 kW. Instead, we determined the relative amount of LG₁₀ light at the output port in dependence of the circulating power. “Relative amount” refers to the fact that the power in the LG₁₀ mode is divided by the current circulating power. For this experiment, GEO was in heterodyne lock with no DFO and the OMC was used as a diagnostic device to analyze the mode content at the dark port. Table 6.1 summarizes the results. It was found that the relative amount of LG₁₀ light at the output port is lowest at a circulating power of 2.2 kW. It gets more

Circulating laser power [kW]	1.5	2.2	2.9	3.2
Relative power of the LG ₁₀ mode [a.u.]	0.66 ± 0.05	0.57 ± 0.03	0.74 ± 0.04	0.76 ± 0.04

Table 6.1: Relative power in the LG₁₀ mode at the dark port for different circulating powers in the DRMI.

for higher *and* more for smaller circulating power.¹ In DC lock, which uses a small DFO, the relative amount of the LG₁₀ mode will not differ significantly. If the LG₁₀ mode would influence the mid-frequency noise, the noise would not get less at low power such as 1.5 kW impinging on the BS.

To further stabilize this statement, a second type of experiment was performed. For it, GEO was operated at a laser power of about 2 kW. In addition, the heater power was lowered to get a similar to slightly higher relative amount of LG₁₀ light at the output port as is typical at a power of about 3 kW impinging on the BS. Still, no effect on the mid-frequency noise was detectable. Thus, the mid-frequency noise seems not to be affected by the amount of LG₁₀ light at the output port or inside the DRMI. Further investigations which only concentrate on the LG₁₀ mode is probably not needed.

Since this experiment happened, the aforementioned MFE side heaters and the reflector for the MFE ring heater have been installed. The additional installed reflector for the ring heater allows for compensating the BS thermal lens for higher laser power levels while the side heaters allow for a reduction of astigmatism [Wit14]. Preliminary observations when using this system to minimize the dark port power in DC lock at high laser power do not show an effect on mid-frequency noise. However, the whole MFE heater system was not yet used for thermal compensation at high laser power in an optimized way, i.e. to reduce the relative dark port power to values as present at default power operation. Furthermore, a thermal compensation system at the BS is just in the process of being installed while this thesis is handed in. If the systems are used to efficiently compensate for the BS thermal lens, it will be worthwhile to do further investigations.

6.2.4 General influence of HOMs in the output beam

A more sophisticated approach, than concentrating on the LG₁₀ mode in the output beam would be to analyze the HOM content at the dark port as done for [Pri12] but for different power levels. The OMC can be used as a diagnostic tool to do this. The HOM content at the dark port could be analyzed in heterodyne lock at different laser powers as well as with and without thermal compensation. The OMC mode scans would provide a detailed understanding of which modes are additionally influenced at different laser powers. If connections to the mid-frequency noise can be made remains to be seen.

¹ The fact that the relative power of the LG₁₀ mode is smallest at 2.2 kW, i.e. default operation power, proves that the ring heater is optimally used to adapt the RoC of MFE in default operation. At that time, the ring heater could not be used to further compensate for thermal lensing in the BS at higher laser power. Higher currents would be necessary for heating the mirror but would have also hold the risk of damaging the heater itself.

6.2.5 The effect of the SRAA on the medium frequencies

The alignment of the SRC shows indications to affect noise at medium frequencies, but it is not clear if this is connected to the laser power dependent noise at medium frequencies. The SRAA already plays an important role with respect to the stability of the IFO lock at high laser power as explained in chapter 5.3. It also seems to affect the sensitivity at medium frequencies.

Figure 6.4 shows the effect in a drastic fashion. Both plots show the sensitivity for the same input laser power. For the reference that is shown in blue, the SRAA operating point was changed to a degree that barely allows to maintain the lock.² The strong mis-alignment of MSR has a significant effect on the sensitivity at all displayed frequency. Furthermore, the circulating power is about 10 % lower for the mis-aligned state compared to the shown reference. Note that 10 % less power does not fully explain the higher shot noise level shown in the figure.

This example also shows the effect of the SRAA operating point on noise at medium frequencies. A not optimally chosen operating point increases noise at medium frequencies but the level of the mid-frequency noise could not be reduced below levels as shown in this chapter by proper alignment of MSR. To date, a not well aligned SRC seems not to be a likely cause for laser power dependent mid-frequency noise. However, further investigation will benefit from an optimal performance of the SRAA. Further noise like caused by a mis-aligned MSR is not desirable because it has an influence on such investigations. Therefore, the implementation of automatic beam centering on the SRAA QPD, as proposed in chapter 5.3, will probably be beneficial with respect to mid-frequency investigations as well as a stability improvement during power up experiments.

6.2.6 Scattering

Observations have shown that scattered light can be a cause for noise at medium frequencies in GEO 600 but there are no clear evidences that scattering is the cause for the laser power dependent mid-frequency noise. Still, scattered light can couple via various ways to the detector output and thus, it is an potential candidate. Scattering is the main loss channel of the PRC. Furthermore, the existence of a serious amount of scattered light in the vacuum system is obvious with respect to the discussed matter of chapter 3.

During a period of time, a further noise at medium frequencies was occasionally visible in the sensitivity. It occurred rather randomly and showed up at slightly higher frequencies as the mid-frequency noise does, i.e. above 300 Hz. The shape was similar to the $1/f$ shape of the mid-frequency noise but its gradient was less steep. Indications arose which led us to us to believe that this noise was caused by scattering. Therefore, we suspected the

² For further explanations about the detector stability for different operating points of the SRAA, see chapter 5.3.

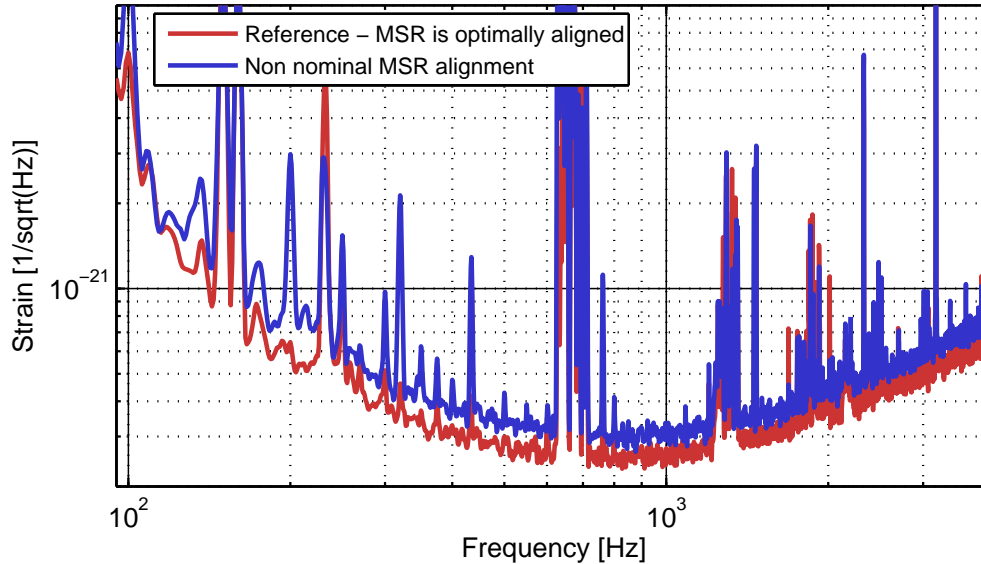


Figure 6.4: An example of the influence of the SRAA operating point to the noise at medium frequencies. In general, the noise at medium frequencies is lowest while MSR in its nominal position.

laser power dependent mid-frequency noise to be related to this noise and scattering itself. Eventually, it was found that this noise was due to scattering at PDs in the transmission of the MI mirrors MCE and MCN but not to be connected to the the power dependent mid-frequency noise. The scattering path in transmission of a mirror is just one example among a variety of possible paths.

An argument for scattering as a possible origin of the power dependent mid-frequency noise is the simple fact that more laser power results in more light to be scattered. This argument gets further weight by the fact that a mis-alignment of MSR increases noise at medium frequencies. If the SRAA is not at its optimal operation point, the mode healing efficiency decreases and the circulating laser power shows more fluctuation. Thus, more light gets lost into HOMs which have a larger cross-section compared to the ground mode.

The chapter at hand caught up with the sensitivity aspect at high power which was neglected in the previous chapter. Thereby, two consequences of the GEO 600 sensitivity at high laser power are shown. First, shot noise gets further suppressed as the laser power that is circulating in the IFO increases. The second consequence is a laser power dependent noise at medium frequencies which degrades the sensitivity between 100 Hz and about 1 kHz. This not yet explained noise is the reason for not routinely using higher

laser power levels. In the next chapter, this thesis will be summarized and an outlook is given which places the results of this chapter in an astrophysical context.

7 Summary and outlook

In this thesis, various challenges were discussed which occurred in the process of increasing the laser power in GEO 600. Their solution allowed for a significant increase of the usable laser power compared to the level at which GEO 600 was operated at before the GEO-HF upgrade.

The first obstacle to overcome was to enable stable operation at full available laser power as provided by the initial laser system. In chapter 3 it was shown that scattered light from inside of the interferometer strongly couples into the displacement sensors of the main suspension local controls. This coupling led to a contamination of the local control error signals which increases with the laser power. Subsequently, this coupling prevented a laser power increase due to decreasing lock stability of the interferometer. The implementation of a modulation-demodulation scheme for the main suspension local controls successfully rejected the stray light signal from the local control error signals. Thereby, it was shown that the modulation-demodulation scheme shows a satisfying noise performance and allows for a significant laser power increase. During the whole three months lasting VIRGO GEO 600 science run in Summer 2011, the instrument was operated at maximum available laser power. Furthermore, it was investigated, whether the displacement sensors of the remaining suspension local controls show a noteworthy contamination of scattered light. For two examples, this is the case. At the suspension local control of the mirror which directs the input beam into the power-recycling cavity, the modulation-demodulation scheme was implemented. At one of the output optics suspension, measures to reject stray light will be most likely necessary before the full available laser power can be used.

Consecutively, a new laser system was installed, which provides 2.5 times more laser power than the old system. In chapter 4 this laser system is described and in particular, the resulting need for modifications at the input optics due to thermal reasons and stability issues are discussed. This upgrade of input optics was composed of a replacement of Electro-Optical modulators, a finesse reduction of the two input mode cleaners and an improvement of the mode-matching onto the power-recycling cavity.

The initial Lithium Niobate Electro-Optical modulators which are used to imprint modulation side bands on the laser beam needed replacement due to poor thermal properties. As replacement *Rubidium Titanyle Phosphate* (RTP) modulators were chosen, tested and successfully implemented. Furthermore, the finesse of the input mode cleaners was reduced to increase their throughput for carrier light and to prevent radiation pressure induced instabilities at high laser power. Therefore, their respective input and output mirrors were replaced by mirrors with higher transmittance of about 1%. Finally, the

mode-matching telescope towards the power-recycling cavity was modified by a simple exchange of one lens. In combination, the upgrade of the input optics enabled the operation at higher laser power levels and provided a further increase of available laser power by a factor of 1.75.

Such high laser power levels as available after the upgrade of the input optics causes various challenges for the operation of the interferometer. In chapter 5 examples such as optimizations in the frequency stabilization loop and the automatic alignment of the Michelson interferometer were discussed. Also, further aspects such as the performance of the signal-recycling cavity automatic alignment at high laser power were described. A remarkable enhancement of the upper limit of the laser power in the dual-recycled Michelson interferometer is shown thereafter. In DC operation, about 4 kW impinging on the *beam splitter* (BS) became easily applicable. This corresponds to twice as high laser powers as used prior to GEO-HF. Additionally, operation at almost three times higher power was demonstrated in initial experiments. In heterodyne lock, the lock stability was shown to be better than in DC lock. Operation at 6 kW to 7 kW was achieved and once, even operation with 8 kW impinging on the BS was briefly realized. As was shown in chapter 5, the thermal lens in the BS becomes more significant for such high laser power. Measures need to be taken to compensate for this in the future. First experiments to compensate for the thermal lensing effect were carried out and the installation of a *thermal compensation system* (TCS) at the BS is ongoing while this thesis is handed in. This TCS is a follow up work of [Wit09] and the last remaining installation which is foreseen in GEO-HF. The process of further extending the laser power limit requires the thermal compensation of the thermal lens in the beam splitter as illustrated in chapter 5. Without such compensation, almost 10 % of the light injected into the power-recycling cavity gets lost into *higher-order modes* (HOMs) at the achieved laser power levels. Besides this power loss, first indications were found that these HOMs disturb the stability of the DC lock. At the dark port these HOMs can also couple via alignment fluctuation into the OMC and will eventually add noise to the detector output. Except for the installation of a TCS, further laser power increase work will in particular benefit from an optimization of the SRAA. Its operating point depends on the used power in a reproducible manner. Subsequently, the need for optimizations at other control loops are likely as the current laser power limit is exceeded.

Finally, chapter 6 completed the discussion of laser power increase commissioning aspects by displaying the sensitivity of GEO 600 at laser powers up to almost 5 kW. It is shown, that the sensitivity improves with the square root of the circulating power in the power-recycling cavity at high frequencies. Thus, it was confirmed that shot noise is the only limiting noise at high frequencies. In particular with respect to squeezing, this is an important result because an efficient application of squeezing at high laser power levels will not be restricted by other noise sources. Operation at 3 kW to 4 kW circulating power with additional squeezing can already routinely be realized.

However, another topic of chapter 6 was the discussion of a not yet understood noise at medium frequencies. This so-called mid-frequency noise reduces the sensitivity between

100 Hz and about 1 kHz with increasing laser power by a similar amount as the sensitivity improves above 1 kHz. Since astrophysical sources are considered to be more likely at lower frequencies, GEO 600 is mostly operated at a lower laser power level of 2 kW to 2.5 kW. Continuing investigations beyond the previously summarized work is needed to understand and remove this noise. The removal of the laser power dependent noise at medium frequencies will allow to fully bail out a main part of GEO-HF: the operation at high laser power. GEO-HF itself can be considered as almost completed except for commissioning aspects at the GEO squeezer and a further extension of the current laser power limit. So far, it allowed to successfully keep up with the sensitivities of Enhanced LIGO and VIRGO+. The first steps to even surpass the Enhanced LIGO sensitivity at high frequencies were already taken as shown in figure 7.1.

Figure 7.1 provides a comparison of sensitivities from VIRGO+ and Enhanced LIGO Livingston to three different sensitivities of GEO 600. The sensitivity from 2009 depicts a typical example from the time just before the GEO-HF upgrade had started. Furthermore, recent sensitivities are shown for 2 kW and 4.8 kW circulating laser power, respectively. For each case, squeezing is applied whereas it was not explicitly optimized for the case of 4.8 kW. However, it shows for the first time that GEO 600 matches a typical Enhanced LIGO sensitivity at any frequencies.

The large gap between the GEO 600 sensitivity curves at high frequencies is the result of the successful accomplishment of almost the whole GEO-HF upgrade. Namely, these are the increase of the signal-recycling bandwidth as well as operation of the dual-recycled Michelson interferometer in the detuned mode, the routinely use of squeezing, and the change of the read-out scheme from heterodyne to DC readout in combination with the installation of the output mode cleaner. In this context, a further improvement of the detected squeezing is an ongoing work. In particular, understanding the losses between the squeezed light source and the IFO are in the focus of current investigations. Optimization of the squeezing for high laser powers will be another important task.

The potential to further increase the sensitivity of GEO 600 by operating at significantly higher laser power levels was one of the commissioning aspects towards an operation of GEO 600 at high laser power. These were discussed in the thesis and summarized in this outlook.

The installation of the TCS and further improvements of the lock stability at high laser power will soon enable operation at more than 12 kW circulating power. At some point, the installation of an even stronger laser system than the one currently in use might get reasonable. In this context, an extension of the current laser system by two additional amplifier stages seems reasonable. Such an extension could provide a further increase of the available laser power by a factor of two [Bog12] and is already considered in the current layout on the laser bench.

All these aspects are part of a continuing effort to further improve the GEO 600 gravitational wave detector. In particular, the laser power dependent noise at medium frequencies that was introduced and described in the previous chapter needs to be further addressed. Its understanding and consequently its complete removal is mandatory to make full use

of the work that is discussed in this thesis with respect to the main goal of GEO 600: The direct detection of GWs.

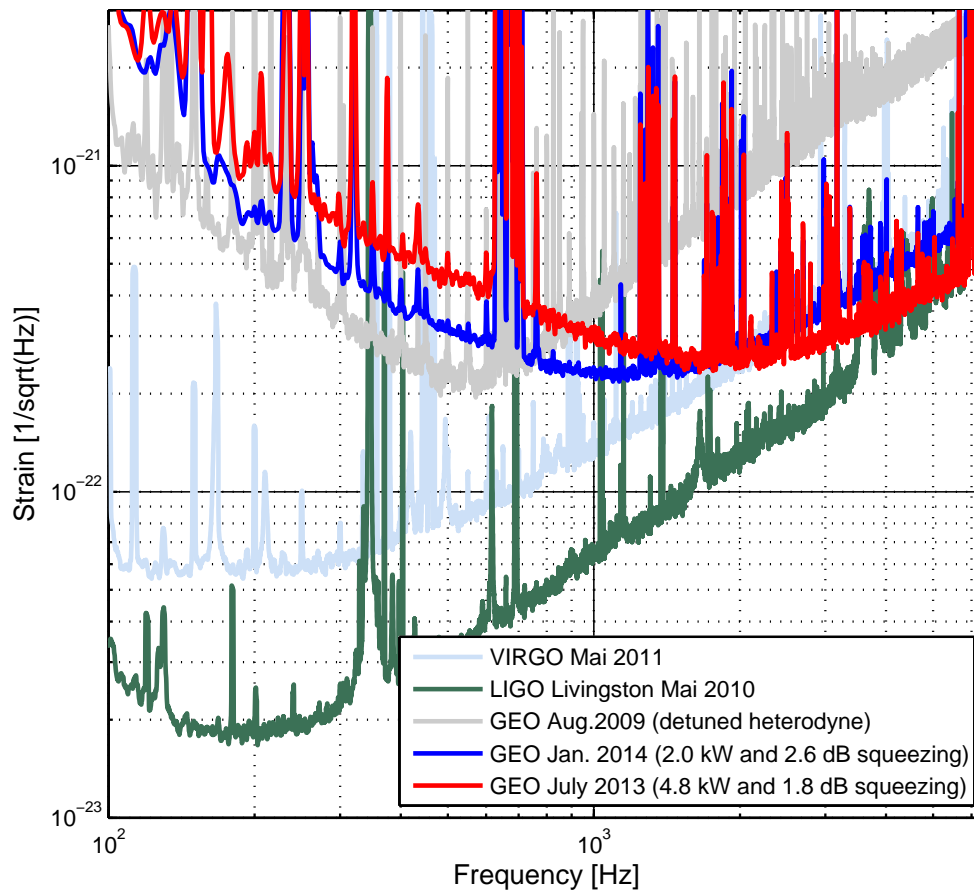


Figure 7.1: Typical sensitivities of GEO 600 compared to exemplary sensitivities of VIRGO+ and Enhanced LIGO (Livingston) at frequencies from 100 Hz to 6 kHz. Three sensitivities of GEO 600 are shown. First, a typical example from the time just before the GEO-HF upgrade had started is shown. The remaining two are recent examples at low and at high laser power in combination with different squeezing levels.

A Straylight measurements at all main suspensions

In chapter 3.2.1, the influence of laser power fluctuations which couple as stray light to the shadow sensors of the GEO 600 main suspension local controls is described. Noise projections were done to determine the amount of laser stray light at all main suspensions LCs. The corresponding results are summarized in table 3.1. At this point, we present the whole set of projections for all main suspension LCs except for the MSR LC. They give a clearer picture of the amount of stray light coupling, because the different flag error signal spectral densities show slight differences compared to each other. These differences depend on the actual suspension and of the degree of freedom the corresponding channel controls.

Additionally, table A.1 provides the projection factors that were used for all projections that are shown below. The projection factor is defined as the inverse of the coupling factor and both are explained in chapter 3.2.1.

It should be noted that the corresponding measurements were done before the installation of the first baffles. In most cases, the baffle installation reduced the amount of stray light coupling into the shadow sensors which are located in the same tank by a factor of 2 to 3. Still, the contamination is sufficiently large after the baffle installation to justify the use of MDs at all main suspension LCs except for MSR. In particular at the BS, MPR and MFN the stray light contamination is to date equal to the presented results, because no baffles were installed in the corresponding vacuum tanks. Before and after the baffle installation, MDs were bypassed to check for their need with respect to the IFO stability at high laser power. All attempts to increase the circulating laser power above a value of 2.5 kW failed if the MDs were bypassed.

A.1 Projection factors and stray light projections for all main suspensions

Table A.1 shows the projection factors that were used for all projections that are shown below. The values for MSR are included, even though no projection is shown. However, there are just two upper limit projection factors for MSR. In all other cases no coupling peak is visible at a circulating power of roughly 2 kW.

Suspension	projection factors [a.u.]					
	Flag 1	Flag 2	Flag 3	Flag 4	Flag 5	Flag 6
MPR	1169	3393	5257	4597	889	2490
BS	568	591	2191	2601	3493	881
MCE	883	1103	8319	7932	12072*	5969
MCN	2738*	7262*	10000*	7374*	1691	1716
MFE	788	711	2278	800	1583*	1527*
MFN	4861	4511	1969	2984	1859	1056
MSR	non	6000*	8000*	non	non	non

Table A.1: Projection factors that were experimentally found and used for the corresponding stray light projections. All cases that are marked with * show upper limits.

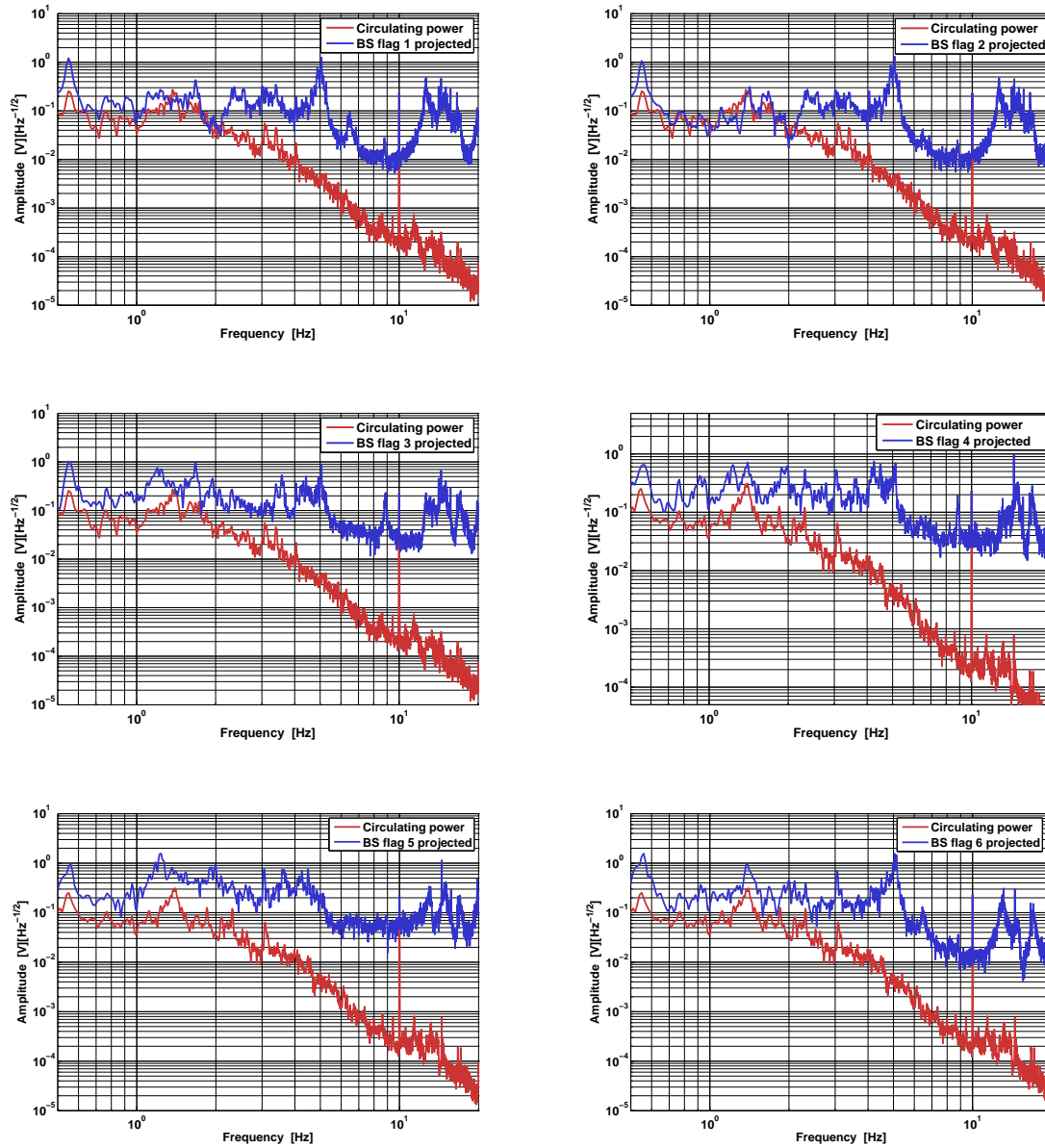


Figure A.1: Laser stray light projections for all six BS flags.

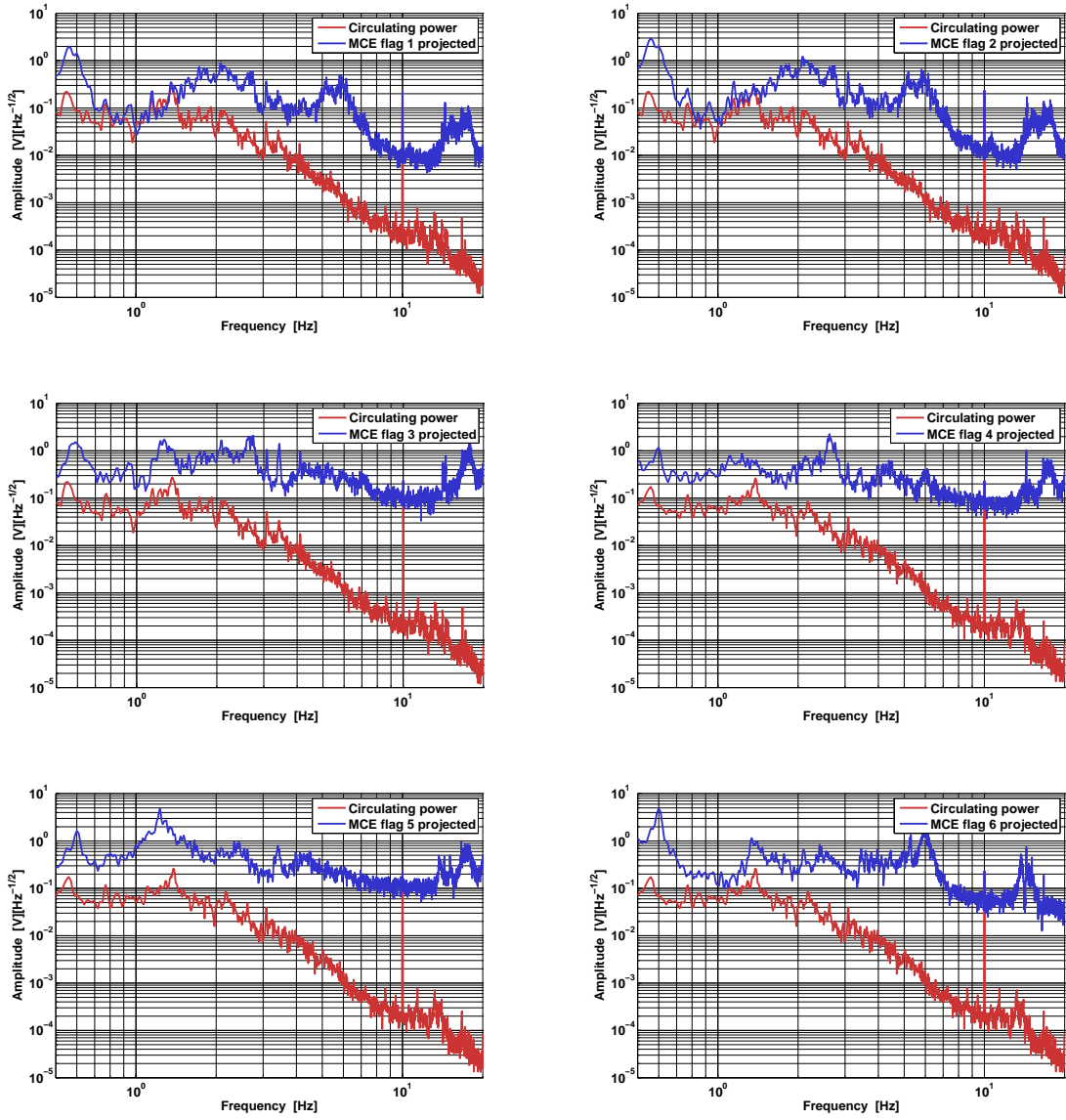


Figure A.2: Laser stray light projections for all six MCE flags.

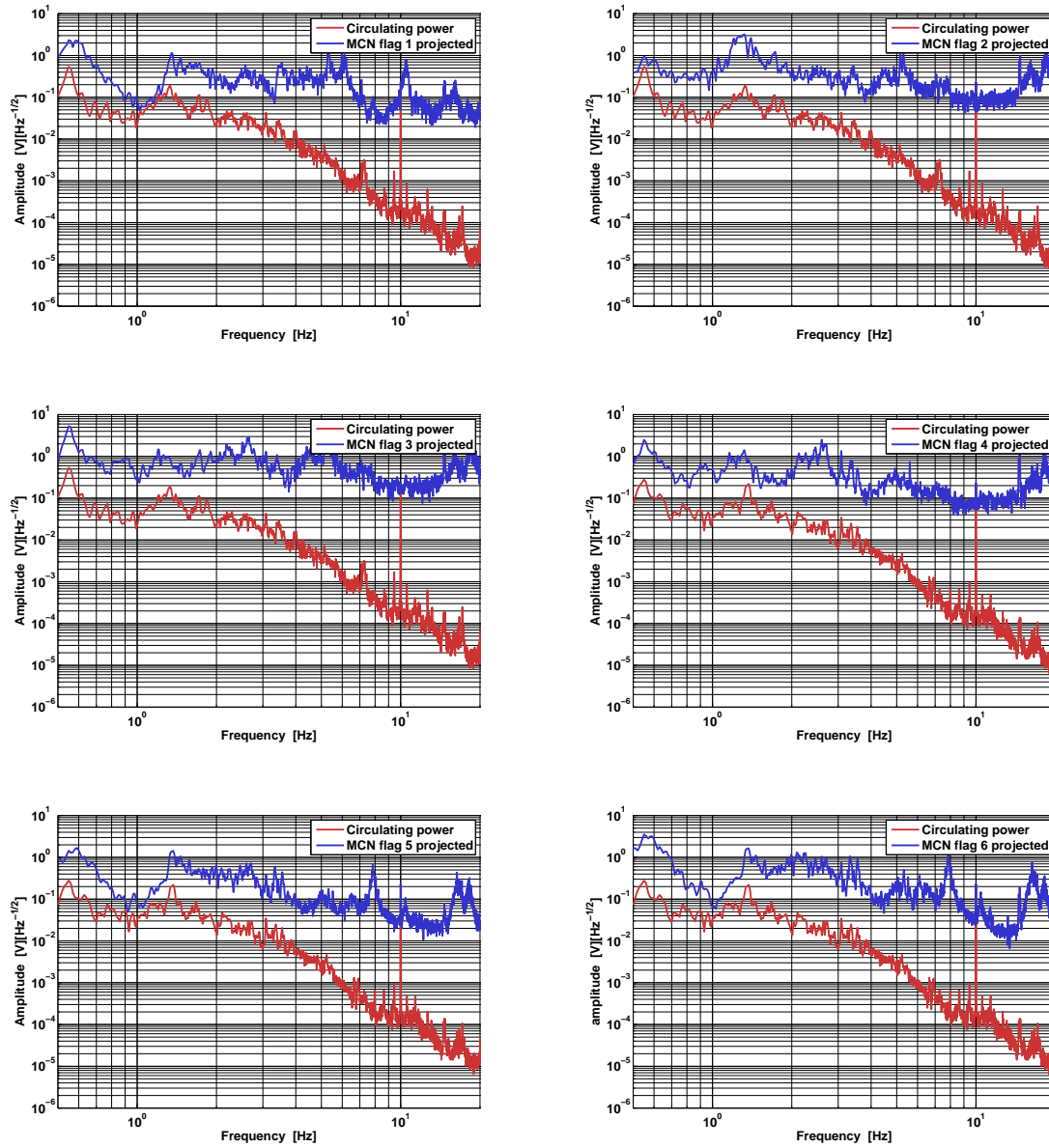


Figure A.3: Laser stray light projections for all six MCN flags.

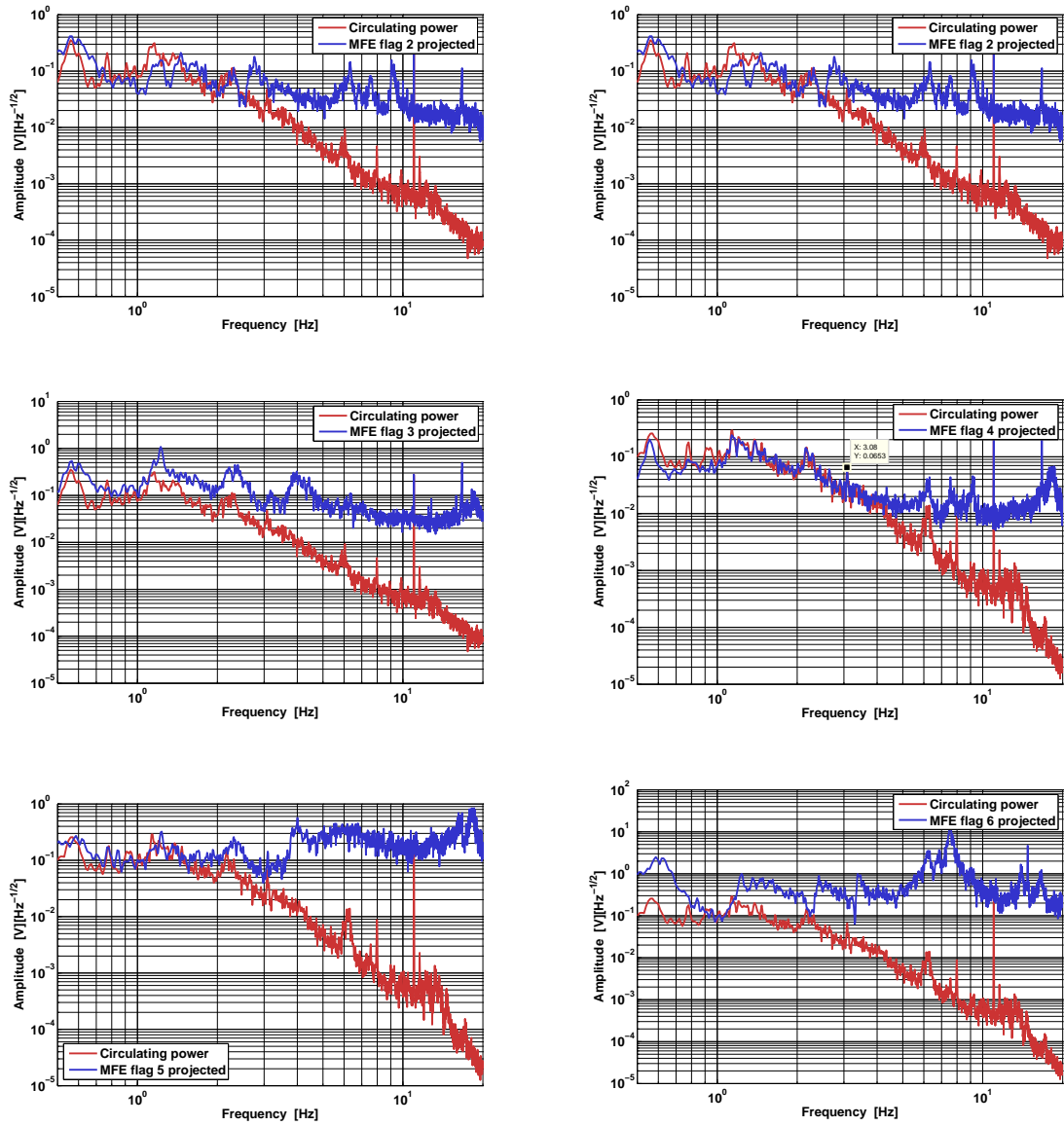


Figure A.4: Laser stray light projections for all six MFE flags.

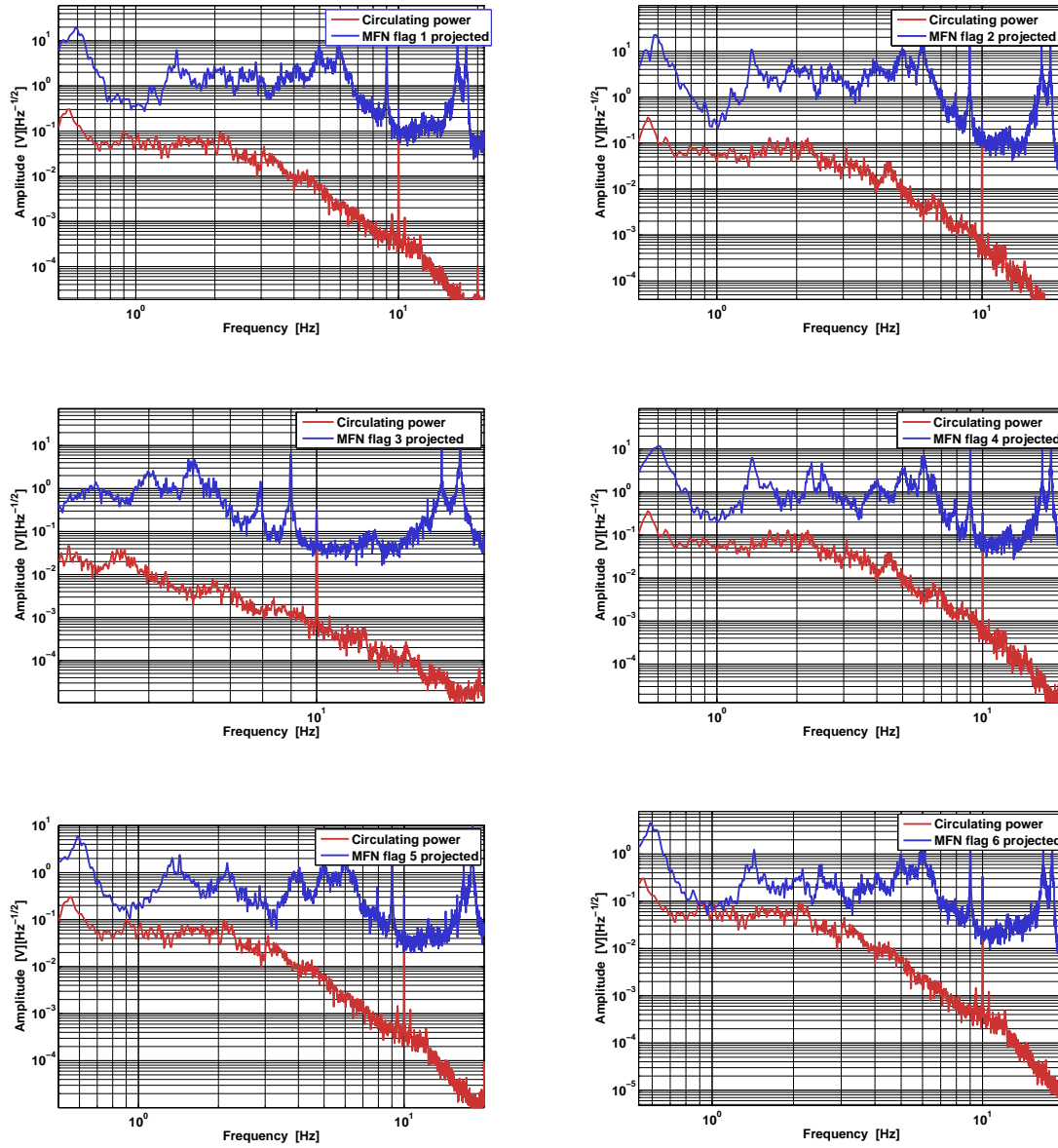


Figure A.5: Laser stray light projections for all six MFN flags.

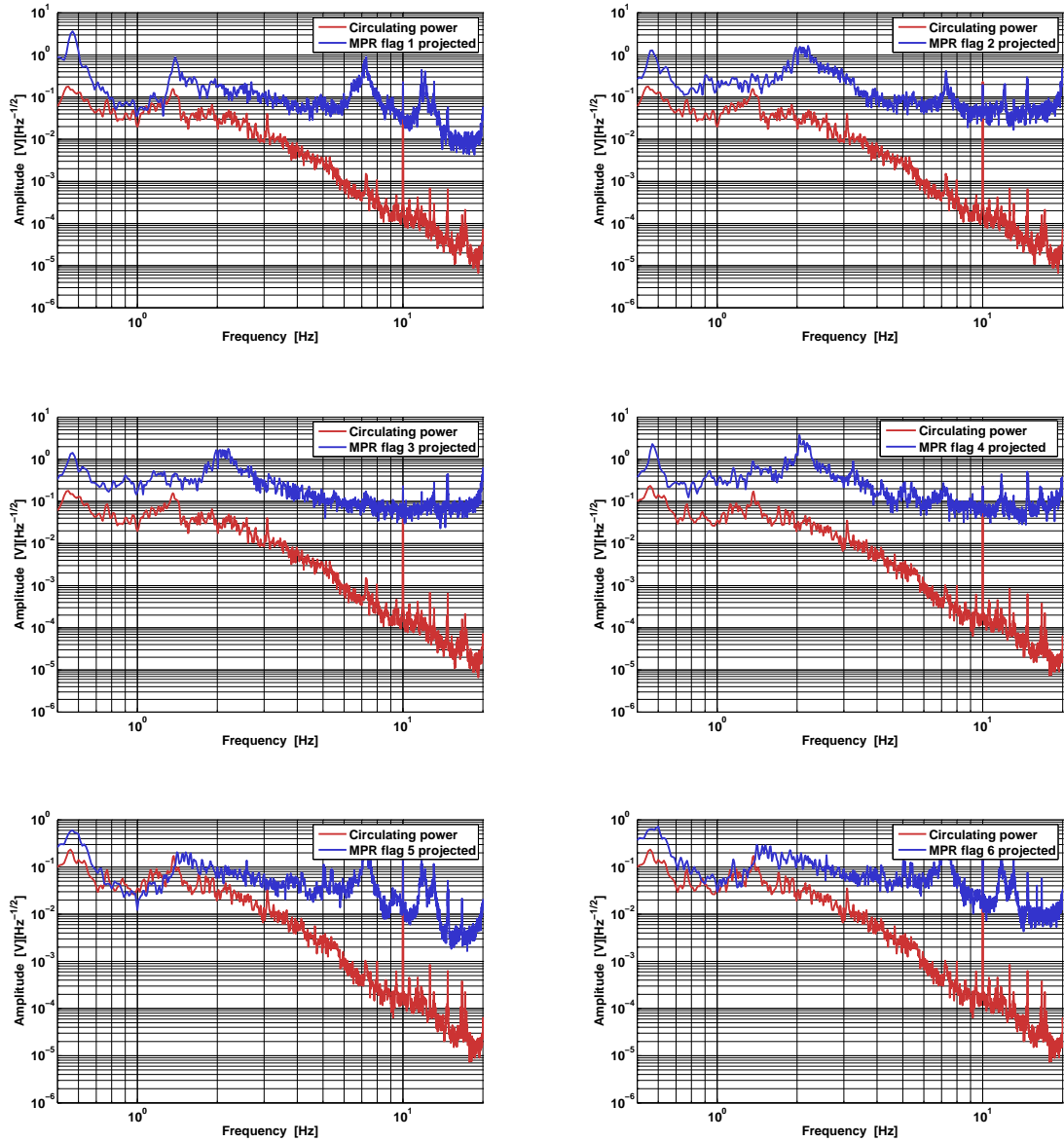


Figure A.6: Laser stray light projections for all six MPR flags.

B The effect of stray light coupling to the LCs of the reaction masses

In chapter 3, we were only interested in a direct way of laser power fluctuations coupling as scattered light into the shadow sensors of a local control and thereby disturbing the stability. In this context, direct means, that due to a stray light contaminated LC error signal the corresponding suspension experiences an actuation. This actuation shakes the mirror in a uncontrolled way and affects the performance of the IFO. Potentially this can even cause a lock loss as shown in figure 3.1.

In the following, it is depicted that an indirect coupling of scattered light is possible. A indirect coupling is possible via the main displacement actuator of the Michelson interferometer, the electrostatic drive (ESD). In order to see this one needs to think about the way the ESD works. The ESD is used to apply feedback on the test mass level via an electrical force. A detailed description about the ESDs is given in [Gro03]. For this consideration, we need the attractive force an ESD applies to the test mass. According to [Gro03] this force is given by

$$F = U^2 \varepsilon \varepsilon_r d^x a, \tag{B.1}$$

where U is the applied voltage which consist of a constant bias voltage and the feedback itself. Furthermore, ε is the dielectric constant, ε_r the relative dielectric constant of the test mass, d (with exponent x) is the distance between the reaction mass and the test mass and a is a constant geometric factor. The distance d is typically between 1 mm and 3 mm for GEO 600 while the value of a depends on the actual electrode pattern design [Gro03]. For a similar electrode pattern, $x \approx 1.5$ was obtained in [Str02].

Since this force is proportional to the distance between the reaction mass and the test mass, it will be modulated by an oscillation of the distance itself. A stray light induced oscillation of the upper mass that is larger than a micrometer is unrealistic while the circulating laser power is as quiet as it is since the installation of MDs. Let us conservatively assume, that the RMS of a stray light induced movement of the reaction mass is about $1 \mu\text{m}$. In this case, the force will not be modulated by more than $(1.001)^x$ if we assume a small distance of 1 mm between the reaction mass and the test mass. Thus, it seems unlikely that scattered light will influence the performance of the alignment systems via this coupling process.

However, this assumption was experimentally checked. It was found, that a reaction

mass needs to be rotated or tilted about 100 times more than the test mass to get a comparable effect on the alignment. In addition, the stray light coupling was measured for the LCs of the MCE and MCN reaction masses. It is in the same order but slightly smaller than it is for the respective main suspensions. Thus, stronger stray light induced movements of the reaction mass as the movements which happened before the MD installations are not expected. This further steadies the statement that no negative effects will occur via the discussed coupling mechanism, even at a laser power as foreseen in GEO-HF.

C Further information about the modulation drive

The following provides the modulation drive circuit diagram and further information about difficulties which occurred during commissioning work at the far MI suspensions in order to run their local controls with the modulation-demodulation scheme.

C.1 Modulation drive circuit diagram

In this section, the circuit diagram of the modulation drive is provided. In addition, figure C.5 shows the circuit diagram of the module that provides the electrical signal used to generate the modulated current to drive the LEDs and as the LO signal for the case of 10 kHz modulation. If a frequency different from 10 kHz is desired, the micro controller needs to be reprogrammed and the 20 kHz and the gain of the output needs adjustment due to the 20 kHz low pass filter.

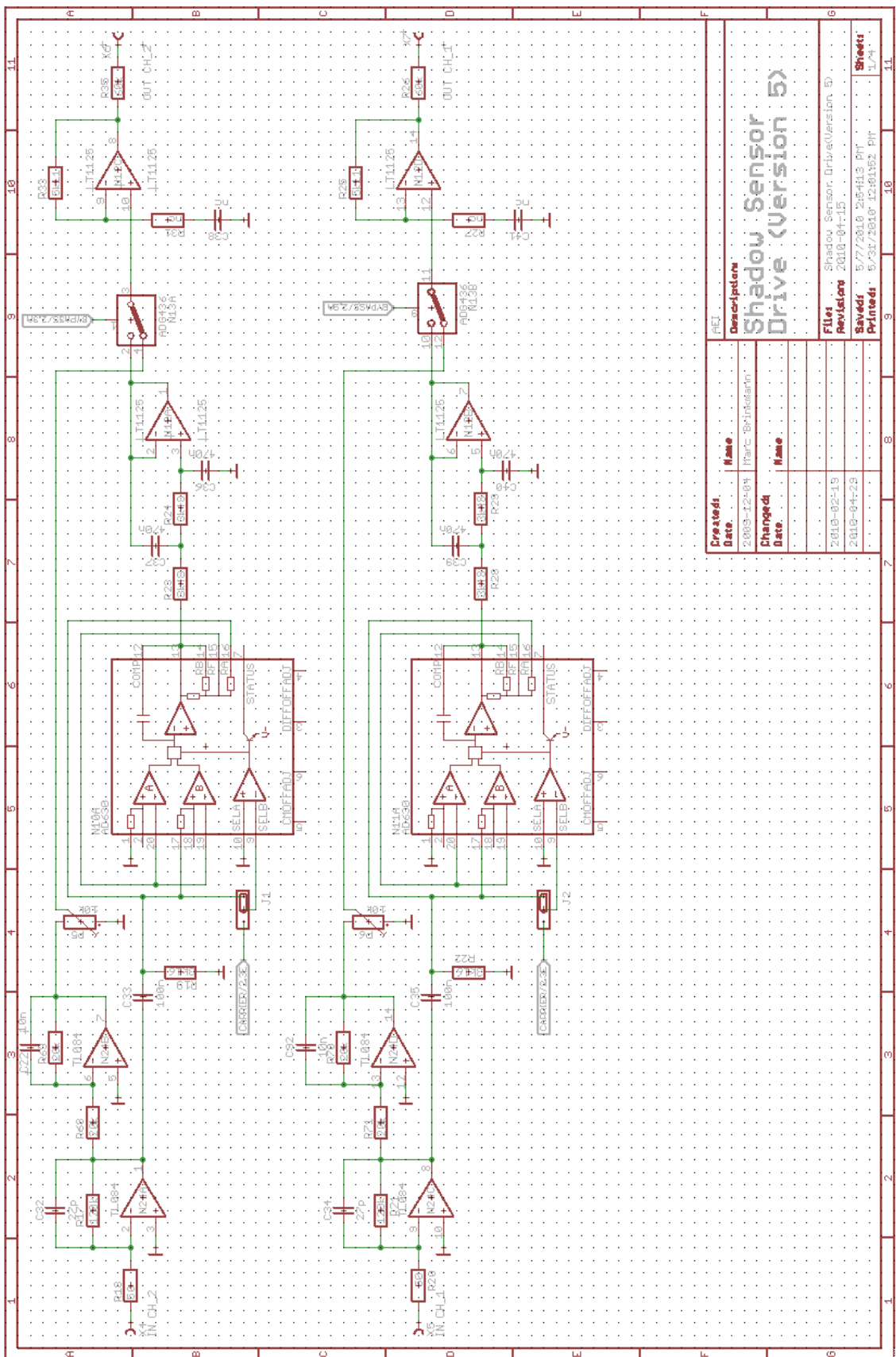
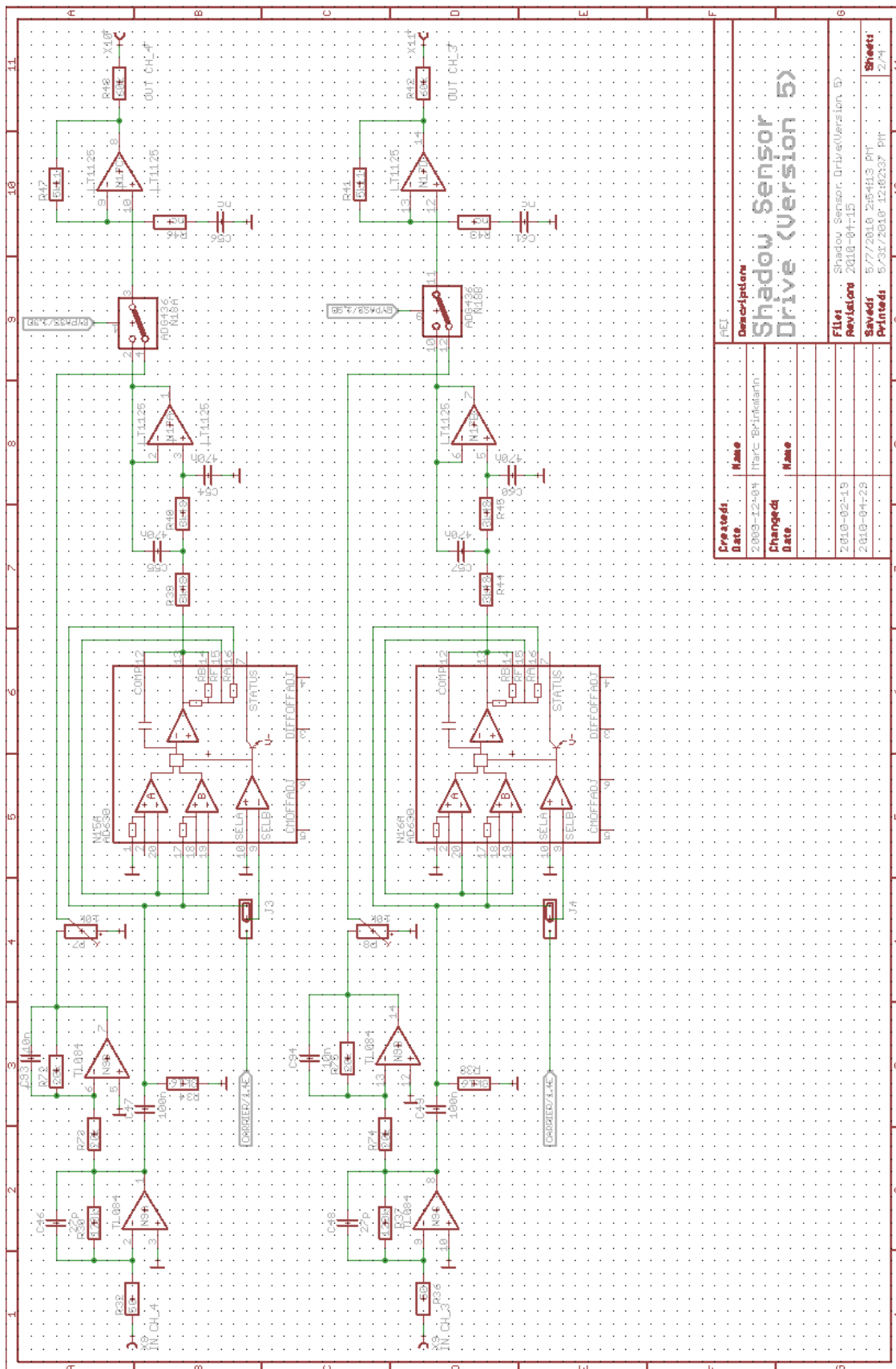


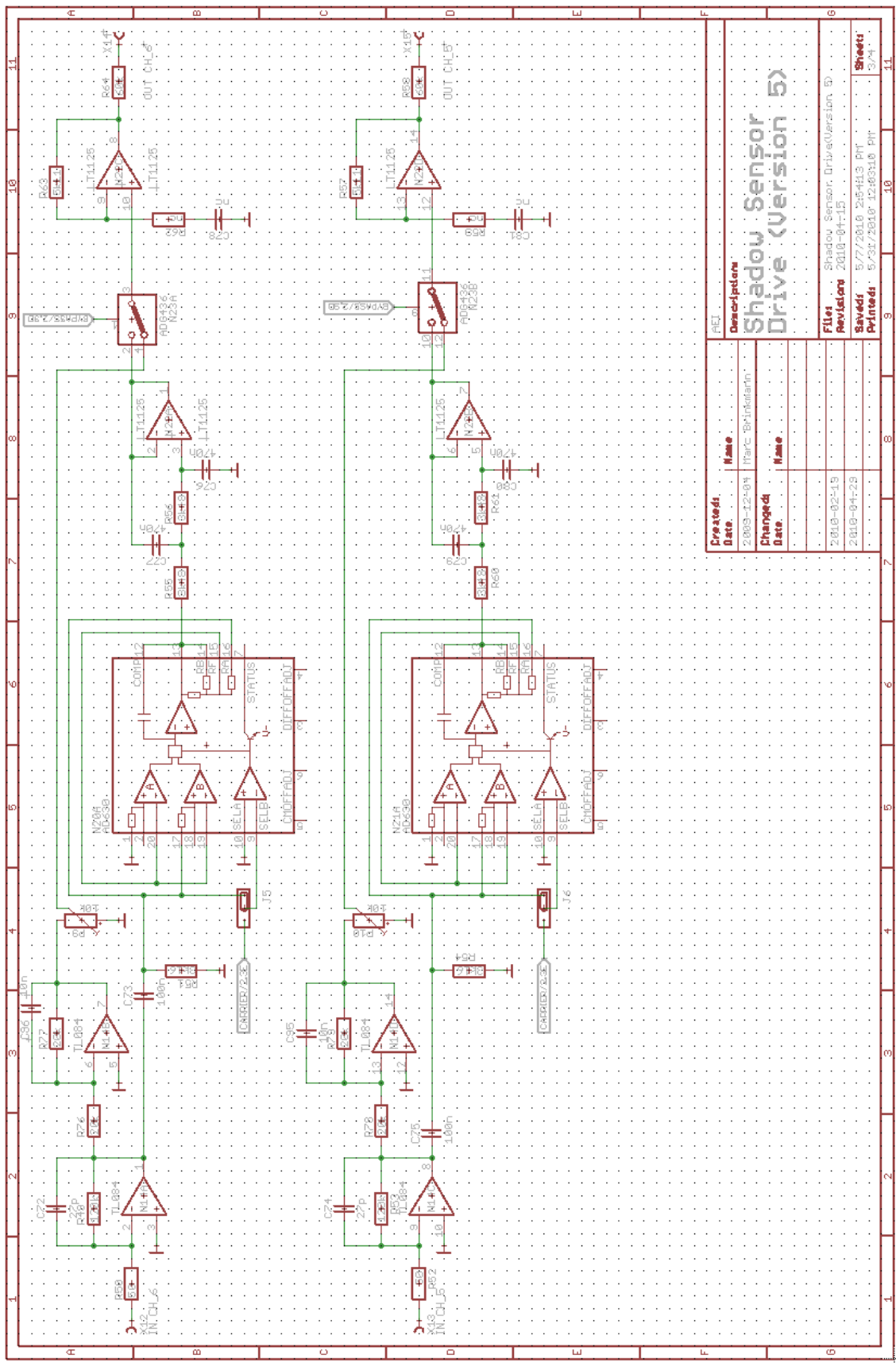
Figure C.1: Modulation drive circuit diagram. Receiving, demodulation and filtering of local control channels 1 and 2. If no external LO is applied the modulation and filtering steps are bypassed.



Created Date	Name
2009-12-04	Harv Brinkmann
Changed Date	Name
2010-02-19	
2010-04-29	
5/7/2010	SB5413.DWG
9/21/2010	12-0237.PLT

File	Description
Shadow Sensor Drive (Version 5)	
Files	Shadow Sensor Drive (Version 5)
Revisions	2010-04-15
Drawn	SB5413.DWG
Printed	9/21/2010 12:02:37 PM

Figure C.2: Modulation drive circuit diagram. Receiving, demodulation and filtering of local control channels 3 and 4. If no external LO is applied the modulation and filtering steps are bypassed.



Created Date	Name	Description
2009-12-04	Marc Brinkmann	Shadow Sensor Drive (Version 5)
Changed Date	Name	
2010-02-19		
2010-04-29		
File: Shadow_Sensor_Drive (Version 5)		
Revision: 2010-04-13		
Saved: 5/7/2010 2:54:13 PM		
Printed: 5/31/2010 12:03:10 PM		
Sheet: 3/4		

Figure C.3: Modulation drive circuit diagram. Receiving, demodulation and filtering of local control channels 5 and 6. If no external LO is applied the modulation and filtering steps are bypassed.

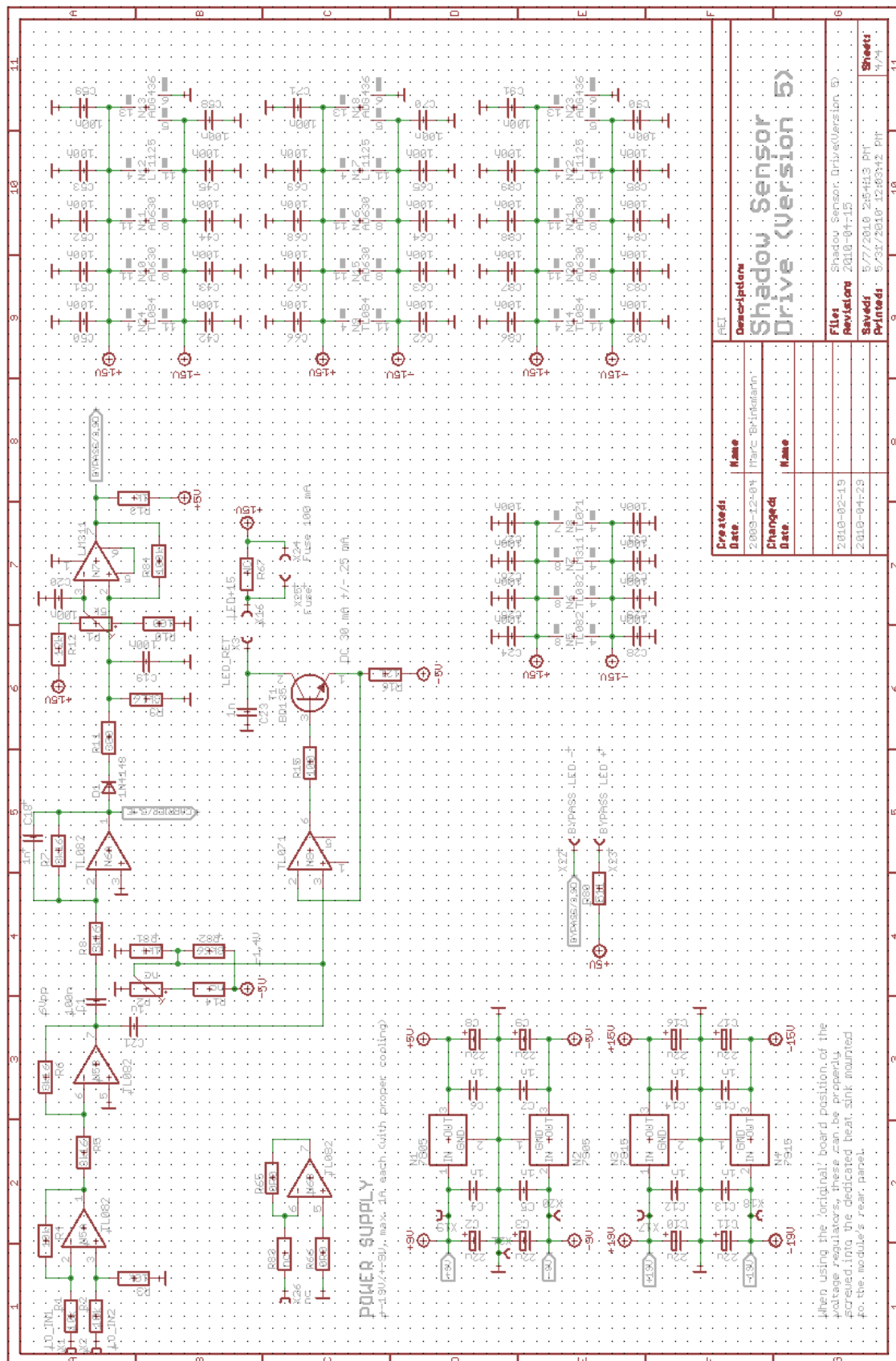


Figure C.4: Modulation drive circuit diagram. Power supply and generation of modulated currents for local control LEDs.

C.2 Further issues at the LCs of MFE and MFN if operated with MD

The error signal of a suspension LCs which is operated with a MD shows some additional noise over a wide frequency range compared to the default case, i.e. without MD, as discussed in chapter 3.3.4. This noise does not affect the operation of the IFO. In particular, it does not significantly contribute to noise in the GEO 600 sensitivity. However, at the suspensions of the folding mirrors, namely MFE and MFN we found an exception to this statement that the IFOs operation is not affected. A further noise source was found in the LC error signals if operated with MD. This noise showed up as noise lines in the spectral density of the error signals that varied in frequency. Eventually, these noise lines reached frequencies at which the active band of the LC electronics is. Thus, they crossed pendulum resonances. Thereby, pendulum resonances were excited, which in some cases caused a lock loss of the IFO. These occasional lock losses could not be tolerated. After all, the MD is designed to increase the detectors stability.

The investigations to eliminate this stability problem did not fully explain the coupling mechanism that causes these lines that vary in frequency. However, it was possible to decrease the amplitude of these lines and to assure that they do not come close to frequencies that are within the active band of the LC electronics. The investigations showed that an interaction of the 10 kHz modulation frequency and the 200th harmonic of the 50 Hz power supply (as well as close by harmonics) caused these noise lines. Depending on the actual load, the “50 Hz” power supply line varies in frequency up to approximately ± 0.1 Hz. Accordingly, the n th harmonic of the 50 Hz line varies by $n \cdot (\pm 0.1 \text{ Hz})$.

Figure C.6 shows a spectrogram of an error signal that belongs to a flag of the MFN suspension and is meant to illustrate the discussed matter. One can see a noise line that varies over a frequency range of about 20 Hz in the displayed time frame. At zero minutes this line is at 14 Hz. Later on, it reaches 0 Hz several times. Thereby, a 50 Hz harmonic that is close in frequency to the modulation frequency gets mixed down to DC. The modulation frequency is 7.154 kHz in the displayed case. The line is misinterpreted as actual movement of the upper mass by the LC and feedback is applied accordingly. At pendulum resonance frequencies this can lead to an excitement of the pendulum resonance that is sufficiently strong to cause a lock loss of the IFO. To reduce the effect of the lines that vary in frequency and to assure that they do not reach frequencies at or below the LC electronics bandwidth we changed the frequency of the LO signal. The change of the LO frequency needed by the MD consisted of two parts.

First of all, the modulation frequency of the MDs at the folding mirror suspensions was slightly reduced. Thereby, n is smaller and therefore the frequency range is smaller the corresponding 50 Hz harmonic varies in. The second step was to set the modulation frequency in between the frequency of two neighboring 50 Hz harmonics. In combination, these changes done at the LO frequency separated the modulation frequency from all 50 Hz harmonics.

By analyzing spectra of the MFE and MFN suspension LC error signals we found several other noise structures at several kHz. These seem to be unrelated to 50 Hz harmonics.

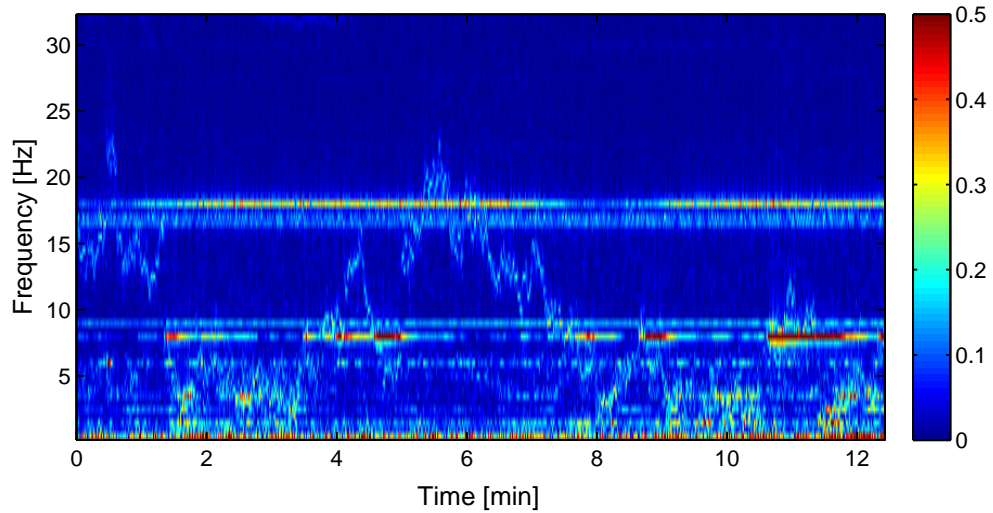


Figure C.6: A spectrogram of one of the MFN LC error signals. A noise line is wandering over a frequency range of about 20 Hz. At several times, this noise line comes close to 0 Hz.

However, they also appear in the demodulated error signals at low frequencies if the modulation frequency is similar to the frequency of these structures. The actual modulation frequency of the MDs at the MFE and MFN suspension therefore needed to be chosen carefully. At the far north station, the frequency of the LO signal was ultimately set to 7123 Hz and at the far east station to 7621 Hz. Since these frequencies have been used for the corresponding MDs, no lock losses or disturbances have been detected that were caused by the discussed mechanism.

A stable operation of the detector with working MDs at the far MI mirror suspension LCs could be obtained, although the coupling mechanism that causes the lines is not fully understood.

D Further information about the EOMs of GEO 600

D.1 Thermal lens measurements of GEO EOMs

At this point, we are going to summarize results of thermal lens measurements which were done for the new GEO 600 RTP EOMs and other optical components of interests. These results originate from [Bog13] and [Kwe11]. Further information about this matter can be found in these references, too. However, these thermal lens measurements have significance for the topics discussed in chapter 4 and for GEO 600 in general with respect to a potential laser power increase *beyond* the scope of GEO-HF. Therefore, they are summarized here, in the appendix of this thesis.

D.1.1 A direct comparison of various thermal lenses

Table D.1 provides measured focal lengths of the two RTP EOM modules that were installed on MU2 and MU3, respectively. Note that these focal lengths are obtained for beam diameters of about 1 mm as present at MU3. These values are compared to selected other optical components. Regarding the unexpected high thermal lensing effect of the MU3 modulator, it needs to be taken into account for potential laser power increase plans beyond the scope of GEO-HF.

component	material	length [mm]	beam diameter [mm]	focal length [m · W / P]
EOM (from MU2)	RTP	4×10	0.873	1809 ± 68
EOM (from MU3)	RTP	2×35	0.858	265 ± 10
EOM (Adv. LIGO)	RTP	40	0.903	2722 ± 206
Faraday	TGG	40	1.036	365 ± 11
BK7	N-BK7	5	0.854	801 ± 31
EOM (GEO spare)	LiNbO ₃	35	1.017	316 ± 12

Table D.1: Measured thermal lenses for the GEO 600 RTP EOMs compared to selected other components as presented in [Bog13]. The beam size at the respective component is given for each measurement. Still, note that slight differences of the beam sizes are present. The results from the LiNbO₃ EOM were obtained from [Kwe11]. According to [Bog12] a factor of two was taken into account. In the same communication it was stated, that one cannot rely on the result for the LiNbO₃ EOM due to the permanent damage this crystal suffered from in the measurement. However, this result is provided to have a hint of the order of magnitude of the thermal lensing effect.

D.1.2 LiNbO₃ crystals

Figure D.1 displays the measurement that showed, that the LiNbO₃ EOMs do not withstand laser power levels as used in GEO-HF for beam diameters below 1 mm. In the course of this measurement, a LiNbO₃ EOM as formerly used on MU2 and MU3 was exposed to a laser beam that had a diameter of about 1 mm. The laser power was tuned between 0 W and 40 W over 28 h. This can be seen in the upper plot of this figure. The bottom plot of figure D.1 shows the power in selected higher order modes. Due to the thermal lensing effect, the power in modes that are different from the TEM00 one is strongly increasing for high laser powers. Furthermore, one can see that at the end of the measurement, the power in higher modes is significantly higher as it is in the beginning for low power in the probe beam. The latter shows the permanent damage that high laser power densities cause at LiNbO₃. It is not clear from this measurement, what the exact threshold for a damage to the crystal is. Therefore, we decided to not expose the LiNbO₃ EOMs on MU2 and MU3 to significantly higher laser powers as were available with the old laser system. Until the IO upgrade, we limited the input laser power that is send to MC1 to 10 W.

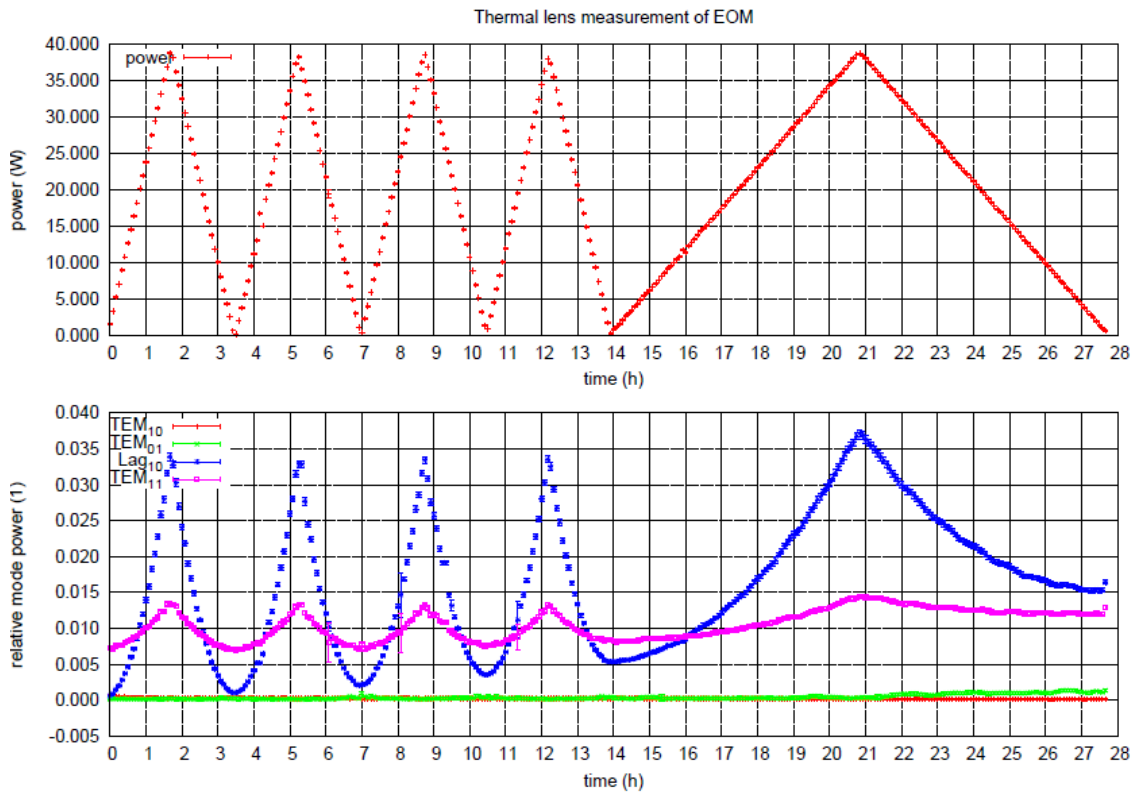


Figure D.1: A thermal lensing measurements of LiNbO_3 EOMs [Kwe11]. This plot shows the permanent damage to LiNbO_3 if exposed to too much laser power. According to [Bog13] a value for the thermal lens cannot be obtained in such a case.

D.1.3 RTP crystals

All five acquired RTP EOM modules were tested by members of the AEI Laser Group in thermal lens measurements similar to the one shown in figure D.1 and results were presented in [Bog13]. Because two particular plots that belong to the RTP EOMS that were installed in GEO 600 do not appear in [Bog13] they are given here.

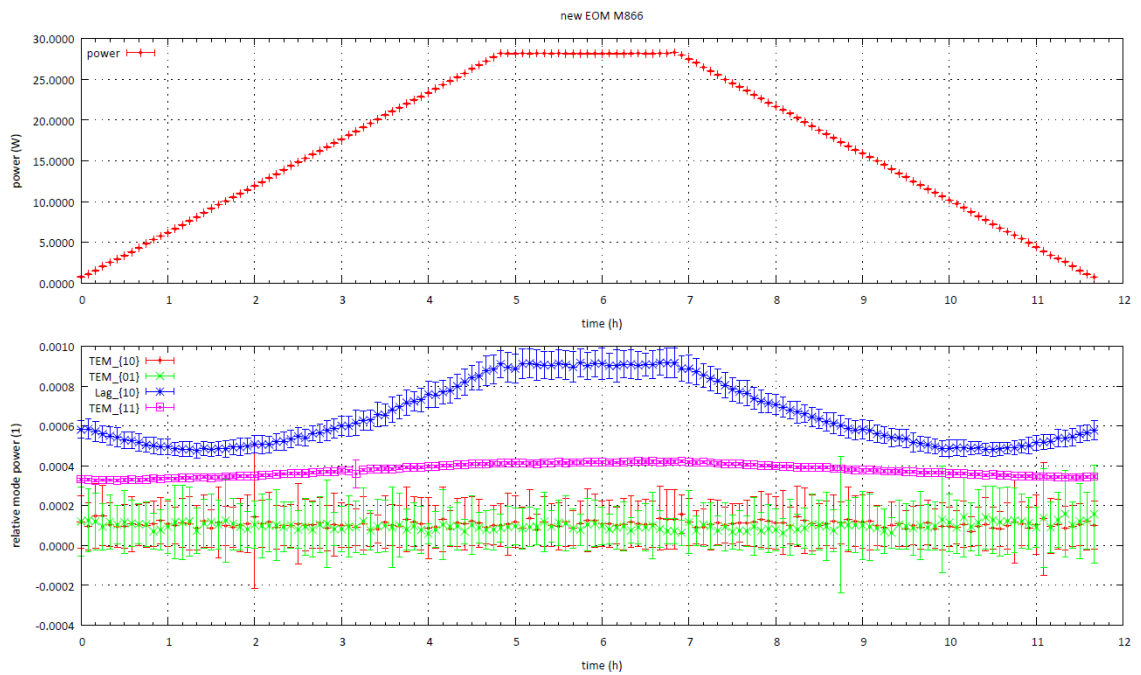


Figure D.2: A thermal lensing measurements of the new RTP EOM unit that was installed on MU2. The unit consists of two EOMs. One EOM consists of *two* RTP crystals with dimensions of $8 \times 8 \times 10 \text{ mm}^3$

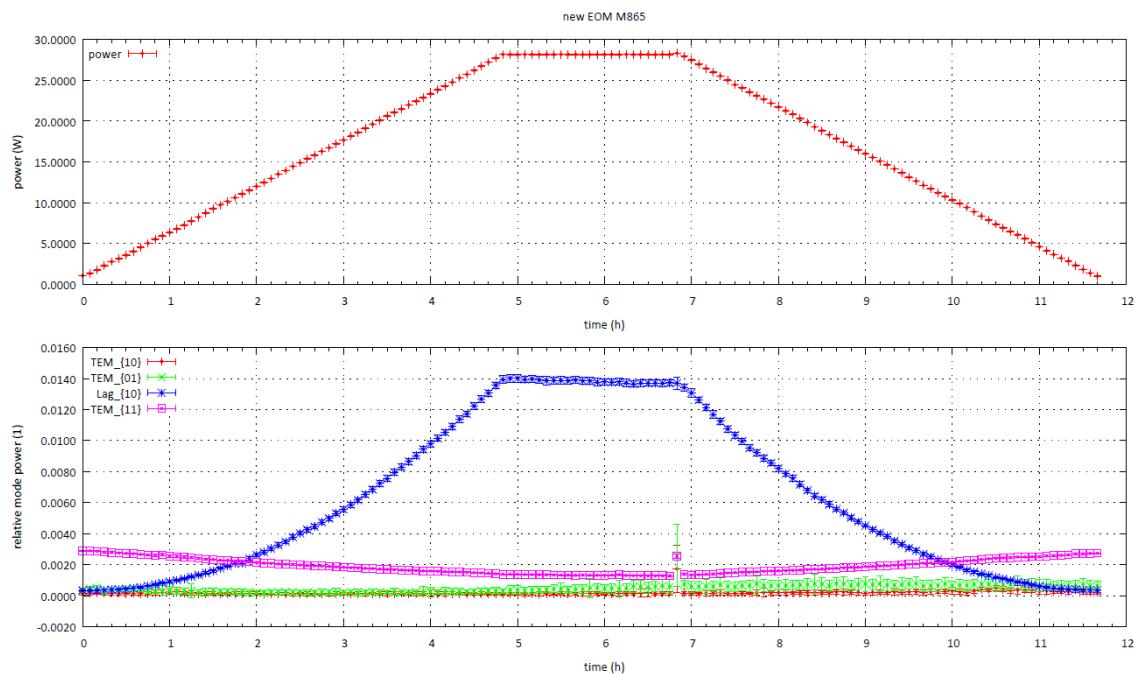


Figure D.3: A thermal lensing measurements of the new RTP EOM unit that was installed on MU3. The unit consists of two EOMs. Each EOM consists of one RTP crystals with dimensions of $6 \times 6 \times 35 \text{ mm}^3$.

D.2 RF matching of the EOMs

Chapter 4.2 discusses the replacement of four EOMs that are used as phase modulators to create modulation SBs. Each EOM is part of a resonant impedance matching circuit which is formed of a so-called matching box, the EOM and the electrical connection between the matching box and the EOM. At the resonance frequency of the matching circuit, the matching box maximizes the power transfer to the load, i.e. the EOM and transforms the amplitude of the RF voltage to higher values at the load. At this point, the principle of these impedance matching circuits is described. They were built at the University of Glasgow with the supervision of Gavin Newton. The following orientates on the explanations that Gavin Newton gave to me and on electrical engineering basics as summarized in [Gro99]. We start this discussion with a simple LC circuit because the resonant matching circuit is actually very similar to it.

A resonant matching circuit as used for the new GEO EOMs is similar to a LC circuit. An LC circuit consists of an inductor with the inductance L and a capacitor with the capacitance C . The capacitor is the EOM in our case and we have to take a resistor R into account which depicts the loss at the EOM. The frequency dependent impedance of this LC circuit is

$$|Z(\omega)| = \frac{1}{\sqrt{\frac{1}{R^2} + \left(\omega C - \frac{1}{\omega L}\right)^2}}. \quad (\text{D.1})$$

If the losses are small, R is large and the resonance frequency $\omega_{\text{res}} = 2\pi f_{\text{res}}$ of this LC circuit can be written as

$$\omega_{\text{res}} = \frac{1}{\sqrt{LC}}. \quad (\text{D.2})$$

At the resonance frequency ω_{res} , the impedance of the LC circuit is maximal and equal to R . Here comes an essential difference between a LC circuit and the resonant matching box into play. The latter is part of the load and has to match the load's impedance to the input impedance of the source which is $50\ \Omega$.¹ Additionally, the creation of sufficiently strong SBs requires voltages across the EOM which are about ten times higher as on the source side. This can be realized by the use of a transformer.

Figure D.4 shows a simplified layout of a resonant matching circuit which fulfills these

¹ Jacobi's Law requires that the impedance of the load is equal to the impedance of the source at the resonance frequency to minimize the reflection r of the RF signal at the resonant matching circuit.

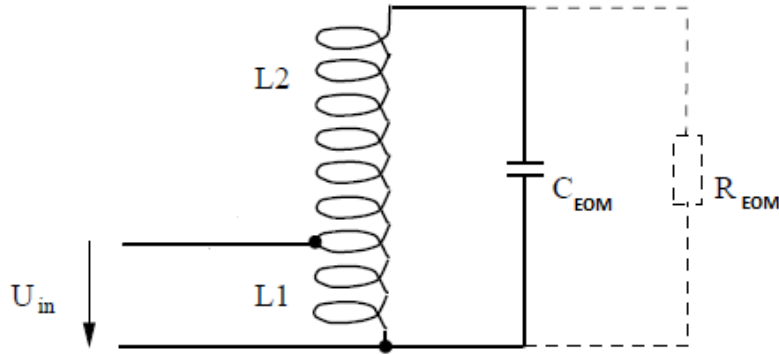


Figure D.4: A simplified RF matching circuit.

tasks. In principle, the inductor of the LC circuit is replaced by a transformer. Its respective coils have the inductance L_1 and L_2 . The input voltage U_1 gets transformed to a secondary voltage at the EOM U_2 . For U_2 , the the known relation

$$\frac{U_1}{U_2} = \frac{N_1}{N_2} = \frac{I_2}{I_1} \quad (\text{D.3})$$

holds. Here, N_1 is the number of turns of the first coil and N_2 the number of turns of the second coil. Furthermore, I_1 and I_2 are the respective currents. Due to $R = U/I$ the impedance is transformed as follows:

$$\frac{Z_1}{Z_2} = \left(\frac{N_1}{N_2}\right)^2. \quad (\text{D.4})$$

Equations D.1 and D.2 stay valid for the resonant circuit. However, the values of the inductance L and the capacitor C include the values for the EOM and the electrical connection between the matching box and the EOM. The EOM has a capacitance C_{EOM} and the wire (“twisted pair cable”) has a capacitance C_{wire} and an inductance L_{wire} . Furthermore, an additional capacitor with tunable capacitance C_{tune} inside the matching box is connected parallel to the EOM. It is used to adjust the resonance frequency of the matching circuit. They are parallel connected, thus the actual L and C of the resonant circuit is the sum of these components. In particular, this trim capacitor can be used to adjust the resonance frequency, while the EOM is placed in the vacuum system. Figure 4.7 in chapter 4.2 shows the whole RF matching setup.

Bibliography

- [Ace08] ACERNESE, F; AMICO, P; ALSHOUBAGY, M A ET AL.: The Virgo 3 km interferometer for gravitational wave detection. *J. Opt. A: Pure Appl. Opt.* (2008), Bd. 10: S. 064009
- [Aso12] ASO, Y; SOMIYA, K; MIYAKAWA, O ET AL.: Length sensing and control strategies for the LCGT interferometer, <http://arxiv.org/pdf/1111.7147v2.pdf> (2012)
- [Bar02] BARR, B. W.; CAGNOLI, G.; CASEY, M. M.; CLUBLEY, D.; CROOKS, D. R. M.; DANZMANN, K.; ELLIFI, E. J.; GOSSLER, S.; GRANT, A.; GROTE, H.; HEP-TONSTALL, A.; HOUGH, J.; JENNRICH, O.; LÜCK, H.; MCINTOSH, S. A.; NEWTON, G. P.; PALMER, D. A.; PLISSI, M. V.; ROBERTSON, D. I.; ROBERTSON, N. A.; ROWAN, S.; SKELDON, K. D.; SNEDDON, P.; STRAIN, K. A.; TORRIE, C. I.; WARD, H.; WILLEMS, P.A.; WILKE, B. und WINKLER, W.: Silica research in Glasgow. *Class. Quantum Grav.* (2002), Bd. 19: S. 1655–1662
- [Bis02] BISHOP, N T und MAHARAJ, S D (Herausgeber): *Proceedings of the 16th International Conference on General Relativity & Gravitation*, World Scientific Publishing Co Pte. Ltd. (2002)
- [Bog11] BOGAN, C.: Layout of the GEO 600 Laser Bench, Techn. Ber., AEI Hannover (2011)
- [Bog12] BOGAN, C: Personal communications (2012)
- [Bog13] BOGAN, C.: *Stabilized High Power Lasers and Spatial Mode Conversion*, Dissertation, Fakultät für Mathematik und Physik der Gottfried Wilhelm Leibniz Universität Hannover (2013)
- [Bon02] BONDU, F. et al.: The VIRGO injection system. *Class. Quantum Grav.* (2002), Bd. 19: S. 1829–1833
- [Bra02] BRACCINI, S.: The VIRGO suspensions. *Phys. Lett. A* (2002), Bd. 175: S. 82–84
- [Cas00] CASEY, M M; WARD, H und ROBERTSON, D I: Computer monitoring and control of the GEO 600 gravitation wave detector. *Phys. Rev. D* (2000), Bd. 63
- [Cav81] CAVES, C M: Quantum-mechanical noise in an interferometer. *Phys. Rev. D* (1981), Bd. 23: S. 1693
- [Dan05] DANZMANN, K: Proposal for upgrading the gravitational wave detector GEO 600 (2005)

- [Deg10] DEGALLAIX, J; GROTE, H; PRIJATELJ, M; HEWITSON, M; HILD, S; AFFELDT, C; FREISE, A; LEONG, J; LÜCK, H; STRAIN, K A; WITTEL, H; WILKE, B und DANZMANN, K: Commissioning of the tuned DC readout at GEO 600. *J. Phys.: Conf. Ser.* (2010), Bd. 228: S. 012013
- [Doo11] DOOLEY, K L: *Design and Performance of high Laser Power Interferometers for Gravitational-Wave Detection*, Dissertation, University of Florida (2011)
- [Doo12] DOOLEY, K L; MUZAMMIL, A A; FELDBAUM, D ET AL.: Thermal effects in the Input Optics of the Enhanced Laser Interferometer Gravitational-wave Observatory interferometers. *Rev. Sci. Inst.* (2012), Bd. 83: S. 033109
- [Dre83a] DREVER, R. et al.: Gravitational wave detectors using laser interferometers and optical cavities: Ideas, principles and prospects. *Proceedings of the NATO Advanced Study Institute on Quantum optics and Experimental General Relativity* (1983), Bd. 11: S. 503–514
- [Dre83b] DREVER, R.W.P.; HALL, J. L.; KOWALSKI, F. V.; HOUGH, J.; FORD, G. M. und MUNLEY, A. J.: Laser phase and frequency stabilisation using an optical resonator. *Appl. Phys. B* (1983), Bd. 31: S. 97–105
- [Ein05] EINSTEIN, A: Zur Elektrodynamik bewegter Körper. *Ann. Phys.* (1905), Bd. 322: S. 891–921
- [Ein16] EINSTEIN, A: Die Grundlagen der allgemeinen Relativitätstheorie. *Ann. Phys.* (1916), Bd. 49: S. 769–822
- [Ein18] EINSTEIN, A: Über Gravitationswellen. *Sitzungsberichte der Königlich Preussischen Akademie der Wissenschaften* (1918), Bd. VIII: S. 154–167
- [Fre03] FREISE, A: *The next Generation of Interferometry: Multi-Frequency Optical Modelling, Control Concepts and Implementation*, Dissertation, Universität Hannover (2003)
- [Fre07] FREDE, M; SCHULZ, B; WILHELM, R; KWEE, P; SEIFERT, F; WILKE, B und KRACHT, D: Fundamental mode, single-frequency laser amplifier for gravitational wave detectors. *Opt. Express* (2007), Bd. 15(2): S. 459–465
- [Fri12] FRICKE, T; SMITH-LEFEBVRE, N; ABBOTT, R ET AL.: DC readout experiment in Enhanced LIGO. *Class. Quantum Grav.* (2012), Bd. 29: S. 065005
- [Goß02] GOSSLER, S; CASEY, M M; FREISE, A; GROTE, H; LÜCK, H ET AL.: The mode-cleaner and suspension aspects of GEO 600. *Class. Quantum Grav.* (2002), Bd. 19: S. 1835–1842
- [Goß04] GOSSLER, S.: *The suspension systems of the interferometric gravitational-wave detector GEO 600*, Dissertation, Universität Hannover (2004), URL <http://edok01.tib.uni-hannover.de/edoks/e01dh04/389559768.pdf>

- [Gra12] GRAVITATIONAL WAVE INTERNATIONAL COMMITTEE: Roadmap: The future of gravitational wave astronomy, <https://gwic.ligo.org/roadmap/> (2012), URL <https://gwic.ligo.org/roadmap/>
- [Gro99] GROTE, H: *Autoalignment am GEO 600 Modecleaner*, Diplomarbeit, Universität Hannover (1999)
- [Gro01] GROTE, H; HEIZEL, A, Gand Freise; GOSSLER, S ET AL.: Automatic beam alignment for the modecleaner cavities of GEO 600. *Applied Optics* (2001)
- [Gro03] GROTE, H: *Making it work: Second generation interferometry in GEO 600!*, Dissertation, Universität Hannover (2003), URL <http://edok01.tib.uni-hannover.de/edoks/e01dh03/373626789.pdf>
- [Gro06] GROUP, UF LIGO und GROUP, IAP: Upgrading the Input Optics for High Power Operation, Techn. Ber. E0660003, LIGO Laboratory (2006)
- [Gro13] GROTE, H; DANZMANN, K; DOOLEY, K L; SCHNABEL, R; SLUTSKY, J und VAHLBRUCH, H: First Long-Term Application of Squeezed States of Light in a Gravitational-Wave Observatory. *Phys. Rev. Lett.* (2013), Bd. 110: S. 181101–181106
- [Har10] HARRY, G M ET AL.: Advanced LIGO: the next generation of gravitational wave detectors. *Class. Quantum Grav.* (2010), Bd. 27: S. 084006
- [Hei99] HEINZEL, G: *Advanced optical techniques for laser-interferometric gravitational-wave detectors.*, Dissertation, Max-Planck-Institut für Quantenoptik (February 1999)
- [Heu04] HEURS, M: *Gravitational waves in a new light - Novel stabilisation schemata for solid-state lasers*, Dissertation, Universität Hannover (2004)
- [Hil06] HILD, S; LÜCK, H; WINKLER, W ET AL.: Measurement of a low-absorption sample of OH-reduced fused silica. *Appl. Opt.* (2006), Bd. 45: S. 7269–7272
- [Hil09] HILD, S; GROTE, H; DEGALLAIX, J ET AL.: DC-readout of a signal-recycled gravitational wave detector. *Class. Quantum Grav.* (2009), Bd. 26: S. 055012
- [Hul75] HULSE, R A und TAYLOR, J H: Discovery of a pulsar in a binary system. *Astrophys. Journal* (1975), Bd. 195: S. 51–53
- [Kha11] KHALAIDOVSKI, A: *Beyond the quantum limit - A squeezed-light laser in GEO*, Dissertation, Gottfried Wilhelm Leibniz Universität Hannover (2011)
- [Kwe11] KWEE, P: Thermal lens measurements, Techn. Ber., AEI Hannover (2011)
- [Lüc04] LÜCK, H; FREISE, A; GOSSLER, S; HILD, S; KAWABE, K und DANZMANN, K: Thermal correction of the radii of curvature of mirrors for GEO 600. *Class. Quantum Grav.* (2004), Bd. 21: S. 985–989
- [Lüc09] LÜCK, H: The Transition to GEO-HF, <https://dcc.ligo.org/cgi-bin/DocDB/ShowDocument?.submit=Number&docid=G0900523&version=> (2009), LIGO document G0900523

- [Lüc10] LÜCK, H; AFFELDT, C; DEGALLAIX, J; GROTE, H; PRIJATELJ, M ET AL.: The upgrade of GEO 600. *J. Phys.: Conf. Ser.* (2010), Bd. 228: S. 012012
- [Mee88] MEERS, B J: Recycling in laser-interferometric gravitational-wave detectors. *Phys. Rev. DD* (1988), Bd. 38: S. 2317
- [Mic81] MICHELSON, A: The relative motion of the Earth and the Luminiferous ether. *The American Journal of Science* (1881), Bd. 22: S. 127–132
- [Miz95] MIZUNO, J: *Comparison of optical configurations for laser-interferometric gravitational-wave detectors*, Dissertation, Universität Hannover (1995)
- [Mor94] MORRISON, E; MEERS, B J; ROBERTSON, D I ET AL.: Automatic alignment of optical interferometers. *Appl. Opt.* (1994), Bd. 33: S. 5041–5049
- [Pei99] PEITHMANN, K.; WIEBROCK, A. und BUSE, K.: Photorefractive properties of highly-doped lithium niobate crystals in the visible and near-infrared. *Applied Physics B: Lasers and Optics* (1999), Bd. 68: S. 777–784
- [Pli00] PLISSI, M V; TORRIE, C I; HUSMAN, M E; ROBERTSON, N A; STRAIN, K A; WARD, H; LÜCK, H und HOUGH, J: GEO 600 tripple pendulum suspension system: Seismic isolation and control. *Rev. Sci. Inst.* (2000), Bd. 71: S. 2539–2545
- [Pri12] PRIJATELJ, M: *Gravitational wave detection with refined light - the implementation of an output mode cleaner at GEO 600*, Dissertation, Universität Hannover (2012)
- [Sal04] SALVESTRINI, J. P.; ABARKAN, M. und FONTANA, M. D.: Comparative study of nonlinear optical crystals for electro-optic Q-switching of laser resonators. *Optical Materials* (2004), Bd. 26: S. 449 – 458
- [Sau94] SAULSON, Peter R.: *Interferometric gravitational wave detectors*, World Scientific Publishing Co Pte. Ltd. (1994)
- [Sav98] SAVAGE, R. L. et al.: A highly stabilized 10-watt Nd:YAG laser for the Laser Interferometer Gravitational-Wave Observatory (LIGO). *Laser Phys.* (1998), Bd. 8: S. 679–685
- [Sch97] SCHNIER, D.; MIZUNO, J; HEINZEL, G; LÜCK, H.; RÜDIGER, A.; SCHILLING, R.; SCHREMPLE, M.; WINKLER, W. und DANZMANN, K.: Power-Recycling in the Garching 30m prototype interferometer for gravitational-wave detection. *Phys. Lett. A* (1997), Bd. 225: S. 210–216
- [Smi04] SMITH, J. R.; CAGNOLI, G.; CROOKS, D. R. M.; FEJER, M. M.; GOSSLER, S.; LÜCK, H.; ROWAN, S.; HOUGH, J. und DANZMANN, K.: Mechanical quality factor measurements of monolithically suspended fused silica test masses of the GEO 600 gravitation-wave detector. *Class. Quantum Grav.* (2004), Bd. 21: S. 1091–1098

- [Smi06] SMITH, J R: *Formulation of Instrument Noise Analysis Techniques and Their Use in the Commissioning of the Gravitational Wave Observatory, GEO 600*, Dissertation, Gottfried Wilhelm Leibniz Universität Hannover (2006)
- [Smi09] SMITH, J R ET AL.: The path to the Enhanced and Advanced LIGO gravitational-wave detectors. *Class. Quantum Grav.* (2009), Bd. 26: S. 114013
- [Str91] STRAIN, K A und MEERS, B J: Experimental Demonstration of Dual Recycling for Interferometric Gravitational-Wave Detectors. *Phys. Rev. Lett.* (1991), Bd. 66: S. 1391–1394
- [Str02] STRAIN, K A: Electrostatic drives for GEO 600, Internal note (2002)
- [The09] THE VIRGO COLLABORATION: Advanced Virgo baseline design, <https://tds.ego-gw.it/itf/tds/index.php?callContent=2&callCode=6616&title=Advanced%20Virgo%20baseline%20design&startPage=> (2009), vIRGO document VIR-0027A-09
- [The11] THE LIGO SCIENTIFIC COLLABORATION: A gravitational wave observatory operating beyond the quantum shot-noise limit. *Nature physics* (2011), Bd. 7: S. 962–965
- [Tor00] TORRIE, C I: *Development of suspension for the GEO 600 gravitational-wave detector*, Dissertation, University of Glasgow, Department of Physics and Astronomy (2000)
- [Vah08] VAHLBRUCH, H: *Squeezed Light for Gravitational Wave Astronomy*, Dissertation, Gottfried Wilhelm Leibniz Universität Hannover (2008)
- [Web60] WEBER, J: Detection and generation of gravitational waves. *Phys. Rev.* (1960), Bd. 117: S. 306–313
- [Wil00] WILKE, B et al.: The GEO stabilized laser system and the current-lock technique. *Gravitational waves AIP, Melville, AIP Conf. Proc* (2000), Bd. 523: S. 215–221
- [Wil06] WILKE, B; AJITH, P; ALLEN, B ET AL.: The GEO-HF project. *Class. Quantum Grav.* (2006), Bd. 24: S. 207–214
- [Wit09] WITTEL, H: *Compensation of thermal lensing in the GEO 600 beam splitter*, Diplomarbeit, Universität Hannover (2009)
- [Wit12] WITTEL, H: Personal communications (2012)
- [Wit14] WITTEL, H; LÜCK, H.; AFFELDT, C; DOOLEY, K L; GROTE, H; LEONG, J; PRIJATELJ, M; SCHREIBER, E; SLUTSKY, J; STRAIN, K A; WAS, M; WILKE, B und DANZMANN, K: Thermal Correction of Astigmatism in the Gravitational Wave Observatory GEO 600. *accepted for publication in Class. Quantum Grav.* (2014)

-
- [Yak10] YAKAUNIN, K N; MARRONETTI, P; MAEZZACAPPA, A ET AL.: Gravitational waves from core collapse supernovae. *Class. Quantum Grav.* (2010), Bd. 27: S. 194005
- [Yao04] YAO, J.; CHEN, Y; YAN, B.; DENG, H.; CHEN, S.; XU, J. und ZHANG, G.: Characteristics of domain inversion in magnesium-oxide-doped lithium niobate. *Physica B: Condensed Matter* (2004), Bd. 352: S. 294–298
- [Zaw02] ZAWISCHA, I; BRENDL, M; DANZMANN, K ET AL.: The GEO 600 laser system. *Class. Quantum Grav.* (2002), Bd. 19: S. 1775–1781

Acknowledgments

It is my pleasure to thank Karsten Danzmann for the opportunity to work at the Albert-Einstein-Institute. The AEI is certainly a great place to do PhD studies and I had the incredible luck to work for its – in my opinion – most interesting project: GEO 600. I am convinced that it is a rare opportunity for a student that was inexperienced in this field to “play” with that much freedom at the heart of a GW detector.

The GEO 600 commissioning team is the group of people that contributed most of all to this work. A big thanks to all of them and to all people who contributed to this amazing project!

It was fun to share an office in most of my “Hannover time” with Mirko Prijatelj. I also thank you for your friendship and the discussions during the time!

I thank Kate Dooley, Birthe Klebow, Hartmut Grote, Christoph Mahrtdt, Jonathan Leong, Holger Wittel, Emil Schreiber and Harald Lück for proofreading parts of this thesis. Any remaining errors are entirely my fault.

A very big thanks goes to the GEO operators: Marc Brinkmann, Michael Weinert, Volker Kringel and Walter Grass. Ihr seid spitze.

A special thanks goes to Glasgow: Stefan Hild for inviting me so many times, the chance to work at the Institute of Gravitational Research of the University of Glasgow, for his interest on the power up story and for leading me on my first Munro. I thank Byran Barr for his help while testing the new EOMs and safely leading me through the JIF lab. Ken Strain for his valuable experience he shared with me, his availability and kind words. Last but not least I thank Gavin Newton for his supervision while building those matching boxes!

I thank my supervisor Hartmut Grote for his support and his patience. I owe you one!

I thank Jonathan R. Leong for the same reason. I am happy to call you a friend!

Ich danke meiner Mutter und meinen Vater für alles!

Zum Schluss möchte ich mich bei meiner Frau Dina bedanken. Du hast einen großen Anteil an dieser Geschichte.

Curriculum vitae

<i>Name</i>	Christoph Affeldt
<i>Date of birth</i>	26th of May 1981
<i>Place of birth</i>	Bad Pyrmont, Germany
<i>Marital status</i>	Married
<i>email</i>	Christoph.Affeldt@aei.mpg.de

- 04.2009–present* Doctoral studies at Albert-Einstein-Institute,
Max-Planck-Institute for Gravitational Physics, Cluster of Excellence QUEST,
and Gottfried Wilhelm Leibniz Universität, Hannover
- 04.2009–present* Member of the International Max Planck Research School (IMPRS)
on Gravitational Wave Astronomy
- 09.2011–present* Member of the LIGO Scientific Collaboration
- 04.2007-05.2008* Diploma thesis at the Institute for Quantum Optics,
Gottfried Wilhelm Leibniz Universität Hannover
Lasersystem zur erzeugung dunkler Solitonen in Bose-Einstein Kondensaten
(translates to “Laser system for the creation of dark solitons in
Bose-Einstein condensates”)
- 10.2002–07.2008* Physics studies, Gottfried Wilhelm Leibniz Universität Hannover
- 07.2001–05.2002* Alternative civilian service
- 06.2001* Abitur (Graduation), Humboldt Gymnasium, Bad Pyrmont

Publications with immediate relation to this thesis

- 1 H. Wittel, H. Lück, C. Affeldt, K.L. Dooley, H. Grote, J.R. Leong, M. Prijatelj, E. Schreiber, J. Slutsky, K. Strain, M. Was, B. Willke and K. Danzmann
Thermal Correction of Astigmatism in the Gravitational Wave Observatory GEO600
accepted for publication in Class. Quantum Grav., 2014
- 2 M. Prijatelj, J. Degallaix, H. Grote, J. Leong, C. Affeldt, S. Hild, H. Lück, J. Slutsky, H. Wittel, K. Strain and K. Danzmann
The output mode cleaner of GEO 600
Class. Quantum Grav., 29:055009, 2012
- 3 J. Abadie, . . . , R. Adhikari, C. Affeldt, B. Allen, . . . , J. Zweizig
A gravitational wave observatory operating beyond the quantum shot-noise limit
Nature Phys., 7:962-965, 2011
- 4 M. Prijatelj, H. Grote, J. Degallaix, M. Hewitson, S. Hild, C. Affeldt, A. Freise, J. Leong, H. Lück, K. A. Strain, H. Wittel, B. Willke and K. Danzmann
Control and automatic alignment of the output mode cleaner of GEO600
J. Phys.: Conf. Ser., 228:012014, 2010
- 5 J. Degallaix, H. Grote, M. Prijatelj, M. Hewitson, S. Hild, C. Affeldt, A. Freise, J. Leong, H. Lück, K. A. Strain, H. Wittel, B. Willke and K. Danzmann
Commissioning of the tuned DC readout at GEO 600
J. Phys.: Conf. Ser., 228:012013, 2010

Further publications

- 1 J. Aasi, . . ., R. Adhikari, C. Affeldt, M. Agathos, . . ., J. Zweizig
Search for long-lived gravitational-wave transients coincident with long gamma-ray bursts
Phys. Rev. D 88(2013) 122004
- 2 J. Aasi, . . ., R. Adhikari, C. Affeldt, M. Agathos, . . ., J. Zweizig
A directed search for continuous Gravitational Waves from the Galactic Center
Phys. Rev. D 88(2013) 102022
- 3 J. Aasi, . . ., R. Adhikari, C. Affeldt, M. Agathos, . . ., J. Zweizig
Parameter estimation for compact binary coalescence signals with the first generation gravitational wave detector network
Phys. Rev. D 88(2013) 062001
- 4 J. Aasi, . . ., R. Adhikari, C. Affeldt, M. Agathos, . . ., J. Zweizig
Enhanced sensitivity of the LIGO gravitational wave detector by using squeezed states of light
Nature Photonics 7 (2013) 613
- 5 J. Aasi, . . ., R. Adhikari, C. Affeldt, M. Agathos, . . ., J. Zweizig
Search for Gravitational Waves from Binary Black Hole Inspiral, Merger and Ringdown in LIGO-Virgo Data from 2009-2010
Phys. Rev. D 87 (2013) 022002
- 6 J. Aasi, . . ., R. Adhikari, C. Affeldt, M. Agathos, . . ., J. Zweizig
Einstein@Home all-sky search for periodic gravitational waves in LIGO S5 data
Phys. Rev. D 87 (2013) 042001
- 7 J. Aasi, . . ., R. Adhikari, C. Affeldt, M. Agathos, . . ., J. Zweizig
A first search for coincident gravitational waves and high energy neutrinos using LIGO, Virgo and ANTARES data from 2007
JCAP 1306 (2013) 008
- 8 J. Aasi, . . ., R. Adhikari, C. Affeldt, M. Agathos, . . ., J. Zweizig
Search for gravitational waves associated with gamma-ray bursts during LIGO science run 6 and Virgo science run 2 and 3
Astrophys. J. 760 (2012) 12
- 9 J. Aasi, . . ., R. Adhikari, C. Affeldt, M. Agathos, . . ., J. Zweizig
Swift Follow-Up Observations Of Candidate Gravitational-Wave Transient Events
ApJS 203 (2012) 28
- 10 J. Aasi, . . ., R. Adhikari, C. Affeldt, M. Agathos, . . ., J. Zweizig
Virgo data characterization and impact on gravitational wave searches
Class. Quantum Grav. 29 (2012) 155002

- 11 J. Aasi, . . ., R. Adhikari, C. Affeldt, M. Agathos, . . ., J. Zweizig
All-sky search for gravitational-wave bursts in the second joint LIGO-Virgo run
Phys. Rev. D 85 (2012) 122007
- 12 J. Aasi, . . ., R. Adhikari, C. Affeldt, M. Agathos, . . ., J. Zweizig
Search for Gravitational Waves from Intermediate Mass Binary Black Holes
Phys. Rev. D 85 (2012) 102004
- 13 J. Abadie, . . ., R. Adhikari, C. Affeldt, M. Agathos, . . ., J. Zweizig
Implications for the Origin of GRB 051103 from LIGO Observations
Astrophys. J. 755 (2012) 2
- 14 J. Abadie, . . ., R. Adhikari, C. Affeldt, M. Agathos, . . ., J. Zweizig
Upper limits on a stochastic gravitational-wave background using LIGO and Virgo interferometers at 600-1000 Hz
Phys. Rev. D 85 (2012) 122001
- 15 J. Abadie, . . ., R. Adhikari, C. Affeldt, M. Agathos, . . ., J. Zweizig
First Low-Latency LIGO+Virgo Search for Binary Inspirals and their Electromagnetic Counterparts
Astron Astrophys 541 (2012) A155
- 16 J. Abadie, . . ., R. Adhikari, C. Affeldt, M. Agathos, . . ., J. Zweizig
Search for Gravitational Waves from Low Mass Compact Binary Coalescence in LIGO's Sixth Science Run and Virgo's Science Runs 2 and 3
Phys. Rev D85 (2012) 082002
- 17 J. Abadie, . . ., R. Adhikari, C. Affeldt, M. Agathos, . . ., J. Zweizig
All-sky search for periodic gravitational waves in the full S5 LIGO data
Phys. Rev. D85 (2012) 022001
- 18 J. Abadie, . . ., R. Adhikari, C. Affeldt, M. Agathos, . . ., J. Zweizig
Implementation and testing of the first prompt search for gravitational wave transients with electromagnetic counterparts
Astron Astrophys 539 (2012) A124